Search for Rare Exclusive Decays of the Higgs and Z Bosons to a Meson and a Photon with the ATLAS Detector

Rhys Edward Owen

A thesis submitted to the University of Birmingham
for the degree of
DOCTOR OF PHILOSOPHY

Particle Physics Group
School of Physics and Astronomy
University of Birmingham
September 2017

Abstract

IN 2015 the ATLAS detector resumed data taking operations after the first long shutdown for the Large Hadron Collider at CERN. During this shutdown upgrades were made to the Level-1 Calorimeter trigger in order to maintain the physics performance in the anticipated Run-2 conditions. Changes to the hardware-based isolation were implemented and validated. These changes allowed for a low threshold Level-1 electromagnetic trigger to be maintained. During the first data-taking a measurement of the W and Z boson cross-sections was performed, which offered the first measurement at the new centre-of-mass energy and was used for the detector commissioning. One of the main goals of the LHC is to understand the nature of the Higgs boson which has been so far mainly observed in its decays to the electroweak bosons. A possible channel to observe the decays to the light quarks is in the final state including a meson and a photon which provides an easily triggerable signature compared to direct quark-antiquark production. The searches for the Higgs and Z bosons decaying to a ϕ or ρ^0 meson and a photon are presented in detail.

Acknowledgements

I would like to thank all of the people on my supervision team without whom it would not have been possible to complete this work: Bruce Barnett, Juraj Bracinik, Stephen Hillier, Konstantinos Nikolopoulos, David Sankey and Alan Watson. I would also like to thank the ATLAS collaboration for providing an interesting and engaging environment to work in. I have been very lucky to be supported and hosted by two institutions The University of Birmingham and The Rutherford Appleton Laboratory in the work and funded by the STFC, RAL and European Research Council (ERC) under the European Union's Horizon 2020 research and innovation programme (grant agreement No. 714893).

I am also indebted to those who have given me emotional support of the years for office mates to house mates when I have found the going particularly tough. Most of all I must thank my parents Helen and Jeff Owen for their unending support for me though 22 years of full time education.

Author's Contribution

THIS thesis covers work which I performed over the course of my post-graduate studies. It begins with a summary of the theoretical background to the work collated from the literature, also presented are examples of the contemporary state of the art searches and measurements surrounding the Higgs boson. Next a summary of the operation and performance of the ATLAS detector at the large hadron collider (LHC) is given as this is the experiment used to perform the analyses presented as well as technical work I completed on the trigger system which is documented in an internal ATLAS document.

Finally the two analyses which I worked on are presented, the first of which was the initial cross-section measurement for the W and Z bosons at the centre-of-mass energy $\sqrt{s} = 13$ TeV. This analysis was performed at the beginning of the Run-2 operating period of the LHC and provided both the first measurement of the production cross-section in this new energy regime and an independent validation of the detector performance after the long shutdown, this is published in Ref. [1]. I was part of the analysis team and contributed various cross-checks of the event selection, as well as developing a data-driven estimation of the "multijet" background the $W \to \mu\nu$ channel detailed in Section 3.4.3.

The second analysis concerns the search for rare decays of the Higgs and Z bosons to a meson and a photon. Both of these processes are exceedingly rare but can provide an insight into the structure of the standard model. For the Higgs boson this decay mode gives a unique opportunity to directly measure the Higgs interactions with light quarks at the LHC. I worked on the previously published iteration of this analysis which looked only at $H/Z \to \phi\gamma$ with 2015 data, Ref. [2]. I was the primary author on the updated version which includes luminosity from the 2016 pp run of the LHC, as well as, extending the analysis to a further final state $H/Z \to \rho\gamma$, which was recently made public as preliminary results and shown at conferences [3].

Contents

Chapter 1

Theory Background

1.1 The Standard Model of Particle Physics

THE Standard Model of Particle Physics (SM) is the most successful description of the interactions of "fundamental" particles which comprise the matter we interact with in the universe. The model contains a family of particles as shown in Figure 1.1. These particles fall into two main categories, the fermions with half-integer spin being matter and bosons with integer spin acting as force carriers.

The model covers several types of interactions, from the electroweak interactions including the interactions of light and β-decay of nucleons, to quantum chromo-dynamics (QCD) which governs the strong nuclear interactions between nucleon constituents.

The final particle in this was the Higgs Boson, discovered by the ATLAS and CMS experiments [4, 5] in 2012 which led to the 2013 Nobel prize was awarded to Englert and Higgs for their contributions to the development of the theory [6].

1.1.1 Quantum Chromo-Dynamics

Quantum Chromo-Dynamics (QCD) is the portion of the SM which deals with the interactions of the quarks and the strong force carrier the gluon. Qualitatively the strong interactions are explained by the introduction of a new charge analogous to the electric charge. However where the electric charge has two possible values $(+, -)$ the strong charge has six possible values $(R, G, B, \bar{R}, \bar{G}, \bar{B})$. Furthermore the only observed particles in the theory are colour singlets so must be composites of partons whose colour charges

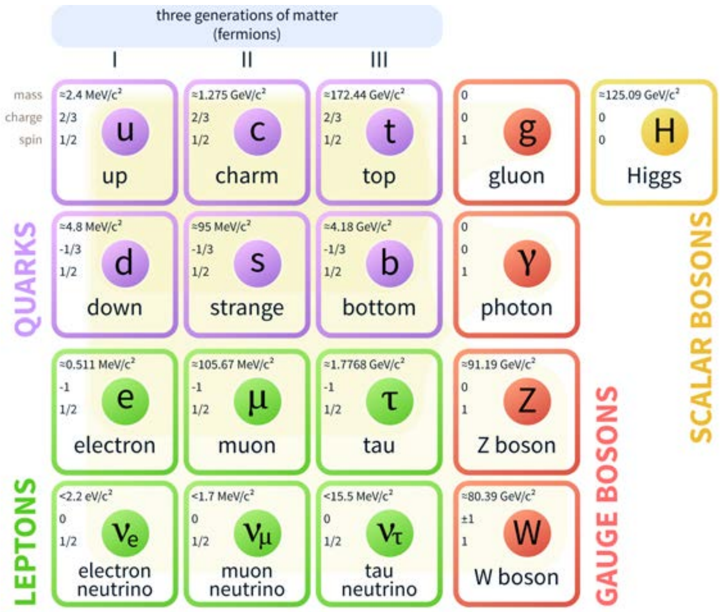

Figure 1.1: Particle content of the Standard Model [7]

sum to zero. The colour neutral combinations can be pairs of colour and anti-colour ($R\bar{R}, G\bar{G}, B\bar{B}$) known as mesons or a combination of all three colours, hence the analogy with macroscopic colour, ($RGB, \overline{RGB}$) known as baryons.

These partons of QCD are understood to be the quarks and gluons shown in Figure 1.1. The quarks are organised into two families based on their electric charge and named after the first generation, with "up-type" quarks having electric charge $+2/3\,\mathrm{e}$ and the "down-type" quarks having an electric charge $-1/3\,\mathrm{e}$. In addition to this, there are three generations each with increasing mass leading to six total quarks.

The most well known baryons are the proton (uud) and neutron (udd) which form the nuclei of the normal matter which surrounds us but several other combinations of quark content are possible which lead to the understanding of the quark model and particle spectrum we have today [8].

While QCD can be defined mathematically as a non-Abelian SU(3) gauge group, in many cases perturbative calculations are impossible as the strong coupling constant α_s is large for small energy scales, but at larger energy scales the running of the coupling leads to it decreasing to a point where perturbative calculations can be performed.

Owing to this long history and the difficulties with calculation, a phenomenological approach is often used for the treatment of QCD in experiments. For example it is common in experiments at pp colliders to estimate the background contribution from the underlying interactions of the two protons directly from the data instead of relying on the Monte Carlo simulations.

Parton distribution functions (PDFs) are a further phenomenological approach taken when dealing with QCD. PDFs are used in calculations and simulation involving the interaction between a hadron and another object (possibly a photon or other hadron). These functions represent the probability of a given parton carrying a given fraction of the total hadron momentum when interacting. For a proton these partons can be one of the valence quarks (uud) which describe the proton state but at higher energies there is also a large contribution from gluons and virtual quark anti-quark pairs which are created spontaneously within the proton as a result of the self-interacting nature of QCD. These are commonly known as sea quarks. Mathematically these PDFs rely on the idea that QCD is factorizable and that these universal objects can be extracted from one set of measurements, for example deep inelastic scattering measurements involving an electron and a proton, and used to make predictions for proton-proton collisions [9].

1.1.2 Electroweak Dynamics

The electroweak sector of the SM follows from the unification of theories governing the electromagnetic interactions between electric charge and the photon, and the weak interactions between weak charge with the W and Z bosons.

Like the rest of the SM these interactions are described by a quantum field theory using a gauge group, in this case the groups in question are $SU(2)$ representing weak isospin and $U(1)$ of hypercharge. The weak interactions are chiral and only interact with so-called "left handed" particles, hence "right handed" particles have an Isospin T value of 0. Hypercharge Y is related to the charge and the third component of weak isospin T^3 by equation 1.1 [10]. This leads to the quantum numbers for leptons and quarks shown in Table 1.1.

$$Q = T^3 + \frac{Y}{2} \tag{1.1}$$

This combination of gauge groups results in four gauge bosons; B_μ of hypercharge and three W^a_μ bosons of isospin. These fields mix in order to produce the physically-observed

	T	T^3	Q	Y
ν_{e_L}	$1/2$	$1/2$	0	-1
e_L^-	$1/2$	$-1/2$	-1	-1
e_R^-	0	0	-1	-2
u_L	$1/2$	$1/2$	$2/3$	$1/3$
d_L	$1/2$	$-1/2$	$-1/3$	$1/3$
u_R	0	0	$2/3$	$4/3$
d_R	0	0	$-1/3$	$-2/3$

Table 1.1: Electroweak quantum numbers for the first generation leptons and quarks

electroweak bosons as described in equation 1.2.

$$\begin{aligned} A_\mu &\equiv \sin\theta_w W_\mu^3 + \cos\theta_w B_\mu && \text{(Photon)} \\ Z_\mu &\equiv \cos\theta_w W_\mu^3 - \sin\theta_w B_\mu && \text{(Z^0 Boson)} \\ W_\mu^\pm &\equiv \frac{1}{\sqrt{2}}(W_\mu^1 \mp iW_\mu^2)^2 && \text{($W^\pm$ Bosons)} \end{aligned} \tag{1.2}$$

1.1.3 Higgs Mechanism

Observations of the electroweak bosons show that while the photon is massless the W and Z bosons are massive. To produce these masses a simple term of the form $M^2 W_\mu W^\mu$ cannot be inserted as this would break the gauge invariance of the model.

The Brout–Englert–Higgs (BEH) mechanism was a proposed solution to this problem. The mechanism introduces an additional complex doublet scalar field into the Standard Model with a characteristic non-zero vacuum expectation value. The potential energy of such a field of the form $V(H) = -m^2|H|^2 + \lambda|H|^4$ is illustrated in Figure 1.2, and when combined with the other electroweak fields gives the Lagrangian shown in Equation 1.3 [11].

$$\mathcal{L} = -\frac{1}{4}(W_{\mu\nu}^a)^2 - \frac{1}{4}B_{\mu\nu}^2 + (D_\mu H)^\dagger(D_\mu H) + m^2 H^\dagger H - \lambda(H^\dagger H)^2 \tag{1.3}$$

This field gives the theory four additional degrees of freedom, three of which become longitudinal states of the electroweak bosons. It also makes a prediction for the relative masses of the W and Z bosons described in equation 1.4 (where θ_w is the weak mixing

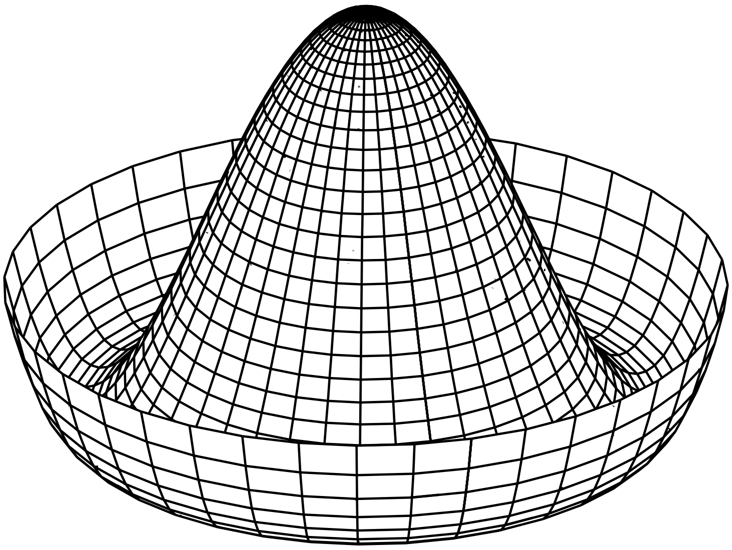

Figure 1.2: Example of Higgs field with symmetric origin but non-symmetric ground state [12]

angle).

$$m_Z = \frac{m_W}{\cos\theta_w} \tag{1.4}$$

The final additional degree of freedom represents an additional massive boson. After the Lagrangian in Equation 1.3 has been expanded out in terms of the physical fields around the vacuum from Equation 1.2 the following terms relating to the Higgs bosons remain [11].

$$\begin{aligned}\mathcal{L}_{\text{Higgs}} = &-\frac{1}{2}h(\Box + m_h^2)h - g\frac{m_h^2}{4m_W}h^3 - \frac{g^2}{32}\frac{m_h^2}{m_W^2}h^4 \\ &+ 2\frac{h}{v}\left(m_W^2 W_\mu^+ W_\mu^- + \frac{1}{2}m_Z^2 Z_\mu Z_\mu\right) + \left(\frac{h}{v}\right)^2\left(m_W^2 W_\mu^+ W_\mu^- + \frac{1}{2}m_Z^2 Z_\mu Z_\mu\right)\end{aligned} \tag{1.5}$$

These terms show the mass term of the Higgs boson as an additional parameter of the model (m_h) as well as the interactions of this new boson with the electroweak bosons which are proportional to their masses squared.

1.1.4 Yukawa Interactions

As described above the masses for the massive bosons in the SM are derived from the BEH mechanism making them directly tied with the Higgs boson. This mechanism does not however intrinsically have any interactions to describe the masses of the fermions.

The minimal solution to this problem is the insertion of the Yukawa couplings into the theory. These are gauge invariant mass terms which lead to a coupling between each of the fermion fields and the Higgs field proportional to the fermion masses.

As discussed above the $SU(2) \times U(1)$ is a chiral theory with a separate set of "left-handed" and "right-handed" particle fields. These two fields should be connected in a mass term which represents the physical particles we observe.

The left-handed fermion fields are arranged into three generations of isospin doublets, their right-handed counterparts are arranged in isospin singlets again indexed by their generation. This is shown explicitly for the quarks below.

$$\begin{aligned} Q^i &= \begin{pmatrix} u_L \\ d_L \end{pmatrix}, \begin{pmatrix} c_L \\ s_L \end{pmatrix}, \begin{pmatrix} t_L \\ b_L \end{pmatrix} \\ u_R^i &= u_R, c_R, t_R \\ d_R^i &= d_R, s_R, b_R \end{aligned} \tag{1.6}$$

The Lagrangian in Equation 1.3 can then be extended with Yukawa terms for the down-type quarks (d, s, b) of the form:

$$\mathcal{L}_{\text{Yukawa}} = -Y_{ij}^d \bar{Q}^i H d_R^j + h.c. \tag{1.7}$$

After symmetry breaking the Lagrangian is left with term such as Equation 1.8 where there is a mass term with $(m_d^i)^2 = \frac{y_d^i v}{\sqrt{2}}$ and a coupling with the Higgs boson proportional to $\frac{y_d^i}{\sqrt{2}} = \frac{m_d^i}{v}$. So unlike the electroweak bosons the fermions obtain mass and should couple to the Higgs boson proportionally to their mass through their own distinct mechanism.

$$\mathcal{L}_{\text{Yukawa}} = \underbrace{-\frac{y_d^j v}{\sqrt{2}} \cdot \bar{d}_L^j d_R^j}_{\text{mass term}} - \underbrace{\frac{y_d^j}{\sqrt{2}} \cdot h \bar{d}_L^j d_R^j}_{\text{Yukawa coupling term}} + h.c. \tag{1.8}$$

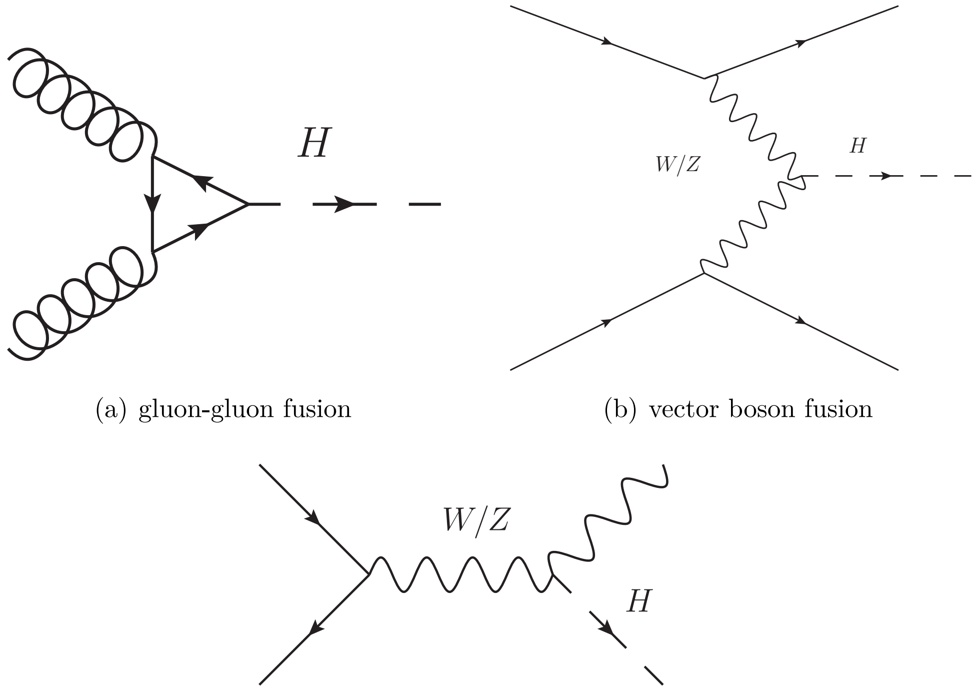

(a) gluon-gluon fusion

(b) vector boson fusion

(c) vector boson assosiated production

Figure 1.3: Common Higgs boson production modes at the LHC

1.1.5 Higgs Production and Decay at the LHC

The Large Hadron Collider (LHC) at CERN is a proton-proton (pp) particle collider now operating at a centre of mass energy of $\sqrt{s} = 13$ TeV. A more detailed description is given in Section 2.1. These conditions affect the possible production modes of Higgs bosons.

The most common production mode is gluon fusion, where two gluons fuse though a heavy quark loop to produce a Higgs boson as shown in Figure 1.3(a). This represents 87% of the Higgs bosons produced at the LHC [13].

The next most important production mechanism observed at the LHC is vector boson fusion. This mode is particularly interesting as there are two quark lines escaping from the Feynman diagram in Figure 1.3(b); these lead to a discriminant tag of two hadronic jets with a large rapidity gap. This tag on the production mode can help enhance sensitivity especially for hadronic final states.

A final common production mode at the LHC is associated production with an electroweak boson as shown in Figure 1.3(c). This is another production mode which can be identified by the decaying boson.

The production cross-sections for these various modes are summarised in Figure 1.4(a)

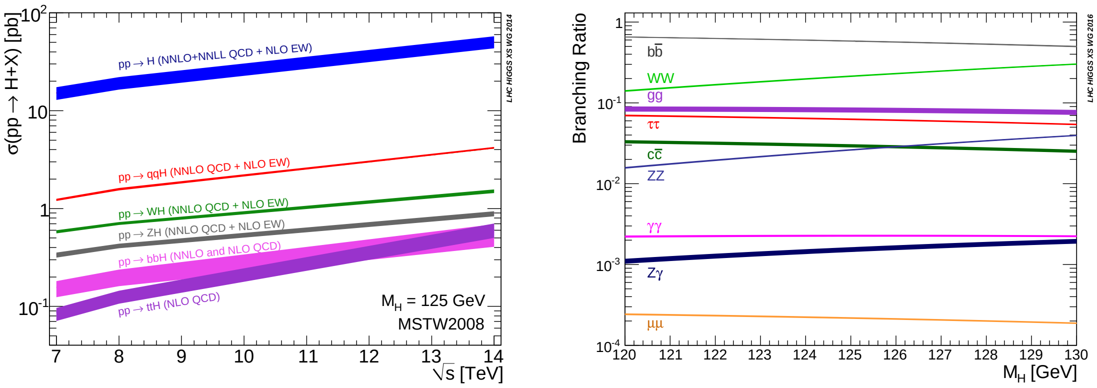

(a) Higgs production cross-sections

(b) Higgs decay branching-ratios

Figure 1.4: Summay of Higgs production and decay modes at the LHC[13]

for various centre-of-mass energies. Also shown in Figure 1.4(b) are the Standard Model prediction for the Higgs boson decay branching ratio. As discussed previously the coupling between the Higgs boson and fermions in the Standard Model are proportional to their mass, whereas the boson couplings are proportional to mass squared. Not shown is the branching ratio to $s\bar{s}$ which is calculated in Ref [14] to be $2.46^{+4.88}_{-4.86} \times 10^{-4}$ for $m_H =$ 125 GeV.

1.2 Summary of the current state of Higgs Boson Measurements

Since the discovery of the Higgs boson in 2012 there have been several analyses seeking to enhance the understanding of its properties. These continued studies are important not just to complete our characterisations of this new boson but also as a window to possible new physics. The scalar field introduced in the BEH mechanism is the simplest in a family of possible fields which could produce the same electroweak symmetry breaking but many of these also lead to additional Higgs-like bosons or other corrections to the Higgs interactions.

The latest cross-section measurement for the Higgs boson has been performed by the ATLAS collaboration at the centre-of-mass energy $\sqrt{s} = 13$ TeV and found to be $57.0^{+6.0}_{-5.9}(\text{stat.})^{+4.0}_{-3.3}(\text{syst.})$ pb [15] assuming the predicted SM branching ratios. This is compared with previous measurements and predictions for a range of centre-of-mass energies

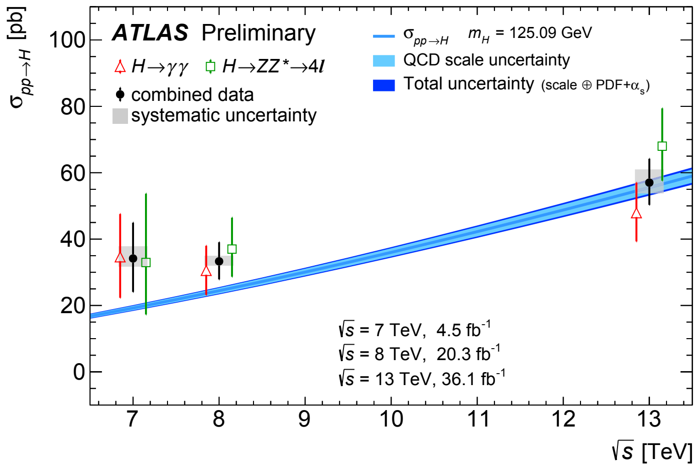

Figure 1.5: Total $pp \to H + X$ cross-sections measured at centre-of-mass energies of 7, 8, and 13 TeV, compared to Standard Model predictions at up to N3LO in QCD. [15]

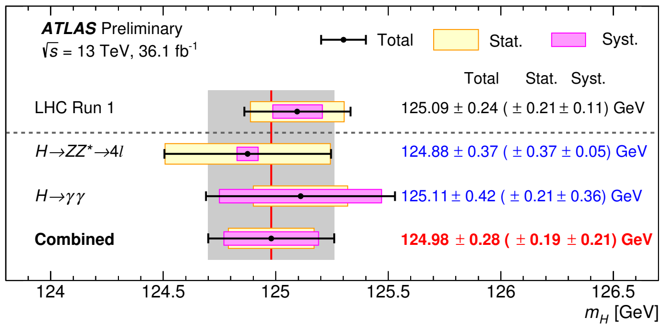

Figure 1.6: Summary of the Higgs boson mass measurements from the individual and combined analyses described in Ref.[16], compared to the combined Run 1 measurement by ATLAS and CMS. [16]

in Figure 1.5.

The same dataset has also been used to measure the mass of the Higgs boson with the $H \to ZZ^* \to 4\ell$ channel and the $H \to \gamma\gamma$ channel. This combination is compatible with the ATLAS and CMS measurements from Run-1 and already has comparable statistical errors [16]. The comparison can be seen in Figure 1.6.

At the same time an independent dataset from the other general purpose detector at the LHC, CMS [17], has also been analysed. Considering the $H \to ZZ^* \to 4\ell$ they also find a cross-section compatible with the SM assuming the SM branching ratios [18]. The clear signal peak in Figure 1.7 is also used to extract the mass of the Higgs Boson. This is found to be $m_H = 125.26 \pm 0.21$ GeV which is compatible with the combined Run-1 measurement from ATLAS and CMS of $m_H = 125.09 \pm 0.21$ (stat.) ± 0.11 (syst.) GeV [19].

The first discovery of the Higgs boson was though its decays to electroweak bosons.

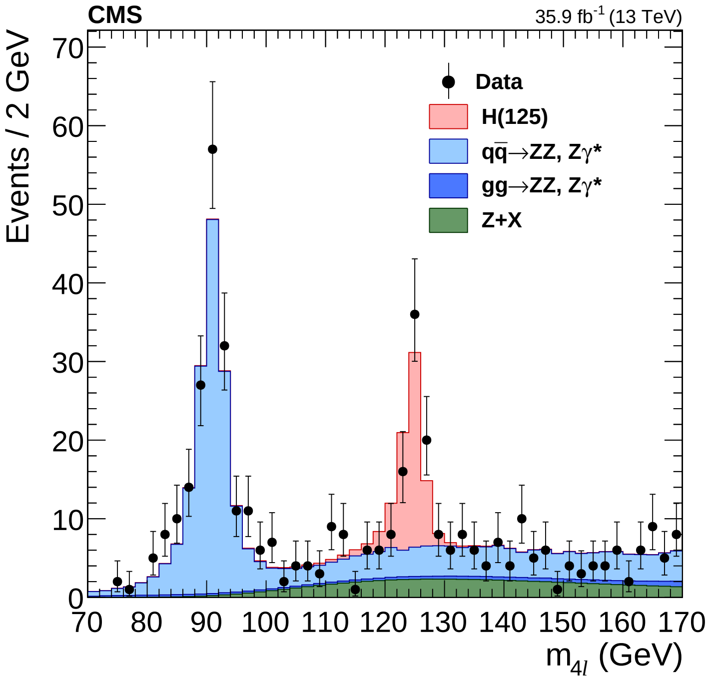

Figure 1.7: Distribution of the invariant mass for candidates showing the major backgrounds and signal for the CMS $H \to ZZ^* \to 4\ell$ analysis [18]

However as discussed above the coupling of the Higgs boson to the fermion sector is though a different mechanism so it is important to also observe these couplings to determine the SM nature of the new boson. These can be observed indirectly by classifying the production mechanisms. The gluon fusion production as shown in Figure 1.3(a) contains a coupling between the Higgs boson and the quark loop. At the LHC the Higgs boson can also be produced by the fusion of two top quarks in a process similar to the VBF production described above. A further important study is the decay of Higgs bosons to two fermions where the individual fermions can be identified (as opposed to the ggF loop where several quarks are in superposition).

The first direct evidence of these Yukawa interactions was in the Higgs boson decays to two τ leptons using ATLAS data from the 2011 and 2012 runs of the LHC [20]. Despite the large branching ratio for this decay mode (shown in Figure 1.4(b)), the complicated further decays of the τ leptons ensure that this is a challenging analysis. The observed signal strength $\mu = \sigma_{Obs}/\sigma_{SM}$ was ultimately measured to be $\mu = 1.43^{+0.43}_{-0.37}$, which is compatible with the Standard Model expectation.

More recently, evidence has been found for the Higgs boson decay to a pair of b quarks [21]. This decay mode has the largest branching ratio for the Higgs boson as it is the

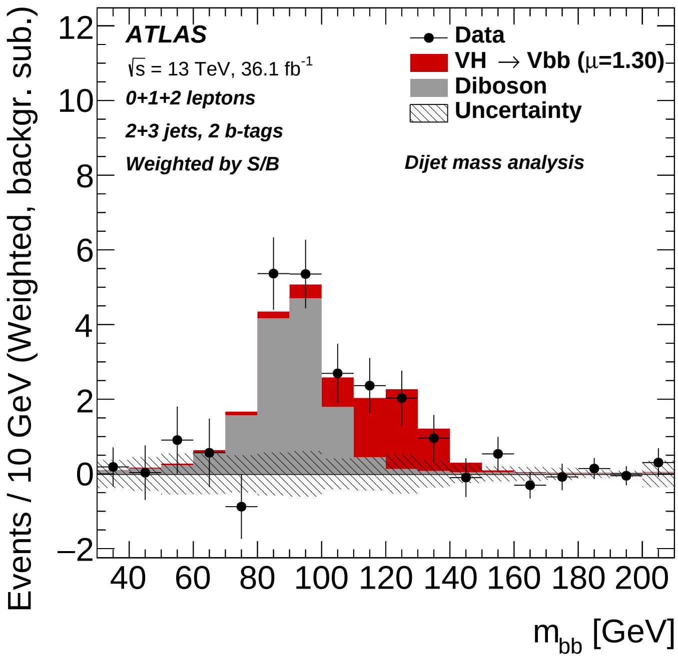

Figure 1.8: The distribution of m_{bb} in data after subtraction of all background contributions considered by the analysis from other SM processes except for the WZ and ZZ diboson processes. [21]

most massive particle to which a 125 GeV boson can decay. Despite this, evidence for the decay has remained elusive due to the difficult final state. Free quarks are not allowed from our understanding of QCD, instead high p_{T} coloured objects lead to a cascade of hadronic particles as $q\bar{q}$ pairs are formed from the potential in the strong fields. These cascades are measured by the tracking detectors and calorimeters in roughly conical-shaped deposits in a phenomenon known as a hadronic jet. These jets are a common background from the underlying pp collisions at the LHC which can drown out the potential signal. In order to combat this large background the jets are "tagged" in order to identify those initiated by a b quark. These tagging algorithms use various parameters of the jet which can discriminate between b-jets and more general hadronic jets. One characteristic is the long lifetime of b-hadrons which lead to a secondary vertex displaced from the jet origin. The sensitivity of this analysis is further improved by searching for the vector boson associated production mode which allows the initial state to be tagged. The invariant mass of the di-jet system (m_{bb}) can then be reconstructed leading to the excess around the Higgs boson mass as shown in Figure 1.8.

1.3 Ideas to probe the Higgs Couplings to First and Second Generation Quarks

In the previous section different state-of-the-art analyses searching for the Higgs boson to fermion couplings are discussed. However in both of these cases only the heaviest third generation fermions have been observed with any experimental evidence. A wealth of beyond-the-SM theories predict substantial modifications of the relevant Higgs boson couplings to fermions. Such scenarios include the Minimal Flavour Violation framework [22], the Froggatt-Nielsen mechanism [23], the Higgs-dependent Yukawa couplings model [24], the Randall-Sundrum family of models [25], and the possibility of the Higgs boson being a composite pseudo-Goldstone boson [26].

The first problem with searches for the first and second generations of fermions is that their lighter masses lead to smaller couplings to the Higgs boson and hence smaller branching ratios. Such searches exist for the decay of the Higgs directly to two muons but due to the available data so far only 95% confidence level limits are set at less than 2.8 times the expected Standard Model decay rate [27].

Searches for the Higgs decays to the light quarks face even greater difficulties from the overwhelming QCD background. Due to the nature of these quarks it is also difficult to perform any form for flavour tagging as is done to identify jets initiated by a b quark with the $b\bar{b}$ analysis.

The rare decays of the Higgs boson to a heavy quarkonium state, J/ψ or $\Upsilon(nS)$ with $n = 1, 2, 3$, and a photon offer sensitivity to the charm- and bottom-quark couplings to the Higgs boson [28–30] and have already been searched for by the ATLAS collaboration [31], resulting in 95% CL upper limits of 1.5×10^{-3} and $(1.3, 1.9, 1.3) \times 10^{-3}$, respectively. The former decay mode has also been searched for by the CMS collaboration [32], yielding the same upper limit. The prospects to observe and study Higgs boson decays to a meson and a photon with an upgraded High Luminosity LHC [13] or a future hadron collider [33] have also been studied.

Currently, the light-quark couplings to the Higgs boson are almost entirely unconstrained by existing data and the large multijet background at the Large Hadron Collider

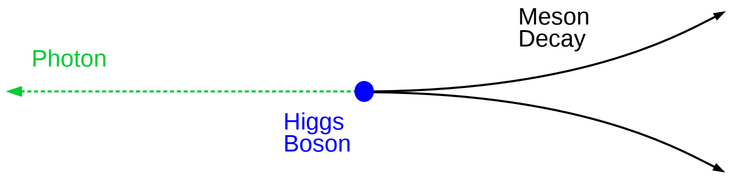

Figure 1.9: A schematic of the decay signature, with a photon recoiling against the pair of oppositely charged meson decay products

(LHC) severely inhibits the study of such couplings with inclusive $H \to q\bar{q}$ decays.

Rare exclusive decays of the Higgs boson to a light meson, M, and a photon, γ have been suggested as a probe of the coupling of the Higgs boson to light (u, d, s) quarks [34–36]. A simple schematic of the final state can be seen in Figure 1.9 where the exclusive nature of the decays allows the full final state to be reconstructed. The Higgs boson decay to a ϕ or ρ meson and a photon represents a unique probe to measure directly its coupling to the strange-quark, and the up- and down-quark, respectively, and to search for potential deviations from the SM prediction. The expected SM branching fractions are $\mathcal{B}(H \to \phi\gamma) = (2.31 \pm 0.11) \times 10^{-6}$ and $\mathcal{B}(H \to \rho\gamma) = (1.68 \pm 0.08) \times 10^{-5}$ [35]. These decay amplitudes receive two dominant contributions that interfere destructively. The first is referred to as direct and proceeds through the $H \to q\bar{q}$ coupling, where subsequently a photon is emitted before the $q\bar{q}$ hadronises exclusively to M. This amplitude is sensitive to the $Hq\bar{q}$ coupling. The second is referred to as indirect and proceeds via the $H\gamma\gamma^*$ coupling followed by the fragmentation of $\gamma^* \to M$. Given that for the u, d, s quarks the Yukawa couplings are extremely small, the interference between the two amplitudes provides the potential to observe couplings as an excess or deficit over the larger indirect process.

Chapter 2

The ATLAS Detector at the CERN Large Hadron Collider

2.1 The Large Hadron Collider

The Large Hadron Collider (LHC) is a proton-proton collider constructed at the CERN laboratory near Geneva on the French-Swiss border [37]. It was constructed in the 26.7 km tunnel which was previously used for the LEP electron positron collider until it ceased operation in the year 2000.

Its design was driven by the target centre-of-mass energy of $\sqrt{s} = 14$ TeV although it has operated at $7, 8, 13$ TeV due to an incident in commissioning during 2008 [38]. The operational periods are commonly separated into two runs. Run-1 was from 2009-2013 and ended with the first scheduled long shutdown on the machine, LS-1. During this shutdown several improvements were made to the accelerator, including updrading the superconducting splices between dipole segments, in order to avoid repeats of the earlier incident and allow operation at centre-of-mass energies closer to the design value.

LS-1 ended in 2015 with the machine operating for the first time at $\sqrt{s} = 13$ TeV [39]. This commissioning year was followed by an impressive data-taking year in 2016 where the delivered luminosity exceeded the target by 60% largely because the LHC was able to provide an impressive up-time in “stable beams” of around 50% [40].

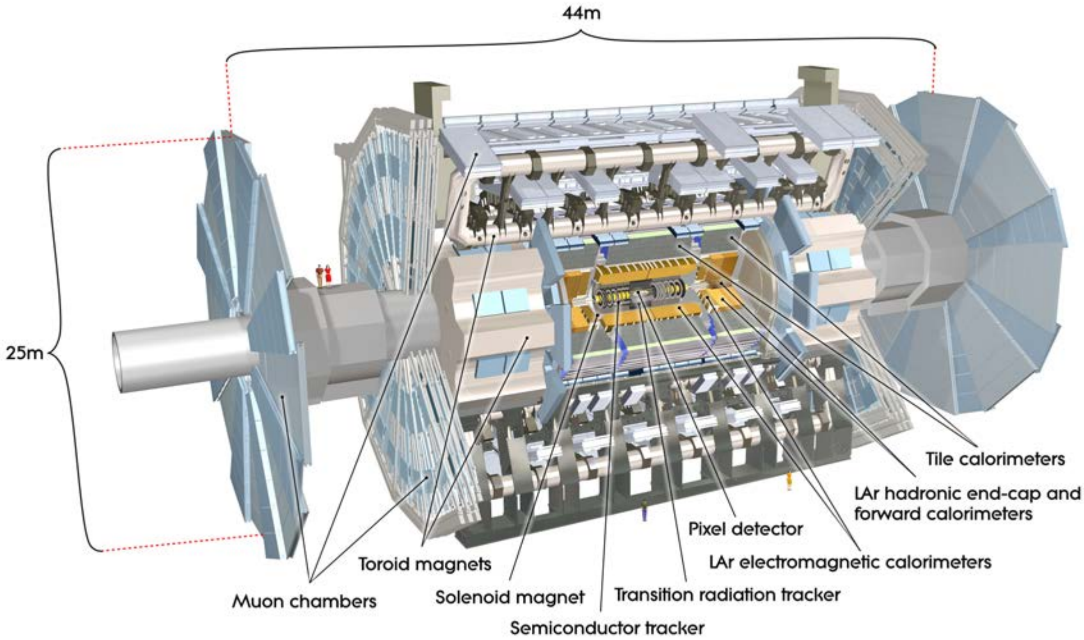

Figure 2.1: A diagram of the ATLAS detector [42]

2.2 ATLAS Detector

ATLAS (**A** **T**oroidal **L**HC **A**peratu**S**) [41] is situated at the LHC interaction point at the CERN Meyrin site. It is a general purpose detector designed to provide hermetic coverage in order to detect as many interactions as possible. The detector is also required to discriminate between several signals corresponding to different types of final state particle.

In order to achieve this coverage and discrimination between signals the detector is constructed of several subsystems. These are arranged in a layered cylinder around the interaction point where the incoming proton beams are brought into collision.

Immediately around the interaction point are the Inner Detector systems (ID) which are comprised of tracking detectors used to reconstruct the tracks of charged particles leaving the interaction points. These are followed by the calorimetry system designed to measure the energy of the escaping particles, these are further subdivided into electromagnetic and hadronic calorimetry optimised to absorb different particles. Surrounding the outside of the calorimeters is the muon system designed to measure the momentum of the minimally-ionising muons which will have travelled though all of the previous layers of the detector.

The detector is described with a right-handed coordinate scheme; the origin at the interaction point (IP), the z-axis parallel to the beam pipe, the x-axis pointing towards the centre of the ring, and the y-axis pointing vertically up. It is also convenient to use cylindrical coordinates in the transverse plane with the angle ϕ about the z-axis. Pseudorapidity (η) is defined by the polar angle (θ) from the z-axis, $\eta = -\ln\tan\theta/2$.

Operation of the system is coordinated by a trigger and data acquisition system (TDAQ) which ensures the coordination between the sub-detectors as well as controlling which events to trigger and subsequently read out.

2.2.1 Inner detector / Tracker

The inner detector and tracker systems are the first detector systems which particles from the collision pass though. They use various technologies to detect the transition of charged particles. All of these detectors are situated within the magnetic field of the ATLAS solenoid hence the curvature of the tracks can be used to reconstruct the momentum of the charged particles.

The first layer of tracking is provided by the silicon insertable b-layer (IBL), which is an upgrade installed during LS1 inside the radius of the existing tracker. This improves the performance of the detector when measuring the point of origin of a given track by providing an additional point of measurement for the tracks closer to the interaction point. This in turn helps with the identification of physics objects such as b-jet tagging which rely on detailed tracking information.

This is followed by two additional sets of silicon detectors, a pixel detector and a strip detector. Finally there is a gas-filled straw tube detector; this is filled with a mixture dominated by Xenon gas. This detector also detects the transition radiation as charged particles move though it. Transition radiation is an electromagnetic radiation emitted by a particle as it moves between two materials of different dielectric properties (in this case a polypropylene-polyethylene fibre mat which surrounds the straw tubes [43]). This effect is strongly dependant on $\gamma = E/m$ meaning it can be used to discriminate between ultra-relativistic particles of a given p_{T} based on their mass [44]. This information is used to help with the discrimination between electrons and pions.

2.2.2 Calorimeters

It is the role of the calorimeters to measure the energy of particles leaving the inner detector. This also includes possible neutral particles which will have remained undetected by the inner detector. The calorimeters are separated into two layers, the first is the electromagnetic calorimeter designed to completely contain the showers resulting from electromagnetic objects such as photons and electrons. The second layer of calorimetry is the hadronic calorimeter designed to contain and absorb the remaining energy in hadronic jets.

For the main barrel of the ATLAS detector the electromagnetic calorimetry is provided by a lead and liquid argon technology, whereas the hadronic calorimetry is performed using steel plates segmented by plastic scintillators. In the forward regions the liquid argon technology is used for both electromagnetic and hadronic layers.

2.2.3 Muon System

The muon system is a combination of gas-based drift chambers with a toroidal magnetic field of up to 2 T. This toroid is where ATLAS gets its name and performs a similar task to that of the solenoid of the inner detector; the magnetic field causes bending in the trajectories of the charged muons and their tracks are detected in the muon chambers. Tracks for muons can be measured twice, once in the inner detector and then again in the muon spectrometer (MS), leading to a high momentum accuracy.

2.2.4 Trigger & Data Acquisition

ATLAS uses a two-level trigger system in order balance the requirements of the physics program with the bandwidth and storage requirements of recording the high rate of collisions provided by the LHC.

The first level of the trigger system is based on custom hardware and is designed to make a first pass decision of events at the full 40 MHz collision rate using reduced granularity information from the calorimeters and muon systems. The central trigger processor (CTP) coordinates the signals received from the various Level-1 trigger subsystems and depending on the programmable menu used to define the physics priorities, can transmit the Level-1 accept message to the various ATLAS sub-detectors. This triggers the read out of all of these subsystems into the data acquisition system. The maximum rate for the level-1 accept messages is 100 kHz driven by the bandwidth restrictions for the various sub-detectors.

As all of the sub-detectors "read out", their information is cached by the event builder and associated with the data from the other detectors for the same collision. These data are then used as they become available by the software trigger, also known as the Higher Level Trigger (HLT). The HLT is able to do offline-like reconstruction of physics objects; this allows for a more refined selection of events. The HLT trigger menu defines a series of "chains"; these are signatures resulting from the passing of a series of algorithms. Some chains are very generic and look for signatures such as a single isolated electron and can be used for a wide range of analyses, whereas some specify very detailed final states in the cases that cannot use the general trigger due to the higher thresholds of inclusive triggers.

The final decision to accept an event and write it to disk is again made based on a trigger menu which describes which chains should be kept, with the option that high rate chains can be prescaled and only kept a fraction of the time at random.

2.2.5 Reconstruction and Data Handling

While not a physical component of the detector, the software used for the reconstruction of physics objects, as well as analysing events, is an integral part of performing an analysis with the ATLAS detector. The primary collection of detector software is called ATHENA [45]. This is built on the commonly used ROOT [46] framework as well as GAUDI [47], which is a software framework originally developed for the LHCb [48] collaboration.

ATHENA is used for dealing with the bulk data and producing ROOT ntuple files which are then used to perform the final analysis. A sample of raw events from each run of the detector are selected to undergo express reconstruction while the run is ongoing. This express stream is used to verify the data quality and provide a calibration pass. The whole run then undergoes prompt reconstruction to transform the raw data into analysis objects. These are stored in a pooled data format known as "xAOD". Before the data is then included in any analysis it undergoes a second processing known as "derivation". In this pass important corrections calculated after the prompt reconstruction are applied to the data and a loose selection is placed on the data depending on the flavour of the derivation. These selections can skim events, rejecting them entirely, but also slim the remaining events pruning out unnecessary information, for example a pure muon analysis may not need detailed shower shape information regarding photons. These Derived xAODs (DxAODs) will be common to a handful of analysis teams, the biggest advantage being that after the loose selection they are much smaller than the original xAODs and so are easier to distribute and analyse.

2.3 Upgrade and commissioning of the L1Calo Cluster Processor

As described in Section 2.2.4, the ATLAS detector uses a two-level split trigger. The first level of this trigger is a fixed-latency hardware trigger, which on issuing a Level-1 accept (L1A) leads to all the detector components reading out the bunch crossing in question. The data is then further interrogated by the software-based higher level trigger (HLT) algorithms in order to determine if the event should be accepted and ultimately written to disk as part of the dataset.

The data volume produced by a single collision is too great to be read out from the detector at the full LHC collision rate, therefore this is only done after an L1A. The Level-1 trigger is constrained by the need to issue the L1A before the event is lost from the detector buffers. To achieve this the Level-1 systems use reduced granularity data at the full event rate to reduce the rate to one supported by the readout bandwidth.

One part of the Level-1 decision making is the Level-1 calorimeter trigger (L1Calo) which uses reduced granularity information from the electromagnetic (EM) and hadronic (HAD) calorimetry systems in the form of "Trigger Towers". A Trigger Tower is a sum of the calorimeter cells in an area typically $\Delta\eta \times \Delta\phi = 0.1 \times 0.1$. These signals are received as analogue pulses which undergo fast digitisation in the L1Calo preprocessor modules (PPM). These towers are then used in trigger algorithms targeting electrons, photons, tau leptons and hadronic jets as well as total and missing transverse energy.

Within the L1Calo system it is the Cluster Processor which handles the triggering for electrons, photons and tau leptons based on collimated energy clusters in the EM calorimeter (electrons and photons) and in both EM and HAD calorimeters (tau leptons).

This system underwent significant updates during LS-1 which allowed for the implementation of an E_{T}-dependent isolation system where previously only a fixed threshold for Level-1 isolation had been possible. The E_{T}-dependent isolation is an improvement as it allows tighter isolation requirements. This in turn allows large reductions of Level-1 rate without a large impact on the efficiency for real electrons.

2.3.1 Hardware

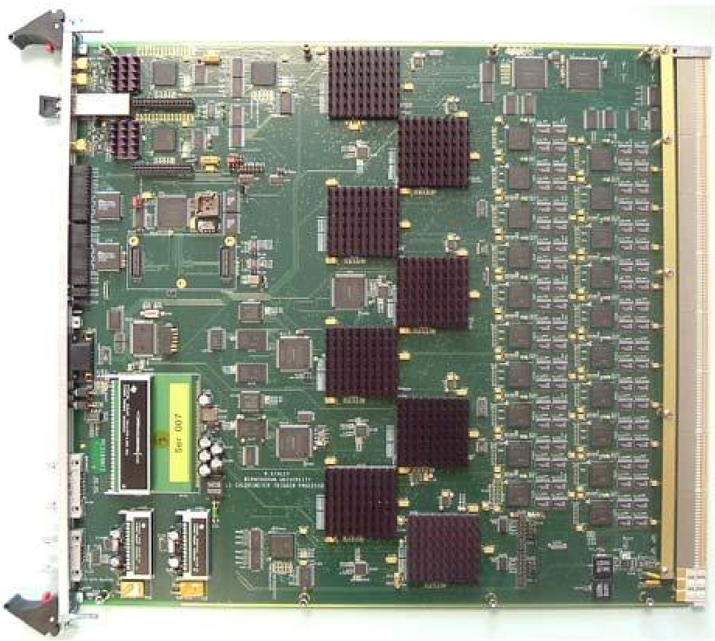

Figure 2.2: One cluster processor module (CPM)[49]

The cluster processor system is comprised of four VME crates containing modules each representing one quarter of the calorimeter for $|\eta| < 2.5$. Each crate contains 14 Cluster Processor Modules (CPMs), shown in Figure 2.2 , which separately process inputs from strips in η for the given quadrant of their particular crate.

The algorithm described below is largely executed in the main processing chips, of which each CPM has eight. The algorithm also requires information about the towers processed by the neighbouring modules; this information is shared though a custom VME backplane.

The backplane is also used to send the Trigger Objects (TOBs) which are the result of the cluster finding algorithm to the merger modules (CMXs). Each crate has two CMXs, one to handle the electromagnetic TOBs and the other to merge the tau TOBs. The CMX on receiving the TOBs counts them and checks which of the defined energy thresholds they have passed, summing these multiplicities between crates and sending the final totals to the Level-1 central trigger processor (CTP) which evaluates the inputs from several sub-systems and makes the Level-1 decision to issue a L1A based on a programmable menu.

In addition to sending the multiplicities to the CTP, the CMXs also forward the TOBs to the Level-1 topological trigger (L1Topo). L1Topo also receives TOBs from the other Level-1 subsystems (jets, missing transverse energy and muons), in order to combine them, using algorithms which give more discriminating power for specific signatures.

Upon receiving a L1A the objects found by the cluster processor are sent directly to the HLT as regions of interest (ROIs) which are used to seed the subsequent software algorithms. A copy of all the input data (trigger towers) and output data (ROIs) are also sent to the ATLAS DAQ system this allows for subsequent checks on the correct operation of the trigger system.

2.3.2 The e/γ Algorithm

The algorithm used by the Cluster Processing system is illustrated by Figure 2.3, here each block represents a Trigger Tower. A sliding window algorithm is used to identify a local maximum of the central four EM and HAD trigger towers. A sliding window algorithm is used in conjunction with this local maximum requirement to ensure the uniqueness of each cluster. The energy of the cluster is taken to be the largest of the four possible sums of adjacent pairs of trigger towers. If the cluster energy passes the minimum energy requirement (typically 4 GeV) a TOB is formed.

Isolation information is also calculated for each TOB based on the trigger towers surrounding the 2×2 local maximum in the EM layer and the sum of the 2×2 towers in the HAD layer behind the local maximum. Up to five different isolation thresholds are

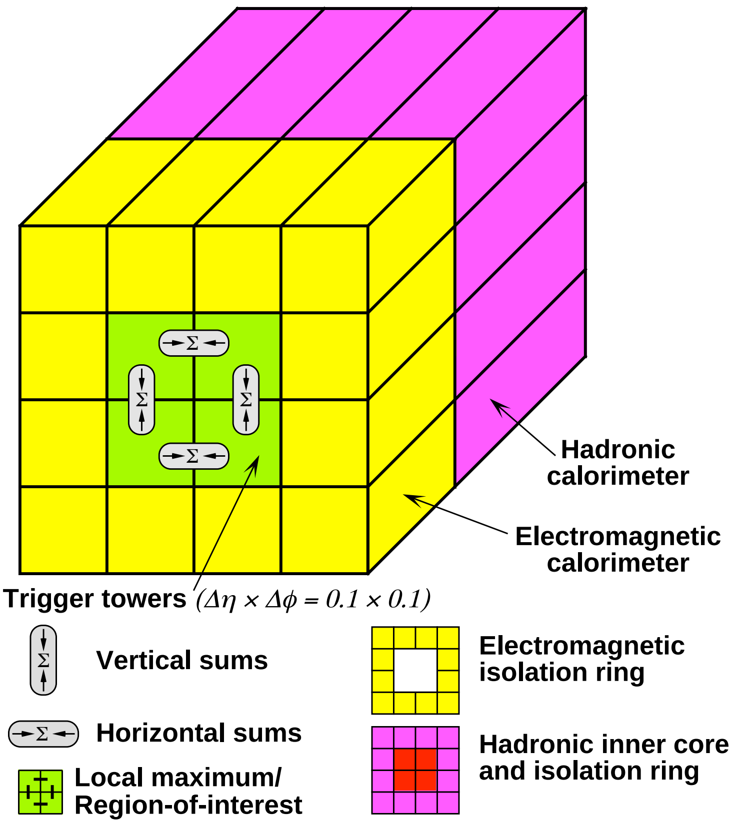

Figure 2.3: A diagram of the algorithm window used in the CPM [50]

defined.

The τ Algorithm

The Cluster Processor system also provides the Level-1 trigger for τ. This algorithm runs in a similar manner to the e/γ algorithm, and the same local maxima of EM and HAD towers is selected. However the E_{T} of the cluster is taken as the sum of the pair of towers selected in the e/γ algorithm and the 2×2 towers in the HAD layer.

Isolation information for the τ algorithm is based on the same EM ring as used for the e/γ algorithm but there is no HAD isolation as those towers are already included in the cluster.

CPM Isolation Scheme

A "look up table" (LUT) is used to determine if a given TOB passes any of the five possible isolation thresholds. A LUT is a memory structure used to associate every allowed combination of input parameters with an output response. In this case the inputs are the cluster E_{T} and the isolation sums with an output 5 bit word representing which

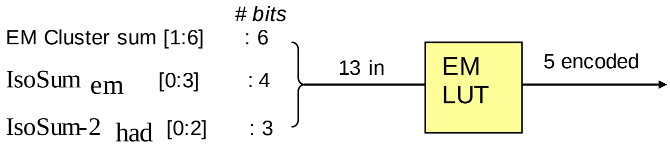

(a) EM LUT

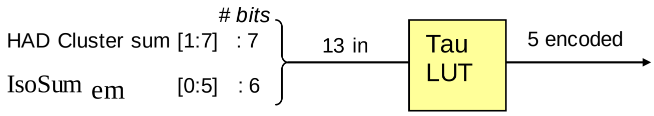

(b) Tau LUT

Figure 2.4: Diagrams of the isolation look up tables [51]

thresholds have been passed, as detailed in Figure 2.4. This requires a large amount of the available chip resources to store the information, but the "look up" operation is fast.

The output words to be assigned to the isolation LUT are calculated in the online software during the configure step of the TDAQ state machine. The calculation is based on a gradient isolation with a linear slope, which would be too slow to calculate on the chips themselves in real time. This calculation is performed using the following parameters provided by the ATLAS Trigger menu:

- Offset: Constant offset used in isolation calculation
- Slope: Slope to use for the isolation calculation.
- Minimum isolation: The minimum isolation that should be applied. This value is used instead of the value from the slope in cases where the gradient isolation would be tighter.
- Maximum Energy: This is the maximum energy of the object to apply isolation. Above this energy the isolation bit is set to always pass.

For the EM cluster isolation two sets of parameters are used, one for the electromagnetic isolation and one for the hadronic. The final result is an AND of these two. By convention, in the software these are referred to as the EM and HAD isolation variables. For the TAU cluster isolation only the electromagnetic isolation is used. To avoid confusion with the EM isolation for the EM cluster, the EM isolation variables for TAU are referred to as the TAU isolation variables in L1Calo software.

The parameter sets are used in conjunction with Equation 2.1, which determines the allowable isolation value for a given cluster E_{T}.

$$\mathrm{IsoSum}_{\mathrm{EM}} < \mathrm{MAX}\left\{ Iso_{Min}, \mathrm{Offset} + \frac{\text{Cluster Sum}}{\text{Slope}} \right\} \tag{2.1}$$

The decision of whether a given address should pass isolation, and therefore have the isolation bit in the LUT output word set high, is as follows:

1. First, the cluster E_{T} is checked for saturation, where the E_{T} measured excedes the number of bits available to store it. If this is saturated the isolation is passed and the algorithm stops here.

2. Second, the maximum energy parameter is checked, and if the cluster E_{T} is greater than it, the isolation is considered passed.

3. Next the slope is checked,

   - If the slope is set to 0, this is interpreted as a request for fixed isolation using only the offset. In this case, if the isolation E_{T} is less than the larger of the offset and minimum isolation parameters, the isolation is considered passed.

   - If the slope is non-zero, the isolation E_{T} is compared with the larger of the minimum isolation and E_{T}-dependant isolation value using Equation 2.1 and again if the isolation E_{T} is less than the compared value, the isolation is considered passed.

4. If the isolation does not meet any of the requirements then the isolation is considered failed. A parameter set can be effectively disabled and set so it will always pass by setting the maximum energy to 0.

5. If the isolation has passed (or the AND of the EM and HAD isolation in the case of the EM clusters) the corresponding bit in the LUT is set high. There are 5 independent bits and corresponding parameter sets which can also be combined with an AND when the thresholds are applied in the CMX.

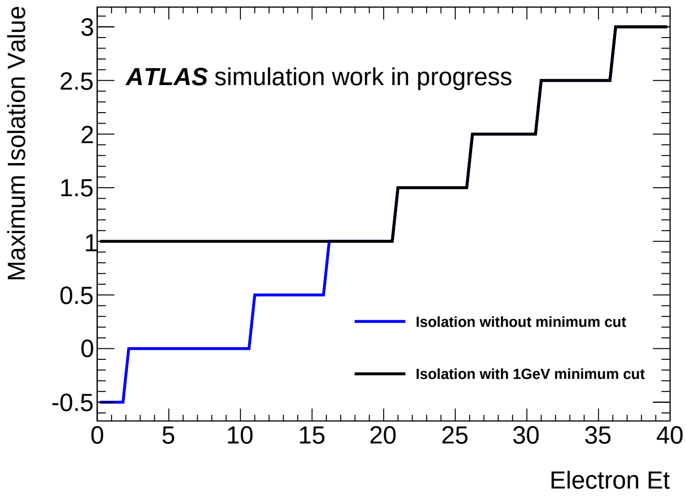

Figure 2.5: An example of an E_{T}-dependent isolation value with and without the minimum cut parameter

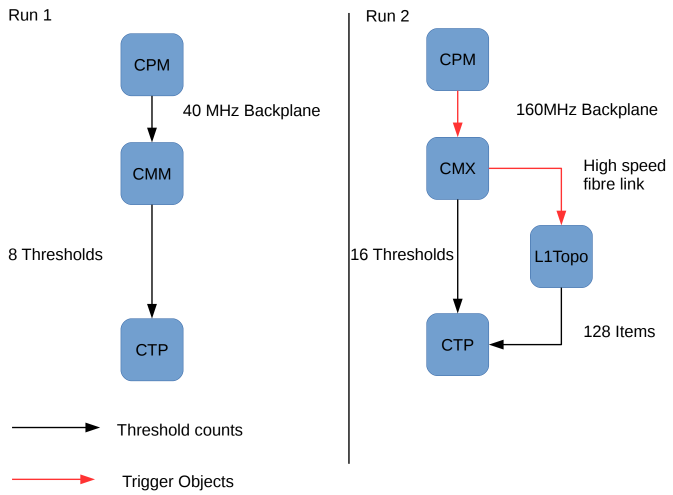

Figure 2.6: A diagram of the LS1 upgrades relevant to the cluster processor system

The resulting isolation selection for an example set of parameters can be seen in Figure 2.5.

2.3.3 Updates and Testing

The behaviour of the cluster processor system described above is a significant change from the system as it was used before the LHC long shutdown 1 (LS1). Before LS1 there was no L1Topo system so it was unnecessary to transfer energy information for every bunch crossing. Instead only multiplicities of ROIs passing thresholds were sent across the backplane to a simpler merging module (CMM) as shown in Figure 2.6.

Due to the significant nature of the change in operation and despite the CPM hardware

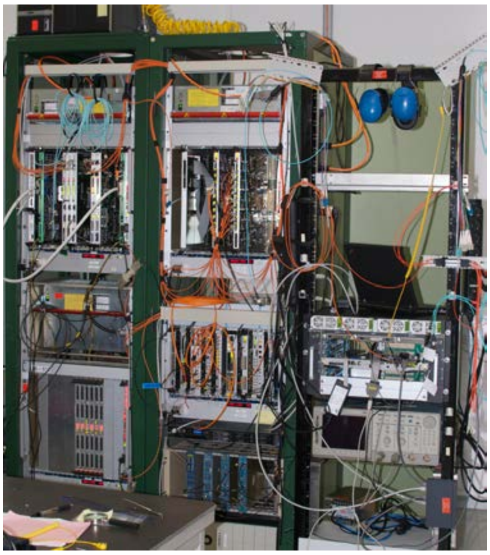

Figure 2.7: An image of the CERN test rig

staying identical significant effort was required to re-test and commission the system.

A large portion of this testing was undertaken at the CERN-based L1Calo test rig shown in Figure 2.7. This test rig represents a minimal L1Calo system with only a handful of each possible type of module. It is also possible to run the full stack of TDAQ software and operate the test rig as a partition similar to that used in the ATLAS control room.

In order to perform the original testing of the system during construction a bitwise simulation of the L1Calo system was created. This simulation contains functional elements representing each stage data takes though the hardware as well as the connections between them. In order to use this to test the updated operation of the system several upgrades were included in the simulation to mirror the changes to hardware and firmware.

It was also necessary to update the online support software used by the CPMs. This software acts as the interface between the hardware and wider TDAQ software infrastructure. It is run on single board PCs included in the cluster processor crates and communicates with the CPMs using the VME backplane.

The calculation of the isolation LUT contents is performed identically for both the online simulation and configuration of the module to ensure that the results are identical.

Testing was carried out using so called "test vectors". These are patterns of tower energies which are inserted directly in the PPM memory in place of an actual calorimeter input. These are then passed to the CPMs in the test rig and the resulting output can be compared to that from simulation. As the simulation is intentionally bit-for-bit identical to the hardware any discrepancies are easy to spot in a direct comparison, but due to the potentially large number of test events this comparison is performed by a monitoring program known as “rodmon” which counts and categorises errors observed during test runs.

After several iterations of both firmware and simulation software on the test rig the updates were deemed to be stable enough to be deployed in the full system. The full system posed further challenges to the testing as the larger number of modules means there are more overlaps where data is shared between modules and edge cases where the algorithm can fail. It also allows for testing up to a greater rate of L1A signals than is possible in the test rig.

2.3.4 Conclusions

In order to meet the challenges posed by the higher centre-of-mass energy and instantaneous luminosity provided by the LHC in Run-2 the L1Calo Cluster Processor underwent several upgrades during LS1. In order to ensure the correct operation of the Level-1 trigger, significant testing of firmware changes was performed. This, combined with the relevant software updates, allowed for the implementation of a much more comprehensive Level-1 isolation scheme for electrons, photons and tau leptons in the trigger system.

This updated isolation scheme is monitored closely in operational data taking, which checks that all of the upgrades are operating correctly. Figure 2.8 shows the efficiency for a Level-1 electron threshold with two different tuned parameter sets [52] showing that the updated flexibility of the gives the ability to fine tune the isolation with changing running condiditons.

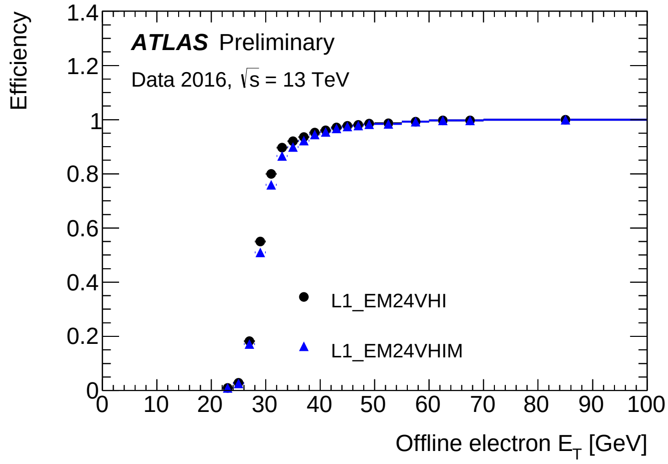

Figure 2.8: The efficiency of two Level-1 electron triggers using different isolation parameter sets. The black circles represent the isolation used in 2016 data-taking, and the blue triangles are an updated tune to be used in the 2017 data-taking. These were calculated using $Z \to ee$ events [52].

2.4 ATLAS Physics Performance

As described above, the data files used for analysis contain calibrated physics objects that can be used for subsequent analysis. The performance of this identification and reconstruction process is a large body of study for the collaboration. This section will detail the latest relevant studies into the performance of the ATLAS detector.

2.4.1 Track Reconstruction

Track reconstruction from individual hits in the inner detector systems to tracks with a measured curvature due to the magnetic field is an important process as fitted tracks feed into the reconstruction of many physics objects described below. The reconstruction is seeded by inner detector hits in the innermost layer of the detector. The algorithm then attempts to build full tracks, finding additional hits further away from the centre of the detector. An ambiguity resolver then considers all the possible tracks which have been created and ensures that a single hit in the detector is only associated to a single track based on the resulting track qualities [53]. The efficiency to reconstruct a track as a function of the tracks transverse momentum is shown in Figure 2.9.

For the $\phi \to K^+K^-$ and $\rho \to \pi^+\pi^-$ described later the tracks are expected to be very close together which increases the difficulty of their reconstruction as true tracks can

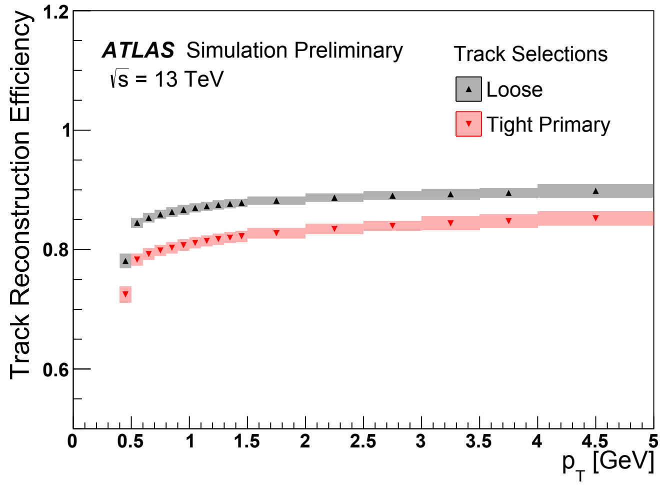

Figure 2.9: The track reconstruction e ciency from simulations of the ATLAS inner detector as a function of transverse momentum [54].

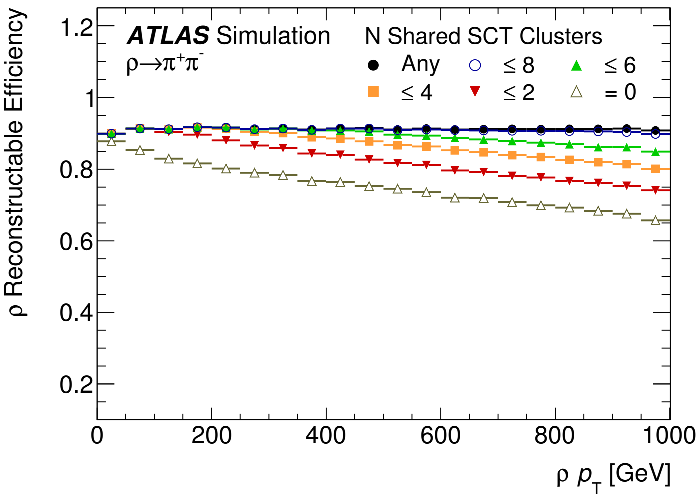

Figure 2.10: The reconstruction e ciency for ρ mesons as a function of p_{T} for di erent numbers of allowed shared clusters in the ambiguity solving [55].

overlap and be removed by the ambiguity resolving algorithms. The e ect on ρ e ciency in simulation is shown in Figure 2.10. This problem is also encountered in hadronic jets where there is a dense environment of tracks leading to the possibility of overlapping signals and ambiguous reconstruction. These cases have also been investigated and the simulation of the expected track e ciency matches the data as expected [55].

2.4.2 Electrons and Photons

The reconstruction of electrons and photons is similar in that they both deposit most of their energy in the electromagnetic calorimeter. The main di erence is that an electron

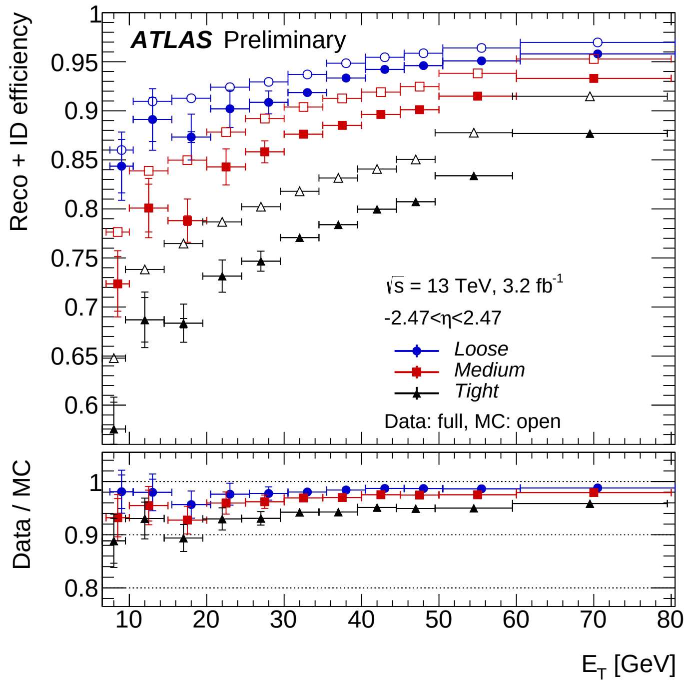

Figure 2.11: The reconstruction and identification efficiency for ATLAS electrons as a function of the electron transverse energy [56].

has an electric charge and will therefore leave a charged track in the inner detector whereas the photon leaves no track and is observed only as a electromagnetic energy cluster.

Electron objects are reconstructed by scanning the calorimeter for electron-like energy clusters. The inner detector is then scanned for tracks which match the selected cluster loosely in η, ϕ space. The selected track then undergoes a second fit to the hits in the inner detector and the centre of the electromagnetic cluster. Finally this electromagnetic cluster and refitted track are reconstructed as an electron candidate [56].

However not all objects reconstructed as electrons are necessarily real electrons as there are several physics backgrounds which can give a similar signal. In order to increase the purity of the electron sample, identification criteria are applied using various parameters of the inner detector track and the electromagnetic shower in the calorimeter. Several standard identification working points are defined, because as the purity of the sample is increased the efficiency for real electrons reduces; depending of the needs of the analysis these working points give some flexibility.

This leads to the efficiencies shown in Figure 2.11, which show an efficiency of $\approx 85\%$ for electrons with $E_{\mathrm{T}} > 60$ GeV and the tightest identification requirement.

Photon reconstruction begins in a similar manner with a scan of the electromagnetic

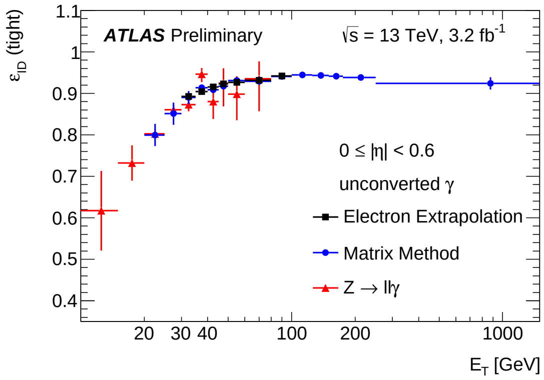

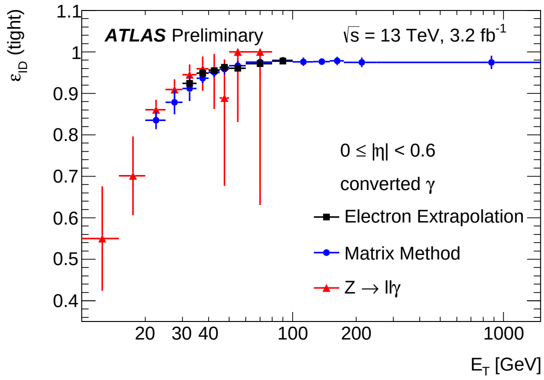

Figure 2.12: The identification efficiency for unconverted (converted) photons on the left (right) for a given η bin [57].

calorimeter except no matching track is required. Clusters without any tracks nearby are considered unconverted photons. Photon conversion is when a photon converts (due to interaction with material in the inner detector) into an electron-positron pair. In cases where a photon-like electromagnetic cluster is found with a pair of oppositely-charged tracks in the outermost tracking layer (TRT) but no hits in the innermost tracking layer the cluster is considered a converted photon.

Again identification requirements are also placed on the variables related to the energy deposited in the calorimeters. Overall the efficiencies for tight photon identification are found to vary from $53-64\%(47-61\%)$ for unconverted (converted) photons at around 10 GeV increasing to $88-92\%(96-98\%)$ for photons with $E_{\mathrm{T}} > 100$ GeV [57]. These efficiencies vary with the transverse energy of the photon as shown in Figure 2.12.

2.4.3 Muons

Muon reconstruction starts independently with track reconstruction both in the inner detector and in the muon spectrometer. After this step the information from the two systems is combined using different algorithms in order to increase the acceptance. Combined muons have a good track in both systems which align when the MS track is extrapolated back to the inner detector, segment-tagged muons have a good inner detector track but only match a partial track segment in the MS, calorimeter-tagged muons have a good inner detector track in the region $|\eta| < 0.1$ which matches a calorimeter signal consistent with a muon and finally extrapolated muons that have a good track only found in the MS but which, when extrapolated back is consistent with coming from the interaction point.

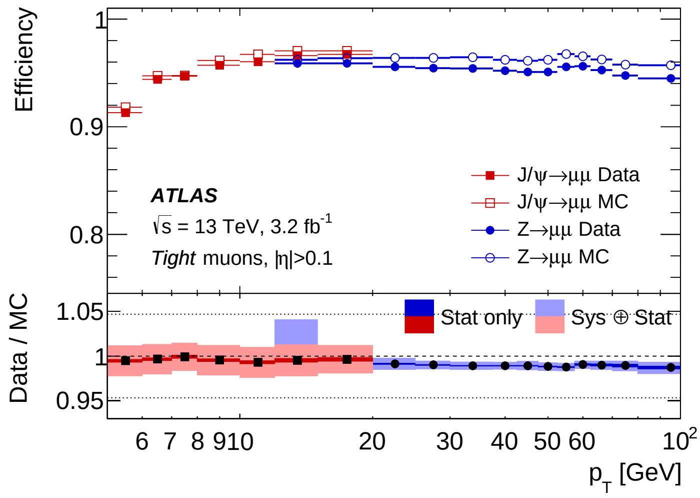

Figure 2.13: The reconstruction and identification efficiency for ATLAS muons as a function of the muon transverse momentum [58].

For muons, identification is performed largely using track-based discriminating variables. This leads to an efficiency of $\approx 95\%$ for muons with $p_{\mathrm{T}} > 6$ GeV using the tight working point [58] as shown in Figure 2.13.

2.4.4 Missing Transverse Energy

Missing transverse momentum is an unusual physics object as it is not directly analogous to a particular particle (like the analysis electrons and real electrons) and as such does not have an analogous identification efficiency. Instead the missing transverse energy is a property of the event. It is of particular interest as by conservation of energy and momentum each event should be balanced in the transverse plane. However if there is an undetected particle such as a neutrino or other as yet undiscovered particle they would leave the detector without interacting and cause an imbalance of the transverse energy.

The total missing energy is calculated using the sum of the missing energy due to the various physics objects defined above; these are known as the hard contributions. For example the contribution from the electrons is the negative sum of all the detected electrons. For a given event not all of the particles will necessarily be reconstructed as hard objects as individually they do not carry enough energy, however they are important to the global energy balance and as such a soft term is also added to account for them. There are two main approaches to calculating the soft term: either using a calorimeter-based soft term, which sums all energy found in the calorimeter not already associated

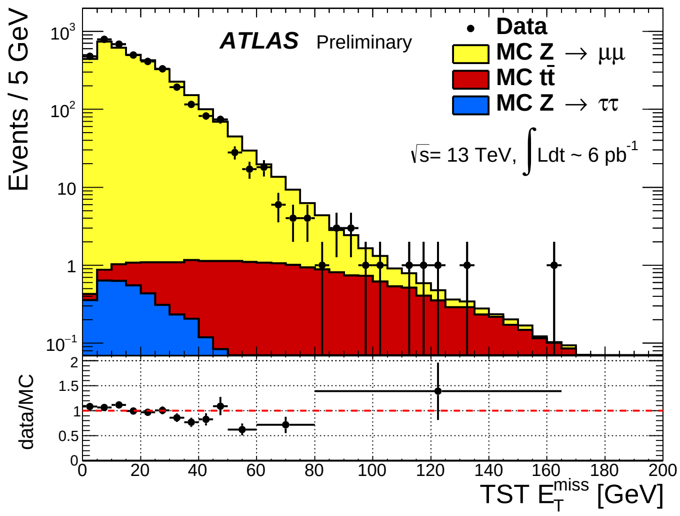

Figure 2.14: Comparison of data and simulation for missing transverse energy using a track-based soft term in $Z \to \mu\mu$ events [59].

with a calibrated object, or a track-based soft term, which uses all of the tracks in the inner detector not associated with a hard physics object.

In order to measure the detector performance for missing energy, $Z \to \mu\mu$ decays are used as they are measured to a high precision and have very little background which could contribute to the missing energy. Therefore the distribution of missing transverse momentum in these events can be used to estimate the resolution [59]. Figure 2.14 shows the good agreement between the data and the simulated detector response for a sample of $Z \to \mu\mu$ events.

2.4.5 Corrections, Scale Factors and Systematic Variations

Based on the results of the studies listed above, systematic effects of the detector are applied on the various analysis objects using analysis tools developed by the collaboration. The output of these tools ranges from calibration corrections on the objects, to scale factors which correct for the relative efficiencies between the Monte Carlo simulations and those observed in data. Additionally, these tools provide uncertainty variations for these corrections; these allow the effect of the uncertainties to be folded into the analysis.

Chapter 3

W Cross-section Measurement

Introduction

In this chapter a measurement of the W boson production cross-section is presented. This analysis was performed at the start of Run-2 of the LHC using the first data at the new operating centre-of-mass energy for the proton-proton collisions, an energy regime in which the W boson cross-section had not yet been measured.

The massive electroweak bosons (Z, W) both have large cross-sections, which are predicted with high accuracy even for the new centre-of-mass energy, and relatively small backgrounds. This makes the measurement of these cross-sections an important benchmark of detector performance, following the upgrades and a period without operation over the first long shutdown of the LHC.

Furthermore, the relative production rates of these bosons have sensitivity to the parton density functions used to describe the initial states of the protons in the hadronic collisions. As such this analysis has power to validate and improve the choice of PDFs used in the Monte Carlo simulations that provide the basis of many other analyses at the ATLAS detector.

This measurement was of the inclusive production cross-section times leptonic branching ratios for the $W \to e\nu$, $W \to \mu\nu$, $Z \to ee$, and $Z \to \mu\mu$ processes. In the case of the W, the cross-section ratio as a function of charge is also measured.

3.1 Cross-section Measurement Methodology

The fiducial phase-space for the measurement of the inclusive W boson production cross-section is defined by the following, where $p_{T,\ell}$ is the transverse momentum of the electron or muon from the W decay:

- $p_{T,\ell} > 25$ GeV
- $p_{T,\nu} > 25$ GeV
- $|\eta_\ell| < 2.5$
- $m_T > 50$ GeV

where $p_{T,\nu}$ is the neutrino transverse momentum, and m_T is the transverse mass defined as

$$m_T = \sqrt{2 p_{T,\ell}\, p_{T,\nu} \left[1 - \cos\left(\phi_\ell - \phi_\nu\right)\right]} \tag{3.1}$$

with ϕ_ℓ the azimuthal angle of the charged lepton, and ϕ_ν the azimuthal angle of the neutrino.

The Z boson decays into leptons that are measured in the phase space defined by:

- $p_{T,\ell} > 25$ GeV
- $|\eta_\ell| < 2.5$
- $66 < m_{\ell\ell} < 116$ GeV

where $p_{T,\ell}$ is the lepton transverse momentum, η_ℓ is the lepton pseudo-rapidity, and $m_{\ell\ell}$ is the di-lepton invariant mass.

The W and Z boson production cross-sections in the fiducial region, which are referred to as fiducial cross-sections, $\sigma^{fid}_{W,Z}$, are related to the total production cross-sections via the formula :

$$\sigma^{fid}_{W,Z} \times BR(W,Z \to \ell\nu, \ell\ell) = \sigma^{tot}_{W,Z} \times BR(W,Z \to \ell\nu, \ell\ell) \cdot A_{W,Z} = \frac{N - B}{C_{W,Z} \cdot \mathcal{L}}. \tag{3.2}$$

The total inclusive production cross-section, $\sigma^{tot}_{W,Z}$, times branching ratio, BR, is determined by the equation

$$\sigma^{tot}_{W,Z} \times BR(W, Z \to \ell\nu, \ell\ell) = \frac{N - B}{A_{W,Z} \cdot C_{W,Z} \cdot \mathcal{L}} \tag{3.3}$$

where

- N is the number of observed candidate events
- B is the expected number of background events
- $\mathcal{L}$ is the integrated luminosity
- $C_{W,Z}$ are the correction factors for the experimental selection and resolution effects
- $A_{W,Z}$ are the fiducial volume acceptances for the W and Z bosons respectively

The $C_{W,Z}$ factors are determined using Monte Carlo simulation and are calculated for each boson and decay product separately. This factor is defined by the ratio of events which pass the full final selection in Monte Carlo (including detector and trigger efficiencies) with the total number of events which fall within the fiducial volume.

The $A_{W,Z}$ factors are similarly determined from Monte Carlo simulation however in this case the relevant ratio is number of events falling within the fiducial volume compared with the full sample of generated events.

Both $A_{W,Z}$ and $C_{W,Z}$ are defined at the "Born level" before the decay leptons emit photons via QED final state radiation [60].

3.2 Data and Simulation Samples

Data used in this measurement were recorded between June 13 and July 16 2015, during Data Periods A4 and C2-C5. In these Periods, the LHC collided 6.5 TeV proton beams with 50 ns bunch spacing.

The data set has been screened for problems with subdetector systems or operational inefficiencies. The analysed data passing these basic data-quality requirements correspond to a total integrated luminosity of 81 pb^{-1}. The uncertainty on the integrated luminosity is ±5%, and is derived, following a methodology similar to that detailed in Ref. [61], from a preliminary calibration of the luminosity scale using a pair of x-y beam-separation scans performed in August 2015. An important difference from the methodology of Ref. [61], which refers to the Run-1 luminosity determination, is that the source of the luminosity information in Run-2 used as its preferred algorithm the LUCID detector luminosity calculation.

The LUCID detector is a luminosity monitor positioned at both forward ends of the ATLAS detector. It determines the luminosity by measuring the Cherenkov light of particles passing though quartz windows with photomultiplier tubes. The pulses over a threshold are counted for each possible 25 ns bunch crossing [62] (although for the data in this analysis only every other bunch was filled). Blocks of time roughly equal to 60 seconds are defined as luminosity blocks by the TDAQ system. For these blocks an integrated luminosity is provided by LUCID.

Simulated event samples from the latest Monte Carlo production reproducing the conditions expected for the early 2015 data taking are used [63, 64]. The events are further processed with the ATLAS software to produce "derived" files containing only the information relevant for this analysis.

Nearly all of the signal and the electroweak background samples are generated with the Powheg Monte Carlo program [65–67], specifically the codes for single boson production [68], interfaced with the Pythia v.8.1 parton shower program [69]. The programs used the CT10 parton distribution functions [70] and the AZNLO CTEQL1 tune for Powheg +Pythia [71]. The EvtGen v1.2.0 program [72] was used to simulate the bottom and charm hadron decays, and Photos version 3.52 [73] was used for QED emissions from electroweak vertices and charged leptons. The expected contributions of the W and Z boson samples are normalised to a cross-section value calculated at NNLO with the FEWZ program [74], using the MSTW2008NNLO parton distribution functions [75].

The distributions of top quark production (both $t\bar{t}$ and single top) were generated with the Powheg-Box v2 generator [76] and Pythia v.6.4 [77] (Perugia 2012 tune), and the pair production is normalised to the cross-section calculated at NNLO+NNLL with the Top++2.0 program [78]. For the $t\bar{t}$ sample, the Powheg model parameter hdamp, which controls matrix element to parton shower matching in POWHEG and effectively regulates the high-pT radiation, was set to the top quark mass, 172.5 GeV, a setting which was found to give the best modelling of the $t\bar{t}$ system at 7 TeV [79].

QCD multijet events are simulated using PYTHIA v.8 and dedicated samples containing $b\bar{b}$ and $c\bar{c}$ quark final states are simulated using Pythia8B [69].

Multiple overlaid proton-proton collisions were simulated with the soft QCD processes of PYTHIA using tune A2 [80] and the MSTW2008LO PDF to simulate the effect of pileup collisions. The pileup distributions of the Monte Carlo samples have been reweighted so that the $\langle\mu\rangle$ distribution matches the observed distribution in the data. All of the samples were processed with the GEANT 4-based simulation [81] of the ATLAS detector [82].

A complete list of all simulated event samples used is given in Table 3.1 for background samples and in Table 3.1 for signal samples.

Table 3.1: Simulated background event samples used in this measurement. Diboson background samples are too numerous to list here individually.

Channel	Generator	$\sigma \cdot \mathrm{BR} \times \epsilon_{\mathrm{filter}}$ [pb]
$W^+ \to \tau\nu$	POWHEG Box [65–67]+PYTHIA8 [69]	11501
$W^- \to \tau\nu$		8579
$Z \to \tau\tau$		1892
$t\bar{t}$	POWHEG Box [65–67]+PYTHIA6 [77]	451
Wt		34
$W\bar{t}$		34
t (t-chan)		44
$\bar{t}$ (t-chan)		26
$ZZ \to qq\ell\ell$	SHERPA2.1.1 [83]	2.3
$WZ \to qq\ell\ell$		3.76
$WZ \to \ell\nu qq$		12.54
$WW \to \ell\nu qq$		25.99
$ZZ \to \ell\ell\nu\nu$		14.02
$ZW \to \ell\ell\ell\nu$ SFMinus		1.84
$ZW \to \ell\ell\ell\nu$ OFMinus		3.62
$ZW \to \ell\ell\ell\nu$ SFPlus		2.56
$ZW \to \ell\ell\ell\nu$ OFPlus		5.02
$ZZ \to \ell\ell\ell\ell$		12.58
$b\bar{b}$	PYTHIA8B [69]	187710
$c\bar{c}$		58528

Table 3.2: Simulated signal event samples used in this measurement.

Channel	Generator	$\sigma \cdot \mathrm{BR} \times \epsilon_{\mathrm{filter}}$ [pb]
$W^+ \to e\nu$	POWHEG Box [65–67]+PYTHIA8 [69]	11501
$W^- \to e\nu$		8579
$W^+ \to \mu\nu$		11501
$W^- \to \mu\nu$		8579
$Z \to ee$		1892
$Z \to \mu\mu$		1892

3.3 Event Selection

Only events recorded with a fully operational detector are used in this analysis. The detector status is stored in the "good run list", which is used to select events contained in good luminosity blocks. Events are furthermore required to have at least one hard scatter vertex with at least 2 associated tracks. The vertex with the largest $\sum p_{\mathrm{T}}^2$ (meeting these requirements) is considered the primary vertex by the reconstruction software [84].

All events are required to pass a high-level trigger (HLT) chain, which depends on the lepton flavour used. The lepton definition and selection is described in the next two sections, followed by the definition of the missing energy in section 3.3.4 and the lepton flavour independent selection of events containing a W or Z boson in sections 3.3.6 and 3.3.7, respectively. All selection criteria are summarized in Table 3.3.

3.3.1 Electron Definition and Selection

Events are required to pass either a loosely-isolated single electron trigger with a threshold of $p_{\mathrm{T}} > 24$ GeV or an unisolated single electron trigger with a threshold of $p_{\mathrm{T}} > 60$ GeV; at larger transverse energies the rate is lower and the need for isolation at the trigger level is removed. In both cases a "medium" electron identification working point is applied in the trigger. Reconstructed electrons are required to pass a "medium" identification selection using a likelihood-based algorithm [56]. The transverse momentum p_{T} has to be larger than 25 GeV and they have to fall within $|\eta| < 2.47$ and not in the calorimeter crack region between $1.37 < |\eta| < 1.52$.

Table 3.3: Overview of the event selection criteria applied. For the definition of leptons and missing energy refer to the text.

Lepton Selection - Electrons	
p_T	$> 25\,\text{GeV}$
η	$\lvert\eta\rvert < 2.47$ and $1.37 < \lvert\eta\rvert < 1.52$
ID	MediumLH
Isolation	gradient isolation
Lepton Selection - Muons	
p_T	$> 25\,\text{GeV}$
η	$\lvert\eta\rvert < 2.4$
ID	Medium Muon
Isolation	gradient isolation
Boson Selection - W	
N leptons	exactly 1
OR	Overlap removal between jets and leptons
$E_{\mathrm{T}}^{\mathrm{miss}}$	$> 25\,\text{GeV}$ and apply MET cleaning
m_{T}	$> 50\,\text{GeV}$
Boson Selection - Z	
N leptons	exactly 2, same flavour and oppositely charged
mass window	$66 < m_{\ell\ell} < 116\,\text{GeV}$

3.3.2 Muon Definition and Selection

Events are required to pass either a loosely-isolated single muon trigger with a threshold $p_{\mathrm{T}} > 20$ GeV or an unisolated trigger with threshold $p_{\mathrm{T}} > 50$ GeV. Muons identified by the "medium" algorithm [58] are considered. The transverse momentum p_{T} has to be larger than 25 GeV and they have to fall within $|\eta| < 2.4$.

3.3.3 Lepton Isolation

Both electrons and muons are required to be isolated, fulfilling the "gradient isolation" requirement discussed in detail in Refs. [56, 58]. The isolation requirement is a p_{T} and η-dependent cut on both calorimeter and track isolation variables and has been tuned to have an efficiency of approximately 90% for leptons of $p_{\mathrm{T}} = 25$ GeV and 99% for leptons of $p_{\mathrm{T}} > 60$ GeV.

The calorimeter isolation variable topoetcone20/p_{T} is defined as the sum of the E_{T} from topologically clustered calorimeter cells not already associated with the reconstructed object within a cone of $\Delta R = \sqrt{\Delta\eta^2 + \Delta\phi^2} < 0.2$ around the reconstructed object. This is then divided by the object p_{T}. The track isolation variables, ptvarcone20/p_{T} for electrons and ptvarcone30/p_{T} for muons, are constructed in a similar way. The sum of the p_{T}'s for tracks within $\Delta R < 0.2(0.3)$ of the reconstructed electron (muon) but not associated with the object is considered in place of the sum of calorimeter E_{T}.

Such an isolation requirement is optimal for the selection of $t\bar{t}$ candidate events. The gradient isolation requirement was chosen in the context of this analysis with the aim to synchronize the top and W, Z inclusive analyses and allow easy combination of the measured cross-sections or cross-section ratios.

3.3.4 Definition of Missing Energy

The reconstruction of the missing transverse momentum (MET) in the events is calculated as the negative vector sum of the momentum of high-p_T calibrated objects (electrons, muons, jets), and of the soft-event contribution which is reconstructed from tracks or calorimeter cell clusters not associated with the hard objects [59], described in more detail in Section 2.4.4.

The pile-up present in the data degrades the resolution of the calorimeter-based measurement of missing transverse momentum. An $O(20\%)$ improvement in resolution is obtained using a track-based measurement of the soft-event contribution, which is chosen as default for this analysis [59].

3.3.5 Overlap Removal

Missing energy reconstruction internally takes into account the overlap between jets and other hard objects, therefore a consistent overlap removal strategy should be applied also at selection level.

This process is provided with selected leptons and jets with $p_{\mathrm{T}} > 20$ GeV and passing jet quality selections. The following selection is then performed:

- Remove jet if within $\Delta R < 0.2$ of a selected electron
- Remove electron if within $0.2 < \Delta R < 0.4$ of a selected jet
- Remove muon if within $\Delta R < 0.4$ of a selected jet, if the jet has $N_{\mathrm{tracks}} > 2$ (considering only tracks with $p_{\mathrm{T}} > 0.5$ GeV). Otherwise remove jet.

The driving principle behind the $\Delta R = 0.2$ value is that the electron clusters plus bremstrahlung should be contained in such cone. However if the electron clusters are still very close to the area of well reconstructed jet, then we should consider the electron likely part of that jet. In the muon case, the track-counting within overlying jets allows us to remove the ambiguity between what is just a muon and what is a jet containing a semi-leptonic decay. $E_{\mathrm{T}}^{\mathrm{miss}}$ reconstruction is not too sensitive to this effect but the overlap removal gives an additional tool to identify multi-jet background events.

Regarding the data and simulation samples under investigation, the overlap removal has a very small effect on the isolated electron selection but the effect has been found to be relevant on the isolated muon selection as the $N_{\mathrm{tracks}} > 2$ requirement tightens the muon isolation requirement. The application of the overlap removal reduced by approximately a factor of 2 the measured multi-jet contamination in the muon channel. The overlap removal is not needed (and not applied) to Z inclusive selection as jets are not used.

3.3.6 *W* Boson Event Selection

Events containing a W boson candidate are selected by requiring exactly one selected lepton and a missing energy of at least 25 GeV. Events containing calibrated jets passing a loose quality requirement [85] and with transverse momentum above 20 GeV are rejected. This is referred to as "MET cleaning". Additionally the transverse mass m_T of the W boson candidate has to be larger than 50 GeV. Table 3.4 summarise the number of $W \to \ell\nu$ candidates in data remaining after each major requirement in the respective analyses.

Table 3.4: Number of W candidates in data and signal MC, remaining after each major requirement. The first entry of the table (Lepton selection) includes also the preselection, OR, and di-lepton veto cuts listed in Table 3.3. The signal MC is normalised to the NNLO cross-section shown in Table 3.6 and to luminosity.

Requirement	Number of candidates							
	$W^+ \to e^+\nu$		$W^+ \to \mu^+\nu$		$W^- \to e^-\bar{\nu}$		$W^- \to \mu^-\bar{\nu}$	
	Data	Signal MC	Data	Signal MC	Data	Signal MC	Data	Signal MC
Lepton selection	446199	270826	376705	290878	381649	210071	302308	219635
$E_{\mathrm{T}}^{\mathrm{miss}} > 25$ GeV	293958	225813	289010	244565	240281	175639	227887	185663
$m_{\mathrm{T}} > 50$ GeV	256858	217999	266592	236540	206092	170156	208616	180223

3.3.7 Z Boson Event Selection

Events containing a Z boson candidate are selected by requiring exactly two selected leptons of the same flavour which are oppositely charged. The invariant mass of the di-lepton pair has to be within $66 < m_{\ell\ell} < 116\,\text{GeV}$.

Table 3.5 summarises the number of $Z \to \ell\ell$ candidates remaining in data after each major requirement has been imposed.

Table 3.5: Number of $Z \to ee$ and $Z \to \mu\mu$ candidates in data, remaining after each major requirement. The signal MC is normalised to the NNLO cross-section shown in Table 3.6 and to luminosity.

Requirement	Number of candidates	
	$Z \to ee$	$Z \to \mu\mu$
Trigger	141600	445400
Two medium ID leptons (ee or $\mu\mu$ with $E_{\mathrm{T}}(p_{\mathrm{T}})$ >25 GeV)	42680	59300
Isolation	36900	46910
Opposite charge ee or $\mu\mu$ pair	36370	46880
$66 < m_{\ell\ell} < 116$ GeV	35009	44898

3.4 Background Expectations for the $W \to \ell\nu$ and $Z \to \ell\ell$ Candidates

The selections described in the previous section define the analysis Signal Regions (SRs) for $W \to \ell\nu$ and $Z \to \ell\ell$ candidate signal events. However additional background processes contributing to the dataset need to be estimated with data-driven techniques, employing different event selections.

Two categories of backgrounds can be defined: the electroweak (single and diboson) and top which are estimated from the appropriate MC samples as described in Section 3.4.1, and the multijet (MJ) background resulting from QCD interaction in the proton proton collisions, estimated from data in both the W and the Z channels, as discussed in Sections from 3.4.2 to 3.4.5.

The values for the predicted cross-sections of the signal and background samples and their estimated uncertainties are given in Table 3.6. This section summarises the evaluation of the expected backgrounds.

Table 3.6: Signal and background processes used in the electron and muon channel analyses, including the production cross-section (multiplied by the relevant branching ratios (BR)) with corresponding theoretical uncertainty. The W, Z, and $t\bar{t}$ cross sections are given at next-to-next-to-leading order (NNLO), while the diboson and single top cross sections are given at next-to-leading order (NLO).

Physics process	Cross section (pb) [× BR]	Theory uncertainty	Order	Reference
W→ $\ell\nu$ ($\ell = e, \mu, \tau$)	20094	5%	NNLO	FEWZ/CT14
$W^+ \to \ell^+\nu$	11548	5%	NNLO	FEWZ/CT14
$W^- \to \ell^-\overline{\nu}$	8546	5%	NNLO	FEWZ/CT14
Z→ $\ell\ell$ ($66 < m_{\ell\ell} < 116$ GeV)	1890	5%	NNLO	FEWZ/CT14
$t\bar{t}$	831	6%	NNLO+NNLL ($m_t = 172.5$ GeV)	TOP++v2.0
single top (t-channel+Wt)	137.5	6%	NLO	POWHEG
WW	108.7	5%	NLO	MCFM/CT10
WZ	42.4	7%	NLO	MCFM/CT10
ZZ	14.7	5%	NLO	MCFM/CT10

Table 3.7: Electroweak background contributions estimated from simulation. Expectations are expressed as a percentage of the total simulated events coming from the sources listed in the table and passing signal selection in each channel. Totals with their uncertainty are given in Table 3.14.

	$W \to e\nu$ % MC	$W \to \mu\nu$ % MC	$Z \to ee$ % MC	$Z \to \mu\mu$ % MC
$W \to \tau\nu$	1.8	1.9	0.00	0.00
$Z \to \tau\tau$	0.12	0.13	0.04	0.05
Diboson	0.08	0.07	0.12	0.12
$t\bar{t}$	1.1	0.8	0.24	0.24
single top	0.2	0.2	0.00	0.00
$W \to e\nu$	95.5	–	0.00	0.00
$W \to \mu\nu$	–	92.3	0.00	0.01
$Z \to ee$	1.2	–	99.60	0.00
$Z \to \mu\mu$	–	4.6	0.00	99.58

3.4.1 Electroweak and top backgrounds

The electroweak and top Monte Carlo samples listed in Table 3.1 are used to estimate the background in the analyses. Their contributions are normalised to the cross-sections shown in Table 3.6, while their uncertainties are used to evaluate the systematic uncertainties on the electroweak and top background expectations. Table 3.7 shows the expected contributions of individual background processes in each measurement channel.

3.4.2 $W \to \ell\nu$ multijet background estimate methodology

The selection of an isolated lepton, high $E_{\mathrm{T}}^{\mathrm{miss}}$, and high m_{T}, effectively rejects most of the MJ QCD production. However a contamination from such a background process remains because of its very high production cross-section, and a small probability of fake W-boson-like signatures from jets mimicking the isolated lepton selection, and $E_{\mathrm{T}}^{\mathrm{miss}}$ generated through energy mismeasurement in the event. The MJ background composition may also be very diverse, depending on the p_{T} range of interest and of the lepton type. It may be composed of heavy-quark leptonic decays, material conversions, or hadrons. Because of the difficulties in the precise simulation of all these effects, data-driven techniques are often used for the MJ estimate in the $W \to e\nu$ and $W \to \mu\nu$ channels.

A generic recipe for template-based background extraction starts with the selection of a suitable discriminant variable. Ideally this variable should be one in which the signal and background have a significantly different distribution. Next a template generation region is defined by altering the analysis selection requirements, this region should be orthogonal to the signal region and as enriched in the background as possible while remaining in a similar phase space to the signal region so the distribution of the background in the discriminant variable should be almost identical. Other backgrounds and any signal contamination are then subtracted from the events in the template generation region leaving only the distribution of the background which we wish to estimate. This template shape is then included in an extended fit to a control region (for example with any selection on the discriminant variable removed). Finally this control region estimate can be extrapolated back to the signal region with an appropriate scale factor.

Primary Determination for $W \to \ell\nu$ Analysis at 13 TeV

For the published analysis several MJ-templates are defined, slicing the lepton isolation variable for values greater than the one used in the SR and progressively further from the SR lepton selection. The MJ extraction fit on a kinematic variable is then repeated for each of the MJ-templates corresponding to each slice. The result is a "scan" of the MJ extractions with templates closer and closer to the SR lepton selection. It is then possible to linearly extrapolate the MJ estimate into the signal region.

The likelihood fit is constructed including a template from the multijet control region in use and the contamination of non-MJ events entering the MJ selection are subtracted for signal (W_{cont}) and other electroweak backgrounds (b_{cont}) during the fit with the following formula:

$$n^i = (\mathrm{MJ}^i - \sum_{b \in \mathrm{BKG}} b^i_{\mathrm{cont}} \times \mathrm{SF}_b - W^i_{\mathrm{cont}} \times \alpha_W) \times \alpha_{\mathrm{MJ}} + \sum_{b \in \mathrm{BKG}} b^i \times \mathrm{SF}_b + W^i \times \alpha_W, \quad (3.4)$$

where, for each bin i of the discriminant variable being fitted, we build the prediction n, to be compared to the data in the likelihood, by summing the contributions from the templates of MJ, signal (W), or other backgrounds (BKG= $Z \to \ell\ell$, $W \to \tau\nu$, top), each of them scaled by an independent parameter of the fit (SF_b). The signal (W) is left free to float, as is the MJ component, and the EWK backgrounds can vary within 5% of their normalization by means of a Gaussian constraint taken into account in the likelihood. In this way the normalisation of the signals subtracted from the MJ control region to form the MJ template is identical to those found by the final fit in the signal region.

Several choices of variable for defining the MJ-enriched control regions were investigated in order to produce the relevant templates. One considered option was using a variation (inverting or otherwise) of the lepton identification requirements. However as a loose selection was already applied at the trigger level the data set was too small and the MJ estimation was dominated by these statistical errors. Therefore it was decided to invert the isolation selection for the construction of the MJ templates, keeping the rest of the selection cuts as in the nominal signal selection. Given the analysis choice of the "Gradient-Iso" isolation working point which is a tuned $p_{\mathrm{T}}-\eta$-dependent cut on both calorimeter and track relative isolation variables, ptvarcone20(30)/p_{T} and topoetcone20/p_{T} for electrons (muons), this is a non-trivial inversion.

The scan of the template definitions was performed in both of the components of the gradient criteria to cover the different effects which may come from the inversion of the calorimeter or track isolation. The scan slice size and interval were identified by analysing the ptvarcone20(30)/p_{T} versus topoetcone20/p_{T} distributions for electrons (muons) in data for events passing or failing the Gradient-Iso selection. The events passing the Gradient-Iso cut appear to be bounded in the regions below for electrons (muons):

$$\frac{\mathrm{ptvarcone20(30)}}{p_{\mathrm{T}}} < 0.08(0.1) \text{ and } \frac{\mathrm{topotetcone20}}{p_{\mathrm{T}}} < 0.1(0.08) \quad (3.5)$$

As the Gradient-Iso phase space is only in a rectangular region of ptvarconeXX/p_{T} versus topoetcone20/p_{T} it was decided to scan in slices of one isolation requirement at a time, applying a fixed cut on the other requirement to avoid biases from pathological un-isolated events. The distribution of events failing the Gradient-Iso selection was investigated in order to determine the optimum selection for slices to scan over.

MJ templates were extracted and fits performed in two separate fitting regions regions (FR's) defined by removing in one case the m_{T}> 50 GeV requirement, and in the other case removing the $E_{\mathrm{T}}^{\mathrm{miss}}$> 25 GeV requirement. In both cases this increases the MJ component, increasing the available statistics to distinguish it from the other backgrounds.

In each fit region separate fits are performed in the distributions of the following four variables: ${p_{\mathrm{T}}}^{\ell}$, $E_{\mathrm{T}}^{\mathrm{miss}}$, m_{T} and $\Delta\phi_{\ell,E_{\mathrm{T}}^{\mathrm{miss}}}$ for each of the scan points, and the fraction of MJ is estimated and extrapolated back to the signal region (re-applying the m_{T}> 50 GeV cut in one case, and the $E_{\mathrm{T}}^{\mathrm{miss}}$> 25 GeV cut in the other).

The stability of the MJ extraction was checked in several ways: the width of the isolation scan slices was varied, the variables were fitted in reduced ranges of the histograms to reduce the impact of mismodelling of the data/MC distributions, and the EW and top backgrounds were kept fixed by considering a very small Gaussian constraint on them. In all these tests, the MJ estimates were compatible with one another, and significantly smaller than the spread in the extrapolation coming from the use of different fit variables.

$W \to \mu\nu$ Scan Results

As discussed in sec. 3.4.2, the events passing the gradient isolation cut and the selection are confined in the region of ptvarcone30/$p_{\mathrm{T}} < 0.1$ and topoetcone20/$p_{\mathrm{T}} < 0.08$. For this reason scans on the two variables, after inverting the gradient isolation, are performed for the values reported in Table 3.8. The scans in topoetcone20/p_{T} are performed for a fixed range of ptvarcone30/p_{T}, so that the two sets of scans are orthogonal, the details are reported in Table 3.8.

The SR point of extrapolation is extracted from the average value of the ptvarcone30/p_{T} and topoetcone20/p_{T} distributions passing the gradient isolation selection cut in data. These values are 0.002 and 0.006 respectively. An example of the extrapolation is shown

Table 3.8: Width of scan slices and boundaries used for $W \to \mu\nu$ channel.

Scan variable	ptvarcone30/p_{T}	topoetcone20/p_{T}
Fixed cut	topoetcone20/$p_{\mathrm{T}} < 0.08$	ptvarcone30/$p_{\mathrm{T}} < 0.1$
Scan starting point	0.1	0.08
Slice width	0.1	0.06
Number of slices	4	6

in Figure 3.1(a) for the $W^+ \to \mu^+\nu$ channel.

The final background yield and its systematic uncertainty are estimated from the spread of the extrapolated curves of the ptvarcone30/p_{T} and topoetcone20/p_{T} variables. To obtain the central value of the estimate the averages of the extrapolated values are computed, weighted by the uncertainty of the fit to a straight line, separately for the calorimeter and track isolation scans and each fitting region. The nominal MJ yield is taken as the average between the four weighted averages (from the different scan variables). An example of the range of values and their uncertainties is shown in Figure 3.1(b).

Seven sources of uncertainties are considered on the method:

- Four come from the errors on the weighted average for each fit region;
- One represents the difference between the choice of scan variables, averaged over fit regions;
- One represents the difference between the choice of fit region, averaged over the scan variable;
- One shows the impact of the jet energy scale variation on the signal template in the estimated MJ yield.

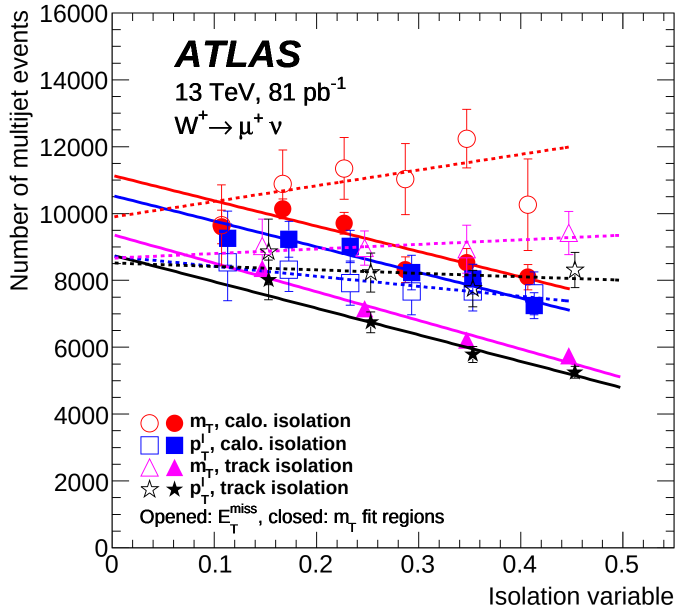

(a) The distribution of multijet estimates as a function of slice in the scan.

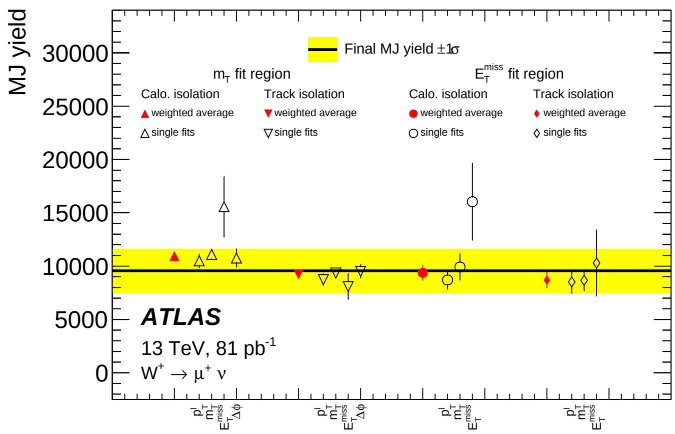

(b) The distribution of extrapolated estimates and their combination. Each hollow point represents the extrapolation to the signal region for one of the four template variables in the two fitting regions for both track and calorimeter isolation scans. The red points represent the weighted average over the different template variables.

Figure 3.1: Detailed plots of the MJ extraction for the $W^+ \to \mu^+\nu$ channel

$W \to e\nu$ Scan Results

For the electron channel the scan proceeds the same as for the muon channel apart from changes to account for the different distributions of the isolation variables. The events passing the gradient isolation cut and the selection are confined in the region of ptvarcone20/$p_{\mathrm{T}} < 0.08$ and topoetcone20/$p_{\mathrm{T}} < 0.11$. For this reason scans on the two variables, after inverting the gradient isolation, are performed for the values reported in Table 3.9. As for the muon channel, the scans in topoetcone20/p_{T} are performed for a fixed range of ptvarcone20/p_{T}, so that the two sets of scans are orthogonal.

Table 3.9: Description of the scans performed in the $W \to e\nu$ channel.

Scan variable	ptvarcone20/p_{T}	topoetcone20/p_{T}
Fixed cut	topoetcone20/$p_{\mathrm{T}} < 0.11$	ptvarcone20/$p_{\mathrm{T}} < 0.08$
Scan starting point	0.08	0.11
Slice width	0.08	0.08
Number of slices	4	4

The SR point of extrapolation is extracted from the average value of the ptvarcone20/p_{T} and topoetcone20/p_{T} distributions passing the gradient isolation selection cut in data using the nominal signal selection. These values are 0.002 and 0.014 respectively. Figure 3.2 shows an example of the MJ extraction for the $W^+ \to e^+\nu$ channel.

The final background yield and its systematic uncertainty are estimated using the same procedure as for the muon channel.

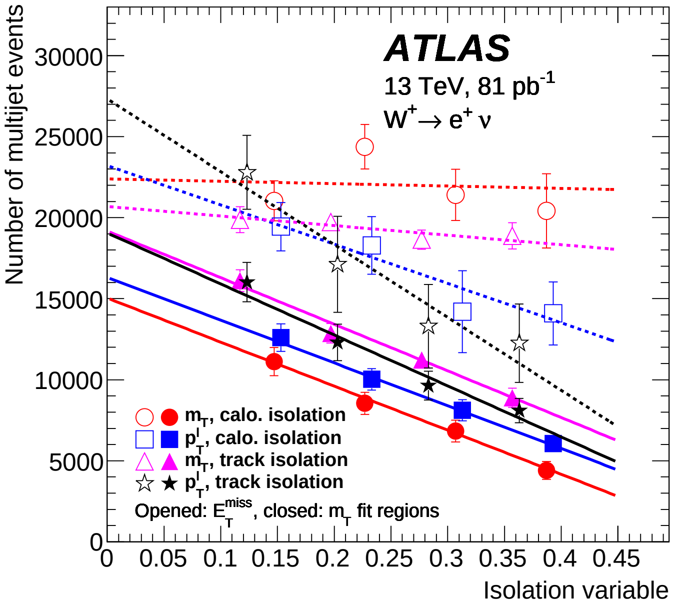

(a) The distribution of multijet estimates as a function of slice in the scan.

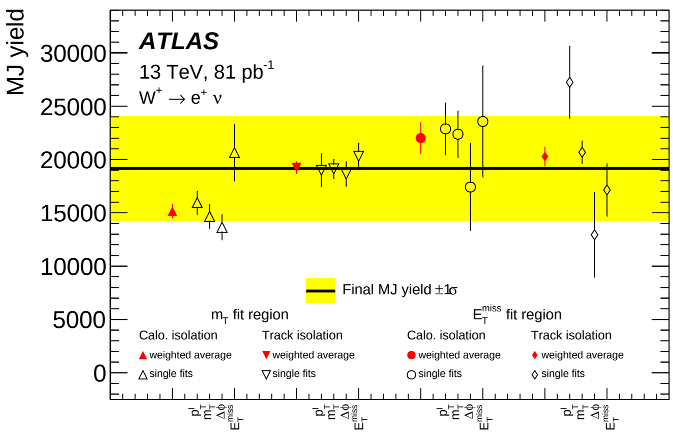

(b) The distribution of extrapolated estimates and their combination. Each hollow point represents the extrapolation to the signal region for one of the four template variables in the two fitting regions for both track and calorimeter isolation scans. The red points represent the weighted average over the different template variables.

Figure 3.2: Detailed plots of the MJ extraction for the $W^+ \to e^+\nu$ channel

3.4.3 Multijet with CR Method in $W \to \mu\nu$ Channel

This section describes an alternative approach to the extraction of the MJ fraction in the $W \to \mu\nu$ channel that has been used to cross check the solidity of MJ results. However the study was completed before the introduction of the Overlap Removal (see Section 3.3.5) which reduced the MJ background in the analysis of the muon channel, as documented above.

The main sources of multijet background for the $W \to \mu\nu$ channel are non-prompt muons from b and c hadron decays. This background is modelled from data using a data-driven template built in a background-enriched region.

The control region used to generate the data template is defined using the full analysis selection applied apart from the following modifications:

- The gradient isolation requirement is inverted.
- Additionally there is a "guard cut" on the relative isolation of < 0.2 for both ptcone20/pt and topoetcone20/pt. This selection is introduced to reject very unsignal like events with large isolation values entering the template while ensuring that there are enough data points.

Those requirements ensure that the template selection is orthogonal to the signal one, and reduce the signal contamination in the template. Also the guard cut avoids accepting muons from a phase space far from the signal region.

Figure 3.3 shows the m_T distribution applying the template selection defined above. The QCD normalisation comes from data, and the other backgrounds are taken from MC and are scaled to the appropriate cross-sections. The data-driven template is generated using these data after using Monte Carlo events to subtract the contamination of the signal and other background processes. The amount of contamination is shown in Table 3.10.

After the template has been produced the shape is compared with that for the $b\bar{b}/c\bar{c}$ Monte Carlo sample in Figure 3.4(a). This Monte Carlo template is generated in the extended signal region with no m_T cut. To account for the luminosity uncertainty when subtracting the background components from MC two additional templates are built where the signal contribution in the control region is increased and decreased by 10%. The difference with

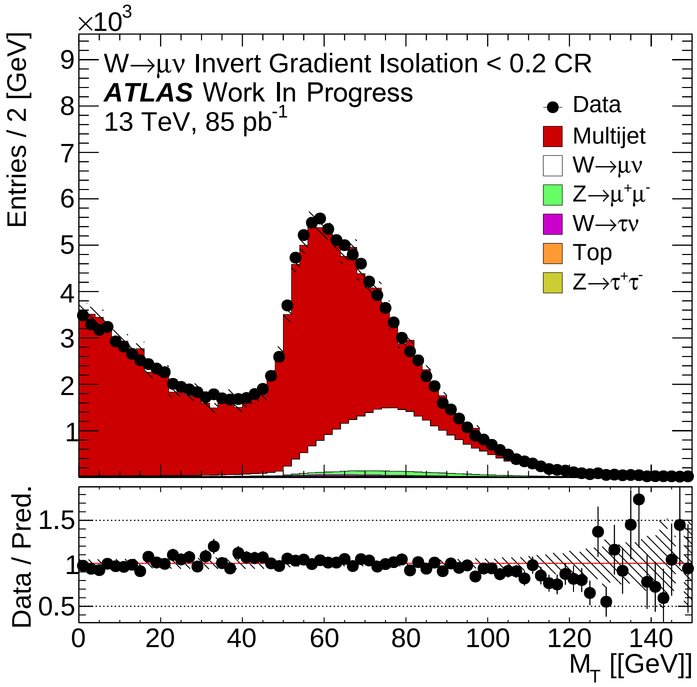

Figure 3.3: The data observed applying the $W \to \mu\nu$ template selection compared with Monte Carlo which has been scaled using contents of the data template and other components scaled to their cross-section.

Table 3.10: Fractional contamination of other background processes and the signal for the $\mu\nu$ multijet template selection defined with inverted gradient isolation and an upper cut of 0.2 on the relative isolation.

Process	Overall Contamination	Low m_T Contamination ($0 < m_T < 46\,\text{GeV}$)
$W \to \mu\nu$	18%	1%
$W \to \tau\nu$	0.5%	0.2%
$Z \to \mu^+\mu^-$	1.4%	0.3%
$t\bar{t}$	0.3%	0.2%
$Z \to \tau^+\tau^-$	0.06%	0.07%
Total	20%	2.4%

the nominal template is shown in Figure 3.4(b).

The effect of systematic variations on the signal shape is also considered by applying a shift of one of the available jet energy scale nuisance parameters to it. The difference in shape is shown in Figure 3.5. In this case the signal subtraction from the template is also performed with the varied signal template.

A further template is generated in a secondary control region where the full analysis selection is applied but an additional cut on the d_0 significance of $|d_0 \text{ significance}| > 4$ is applied to remove the signal component.

Once the multijet background template has been generated, it is used to provide an estimate for the multijet normalisation. This is done through a fit in the control region (CR) after the full event selection, defined as $0 < m_T < 46\,\text{GeV}$, to exploit the slope difference in the low m_T region. The m_T distributions for signal and the other background components are taken from Monte Carlo simulation.

In the fit the signal and multijet background yields are free. The other background components are normalised to their expectation based on the estimated cross-section and integrated luminosity. Systematic uncertainties on these expected yields are applied through multiplicative scale factors on the yields and Gaussian constraint terms for these scale factors are added in the likelihood. The uncertainty on the integrated luminosity, $\approx 9\%$, is correlated among the various background contributions, while appropriate cross-section uncertainties (e.g. $\approx 5\%$ for Z production) are added independently for each background contribution.

RooFit is then used to perform the fit and extract the expected number of multijet background events in the Signal region, $m_T > 50$ GeV, for both the $W^+$and W^-selections. In both cases the multijet template is built to be charge-independent to increase the statistics as studies of the available data templates and MC templates show no difference between the m_T shape. The fit results can be seen in Fig. 3.6(a), 3.6(b) and in Tables 3.11, 3.12 where the MINOS [86] uncertainties are reported. In the fits in Tables 3.11, 3.12 and 3.13 marked with a † `TH1->Smooth()` has been used to remove statistical fluctuations from the templates due to low statistics in the available simulation samples compared with the data template generation regions. The same exercise is done

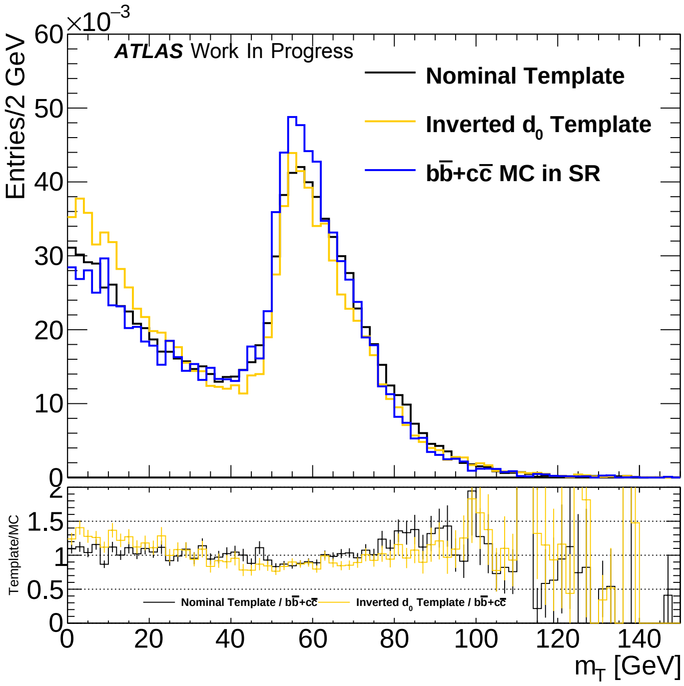

(a) Comparison of the data-driven templates and template generated from $b\bar{b}/c\bar{c}$ Monte Carlo samples.

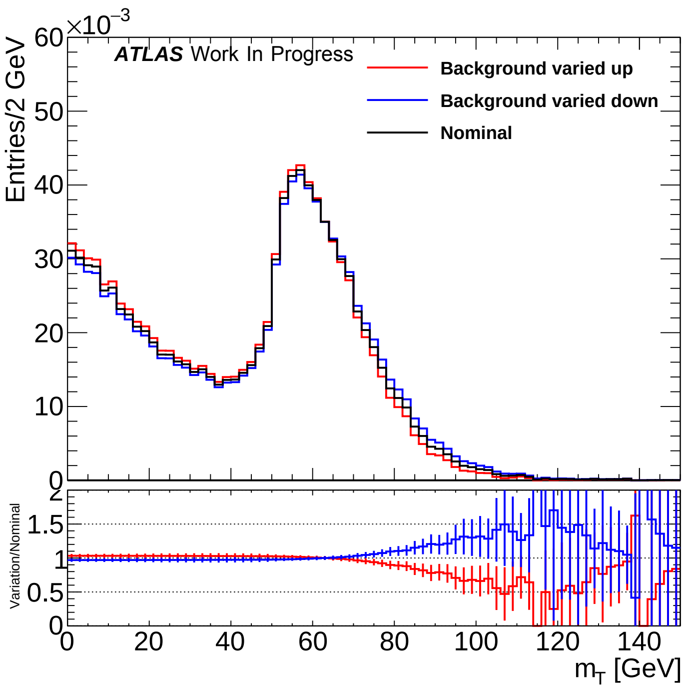

(b) Comparison of the data-driven template with the background subtraction varied ±10% samples.

Figure 3.4: The template extracted from data compared with the MC template as well as variations in the background subtraction.

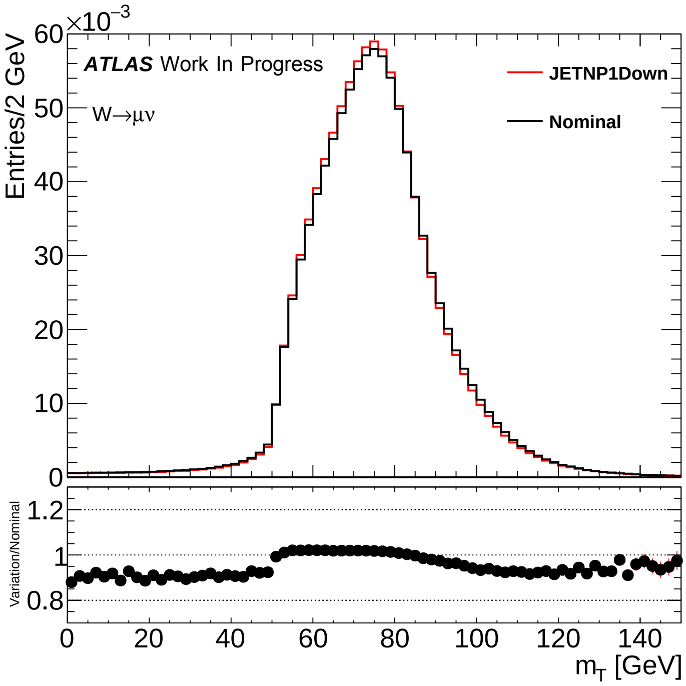

Figure 3.5: Comparison of the signal shape where one of the available nuisance parameters representing the systematic variations on the jet energy scale has been shifted by 1σ.

for the inclusive W samples and the results are shown in Table 3.13.

The quoted uncertainty from the fit includes the statistical error as well as the uncertainties related to luminosity and cross-section. In addition to this error, extra systematic errors are assigned to take account the shape differences which can affect the result of the fit.

The template is dependant on the exact criteria used to produce it, therefore alternate templates are also produced and the variation in the final MJ estimate is observed.

For all of the data templates in Tables 3.11 and 3.12 a guard cut is placed on the relative isolation of 0.5 for the track isolation (ptcone20/pt) and 0.3 for the calorimeter isolation (topoetcone20/pt) on top of the specified cuts used when generating the templates. The gradient isolation requirement is also removed from the selection of the data templates which use additional isolation criteria.

The results of these fits are found to be compatible with the results of fits using the available $b\bar{b}/c\bar{c}$ MC. The $b\bar{b}$ and $c\bar{c}$ components are also fitted separately to estimate possible uncertainties from the relative composition in the MC. The compatibility test of the result from the data template with one derived from the MC is shown in Figure 3.7. The

Table 3.11: Results of the fit in the low m_T region for W^+events, where the results have been extrapolated to the signal region. Templates marked with † have been smoothed to remove statistical fluctuations.

Template definition	MJ Estimate	Fit Error
Invert Gradient Isolation + Upper Isolation limit of 0.2	13 400	300
Calo + track cut $0.05 \leq Iso < 0.1$	12 200	300
Calo cut $0.05 \leq Iso < 0.1$	12 300	300
Track cut $0.05 \leq Iso < 0.1$	13 900	300
SR bb+cc MC Fit†	13 500	300
SR bb+cc MC Fit MET Reweighted†	13 600	300
SR bb MC Fit†	14 400	300
SR cc MC Fit†	12 000	300
Data SR $\lvert d_0Sig\rvert > 2.5$	11 000	300
Data SR $\lvert d_0Sig\rvert > 4.5$	9000	200
MC SR $\lvert d_0Sig\rvert > 2.5$†	13 300	300

Table 3.12: Results of the fit in the low m_T region for W^-events, where the results have been extrapolated to the signal region. Templates marked with † have been smoothed to remove statistical fluctuations.

Template selection	MJ Estimate	Fit Error
Invert Gradient Isolation + Upper Isolation limit of 0.2	13 700	300
Calo + track cut $0.05 \leq Iso < 0.1$	12 600	300
Calo cut $0.05 \leq Iso < 0.1$	12 600	300
Track cut $0.05 \leq Iso < 0.1$	14 300	300
SR bb+cc MC Fit†	14 000	300
SR bb+cc MC Fit MET Reweighted†	14 000	300
SR bb MC Fit†	14 900	300
SR cc MC Fit†	12 300	300
Data SR $\lvert d_0Sig\rvert > 2.5$	11 300	300
Data SR $\lvert d_0Sig\rvert > 4.5$	9240	200
MC SR $\lvert d_0Sig\rvert > 2.5$†	13 700	300

Table 3.13: Results of the fit in the low m_T region for Wevents, where the results have been extrapolated to the signal region. Templates marked with † have been smoothed to remove statistical fluctuations.

Template selection	MJ Estimate	Fit Error
Invert Gradient Isolation + Upper Isolation limit of 0.2	27 000	500
Calo + track cut $0.05 \leq Iso < 0.1$	24 700	500
Calo cut $0.05 \leq Iso < 0.1$	24 800	400
Track cut $0.05 \leq Iso < 0.1$	28 200	500
SR bb+cc MC Fit†	27 500	500
SR bb MC Fit†	29 300	500
SR cc MC Fit†	24 200	400
Data SR $\lvert d_0Sig\rvert > 2.5$	22 100	400
Data SR $\lvert d_0Sig\rvert > 4.5$	18 200	300
MC SR $\lvert d_0Sig\rvert > 2.5$†	27 000	500

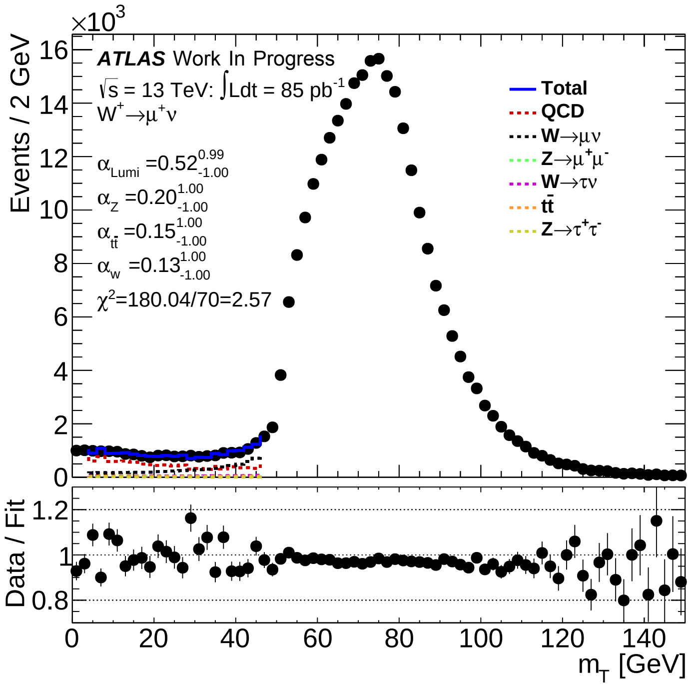

(a) W^+fit using the nominal data template

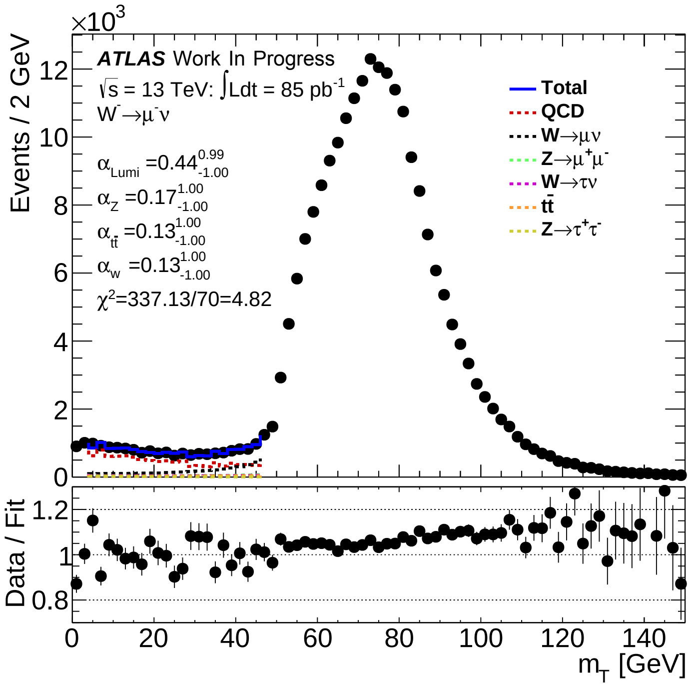

(b) W^-fit using the nominal data template

Figure 3.6: The result of the fit in the signal region using the nominal data-driven template. The α's represent the shifts in the constrained quantities measured in standard deviations from the central value. The uncertainties being ≈ 1 shows that these are not constrained by the fit.

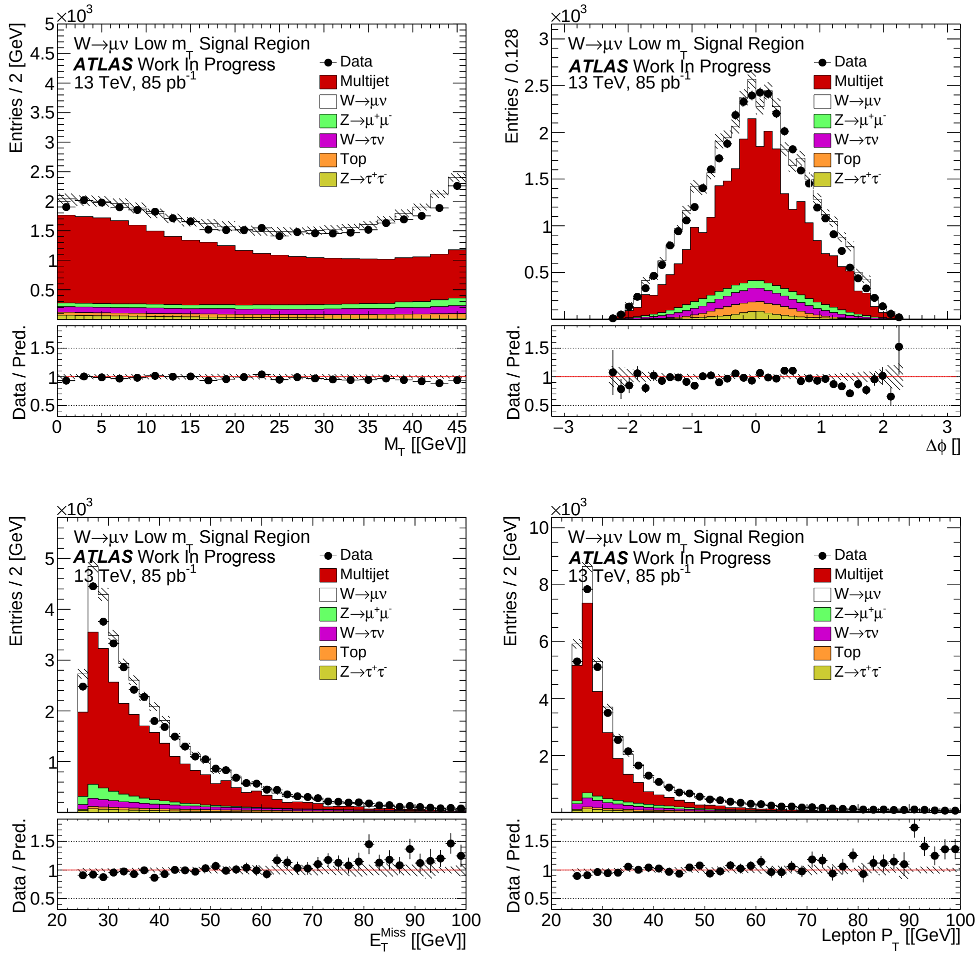

Figure 3.7: The kinematic distributions observed in the low m_T region used to perform the fit.

MC template is generated using the full signal selection neglecting the m_T requirement.

A slight difference is observed in the MET and lepton p_T distributions with the data-driven template normalised by the fit in the m_T variable, demonstrated in Figure 3.7. To investigate the effect of these on the m_T fit an additional fit is performed where the templates have been re-weighted to the MET distribution as observed in data, these templates are shown in Figure 3.8. This corrects both the MET and lepton p_T distributions but leads to a small ($< 1\%$) difference in the fit result.

With this method the estimate of multi-jet background is $13400 \pm 300(\text{stat}) \pm 2000(\text{syst})$ for $W^+$and $13700 \pm 300(\text{stat}) \pm 2000(\text{syst})$ for W^-. The total systematic uncertainty is obtained by combining the maximum differences in the final MJ estimate observed when varying the data template and the MC template definition.

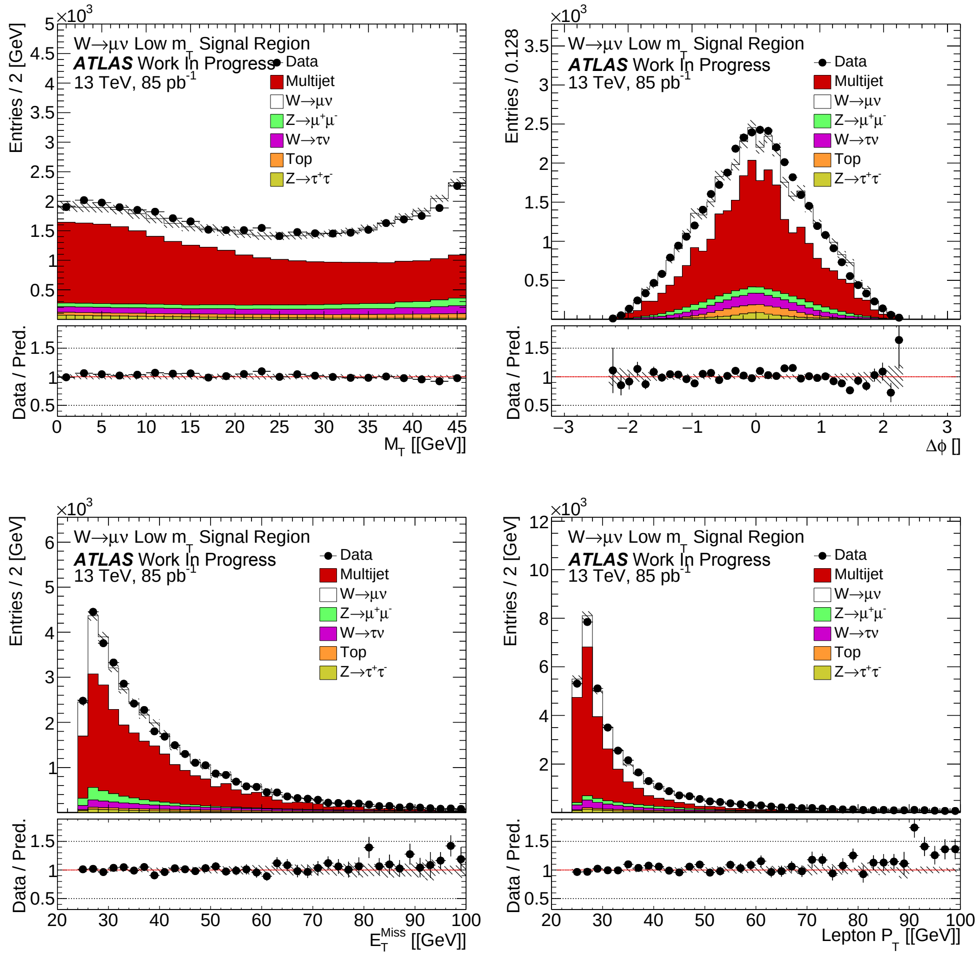

Figure 3.8: The kinematic distributions observed in the low m_T region used to perform the fit where the multijet component has been re-weighted so that the MET distribution matches the data.

These numbers are compatible within the uncertainties with the ones obtained with the isolation scans method, when performed without the overlap removal tool, and with the preliminary luminosity evaluation of 85 pb^{-1}, of: 13932 ± 2368 for $W^+ \to \mu^+\nu$ and of 12092 ± 2660 for $W^- \to \mu^-\nu$.

3.4.4 $Z \to ee$ channel

Estimates of the multijet background based on the filtered MC jet samples with relaxed isolation criteria indicate that this background is $< 0.1\%$. This estimation agrees well with the multijet background found for $\sqrt{s} = 7$ TeV analysis of 0.02% to 0.15% [87].

3.4.5 $Z \to \mu\mu$ channel:

A first look at the multi-jet background is performed by fitting the d_0 distribution in data, using C2-C5-period samples. The background template is obtained by inverting the isolation cut and requiring $|d_0| > 0.1$ mm for one of the muons. The tag-and-probe method is used to obtain the d_0 distribution for the multijet background, with the muon failing $|d_0| > 0.1$ mm cut selected as the tag and the second as the probe. The invariant mass distribution of the two muon candidates for the template shows no peak around the Z-boson mass, indicating a high background purity of the template. The fit estimates a background of $(0.06 \pm 0.04)\%$, consistent with being below 0.1%.

3.5 Summary of Background-subtracted Candidate Events and Kinematic Distributions

3.5.1 Numbers of W and Z Candidate Events

Tables 3.14 and 3.15 summarise the numbers of observed candidate events for the $W \to \ell\nu$ and $Z \to \ell\ell$ channels, respectively, and include the number of expected background events from both the multijet process and electroweak plus top processes and the number of background-subtracted signal events. In the Z table, the first uncertainty is due to statistics, and the second uncertainty is a systematic one. Monte Carlo statistical uncertainties are considered to be negligible in comparison to the statistical uncertainties associated to the data and to the estimation of the QCD background. In the W table,

Table 3.14: Numbers of observed candidate events for the $W \to \ell\nu$ channel, electroweak (EW) plus top, and data-derived QCD background events, and background-subtracted signal events.

ℓ	Observed candidates	Background (EW+top)	Background (Multijet)	Background-subtracted data N_W^{sig}
e^+	256858	9625 ± 522	19169.59 ± 4888.79	$228063.4 \pm 506.8 \pm 4916.6$
e^-	206092	8667 ± 470	19530.30 ± 6092.49	$177894.7 \pm 454.0 \pm 6110.6$
μ^+	266592	19314.1 ± 756.2	9556.93 ± 2076.2	$237721.0 \pm 516 \pm 2209.6$
μ^-	208616	17340.2 ± 684.6	8093.2 ± 2425.3	$183182.5 \pm 457 \pm 2520.1$

Table 3.15: Numbers of observed candidate events for the $Z \to \ell\ell$ channel, electroweak (EW) plus top, and multijet background events, and background-subtracted signal events. The first uncertainty is statistical. The second uncertainty represents the systematics (as described in the text).

ℓ	Observed candidates	Background (EW+top)	Background (Multijet)	Background-subtracted data N_Z^{sig}
$e^{\pm}$	35009	$143.9 \pm 1.0 \pm 7.5$	$< 0.1\%$	$34865.1 \pm 187.1 \pm 6.9$
$\mu^{\pm}$	44898	$191.3 \pm 1.2 \pm 9.8$	$< 0.1\%$	$44706.7 \pm 211.9 \pm 9.0$

the uncertainty considered for the EW+top backgrounds is the combination of the experimental uncertainties, described in Section 2.4.5, the NNLO (where present) or NLO uncertainties normalisation uncertainties, described in Table 3.6, and the statistical uncertainty on the MC, which is very small. For the multijet background, the uncertainties coming from the extrapolation method, and described in detail in Section 3.4.2 and 3.4.2 are presented. For the background-subtracted events the statistical uncertainty is quoted first, followed by the total systematic uncertainty, derived from the EW+top and multijet background ones, considering the sources as uncorrelated.

These numbers form the basis of the cross-section measurements.

3.5.2 Kinematic distributions

Kinematic distributions for W and Z events passing the selection requirements described in Section 3.3 are presented in this section. The distributions for both $W \to e\nu$ and $W \to \mu\nu$ are shown inclusively in Figs. 3.9-3.12 with the charge separated plots included as Appendix A. The equivalent distributions for both $Z \to e^+e^-$ and $Z \to \mu^+\mu^-$are shown in Appendix B. The uncertainty bands shown in these distributions are described in Section 2.4.5 and are calculated from the following components:

- uncertainty due to the multijet background estimation method
- lepton energy and momentum scale and resolution;
- lepton trigger efficiency;
- lepton reconstruction and identification efficiency, including lepton isolation;

- jet energy scale and resolution;
- soft (unclustered) energy contributions in the $E_{\mathrm{T}}^{\mathrm{miss}}$reconstruction;
- uncertainties in cross-section calculations for electroweak and top quark production; and
- statistical uncertainty due to limited Monte Carlo sample sizes.

These uncertainties are included in the histograms as a shaded band, but the luminosity uncertainty is explicitly omitted from this band. The expected background contributions in the shown distributions are estimated using Monte Carlo simulations, apart from the case of the multijet background in the W distributions, for which both the shape and the normalisation are estimated with a data-driven method. The multi-jet shape is taken from the inverted isolation MJ-template closer to the signal region: with $0.1 <$ ptvarcone30$/p_{\mathrm{T}} < 0.2$ for the muon channel, and with $0.11 <$ topoetcone20$/p_{\mathrm{T}} < 0.19$ for the electron channel.

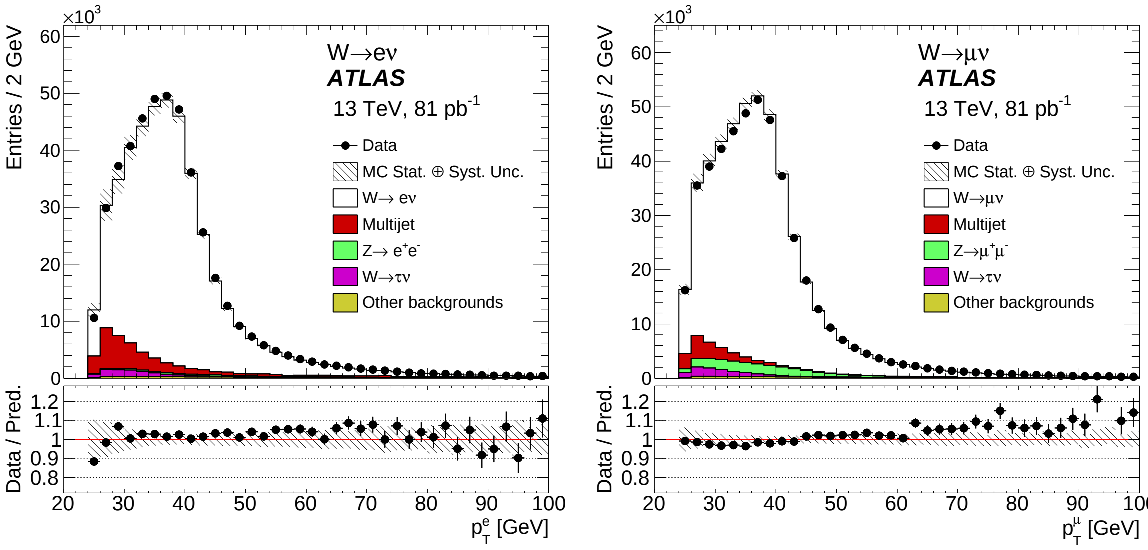

Figure 3.9: Lepton transverse momentum distribution from the $W \to e\nu$ selection (left) and the $W \to \mu\nu$ selection (right).

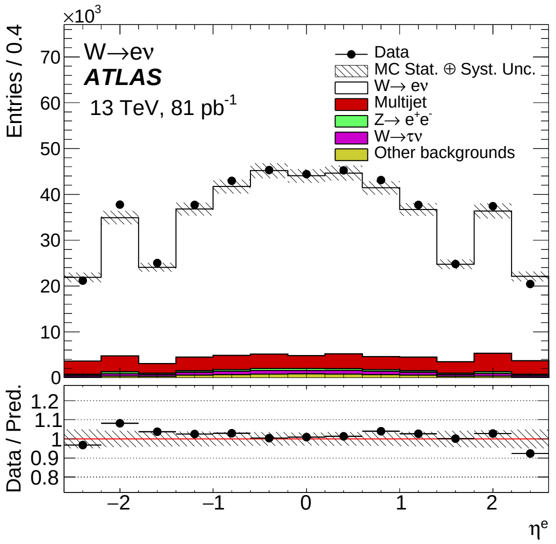

Figure 3.10: Lepton pseudorapidity distribution from the $W \to e\nu$ selection (left) and the $W \to \mu\nu$ selection (right).

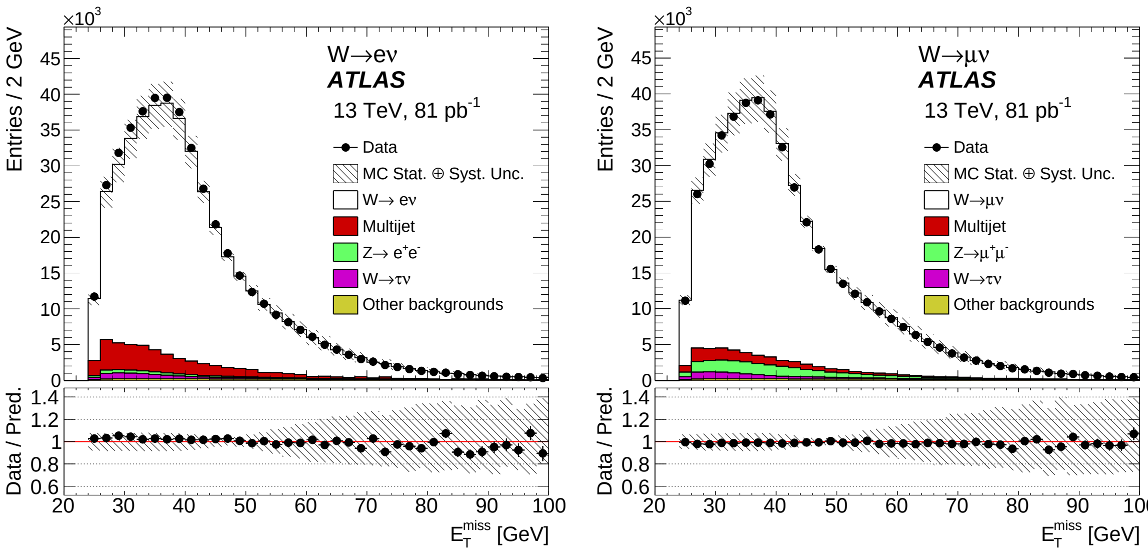

Figure 3.11: Missing transverse energy distribution from the $W \to e\nu$ selection (left) and the $W \to \mu\nu$ selection (right).

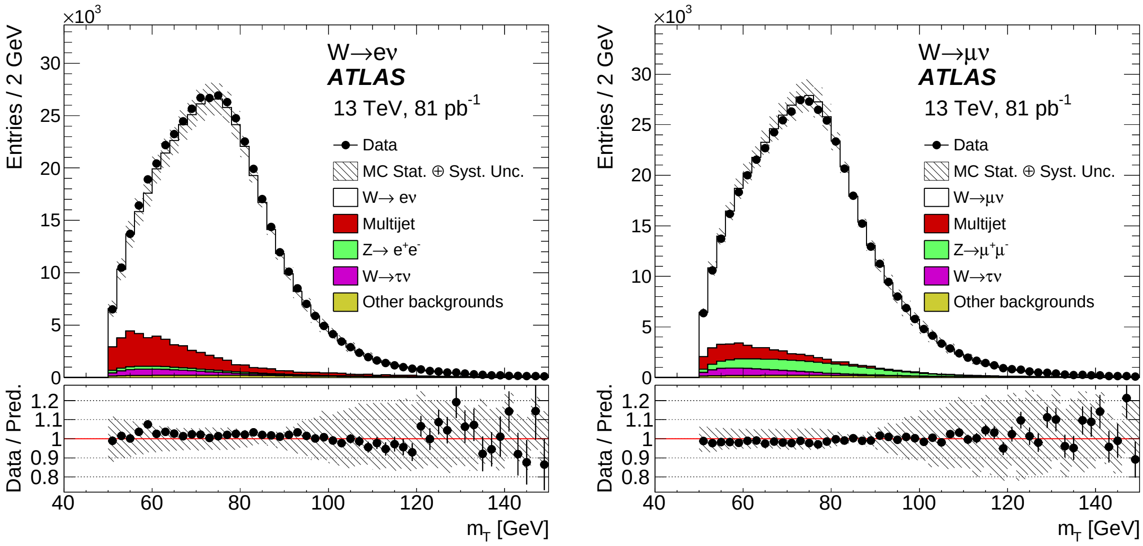

Figure 3.12: Transverse mass distribution, calculated from the lepton and the $E_{\mathrm{T}}^{\mathrm{miss}}$ from the $W \to e\nu$ selection (left) and the $W \to \mu\nu$ selection (right).

3.6 Correction Factors: $C_{W,Z}$, $A_{W,Z}$, and Results

The correction factors $C_{W,Z}$ that feed directly into the cross-section Eq. 3.3 and Eq. 3.2 are defined using MC as the ratio of the total number of generated events which pass the final selection requirements after reconstruction and the total number of generated events within the fiducial acceptance. These correction factors include the efficiencies for triggering, reconstructing, and identifying the boson decays falling within the fiducial acceptance.

The primary components of the uncertainty on the correction factors $C_{W,Z}$ come from detector-related efficiencies, such as triggering and reconstruction/identification of leptons. These systematic contributions are described below. The final values for $C_{W,Z}$ will be presented in Table 3.16.

$$A_{W,Z} = \left(\frac{N^{acc}}{N^{all}}\right)_{gen}, \tag{3.6}$$

The calculation of the total cross-section takes into account the phase-space requirements applied in the fiducial cross-section measurement and is entirely based on FEWZ3.1 NNLO QCD. This geometrical acceptance factor, $A_{W,Z}$, is defined in Equation 3.6 where N^{acc} is the number of generated events that pass the fiducial requirements (as defined in Section 3.1) and N^{all} is the total number of generated events at truth level. The quantity

$A_{W,Z}$ is determined at Born level, i.e. before the decay lepton may emit photons (QED final-state radiation) and the losses due to this effect become a component of the $C_{W,Z}$, evaluated with the full simulation of the detector response. The final values for $A_{W,Z}$ will be presented in Table 3.16.

3.6.1 Calculation of $C_{W,Z}$ for the Electron and Muon Channel

For the boson decays the correction factors are calculated as described above considering the following major effects.

- **Trigger:** MC efficiency is corrected with data-driven scale factors derived from the full 50ns data.
- **Identification and reconstruction:** the efficiencies of the muon offline selection (identification and isolation) are corrected with data-driven SFs obtained using the Tag and Probe method.
- **Momentum Scale and Resolution:** the uncertainty on the muon momentum calibration gives a small change in the acceptance because of the migration of events below and above the p_T, $E_{\mathrm{T}}^{\mathrm{miss}}$and m_T selection cut.
- **Jet Energy scale and resolution:** Jets with calibrated p_T above 20 GeV that pass the Jet-Vertex-Tagger algorithm requirements are considered as hard objects in the calculation of the $E_{\mathrm{T}}^{\mathrm{miss}}$, and the corresponding uncertainty on the energy calibration and resolution is propagated to it. The migration of events above and below the cuts in $E_{\mathrm{T}}^{\mathrm{miss}}$and m_T produces systematic uncertainties at the level of $\approx 1\%$.
- **$E_{\mathrm{T}}^{\mathrm{miss}}$ scale and resolution:** Several possible sources of uncertainty on the soft-component of the $E_{\mathrm{T}}^{\mathrm{miss}}$ scale and resolution have been considered as discussed Section 3.3, resulting in estimated uncertainties below the percent level.
- **PileUp:** The average number interaction per bunch crossing ($\langle\mu\rangle$) in simulation is reweighted to match the value observed in data. An additional scale factor of 1/1.16 is applied to simulated events before the reweighting to correct mismodelling

of diffraction in MC to match both $< \mu >$ and number of reconstructed vertex distributions. This is the result of a study on the reweighting to the number of interaction vertices compared to the $\langle\mu\rangle$ reweighting.

- **PDFs**: uncertainty on the signal reconstruction efficiency due to PDFs is small. The 0.1% value extracted from previous analysis [87] is quoted.

- **Monte Carlo generator uncertainty:** Monte Carlo generator modelling and tunes on tracks associated to jets could have an effect on the MET modelling comparing to data. From Figure B.3 an excellent agreement between data and MC on the $E_{\mathrm{T}}^{\mathrm{miss}}$ distribution in the Z channel is observed. The effects of the Monte Carlo generator are taken into account in the systematic uncertainty associated to the MET soft term described above [88] by comparing the Powheg+Pythia8 sample with HERWIG++. Therefore are not considered here explicitly to avoid double counting.

- **Charge misidentification:** present in the electron channel only. It is evaluated in $Z \to e^+e^-$ events, considering the case where the charge of one of the electrons can be mis-reconstructed causing the event to be rejected by the opposite charge requirement. This has an effect on $W \to e\nu$ events of 0.1%.

The final values for $C_{W,Z}$ for the electron and muon channels and their uncertainties are summarised in Table 3.16.

3.6.2 Geometrical Acceptances $A_{W,Z}$ and Their Uncertainties

The geometrical acceptances are calculated using using DYNNLO 1.5 [89] for the central value and Fewz3.1 [90–93] for the PDF variations with the NNLO parton distribution function (PDF) CT14nnlo [94] for the baseline value (see Sect. 3.7). The statistical uncertainties resulting from these evaluations are negligible.

The systematic uncertainties on the acceptance are dominated by the limited knowledge of the proton PDFs. The systematic uncertainties are derived from the following sources:

- PDF: The PDF uncertainty of CT14NNLO PDF set was rescaled from 90% CL to 68% CL. Additionally, an envelope of predictions with various PDFs was taken as a conservative estimate of extra PDF uncertainty. The envelope was evaluated with four different NNLO PDFs: CT10NNLO, NNPDF3.0, MMHT14NNLO68CL, and ABM12LHC.

- Scale: The scale uncertainty is defined by the envelope of variations in which the scales are changed by factors of two subject to the constraint $0.5 \leq \mu_R/\mu_F \leq 2$, excluding the variations in opposite directions.

- α_S: The uncertainty due to α_S was estimated following the prescription given with the CT14nnlo PDF [94], varying α_S by ± 0.001 to correspond to 68% CL. This source was found to be sub-dominant due to cancellation in the ratio.

- Comparison with POWHEG +PYTHIA: The difference between fixed-order predictions and Monte Carlo simulations was taken as an additional uncertainty.

- Contribution from other sources mentioned in Sect. 3.7 were neglected due to cancellation in the ratio.

- Parton showers and hadronisation description: These are taken from the publication of the 2010 $W$and Z inclusive cross-sections [95]. The values are 0.8% for the W channel and 0.7% for the Z channel. They were derived as the difference in the acceptances calculated with POWHEG Monte Carlo, using the CTEQ 6.6 PDF set but different models for parton shower and hadronisation descriptions, namely the HERWIG or PYTHIA programs.

These components added in quadrature result in systematic uncertainties on the acceptance values for W and Z production. The uncertainties were symmetrised taking the larger value to have a conservative estimate. The final geometrical acceptance corrections are given in Table 3.16.

Table 3.16: Results for the fiducial cross-sections σ^{fid} and total cross section σ^{tot} including the correction and acceptance factors.

	W^+	W^-	Z
	Electron channel (value ± stat ± syst ± lumi)		
Signal events	$228060 \pm 510 \pm 4920 \pm 200$	$177890 \pm 450 \pm 6110 \pm 180$	$34865 \pm 187 \pm 7 \pm 3$
Correction $C_{W,Z}$	0.602 ± 0.012	0.614 ± 0.012	$0.552\,^{+0.006}_{-0.005}$
$\sigma^{\rm fid}$ [nb]	$4.68 \pm 0.01 \pm 0.14 \pm 0.10$	$3.58 \pm 0.01 \pm 0.14 \pm 0.08$	$0.781 \pm 0.004 \pm 0.008 \pm 0.016$
Acceptance $A_{W,Z}$	0.383 ± 0.007	0.398 ± 0.007	0.393 ± 0.007
$\sigma^{\rm tot}$ [nb]	$12.23 \pm 0.03 \pm 0.42 \pm 0.27$	$9.00 \pm 0.02 \pm 0.39 \pm 0.20$	$1.987 \pm 0.011 \pm 0.041 \pm 0.042$
	Muon channel (value ± stat ± syst ± lumi)		
Signal events	$237720 \pm 520 \pm 2210 \pm 410$	$183180 \pm 460 \pm 2520 \pm 360$	$44706 \pm 212 \pm 9 \pm 4$
Correction $C_{W,Z}$	0.653 ± 0.012	0.650 ± 0.012	0.711 ± 0.008
$\sigma^{\rm fid}$ [nb]	$4.50 \pm 0.01 \pm 0.09 \pm 0.10$	$3.48 \pm 0.01 \pm 0.08 \pm 0.08$	$0.777 \pm 0.004 \pm 0.008 \pm 0.016$
Acceptance $A_{W,Z}$	0.383 ± 0.007	0.398 ± 0.007	0.393 ± 0.007
$\sigma^{\rm tot}$ [nb]	$11.75 \pm 0.03 \pm 0.33 \pm 0.27$	$8.75 \pm 0.02 \pm 0.25 \pm 0.20$	$1.977 \pm 0.009 \pm 0.041 \pm 0.042$

3.6.3 Results

All of the elements necessary to calculate the fiducial and total cross-sections for W^+, W^-, $W^\pm$ and Z production and decay in the electron and muon channels are summarized in Table 3.16. The derived fiducial and total cross sections are also presented in this table, along with their statistical, systematic and luminosity uncertainties.

The results obtained in the electron and muon channels are expected to agree, following lepton universality of the Standard Model, which has been probed with high accuracy at LEP [96–99] and by the ATLAS [87] and CMS [100] experiments. The ratio of the electron and muon channel measurements, calculated taking into account correlated systematic uncertainties, is shown in Figure 3.13. Within uncertainties, the ratios agree with the Standard Model expectations.

Since the results in the two channels agree well, they are combined together, taking into account correlated systematic uncertainties. The combination is performed for the W^+, W^- and Z fiducial cross-sections simultaneously using the `HERAverager` [102, 103] tool. For the combination, the systematic uncertainties are symmetrized as $\Delta_{sym} = 0.5(\Delta_+ - \Delta_-)$. Sources corresponding to lepton reconstruction and identification are naturally uncorrelated between electron and muon channel. Other sources may affect $W^\pm$ measurements only, e.g. those which affect missing E_T reconstruction. A few sources, such as PDF uncertainties, affect all the results. The common normalization uncertainty due to the luminosity calibration is excluded for the combination of the channels.

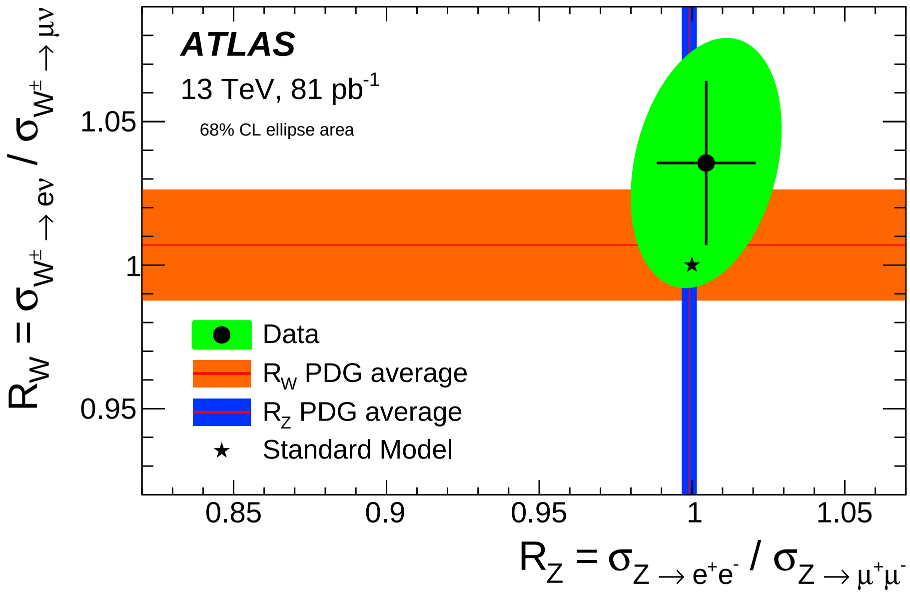

Figure 3.13: Ratio of Z and $W^{\pm}$-boson production fiducial cross-sections obtained in electron and muon channels compared to the expectations of the Standard Model and previous experimental checks of the lepton universality provided as PDG average bands [101]. The green ellipse shows the 68% confidence level for the cross-sections.

The sources estimated using the toy MC method (electron identification, trigger and isolation as well as muon trigger efficiency scale factor) are not fully correlated. The correlation is stronger for W^+ vs W^- compared to Z vs W. This is taken into account by representing these sources by 3 nuisance parameters for each source, determined using eigenvector decomposition of the covariance matrices for each of them.

The systematic uncertainties from electroweak background sources are treated as uncorrelated between W and Z channels and 100% correlated for different W and Z channels. The systematic uncertainties are split in two sources: related to theoretical cross-section determination, which is considered uncorrelated for individual processes, and common luminosity uncertainty. The multijet background for the W channel is split into three components, as discussed in section 3.4.2. The correlations of W^+ and W^- background estimates are determined and as a result, the multijet background in the W channel is described by 2×5 nuisance parameters, 5 parameters per each lepton flavour split into 3 correlated and 2 anti-correlated sources for the different charges.

The combination using `HERAverager` tool the yields a good $\chi^2/N_{\mathrm{d.f.}} = 3.0/3$ indicating compatibility of the measurements. Table 3.17 gives the resulting combined cross-section. There is a sizeable reduction of uncertainty compared to individual electron and muon

Table 3.17: Results for the fiducial cross-section σ^{fid} and total cross-section σ^{tot} for the combined electron and muon channel W^-, W^+, $W^\pm$, and Z-production measurements.

	Measured cross section × BR($W \to \ell\nu$, $Z \to \ell\ell$) [nb] (value ± stat ± syst ± lumi)		**Predicted cross section × BR($W \to \ell\nu$, $Z \to \ell\ell$) [nb]** (value ± PDF ± scale ± other)	
Channel	Fiducial	Total	Fiducial	Total
W^-	$3.50 \pm 0.01 \pm 0.07 \pm 0.07$	$8.79 \pm 0.02 \pm 0.24 \pm 0.18$	$3.40^{+0.09}_{-0.11} \pm 0.04 \pm 0.06$	$8.54^{+0.21}_{-0.24} \pm 0.11 \pm 0.12$
W^+	$4.53 \pm 0.01 \pm 0.09 \pm 0.10$	$11.83 \pm 0.02 \pm 0.32 \pm 0.25$	$4.42^{+0.13}_{-0.14} \pm 0.05 \pm 0.08$	$11.54^{+0.32}_{-0.31} \pm 0.15 \pm 0.16$
$W^\pm$	$8.03 \pm 0.01 \pm 0.16 \pm 0.17$	$20.64 \pm 0.02 \pm 0.55 \pm 0.43$	$7.82^{+0.21}_{-0.25} \pm 0.09 \pm 0.13$	$20.08^{+0.53}_{-0.54} \pm 0.26 \pm 0.28$
Z	$0.779 \pm 0.003 \pm 0.006 \pm 0.016$	$1.981 \pm 0.007 \pm 0.038 \pm 0.042$	$0.74^{+0.02}_{-0.03} \pm 0.01 \pm 0.01$	$1.89 \pm 0.05 \pm 0.03 \pm 0.03$
	Measured ratio (value ± stat ± syst)		**Predicted ratio** (value ± PDF)	
W^+/W^-	$1.295 \pm 0.003 \pm 0.010$	–	1.30 ± 0.01	–
W/Z	$10.31 \pm 0.04 \pm 0.20$	–	10.54 ± 0.12	–

channel measurements since most of the systematic error sources are uncorrelated.

The combined fiducial cross-sections are extrapolated to the full phase space using the $A_{Z,W}$ factors. The resulting combined total cross-sections are also given in Table 3.17.

3.6.4 Cross-section Ratios

Ratios of the measured cross-sections benefit from the cancellation of the experimental uncertainties. The ratios of W^+ to W^- and $W^\pm$ to Z-production were measured by the ATLAS and CMS collaborations in the past [95, 100, 104] and proved to be powerful tool to constrain PDF uncertainties. The ratio of W^+ to W^- cross-sections is sensitive to the u_v minus d_v valence-quark distribution at low Bjorken-x while the ratio of $W^\pm$ to Z cross-sections constrains the strange-quark distribution. Studies from Ref. [105] show that starting from an accuracy of about 2% the measurements at $\sqrt{s} = 13$ TeV begin to have significant constraining power on PDFs, compared to the modern PDF sets such as CT10, MMHT14 and NNPDF3.0.

The systematic uncertainties of the cross-section measurements are to a large extent uncorrelated between electron and muon channels, apart from the common luminosity uncertainty. On the other hand there is a very strong correlation between W^+ and W^- measurements. There is also significant correlation for the $W^\pm$ and Z results for the same flavour measurement.

The ratios can be performed using uncombined electron and muon channel measurements first and combining them as the second step. An alternative strategy is to take ratios for already combined measurements. Both approaches are tried as a cross check and found to agree well, and the ratio of the combined cross-sections is taken as the baseline result.

The results for the ratios of fiducial cross-sections for W^+ to W^--boson production and for $W^\pm$ to Z-boson production are given in Table 3.17. The ratios obtained in electron and muon channel agree with each other well. The ratios of the combined results are compared to theory predictions in Figures 3.14 and 3.15.

There is a significant scatter for different PDF predictions. The measurement agrees reasonably well with the prediction based on MMHT14 and from the CT14 based prediction.

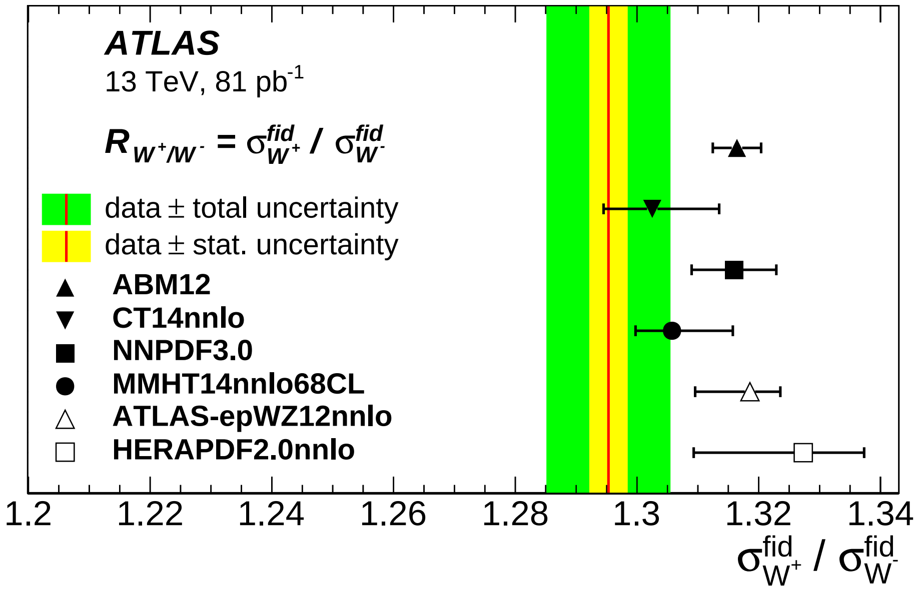

Figure 3.14: Ratio of W^+ to W^--boson production fiducial cross-sections compared to predictions based on different PDF sets. The inner shaded band corresponds to statistical uncertainty while the outer band shows statistical and systematic uncertainties added in quadrature. The theory predictions are given with the corresponding PDF uncertainties shown as error bands. Scale uncertainties are not included in the error bands.

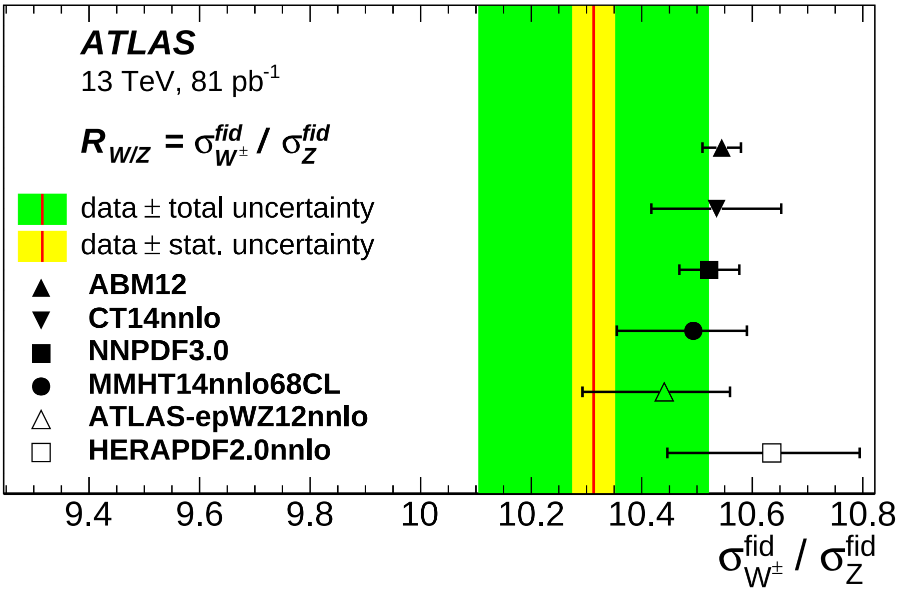

Figure 3.15: Ratio of $W^{\pm}$ to Z-boson production fiducial cross-sections compared to predictions based on different PDF sets. The inner shaded band corresponds to statistical uncertainty while the outer band shows statistical and systematic uncertainties added in quadrature. The theory predictions are given with the corresponding PDF uncertainties shown as error bands. Scale uncertainties are not included in the error bands.

3.7 Theoretical Predictions

Theoretical predictions of the fiducial and total cross-sections are computed for comparison to the measured cross-sections using DYNNLO 1.5 [89] and Fewz 3.1 [90–93], thereby providing full NLO and NNLO QCD calculations. The NLO EW corrections were calculated with Fewz 3.1 for Z and with the MC Sanc [106, 107] for W. The calculation was done in the G_{μ} EW scheme [108]. The following input parameters were taken from the PDG [109]: the Fermi constant, masses and widths of W and Z bosons as well as elements of the CKM matrix.

The cross-sections were calculated for vector boson decays into leptons at the Born level to match the definition of the measured cross-sections in the data. Thus, from complete NLO EW corrections the following components were included: virtual QED and weak corrections, real initial state radiation (ISR) and interference between ISR and real final state radiation (FSR) [110]. QED FSR effects as simulated in Photos were used to correct the data.

Table 3.18: The total cross section predictions as a result of varying the PDF set

PDF	σ^{tot}_{W+} [nb]	σ^{tot}_{W-} [nb]	$\sigma^{tot}_{W\pm}$ [nb]	σ^{tot}_{Z} [nb]
CT14nnlo	$11.54^{+0.32}_{-0.31}$	$8.54^{+0.21}_{-0.24}$	$20.08^{+0.53}_{-0.54}$	1.89 ± 0.05
NNPDF3.0	11.36 ± 0.26	8.40 ± 0.20	19.76 ± 0.45	1.86 ± 0.04
MMHT14nnlo	$11.61^{+0.20}_{-0.17}$	$8.63^{+0.14}_{-0.13}$	$20.24^{+0.33}_{-0.29}$	1.91 ± 0.03
ABM12	11.74 ± 0.15	8.58 ± 0.10	20.33 ± 0.25	1.91 ± 0.02
HERAPDF2.0nnlo	$12.13^{+0.31}_{-0.22}$	$8.96^{+0.22}_{-0.14}$	$21.11^{+0.53}_{-0.35}$	$1.98^{+0.06}_{-0.03}$
ATLAS-epWZ12nnlo	$11.89^{+0.18}_{-0.19}$	$8.81^{+0.16}_{-0.14}$	$20.69^{+0.31}_{-0.32}$	$1.97^{+0.03}_{-0.03}$

Very good agreement in the QED FSR predictions were found between PHOTOS and SANC [106, 107], confirming that the splitting of EW parts is consistent between the two codes [107].

DYNNLO is used for the central values of the predictions while FEWZ is used for the PDF variations and all other systematic variations such as QCD scale and α_S. The predictions are calculated using the CT14NNLO [111], NNPDF3.0 [112], MMHT14NNLO68CL [113], ABM12LHC [114], HERAPDF2.0 [115], and ATLAS-EPWZ12NNLO [116] PDF sets. The effect on the total cross section from varying the PDF set is detailed in Table 3.18. The dynamic scale $m_{\ell\ell}$ and fixed m_W scale were used as the nominal renormalisation, μ_R, and factorisation, μ_F, scales for Z and W predictions, respectively.

The central values of the fiducial and total cross-sections are provided in Table 3.17. The predictions are compared with the measured values for fiducial and total cross-section in Figures 3.16 and 3.17 respectively.

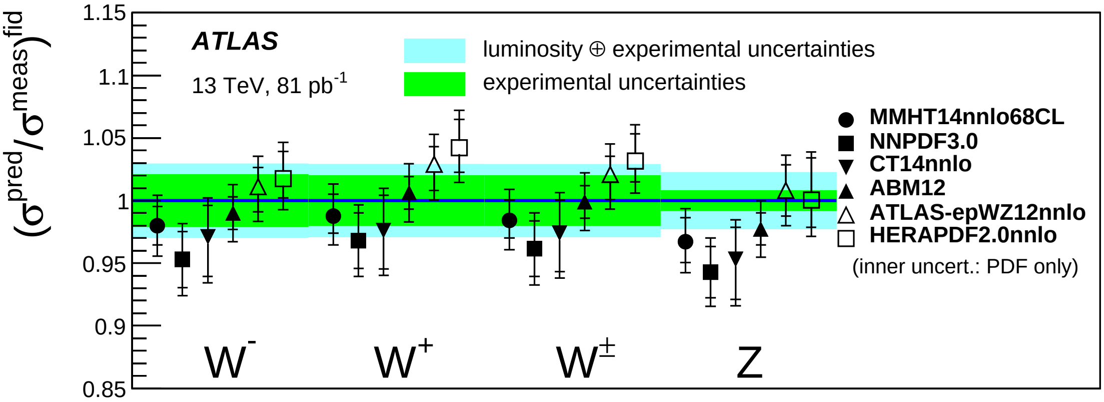

Figure 3.16: Predictions for the fiducial cross-section $\sigma^Z_{fid}, \sigma^W_{fid}, \sigma^{W+}_{fid}, \sigma^{W-}_{fid}$ for the six PDFs compared to the measured fiducial cross sections as given in Table 3.17.

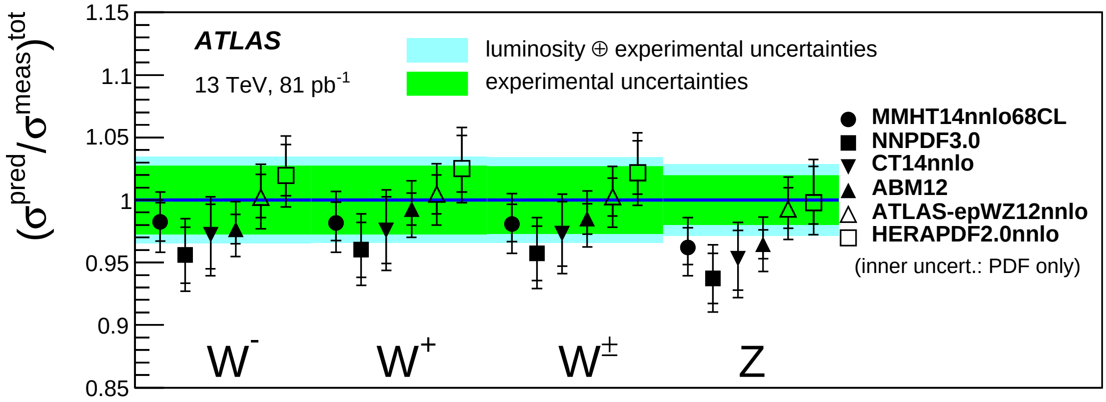

Figure 3.17: Predictions for the total cross-section $\sigma^{Z}_{tot}, \sigma^{W}_{tot}, \sigma^{W^+}_{tot}, \sigma^{W^-}_{tot}$ for the six PDFs compared to the measured total cross sections as given in Table 3.17.

3.7.1 Theoretical uncertainties

Uncertainties on the predictions are dominated by the limited knowledge of the proton PDFs. The uncertainties are derived from the following sources:

- PDF: these uncertainties are evaluated with six NNLO PDFs: MMHT14NNLO68CL, NNPDF3.0, CT14NNLO, ABM12LHC, ATLAS-EPWZ12NNLO, and HERAPDF2.0. The PDF uncertainty of CT14NNLO was rescaled from 90% CL to 68% CL. The predictions determined with these alternate PDFs are presented in Table 3.18.

- Scales: the scale uncertainties are defined by the envelope of variations in which the scales are changed by factors of two subject to the constraint $0.5 \leq \mu_R/\mu_F \leq 2$, i.e. excluding the variations in opposite directions.

- α_S: The uncertainty due to α_S was estimated following the prescription given with the CT14nnlo PDF [111], varying α_S by ± 0.001 to correspond to 68% CL. The uncertainty was calculated to be $\approx 0.9\%$ for Z and W predictions and correlated between the two. The uncertainty amounts to $\pm 0.9\%$ and $\pm 0.9\%/\pm 0.92\%/\pm 0.9\%$ ($\pm 0.9\%$ and $\pm 0.9\%/\pm 0.95\%/\pm 0.92\%$) for the fiducial (total) Z and $W^+/W^-/W$ boson cross-sections, respectively.

- Beam-energy uncertainties: The uncertainty per 1% E_{beam} change was estimated to be 1.1% for $W$and Z. The uncertainty amounts to $^{+0.8}_{-1.0}\%$ and $\pm 0.7\%/\pm 0.9\%/\pm 0.8\%$

($\pm 1.1\%$ and $\pm 1.0\%/\pm 1.1\%/\pm 1.0\%$) for the fiducial (total) $Z$and $W^+/W^-/W$ boson cross-sections, respectively.

- Intrinsic theory uncertainties: these uncertainties are related to the limitations of NNLO calculations, internal nonperturbative parameters, and comparison between different codes. These are small for the fiducial ($\sim 0.2\%$ for W and $\sim 0.1\%$ for Z) and total cross-sections ($\sim 0.4\%$), and therefore were neglected.

3.7.2 Total and fiducial cross-section predictions

The final predicted fiducial and total cross sections can be found in Table 3.17. The first uncertainty corresponds to the variations of the PDFs, the second to the variations of the scale, and the third to an estimate of all remaining systematics described in Section 3.7.1 added in quadrature.

In Figures 3.18 and 3.19, the measured total combined electron and muon measurements at $\sqrt{s} = 13$ TeV shown in Table 3.17 are compared to the theoretical predictions. The calculations were performed with the program FEWZ [90–93] using the CT14nnlo NNLO structure function parameterisation. The renormalisation scale μ_R and factorisation scale μ_F were chosen to be $\mu_F = \mu_R = m_W$. The theoretical predictions are in good agreement with all measurements. The energy dependence of the total W and Z production cross-sections is well described.

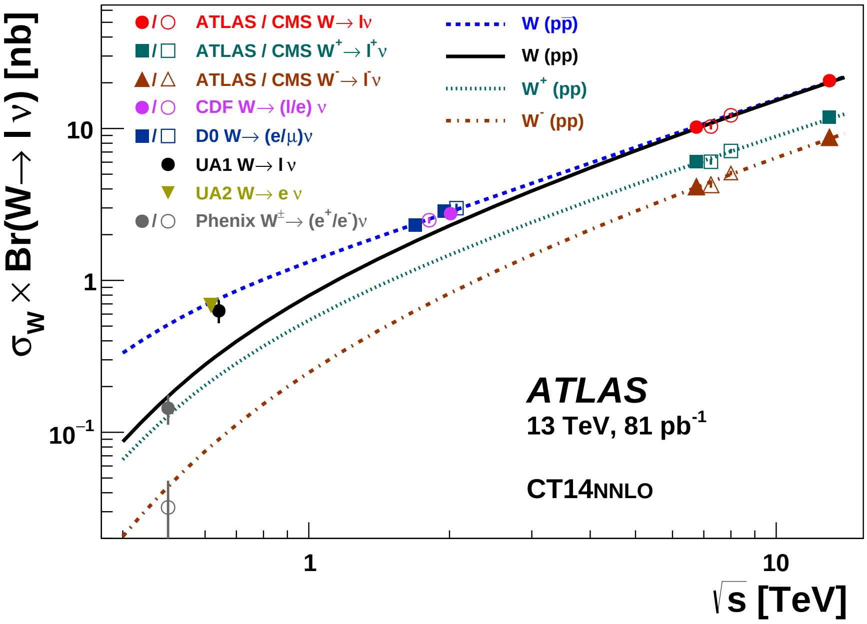

Figure 3.18: The measured values of $\sigma_W \cdot \mathrm{BR}\ (W \to \ell\nu)$ for W^+, W^- and for their sum compared to the theoretical predictions based on NNLO QCD calculations (see text). Results are shown for the combined electron-muon results. The predictions are shown for both proton-proton (W^+, $W^-$and their sum) and proton-antiproton colliders (W) as a function of $\sqrt{s}$. In addition, previous measurements at proton-antiproton and proton-proton colliders are shown. The data points at the various energies are staggered to improve readability. The CDF and D0 measurements are shown for both Tevatron collider energies, $\sqrt{s} = 1.8$ TeV and $\sqrt{s} = 1.96$ TeV. All data points are displayed with their total uncertainty. The theoretical uncertainties are not shown.

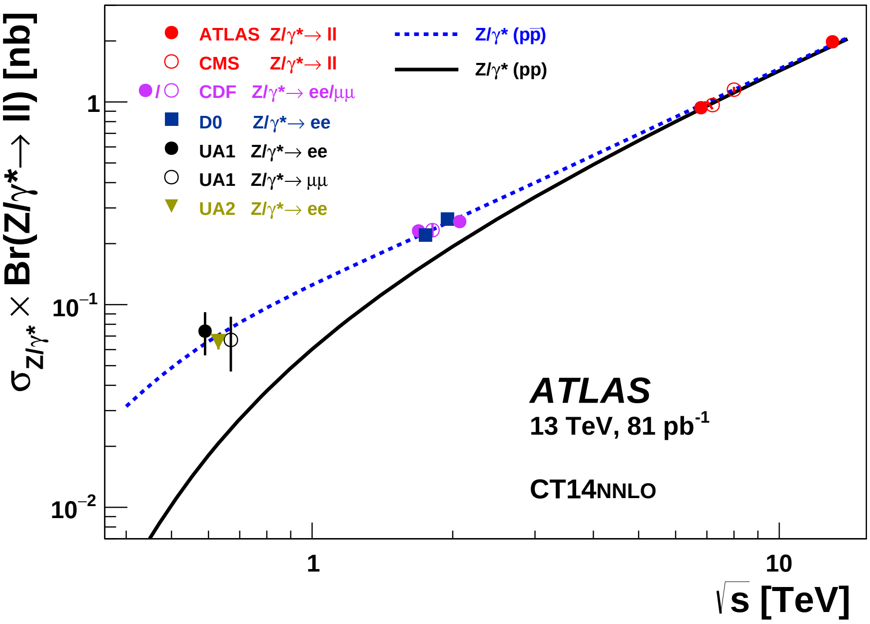

Figure 3.19: The measured value of $\sigma_{Z/\gamma^*} \times \mathrm{BR}\ (Z/\gamma^* \to \ell\ell)$ where the electron and muon channels have been combined, compared to the theoretical predictions based on NNLO QCD calculations (see text). The predictions are shown for both proton-proton and proton-antiproton colliders as a function of $\sqrt{s}$. In addition, previous measurements at proton-antiproton colliders are shown. The data points at the various energies are staggered to improve readability. The CDF and D0 measurements are shown for both Tevatron collider energies, $\sqrt{s} = 1.8$ TeV and $\sqrt{s} = 1.96$ TeV. All data points are displayed with their total uncertainty. The theoretical uncertainties are not shown.

3.8 Conclusion

This chapter presents measurements by the ATLAS experiment of the $W \to \ell\nu$ and $Z \to \ell\ell$ production cross-sections based on $938,158$ and $79,907$ candidates, respectively, produced from $\sqrt{s} = 13$ TeV proton-proton collisions at the LHC. These results correspond to a total integrated luminosity of approximately 81 pb^{-1}. The total inclusive W-boson production cross-sections times the leptonic branching ratios are $\sigma^{tot}_{W^+} = 11.83 \pm 0.02$ (stat) $\pm\, 0.32$ (syst) $\pm\, 0.25$ (lumi) nb and $\sigma^{tot}_{W^-} = 8.79 \pm 0.02$ (stat) $\pm\, 0.24$ (syst) $\pm\, 0.18$ (lumi) nb while total inclusive Z-boson production cross-section times the charged leptonic branching ratio within the invariant mass window $66 < m_{\ell\ell} < 116$ GeV is $\sigma^{tot}_{Z} = 1.981 \pm 0.007$ (stat) $\pm\, 0.038$ (syst) $\pm\, 0.042$ (lumi) nb. The results obtained are in agreement with theoretical calculations based on NNLO QCD.

Chapter 4

Search for Higgs and Z Boson Decays to a ϕ or ρ^0 Meson and a Photon

4.1 Introduction

This chapter describes a search for Higgs boson decays to the exclusive final states $\phi\,\gamma$ and $\rho^0\,\gamma$. The decay $\phi \to K^+K^-$ is used to reconstruct the ϕ meson, while the decay $\rho^0 \to \pi^+\pi^-$ is used to reconstruct the ρ^0 meson. The search presented here uses approximately 13 times more integrated luminosity with respect to the first search for $H \to \phi\,\gamma$ decays [2] that led to a 95% confidence level (CL) upper limit of $\mathcal{B}\,(H \to \phi\,\gamma) < 1.4 \times 10^{-3}$, assuming SM Higgs boson production, to which I also contributed. Before the analysis described here, no other experimental information on the $H \to \rho^0\,\gamma$ decay mode existed.

The searches for the analogous decays of the Z boson to a meson and a photon are also presented. These have been considered from a theoretical perspective [117, 118], since measurements of the branching fractions for such decays would provide a unique precision test of the SM and the factorization approach in quantum chromodynamics, in an environment where the power corrections in terms of the QCD energy scale over the vector boson mass are small [118]. Owing to the large Z boson production cross-section at the LHC, rare Z boson decays can be probed at branching fractions much smaller than for Higgs boson decays to the same final state. The SM prediction of the branching fraction has been calculated to be $\mathcal{B}(Z \to \phi\,\gamma) = (1.04 \pm 0.12) \times 10^{-8}$ [117, 118] and $\mathcal{B}(Z \to \rho^0\,\gamma) = (4.19 \pm 0.47) \times 10^{-8}$ [118]. The first search for $Z \to \phi\,\gamma$ decays was presented in Ref. [2] and a 95% CL upper limit of $\mathcal{B}(Z \to \phi\,\gamma) < 8.3 \times 10^{-6}$ was obtained. No direct experimental information on the decay $Z \to \rho^0\,\gamma$ existed before the analysis described here.

Some limits exist exist from the DELPHI experiment for decays of the Z to a meson and a photon where the meson in turn decays to two photons $Z \to M\gamma \to \gamma\gamma(\gamma)$[119]. However the author is unable to find any reference to searches for the particular ($\phi\gamma$, $\rho^0\gamma$) decay modes in the literature and no other limits are listed for these branching ratios by the particle data group[101].

4.2 Data and Simulation Samples

4.2.1 Data Sample

The $\phi\gamma$ analysis is performed with a data sample collected between runs 280319 in 2015 to 311481 in 2016 at $\sqrt{s} = 13$ TeV, corresponding to a total integrated luminosity of $35.6\,\mathrm{fb}^{-1}$, with 3.2% uncertainty. It is derived, following a methodology similar to that detailed in Ref. [120], from a preliminary calibration of the luminosity scale using x-y beam-separation scans performed in May 2016. Runs are required to be included in the "Good Run List". The sample of data was limited by the choice of triggers, the details of which are described in Section 4.4. Data is used from `DxAOD_HIGG2D5` derivation (p2977). Events are retained by `DxAOD_HIGG2D5` if they satisfy the following requirements:

- The event must contain two reconstructed inner detector tracks that satisfy $p_{\mathrm{T}} > 15$ GeV
- There must be a pair of inner detector tracks with a mass loosely consistent with that of a ϕ or ρ^0 meson.
- The event must also contain one photon candidate with $p_{\mathrm{T}}^{\gamma} > 15$ GeV

The $\rho^0\gamma$ analysis relies on a trigger which was only introduced during the 2016 pp data collection from May 2016 onwards. This leads to a dataset of $32.3\,\mathrm{fb}^{-1}$ included in the analysis.

As with the $\phi\,\gamma$ analysis, the data is taken from the derivation `DxAOD_HIGG2D5` and is triggered with a dedicated trigger chain selecting on a photon and a pair of tracks within the relevant mass window.

4.2.2 Simulated Samples

Samples of Higgs production through gluon fusion and vector boson fusion, as well as the Z boson production samples, were obtained using the POWHEG NLO generator [121, 122] interfaced with PYTHIA8.1 [123] to model the parton shower, hadronisation and underlying event with parameters set according to the AZNLOCTEQ6L1 tune. POWHEG events are generated using the CT10 parton distribution function (PDF) set [70]. The WH and ZH productions are obtained at LO using PYTHIA8.1 and A14NNPDF23LO. The MC simulation samples used to model the $H/Z \to \phi\,\gamma$ and $H/Z \to \rho^0\,\gamma$ signal are detailed in Table 4.1. Each sample contains 10^5 simulated events.

Table 4.1: Simulated signal samples used for the $\phi\gamma$ and $\rho^0\gamma$ final state.

Sample Name	Number of Events
`PowhegPythia8EvtGen_AZNLOCTEQ6L1_ZPhiGamma`	97000
`PowhegPythia8EvtGen_CT10_AZNLOCTEQ6L1_ggH125_PhiGamma`	94600
`PowhegPythia8EvtGen_CT10_AZNLOCTEQ6L1_VBFH125_PhiGamma`	99200
`Pythia8EvtGen_A14NNPDF23LO_WH125_PhiGamma`	99400
`Pythia8EvtGen_A14NNPDF23LO_ZH125_PhiGamma`	94800
`PowhegPythia8EvtGen_AZNLOCTEQ6L1_ZRhoGamma`	99000
`PowhegPythia8EvtGen_CT10_AZNLOCTEQ6L1_ggH125_RhoGamma`	97000
`PowhegPythia8EvtGen_CT10_AZNLOCTEQ6L1_VBFH125_RhoGamma`	99000
`Pythia8EvtGen_A14NNPDF23LO_ZH125_RhoGamma`	99000
`Pythia8EvtGen_A14NNPDF23LO_WH125_RhoGamma`	99000

4.3 Polarisation effects

The observed final state is a cascade of two two-body decays. As such the polarisations of the initial particles and the possible spin states of the final products can have a large effect on the decay kinematics. These are estimated in this section following Ref. [124].

4.3.1 Higgs boson decays to $\phi\gamma \to K^+K^-\gamma$ and $\rho^0\gamma \to \pi^+\pi^-\gamma$

The Higgs boson has spin 0. The ϕ and ρ^0 mesons have $J^{PC} = 1^{--}$ and the photon is a massless vector boson $J = 1$, $m_J = \pm 1$. For K^+ and π^+ we have $J^P = 0^-$.

For $H \to \phi\gamma \to K^+K^-\gamma$ and $H \to \rho^0\gamma \to \pi^+\pi^-\gamma$ in the helicity basis:

$$I(\theta') = \frac{1}{\Gamma_1\Gamma_2}\frac{2s_2+1}{2}\sum_{\lambda_1\lambda_2\lambda_3\lambda_4}\left|d^{s_2}_{\lambda_2,\lambda_4-\lambda_5}\right|^2 |A_{\lambda_2\lambda_3}|^2 |B_{\lambda_4\lambda_5}|^2 \tag{4.1}$$

where particle 1 is the Higgs, 2 is the meson, 3 is the photon, and 4 and 5 the positively and negatively charged decay product of the meson, respectively. θ' is the angle between the momentum of particle 4 in the rest frame of particle 2, with respect to the direction of particle 2 in the rest frame of particle 1. s_i is the spin of particle i and λ_i is the helicity of particle i measured in the rest frame of its parent. $A_{\lambda_2\lambda_3}$ are the helicity amplitudes for $1 \to 23$ and $B_{\lambda_4\lambda_5}$ the helicity amplitudes for $2 \to 34$.

The allowed helicity amplitudes, given the selection rule $|\lambda_2 - \lambda_3| \leq s_1$ and $|\lambda_3 - \lambda_4| \leq s_2$, due to conservation of angular momentum, are: $A_{1,1}$ and $A_{-1,-1}$, this means that the meson should also be transversely polarised given $s_1 = 0$ and the photon does not have the longitudinal polarisation. Correspondingly for $B_{\lambda_4\lambda_5}$ we have: $B_{0,0}$ as the only option, given $s_4 = s_5 = 0$. Thus, the only contributions to the angular distributions are $d^1_{1,0} = d^1_{-1,0} = -\frac{\sin\theta'}{\sqrt{2}}$, and the angular distribution is $\sin^2\theta' = 1 - \cos^2\theta'$, where θ' is direction of the positively charged meson decay product with respect to the spin quantisation axis of the meson.

4.3.2 Z boson decays to $\phi\gamma \to K^+K^-\gamma$ and $\rho^0\gamma \to \pi^+\pi^-\gamma$

This is a bit more convoluted as $s_1 = 1$, and the Z boson is produced with a mixture of polarisations. However, as pointed out in Ref. [117], the decay rate to a transversely-polarized meson vanishes to leading order in $m^2_{\mathcal{M}}/M^2_Z$. Thus, the mesons in the decay will be longitudinally polarised.

The allowed helicity amplitudes, given the selection rule $|\lambda_2 - \lambda_3| \leq s_1$ and the above comment are: $A_{0,1}$ and $A_{0,-1}$. Then, according to the selection rule $|\lambda_3 - \lambda_4| \leq s_2$, for $B_{\lambda_4\lambda_5}$ we have: $B_{0,0}$ as the only option, given $s_4 = s_5 = 0$. Thus, the only contributions to the angular distributions are: $d^1_{0,0} = \cos\theta'$, and the angular distribution is $\cos^2\theta'$.

4.3.3 Kinematic Acceptance

Estimations of the analysis kinematic selection acceptances from the MC simulation samples are shown in Table 4.2. The selection applied on the samples uses kinematic requirements similar to those of the analysis:

- Both tracks must satisfy $|\eta^K| < 2.5$
- Both tracks must have $p_T^K > 15$ GeV
- At least one track must have $p_T^K > 20$ GeV
- The transverse momentum of the photon must satisfy $p_T^\gamma > 35$ GeV
- Photons must be within $|\eta^\gamma| < 2.37$ and outside of $1.37 < |\eta^\gamma| < 1.52$
- The difference in azimuthal angle between the $\phi \to K^+K^-$ candidate and photon must satisfy $\Delta\Phi(\phi\,\gamma) > 0.5$.
- The transverse momentum of the ditrack system must satisfy:

$$p_T^{K^+K^-} > \begin{cases} 40 \text{ GeV}, & \text{if } m_{K^+K^-\gamma} \leq 91 \text{ GeV} \\ 40 + 5/34 \times (m_{K^+K^-\gamma} - 91) \text{ GeV}, & \text{if } 91 \text{ GeV} < m_{K^+K^-\gamma} < 125 \text{ GeV} \\ 45 \text{ GeV}, & \text{if } m_{K^+K^-\gamma} \geq 125 \text{ GeV} \end{cases} \tag{4.2}$$

Table 4.2: Analysis kinematic selection acceptances estimated from the simulated Higgs and Z boson samples. This initial acceptance study was carried out for the $\phi\gamma$ final state only.

Sample	$\phi \to K^+K^-$	Analysis Kinematics	Acceptance
ggH	44956	20209	45.0 ± 0.4%
VBF	46715	19098	40.9 ± 0.4%
WH	46870	16971	36.2 ± 0.3%
ZH	44698	16443	36.8 ± 0.3%
Z	28277	5716	20.2 ± 0.3%

The Higgs and Z boson decays are simulated as a cascade of two-body decays. Effects of the helicity of the meson on the $K^{\pm}$ kinematics are discussed in Section 4.3. Consequently, the effects on the relative efficiency, defined as the efficiency of the SR selection region (defined in Section 4.5.3), are detailed for each sample in Table 4.3. Accounting for the angular distribution in the $\phi\gamma$ is found to modify the relative efficiency by 5.3% and 9.9% for the Higgs and Z boson cases, respectively. However in the $\rho^0\gamma$ case the angular distribution is found to modify the relative efficiency by 33.5% and 83.0% for the Higgs and Z boson cases. These effects are corrected for in both the Higgs and Z boson cases.

Table 4.3: Effect on the efficiencies, with respect to the SR selection region, when applying the polarisation weight to simulated Higgs and Z boson samples for the $\phi\gamma$ analysis.

Samples	Efficiency without polarisation	Efficiency with polarisation
`ggH`	16.8%	17.8%
`VBF`	11.4%	12.1%
`WH`	9.4%	9.9%
`ZH`	9.4%	9.9%
`Total H`	16.1%	17.0%
`Z`	8.9%	8.1%

4.4 Dedicated Trigger

The energies of the individual decay products are too low to be triggered on by the unprescaled inclusive single object triggers (e.g. a single photon).

Instead the unique topology of a photon and isolated tracks in the final state is used to implement dedicated triggers using variations of the standard tau trigger objects. These are chosen due to the similarity between the meson decay to pions or kaons with the hadronic tau decays. They are then combined with a photon chain at a much lower threshold then previously possible. These HLT algorithms are seeded by a low threshold unprescaled Level-1 EM object.

4.4.1 Standard Tau Selection Variables

The standard HLT tau trigger object uses several variables on which selections are made in the trigger. For the decays involving a meson decaying to hadrons, the following variables are used:

Tau p_T: The transverse momentum of the tau object.

Leading track p_T: The transverse momentum of the track with the highest p_T. This is presented in Fig. 4.1.

Number of tracks: Used to select tau objects with two tracks.

EMPOverTrkSysP: The ratio of the p_T of the em cluster associated with the tau and p_T of the di-track system. The distribution of this variable in $H \to \phi\gamma$ signal MC and background dominated data can be seen in Fig 4.2.

4.4.2 Di-track Mass Requirements

In addition to the tau selection variables an additional di-track mass is calculated for the track system associated with the tau object. This is calculated using di erent mass hypotheses for the individual tracks to allow for the di erent possible decay products. A selection is then performed based on the desired meson mass and width.

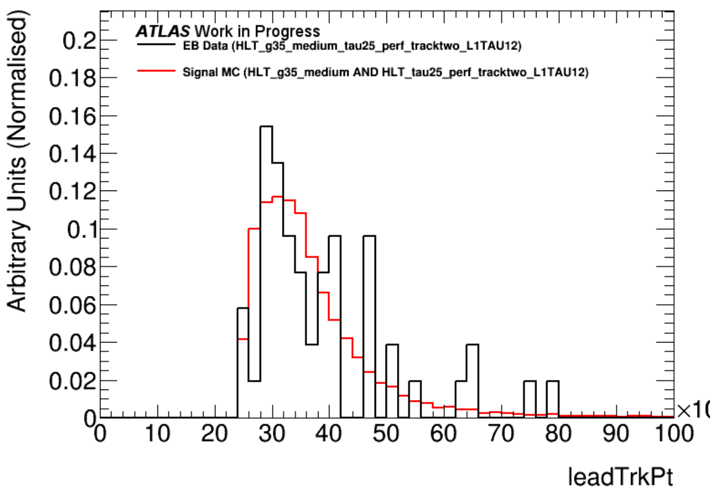

Figure 4.1: The distributions of the trigger variable leadTrkPt in $H \to \phi\gamma$ signal MC and background dominated data from a random trigger.

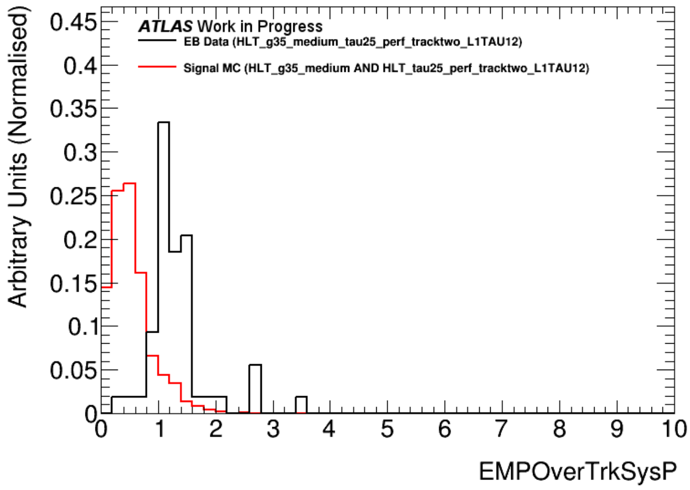

Figure 4.2: The distributions of the trigger variable EMPOverTrkSysP in $H \to \phi\gamma$ signal MC and background dominated data from a random trigger.

4.4.3 $\phi\gamma \to K^+K^-\gamma$ Triggers

2015 Data Taking

For the 2015 $H \to \phi\gamma$ analysis the following triggers were prepared and used in the first published search [2]. Several combinations of threshold are defined so that if the trigger rate becomes too high a lower rate trigger is immediately available. In operation these triggers ran at ≈ 1 Hz .

– HLT_g35_medium_tau25_dikaon_tracktwo_L1TAU12

– HLT_g35_medium_tau35_dikaon_tracktwo_L1TAU12

– HLT_g35_medium_tau25_dikaontight_tracktwo_L1TAU12

– HLT_g35_medium_tau35_dikaontight_tracktwo_L1TAU12

These triggers are named in a modular fashion describing their composition of sub-chains and thresholds. HLT describes that the chain is a HLT chain, g35_medium is a photon trigger with a threshold of $E_{\mathrm{T}} > 35$ GeV, and tau25_..._L1TAU12 is a τ trigger with $E_{\mathrm{T}} > 25$ GeV seeded by the level-1 tau theshold of 12 GeV. dikaon_tracktwo is the analysis specific part of the trigger selecting two tracks with a mass requirement described below.

These exploit the combination of a hard photon ($E_{\mathrm{T}} > 35$ GeV) recoiling against two ID tracks. The tracking component is provided by the trigger tau object coming from the custom chain `HLT_tau[25,35]_dikaon(tight)_tracktwo` where the normal tau ID discrimination is not applied, but the following selections are applied instead.

- Tau p_{T} cut of $[25, 35]$ GeV
- Leading track p_{T} cut of $[15, 25]$ GeV
- 2 tracks (each with $p_{\mathrm{T}} > 1$ GeV)
- Track system mass under pion hypothesis 200 MeV − 450 MeV (this requirement e ectively selects two track systems). This is presented in Fig. 4.3.
- EMPOverTrkSysP < 1.5 (or < 1 for tight); this is the ratio of the p_{T} of the em cluster associated with the tau and p_{T} of the ditrack system.

For the analysis `HLT_g35_medium_tau25_dikaontight_tracktwo_L1TAU12` remained without prescale for the 2015 data taking with an average rate of 0.2Hz.

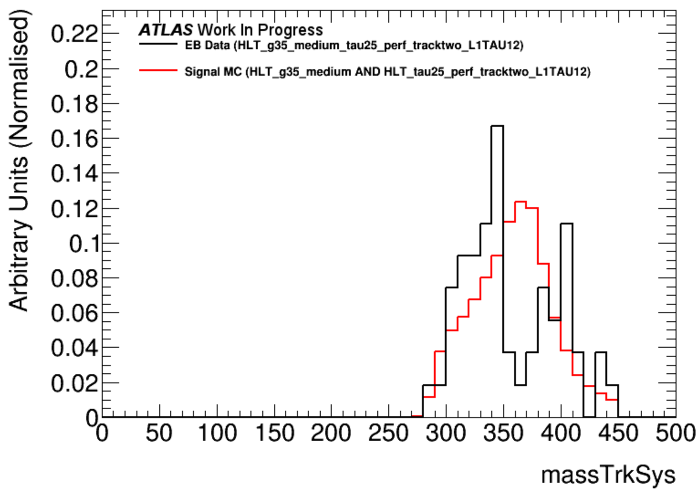

Figure 4.3: The trigger variable massTrkSys in $H \to \phi\gamma$ signal MC and background dominated data from a background dominated trigger.

2016 Data Taking

To further study similar decays more triggers have been developed for the 2016 data taking run.

The first of these is a copy of the 2015 dikaon triggers but with an updated value for the mass for the track system using a charged kaon particle hypothesis. This allows the ditrack mass cut to be much tighter around the known ϕ mass.

These triggers are named:

- HLT_g35_medium_tau25_dikaonmass_tracktwo_L1TAU12
- HLT_g35_medium_tau35_dikaonmass_tracktwo_L1TAU12
- HLT_g35_medium_tau25_dikaonmasstight_tracktwo_L1TAU12
- HLT_g35_medium_tau35_dikaonmasstight_tracktwo_L1TAU12

with the following requirements.

- Tau p_{T} cut of $[25, 35]$ GeV
- Leading track p_{T} cut of $[15, 25]$ GeV
- 1 or 2 tracks (each with $p_{\mathrm{T}} > 1$ GeV)
- Track system mass under kaon hypothesis 987 MeV – 1060 MeV
- EMPOverTrkSysP < 1.5 (or < 1 for tight) this is the ratio of the p_{T} of the em cluster associated with the tau and p_{T} of the ditrack system.

Further improvements to this chain were implemented during the 2016, these were able to lower the photon p_{T} requirement to 25 GeV by adding an invariant mass cut on the photon and di-track system.

- HLT_g25_medium_tau25_dikaonmasstight_tracktwo_60mVis10000
- HLT_g25_medium_L1EM24VHI_tau25_dikaonmasstight_tracktwo_60mVis10000

The other requirements are identical to the previous `dikaonmasstight` trigger with the addition of the invariant mass requirement that the system have an invariant mass greater than 60 GeV.

The primary trigger used by the analysis follows the deployment of these triggers.

- $280319 \leq$ Run Number < 298591
  - 2015 and a single run of 2016
  - HLT_g35_medium_tau25_dikaontight_tracktwo_L1TAU12

- $298591 \leq$ Run Number
  - The rest of 2016
  - HLT_g35_medium_tau25_dikaonmass_tracktwo_L1TAU12

For the $\phi\gamma$ analysis these triggers are determined to be $75 \pm 1\%$ efficient for both the H and Z boson searches. This was evaluated using the simulation of the trigger response in the signal MC samples.

4.4.4 $\rho^0\gamma \rightarrow \pi^+\pi^-\gamma$ Triggers

These triggers are designated:

- HLT_g35_medium_tau25_dipion1_tracktwo_L1TAU12
- HLT_g35_medium_tau35_dipion1_tracktwo_L1TAU12

These triggers, introduced for the 2016 data taking, both use the default pion mass hypothesis for the ditrack mass. They are numbered to allow for several independent triggers should the need arise.

- Tau p_{T} cut of $[25, 35]$ GeV
- Leading track p_{T} cut of $[15, 25]$ GeV
- 1 or 2 tracks (each with $p_{\mathrm{T}} > 1$ GeV)
- Track system mass under π hypothesis 475 MeV–1075 MeV
- EMPOverTrkSysPMax < 1

For the $\rho^0\gamma$ analysis described below the following version was chosen. It was found to be $79 \pm 1\%$ and $77 \pm 1\%$ efficient for the H and Z boson searches respectively. This was determined from MC.

- HLT_g35_medium_tau25_dipion1_tracktwo_L1TAU12

4.5 Event Selection

A number of selection criteria are applied to candidate $H/Z \to \phi\gamma \to K^+K^-\gamma$ decays before they are included in further analysis. The event selection of the $\rho^0\,\gamma$ analysis is essentially identical to that of the $\phi\,\gamma$ analysis with the exception that the inner detector tracks are now considered $\pi^\pm$ candidates and the $m_{\pi^+\pi^-}$ window is adjusted for the mass and width of the ρ^0 resonance. This selection is optimised with the sliding p_{T} requirement, defined in Equation 4.3, in order to use a single data sample for both the Z boson which favours the increased acceptance at low p_{T} and the H boson for which has a harder p_{T} spectrum and gains from the additional rejection of a higher p_{T} requirement.

The search was blinded until the analysis selection had been finalised in order to avoid bias. While optimising the analysis selection the events satisfying the requirement $120\ \text{GeV} < m_{M\gamma} < 130\ \text{GeV}$ and $80\ \text{GeV} < m_{M\gamma} < 100\ \text{GeV}$ are removed.

4.5.1 Photon Selection

Photons are selected that satisfy the following requirements:

- Photons must satisfy the "tight" photon identification criteria [57]
- The transverse momentum of the photon must satisfy $p_{\mathrm{T}}^{\gamma} > 35$ GeV
- Photons must be within $|\eta^{\gamma}| < 2.37$ and outside of $1.37 < |\eta^{\gamma}| < 1.52$
- To minimise the contamination from jets, the "`FixedCutTight`" photon isolation working point is used.

The e/gamma ambiguity resolver tool was used to resolve ambiguities between reconstructed electrons and photons. This was found to have only a small effect on events passing the full selection: 0.04% in MC and 0.5% in data.

4.5.2 Meson Decay Selection

- Tracks are required to pass the Tracking combined performance group "Loose" selection working point [55]

- The tracks must have opposite charge
- Both tracks must satisfy $|\eta^{Trk}| < 2.5$ and $p_{\mathrm{T}}^{Trk} > 15$ GeV
- At least one track must have $p_{\mathrm{T}}^{Trk} > 20$ GeV
- The di-track system transverse momentum must satisfy the following p_{T} requirement as a function of the three-body mass including the selected photon ($m_{M\gamma}$):

$$p_{\mathrm{T}}^{M} > \begin{cases} 40 \text{ GeV}, & \text{if } m_{M\gamma} \leq 91 \text{ GeV} \\ 40 + 5/34 \times (m_{M\gamma} - 91) \text{ GeV}, & \text{if } 91 \text{ GeV} < m_{M\gamma} < 140 \text{ GeV} \\ 47.21 \text{ GeV}, & \text{if } m_{M\gamma} \geq 140 \text{ GeV} \end{cases} \tag{4.3}$$

- The sum of the p_{T} of the reconstructed inner detector tracks within $\Delta R < 0.2$ from the leading pion is required to be less than 10% of its p_{T} (excluding the leading and sub-leading tracks).
  - For the $\rho^0\gamma$ analysis the ditrack invariant mass under a pion mass hypothesis must satisfy 635 MeV $< m_{\pi^+\pi^-} <$ 915 MeV, ie within 140 MeV from m_{ρ^0} where $m_{\rho^0} = 775$ MeV
  - For the $\phi\gamma$ analysis the ditrack invariant mass under a kaon mass hypothesis must satisfy $|m_{K^+K^-} - m_{\phi}| < 8$ MeV

The choice of the "Loose" track selection has been investigated. It was found that requiring instead "Tight" tracks reduced the background by 9% but also resulted in a drop of signal efficiency of 6%. As such it was decided to stick with the loose working point to maximise sensitivity.

4.5.3 Selection of Candidate Events

Candidate events are selected which contain both a meson decay and a photon satisfying the requirements described above. These candidates are retained for further analysis if they satisfy the following additional requirements:

- The event has passed the relevant trigger chain described in Section 4.4.

– The difference in azimuthal angle between the meson candidate and photon must satisfy $\Delta\phi(M\,\gamma) > \pi/2$

4.5.4 Control and Validation Region Definitions

The baseline selection, comprised of the requirements summarised above, is defined as "SR". A looser selection that excludes the requirement on the momentum of the di-track system as well as the isolation criteria on both the photon and di-track system is defined as "GR". Three validation regions are defined: "VR1", which applies the same requirements as "GR" with the inclusion of the signal region p_{T}^{M} requirement ; "VR2", which uses the "GR" selection but with the addition of the "FixedCutTight" photon isolation working point; and "VR3", which uses the "GR" selection but with the di-track isolation applied. These three validation regions are only used to check the background model. A further validation region, "VR4", is also defined including the signal p_{T}^{M} but requiring at least one of the isolation selections to have failed the selection cut while still requiring a nominal guard cut on the isolations to be within the region of the background model with adequate statistics (relative meson track isolation, relative photon track isolation and relative photon calorimeter isolation are all required to be less then 0.5). The defined regions are summarised in Table 4.4.

Table 4.4: Several control regions are defined which start from the basic GR selection

Region	p_{T}^{M}	Photon Isolation	M Isolation
GR	-	-	-
VR1	Eq. 4.3	-	-
VR2	-	Fixed Cut Tight	-
VR3	-	-	M Isolation < 0.1
VR4	Eq. 4.3	Fail Either Isolation + guard cut on both relative isolations ($Iso < 0.5$)	
SR	Eq. 4.3	Fixed Cut Tight	M Isolation < 0.1

4.5.5 Selection Optimisation Procedure

The nominal selection cut values for track p_{T}, p_{T}^{γ} and $p_{\mathrm{T}}^{K^+K^-}$ in addition to the requirement on the sum fractional isolation the dikaon system $F_{K^+K^-}$, are chosen based on several pieces of information. The isolation of the photon has been fixed to the working point

FixedCutTight. This selection was first optimised for the $\phi\gamma$ performance. For the $\rho^0\gamma$ it was found to be comparable.

Table 4.5 shows a simplified sensitivity calculated for both the H and Z bosons as part of an additional optimisation study into the effect of loosening the requirements previously dictated by trigger thresholds. Here the backgrounds are estimated using the normal background procedure 4.6 with the selections adjusted accordingly. This table shows that the choice of the $p_{\mathrm{T}}^{K^+K^-}$requirements is very important, with the Higgs signal preferring a larger value.

In order to produce a signal selection for both the H and Z bosons a gradient $p_{\mathrm{T}}^{K^+K^-}$ requirement based on the three body mass is introduced such that the cut is 40 GeV around the Z mass and 45 GeV around the H mass as detailed by Eq. 4.3.

Table 4.5: Sensitivities for both Higgs and Z boson signal using a variety of pT requirements. Values are normalised to the highest sensitivity. For these optimisation studies a requirement of 15 GeV is applied to both tracks.

Higgs Boson Sensitivity

Photon p_{T}/ DiTrack p_{T}	30	35	40	45
25	0.85	0.87	0.92	0.98
30	0.86	0.88	0.93	0.99
35	0.88	0.90	0.94	1

Z Boson Sensitivity

Photon p_{T}/ DiTrack p_{T}	30	35	40	45
25	0.91	0.95	0.95	0.71
30	0.93	0.97	0.98	0.74
35	0.92	0.97	1	0.75

4.5.6 $\phi\gamma$ Cut Flow and Expected Signal Yields

Table 4.6: $\phi\gamma$ Cut Flow in signal MC. $\mathcal{B}(H \to \phi\gamma) = 5 \times 10^{-3}, \mathcal{B}(Z \to \phi\gamma) = 1 \times 10^{-6}$ and an integrated luminosity of 35.6 fb^{-1} is assumed. Preselection includes the following selection requirements: Photons:-tight, $p_{\mathrm{T}}^{\gamma} > 25$ GeV, η^{γ} requirements described in Section 4.5.1; Tracks:-loose, $p_{\mathrm{T}}^{K} > 15$ GeV, $|\eta^k| < 2.5$; and $|m_{K^+K^-} - m_{\phi}| < 150$ MeV.

	Signal					Data
	ggF	VBF	WH	ZH	Z	H + Z
All ϕ events	8600	700	250	160	2200	4.2×10^6
All $\phi \to K^+K^-$ events	4100	330	120	77	1000	4.2×10^6
Preselection	1900	160	50	32	320	4.2×10^6
Passed Trigger	1900	160	50	32	320	4.2×10^6
1.012 GeV $< m_{K^+K^-} <$ 1.028 GeV	1400	110	33	22	270	680 000
$\Delta\phi(\phi\,\gamma) > \pi/2$	1300	78	25	16	260	100 000
GR – $p_{\mathrm{T}}^{\gamma} > 35$ GeV+ $p_{\mathrm{T}}^{K^+K^-} > 40$ GeV	970	57	18	11	120	54 000
SR – Isolation + sliding $p_{\mathrm{T}}^{K^+K^-}$ cut	720	40	12	7.6	83	12 000

The yields have been estimated for signal and background in the Higgs and Z boson mass regions at the SR (described in Section 4.5.3). These are presented in the from of a cutflow in Table 4.6 showing the impact of each of the selection criteria. Table 4.7 shows the expected yields for the signal and backgrounds for various $m_{K^+K^-\gamma}$ regions around the expected signals.

Table 4.7: Estimated yields in signal and background events in a three-body mass region of $120 < m_{K^+K^-\gamma} < 130$ GeV for Higgs and $86 < m_{K^+K^-\gamma} < 96$ GeV for Z following the full event selection. $\mathcal{B}(H \to \phi\gamma) = 5 \times 10^{-3}, \mathcal{B}(Z \to \phi\gamma) = 1 \times 10^{-6}$ is assumed and an integrated luminosity of 35.6 fb^{-1}.

Sample	Yield $120 < m_{K^+K^-\gamma} < 130$ GeV	Yield $86 < m_{K^+K^-\gamma} < 96$ GeV
ggF Signal	700 ± 30	-
VBF Signal	39 ± 6	-
WH Signal	12 ± 3	-
ZH Signal	7 ± 3	-
Total H Signal	760 ± 30	-
Z Signal	-	72 ± 8.5
Background Model	1050 ± 10	3610 ± 40

4.5.7 $\rho^0\gamma$ Cut Flow and Signal Yields

The selection cutflow for the Higgs and Z boson signals is presented in Table 4.8.

Table 4.8: $\rho^0\,\gamma \to \pi^+\pi^-\,\gamma$ Cut Flow in Higgs and Z boson signal MC. $\mathcal{B}(H \to \rho^0\gamma) = 1 \times 10^{-3}, \mathcal{B}(Z \to \rho^0\gamma) = 1 \times 10^{-5}$ and an integrated luminosity of 32.3 fb^{-1} is assumed. Preselection includes the following selection requirements: Photon:- tight, $p_T^\gamma > 30$ GeV, η^γ requirements described in Section 4.5.1; Track:- loose, $p_T^\pi > 15$ GeV, $|\eta^\pi| < 2.5$; and $|m_{\pi\pi} - m_{\rho^0}| < 300$ MeV.

	Signal					Data
	ggF	VBF	WH	ZH	Z	H + Z
Starting events	1500	120	44	29	19 000	1.4×10^6
Detector Acceptance	630	54	18	12	390	1.4×10^6
Preselection	380	35	11	7.4	260	570 000
Passed Trigger	270	24	7.2	4.7	150	570 000
ρ^0 mass window	220	19	5.7	3.7	110	250 000
$\Delta\phi(\rho^0\,\gamma) > \pi/2$	200	13	4.0	2.6	97	220 000
Pass GR	200	13	4.0	2.6	96	220 000
Pass SR	160	9.7	2.9	1.9	75	62 000

The yields have been estimated for signal and background in the Higgs mass region $120 < m_{\pi^+\pi^-\gamma} < 130$ GeV at the SR (described in Section 4.5.3). Table 4.9 shows the estimated yields for the four different categories and the inclusive, for various $m_{\pi^+\pi^-\gamma}$ regions.

Table 4.9: Estimation of yields in signal and background events in a three-body mass region of $120 < m_{\pi^+\pi^-\gamma} < 130$ GeV for Higgs boson and $86 < m_{\pi^+\pi^-\gamma} < 96$ GeV for Z boson, after the complete event selection. $\mathcal{B}(H \to \rho^0\gamma) = 1 \times 10^{-3}$ and $\mathcal{B}(Z \to \rho^0\gamma) = 1 \times 10^{-5}$ are assumed with an integrated luminosity of 32.3 fb^{-1}.

Sample	Yield
Total H Signal	160
ggF Signal	150
VBF Signal	8.9
WH Signal	2.7
ZH Signal	2
Z Signal	53
Higgs Background Model	5540 ± 20
ZBoson Background Model	$13\,200 \pm 50$

4.5.8 Event Categorisation

The analysis is performed inclusively using a category denoted `INC`, which is used for the final statistical analysis. However as an additional cross check of the modelling in the analysis the following four categories are defined:

- Barrel Unconverted (`B_UNCONV`): Both meson decay products within $|\eta^K| < 1.2$ and an unconverted photon
- Barrel Converted (`B_CONV`): Both meson decay products within $|\eta^K| < 1.2$ and a converted photon
- Endcap Unconverted (`EC_UNCONV`): At least one meson decay product with $|\eta^K| > 1.2$ and an unconverted photon
- Endcap Converted (`EC_CONV`): At least one meson decay product with $|\eta^K| > 1.2$ and a converted photon

While not used in the analysis control plots showing the distributions of the important analysis variables can be found in Appendices C and D.

4.5.9 Signal Resolution

For each of the $\phi\gamma$ and $\rho^0\gamma$ analyses the $m_{M\gamma}$ distributions are modelled by fitting analytical functions to the simulated samples. For the Higgs boson the sum of two Gaussians with a common mean is used. For the Z boson the sum of two Voigtian functions with a width fixed to the PDG value of 2.495 GeV convoluted with an efficiency function derived from the truth acceptance is used. For the $\phi\gamma$ analysis the efficiency function is required to account for the mass-dependent acceptance of the di-track system and is shown in Figure 4.5 and for the $\rho^0\gamma$ in Figure 4.9. The final $m_{K^+K^-\gamma}$ distributions are shown in Fig. 4.4 as well as separately for the defined detector categories in Figures 4.6 and 4.7. The corresponding final distributions for the $\rho^0\gamma$ analysis are shown in Figure 4.8.

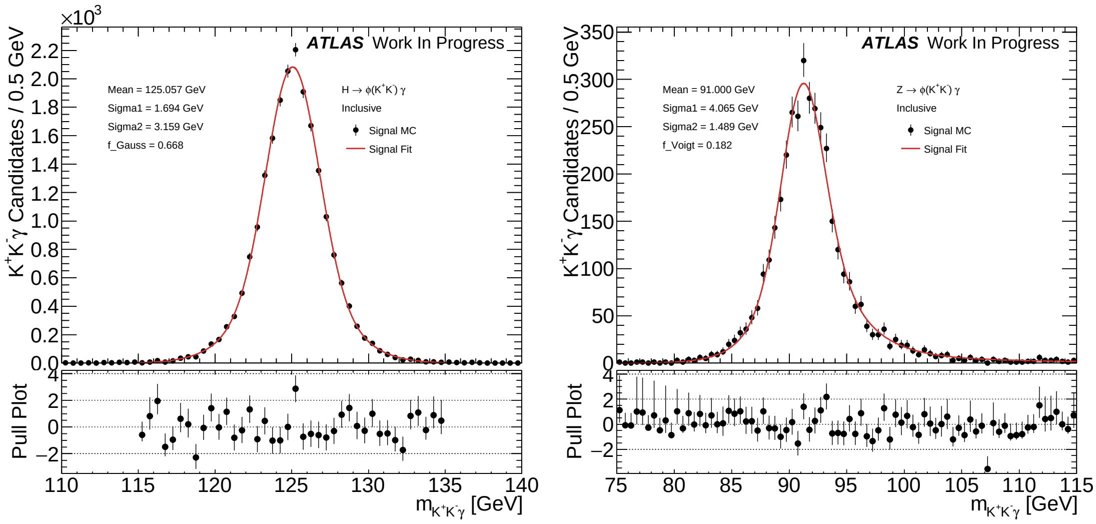

Figure 4.4: The $m_{K^+K^-\gamma}$ distribution model for the Higgs and Z bosons. For the Higgs mass distribution the sum of two Gaussians with a common mean is used, where `Sigma1` and `Sigma2` are the widths of each Gaussian and `f_gauss` is the fraction of the smaller Gaussian. For the Z boson mass distribution a sum of Voigtians convoluted with an efficiency function (see text) is used.

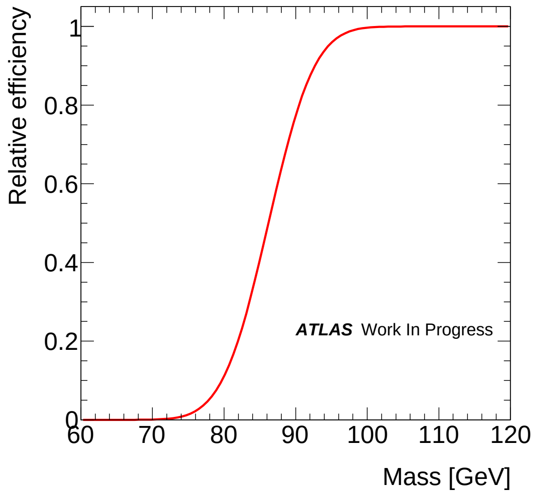

Figure 4.5: The mass dependant efficiency function for the $\phi\gamma$ analysis derived from the truth acceptance.

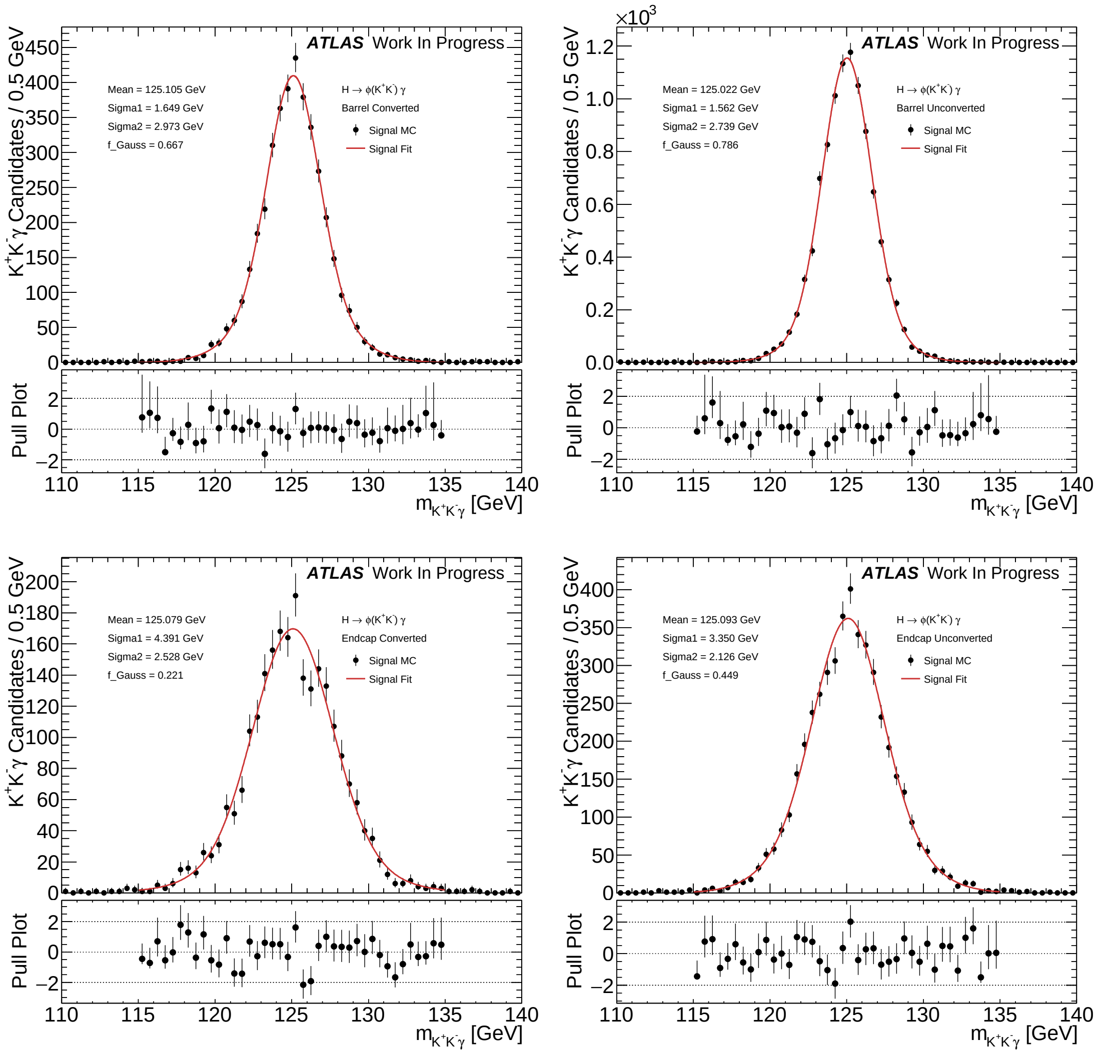

Figure 4.6: Mass resolution fits of the combined simulation samples divided between the four categories for the Higgs boson signal. The categories are defined in Section 4.5.8.

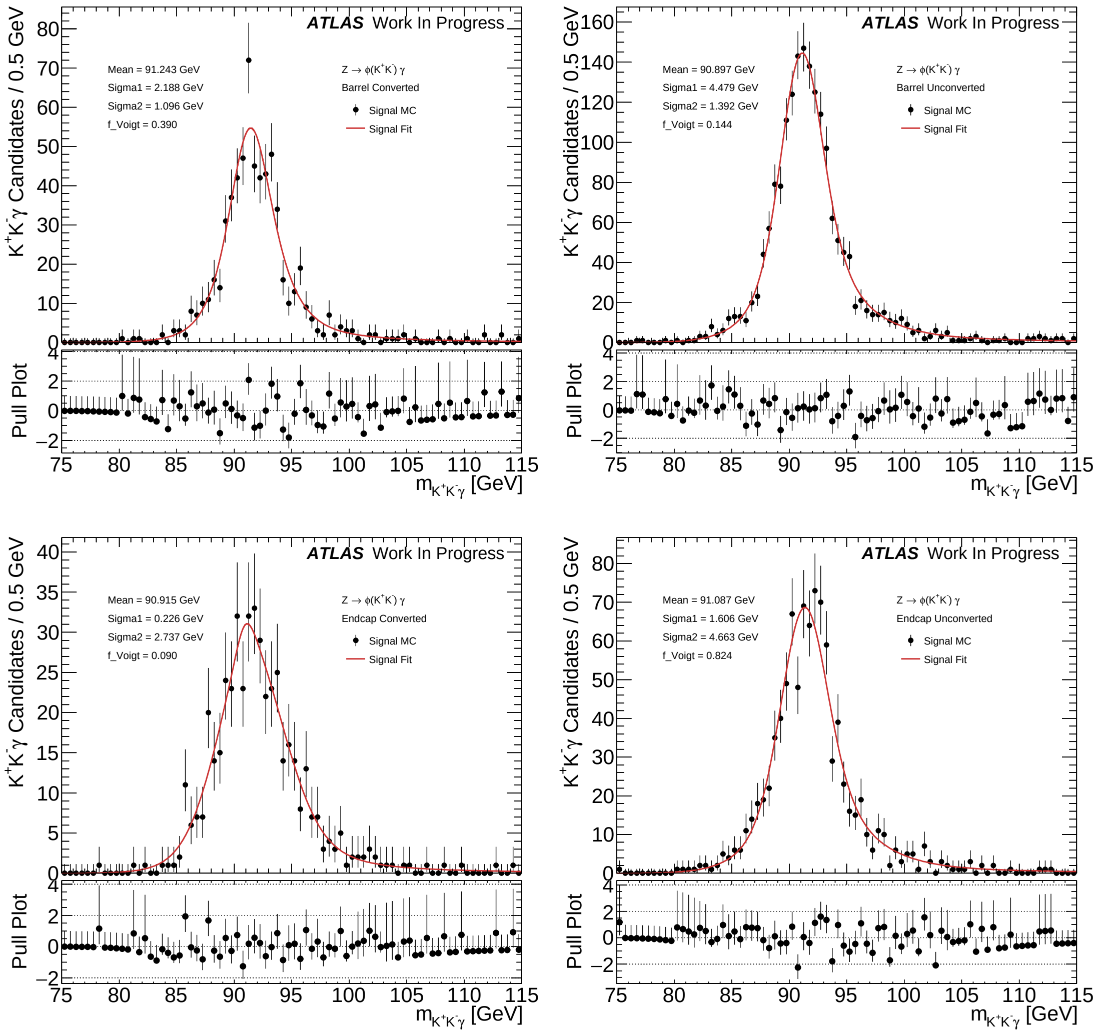

Figure 4.7: Mass resolution fits of the combined simulation samples divided between the four categories for the Z boson signal. The categories are defined in Section 4.5.8.

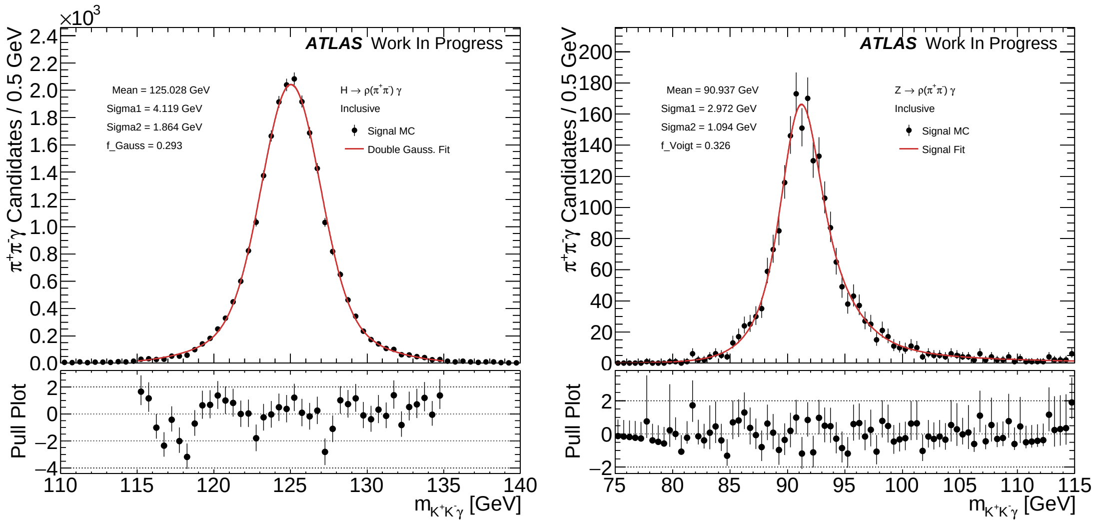

Figure 4.8: The $m_{\pi^+\pi^-\gamma}$ distribution model for the Higgs and Z bosons. For the Higgs mass distribution the sum of two Gaussians with a common mean is used, where `Sigma1` and `Sigma2` are the widths of each Gaussian and `f_gauss` is the fraction of the smaller Gaussian. For the Z boson mass distribution a Voigtian fit is used.

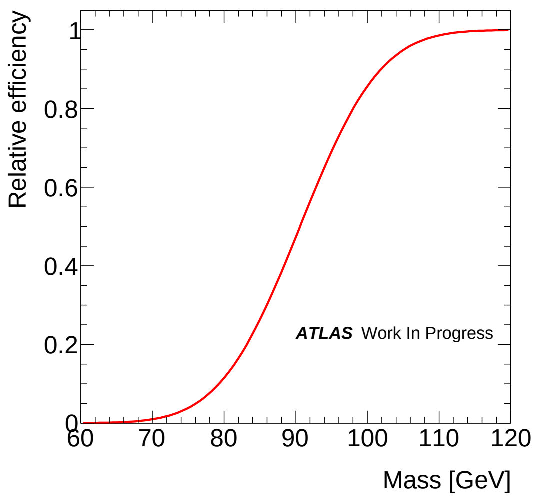

Figure 4.9: The mass dependant efficiency function for the $\rho\gamma$ analysis derived from the truth acceptance.

4.6 Background Modelling

The main source of the inclusive background events is expected to be dijet production and γ+jet production, where a meson candidate is reconstructed within a jet. This background can not be reliably modelled with MC simulation due to the complicated mixture of the contributing processes. Instead, this contribution to the total background is modelled with a data-driven non-parametric approach. This approach was used previously for the J/ψ and ϕ analyses [2, 31].

The same approach is taken for both the $\phi\gamma$ and $\rho^0\gamma$ analyses with slight differences in the correlations due to slightly different behaviours observed in the control sample.

4.6.1 Background Modelling Methods

The inclusive background is modelled with a non-parametric data-driven approach. The approach involves using the kinematic and isolation distributions of a large sample of loose candidates in data (the GR region described in Section 4.5.4) to generate an ensemble of "toy" candidates. These loose "toy" candidates are then subjected to the same final tight kinematic and isolation cuts as the data to form a sample which can be used to model the kinematic distributions of the inclusive background that remains after all selection cuts have been applied.

The control sample of loose candidates (the GR region) is formed by relaxing the p_{T}^{M} and isolation requirements from SR. These requirements are loose enough that the contributions from inclusive background processes will dominate over any possible signal contribution to the kinematic distributions.

The model is built upon an investigation of the correlations between variables sensitive to the $m_{M\gamma}$ distribution. The important correlations are shown in Figure 4.10 for the $\phi\gamma$ analysis.

Each "toy" background candidate is formed according to the following procedure:

1. A value for p_{T}^{M} is sampled from the p_{T}^{M} distribution of the data sample.
2. The p_{T}^{γ} variable is described in bins of p_{T}^{M}. Given the value of p_{T}^{M} chosen in the previous step, a value for p_{T}^{γ} is chosen from parametrisation of the p_{T}^{γ} distribution

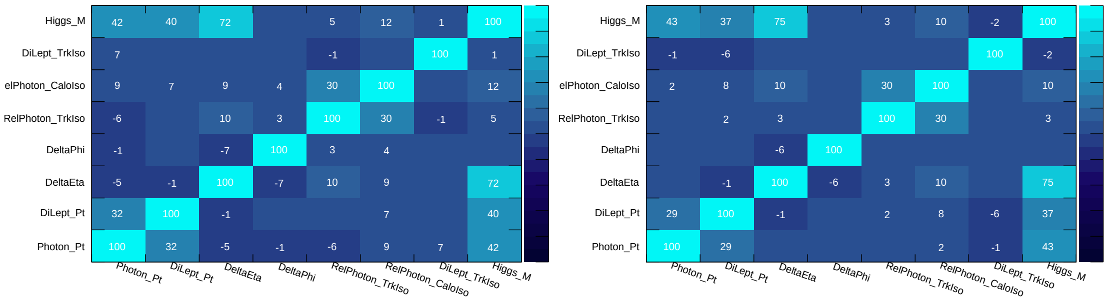

(a) Correlations observed in Data. (b) Correlations produced by the Model.

Figure 4.10: Linear correlations between variables used in the background modelling. Distribution for the data events within inclusive GR. These correlations are indicative of strength of the correlation between variables. Note: “DiLept” in these plots means “DiTrack” and “Higgs_M” means “$m_{K^+K^-\gamma}$”.

of the data control sample.

3. The M isolation distribution of the data control sample is described in bins of p_{T}^{M} for the $\phi\gamma$ analysis and p_{T}^{γ} for the $\rho^0\gamma$ analysis. This difference is believed to be due to the differences in background compositions for the two analysis, with the $\phi\gamma$ analysis selecting a significantly larger number of “real” ϕ candidates. Given the appropriate chosen value, a value for M isolation is chosen from the ϕ isolation distribution of the data control sample in the corresponding bin.

4. Values for $\Delta\eta(M,\gamma)$ and relative photon calorimeter isolation are sampled simultaneously from a 2D distribution given the previously chosen value of p_{T}^{M}

   (a) Given the selected value of relative photon calorimeter isolation a value for relative photon track isolation is sampled for the distribution in the data control sample.

   (b) Given the selected value of $\Delta\eta(M,\gamma)$ a value for $\Delta\phi(M,\gamma)$ is also chosen from the control sample.

5. Values for $\eta^{K^+K^-}$ and the ϕ angle of the di-track system sampled from a binned histogram of the corresponding distributions of the data control sample. This is then used, given the chosen value of $\Delta\eta(M,\gamma)$ and $\Delta\phi(M,\gamma)$, to define the value of η^{γ} and ϕ_{γ} for the “toy” candidate.

6. A value for the di-track invariant mass is sampled from a histogram of the m_M, within the region of the m_M requirement.

After an ensemble of "toy" candidates has been generated, the sample is assigned a weight which is chosen to match the normalisation of the loose data control sample (before unblinding, to obtain the "expected" normalisation of the background events observed in the $M\gamma$ mass distribution at the GR selection, outside the blinded region 120–130 GeV are used). The nominal tight cuts on the isolation of the di-track system and photon are then applied to these loose "toy" candidates to form a sample of "toy"candidates that provides a good description of the contributions from the inclusive backgrounds to the distributions used as signal discriminants. Given that the normalisation of the background sample is performed before any tight cuts are applied, this sample also provides a description of the background normalisation. However, this normalisation serves only as a validation of the consistency of the model and is not used in the final fit to data, where the background normalisation is a free parameter.

The final signal region background template is then generated from a Kernel Density Estimation (KDE) of this normalised sample of "toy" events corresponding to the signal region.

4.6.2 Background Systematic Uncertainties

To provide freedom to the inclusive background model to adjust to the observed, alternative shapes are derived. These are either through the generation of alternative background models (e.g. p_{T}^{M}-shift and $\Delta\phi(M,\gamma$-distortion) or through distortion of the final shape (e.g. "tilt").

The alternative model is generated with the same method as used to generate the nominal model with a single modification: the parametrisation of the p_{T}^{γ} distributions used, Figure 4.11, are artificially shifted by ± 5 GeV. Such a shift is larger than the observed p_{T}^{γ} distribution in data can accommodate and thus represents an appropriate upper/lower limit for the interpolation PDF to operate within and is considered to correspond to $\pm 5\sigma$ variation of the associated profiled nuisance parameter in the subsequent maximum likelihood fit. This designation of the nuisance parameter is arbitrarily chosen to match the large impact of the variation, however this parameter is then successfully constrained by the final fit.

An additional re-weighting of the $\Delta\phi(\phi, \gamma)$ distribution around $\pi/2$ is implemented leading to a 40% shift up and down in the final distribution. To implement this variation each bin of $\Delta\phi/\pi$ is re-weighted by $1 + 10 * \delta\phi/\pi$ so at $\delta\phi/\pi = 1$ this is an eleven fold increase but only a factor of 6 at $\delta\phi/\pi = 0.5$. The down variation is inverted to enhance the lower values of $\delta\phi/\pi$ so the bins are scaled by $1 + 2 * (1 - \delta\phi/\pi)$ where the pre-factors (10 and 2) were chosen in both cases to give a symmetrical shift of approximately equal magnitude. These weights do not conserve the normalisation of the distributions however this is not necessary as the ensamble of psuedo candidates is explicitly normaliused to the data in the GR after this step. The resulting effect on the $\Delta\phi/\pi$ distributions can be seen in Figures 4.12(a) – 4.12(c) giving an approximately linear trend in the Data/Model.

Figures 4.11 and 4.12(d) show the characteristic shape changes associated with these distortions. This corresponds to $\pm 5\sigma$ variation of the associated profiled nuisance parameter in the subsequent maximum likelihood fit. These shifts provide different $m_{M\gamma}$ templates, which are included in the final background model as constrained uncertainties that the fit is able to morph between.

Both of these systematic shifts provide lateral movement of the peak of the $m_{M\gamma}$ distribution. Another kind of distortion of the shape could be an overall "tilt" of the distribution. To allow for such a possibility, an additional systematic template variation is included, where the $m_{M\gamma}$ distribution is artificially tilted to match this discrepancy. A linear fit is performed to the ratio of the data and the prediction from the model in the VR2 region. The parameters from this fit are used to re-weight the model to match the data. The reflection of this line about $y = 1$ is also taken as a variation in the opposite direction. The parameters for this tilt are detailed in Eq 4.4.

$$\begin{aligned} \text{Up} :& y = -0.0021x + 1.23 \\ \text{Down} :& y = 0.0021x + 0.77 \end{aligned} \tag{4.4}$$

Unlike the previous two variations this "tilt" is left without a constraint in the fit and

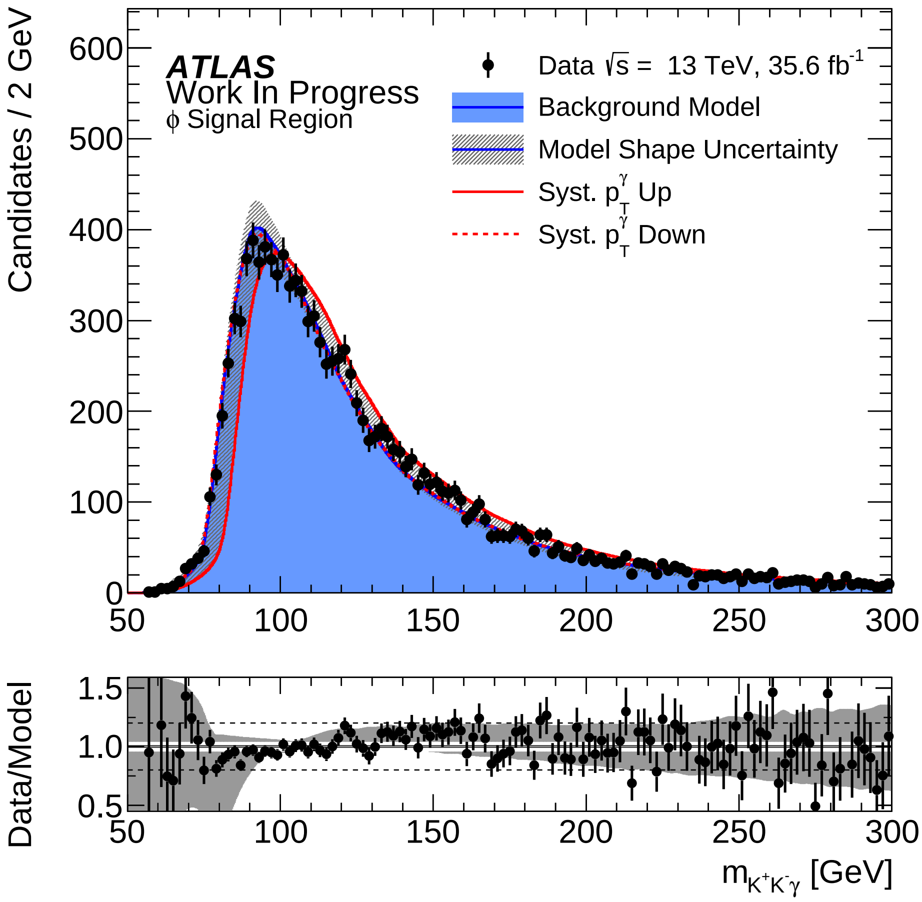

Figure 4.11: Effect on $m_{K^+K^-\gamma}$ in SR. The systematic uncertainty band on the background represents the maximum deviation of all the alternative shapes from the nominal prediction.

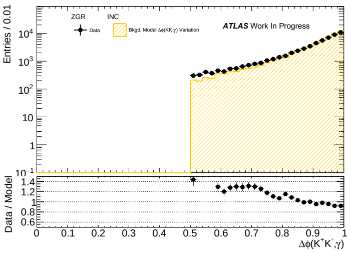

(a) Distribution shifted up (GR) $\Delta\phi(K^+K^-,\gamma)/\pi$

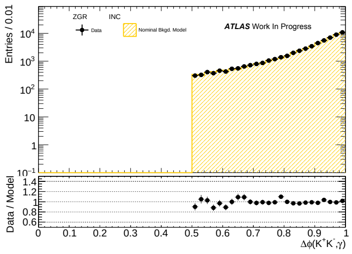

(b) Nominal (GR) $\Delta\phi(K^+K^-,\gamma)/\pi$

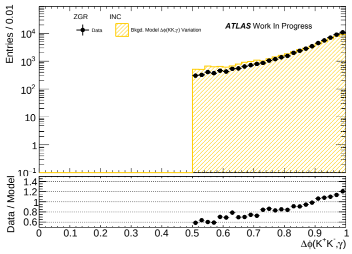

(c) Distribution shifted down (GR) $\Delta\phi(K^+K^-,\gamma)/\pi$

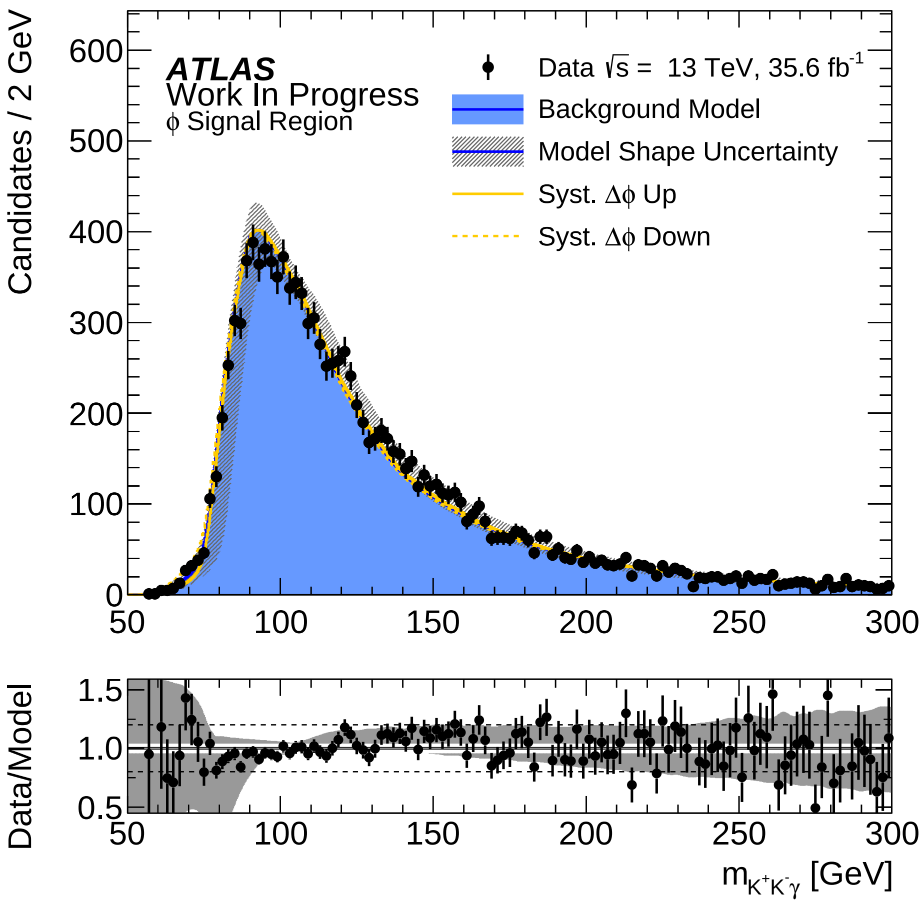

(d) Effect on $m_{K^+K^-\gamma}$ in SR. The systematic uncertainty band on the background represents the maximum deviation of all the alternative shapes from the nominal prediction.

Figure 4.12: Effect of the $\Delta\phi(K^+K^-,\gamma)$ distortion to the $m_{K^+K^-\gamma}$ distribution.

the final value is fully determined from the data (as with the normalisation). The effect of this shape variation is shown by Figure 4.13

The magnitude of the resulting changes in the $m_{K^+K^-\gamma}$ distribution are then constrained by the data in the fitting procedure used to obtain the limits. The ultimate effect of the shape systematics is constrained in the fit by the data through the implementation of shape morphing nuisance parameters. The uncertainty on the nuisance parameters in the fit is around 50%.

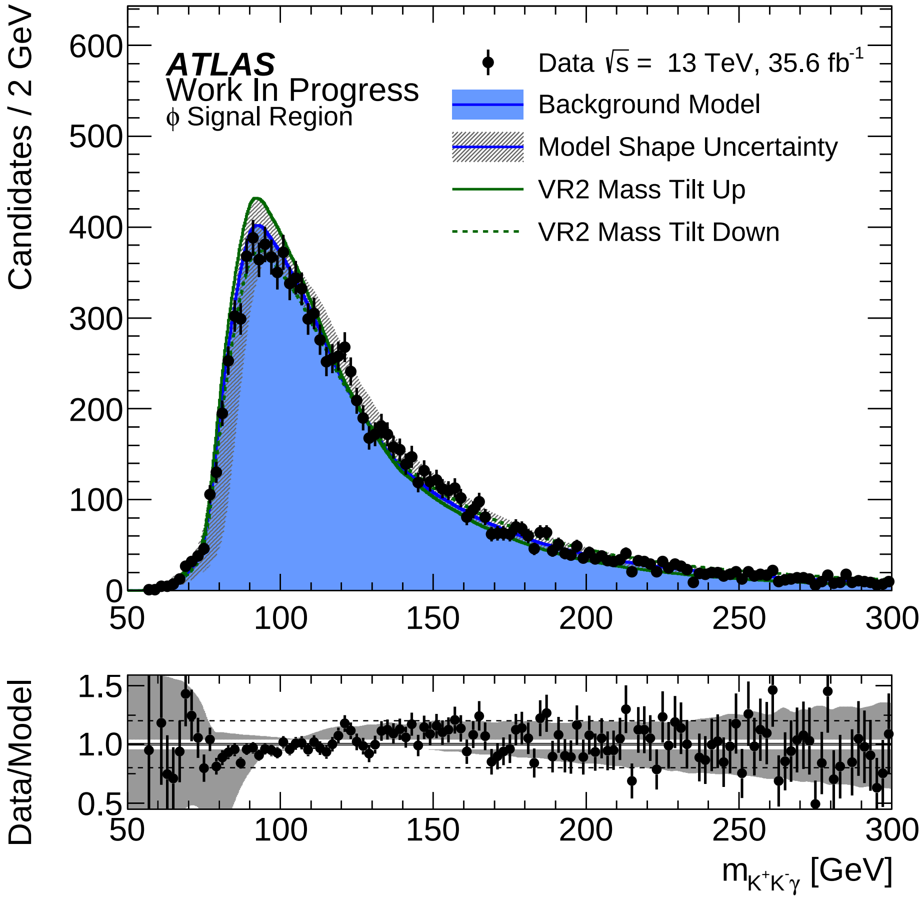

Figure 4.13: The distribution of $m_{K^+K^-\gamma}$ in data compared to the prediction of the background model, the shape variation derived from the "VR2 tilt" is also shown. The systematic uncertainty band on the background represents the maximum deviation of all the alternative shapes from the nominal prediction.

4.6.3 Signal Injection Tests

The effect of signal contamination in the GR is assessed by injecting 1000 Higgs signal events into the data sample used to build the background model. This level of injection was chosen such that it would be clearly visible in the GR $m_{K^+K^-\gamma}$ distribution and is equivalent to a signal branching fraction of around 5×10^{-3}. Figure 4.14 shows the injected signal in the GR and also demonstrates the associated change in the background model due to the signal injection. The effect of the injected signal is largely inconsequential to the shape of the background model and does not lead to any peaking structures in the background templates. The presence of a signal contribution at this level is clearly excluded by the data observed in the GR, as shown in Figure 4.14.

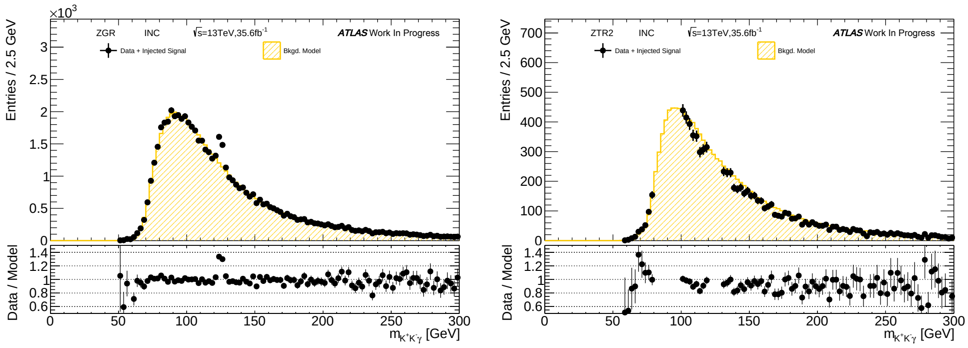

Figure 4.14: The effect of injecting 1000 signal events in the GR. $m(K^+K^-\gamma)$ shape comparison for the background model a) in the GR and b) in the signal region.

4.6.4 Background Model Validation with Data in the Meson Mass Sideband

A further validation of the background modelling is performed using a sideband region. This region is defined as a sideband in the meson mass orthogonal to the signal region and sufficiently far away to remove any sensitivity to the signal. For the $\phi\gamma$ analysis the window chosen is 1.035 GeV $< m_{K^+K^-} <$ 1.051 GeV and for the $\rho^0\gamma$ the corresponding window is 950 MeV $< m_{\pi\pi} <$ 1050 MeV. In this side band all other selections and procedures are preserved to provide a test of the background methodology. Figures 4.15 to 4.20 show the final distributions at the generation region (GR) as well as the validation regions defined above and finally the sideband region with cuts equivalent to the signal region for the $\phi\gamma$ analysis. The equivalent plots for the $\rho^0\gamma$ can be found in Figure 4.21.

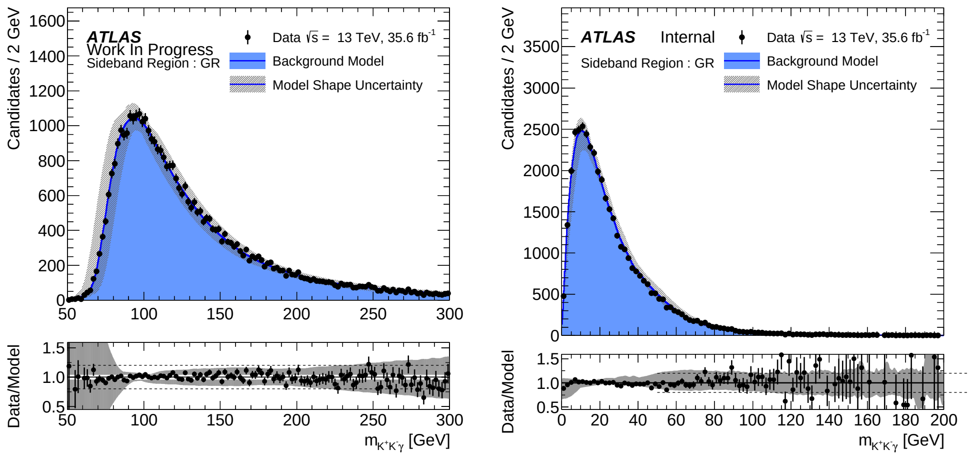

Figure 4.15: Sideband $m_{K^+K^-\gamma}$ and $p_T^{K^+K^-\gamma}$ distributions in data compared to the background model prediction. The systematic uncertainty band on the background represents the maximum deviation in the alternative background model from the nominal prediction. The distributions are shown for the `GR` region.

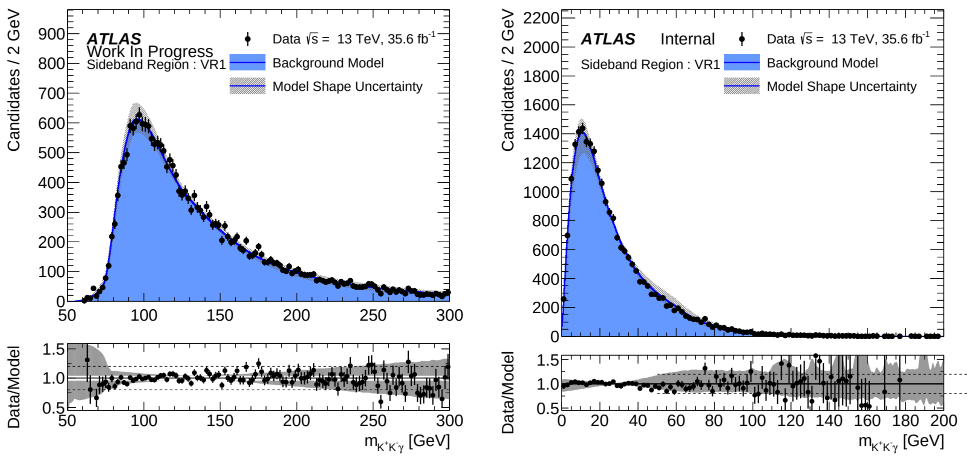

Figure 4.16: Sideband $m_{K^+K^-\gamma}$ and $p_T^{K^+K^-\gamma}$ distributions in data compared to the background model prediction. The systematic uncertainty band on the background represents the maximum deviation in the alternative background model from the nominal prediction. The distributions are shown for the `VR1` region.

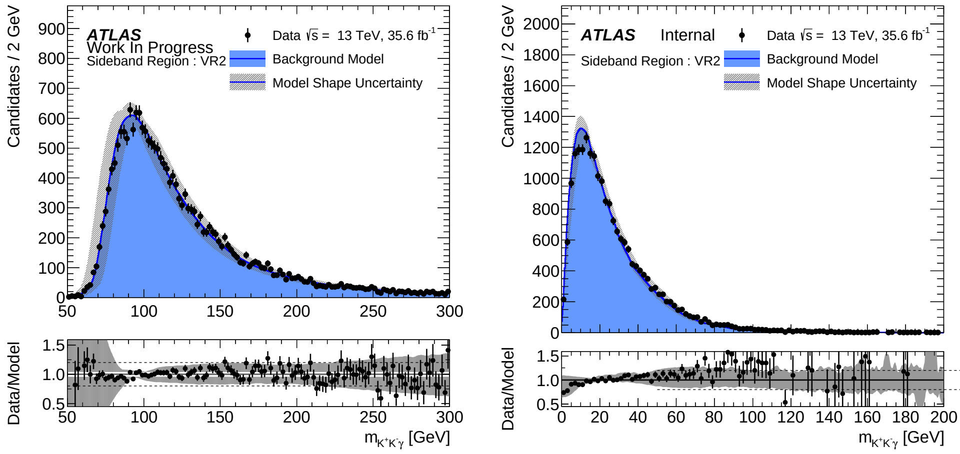

Figure 4.17: Sideband $m_{K^+K^-\gamma}$ and $p_T^{K^+K^-\gamma}$ distributions in data compared to the background model prediction. The systematic uncertainty band on the background represents the maximum deviation in the alternative background model from the nominal prediction. The distributions are shown for the `VR2` region.

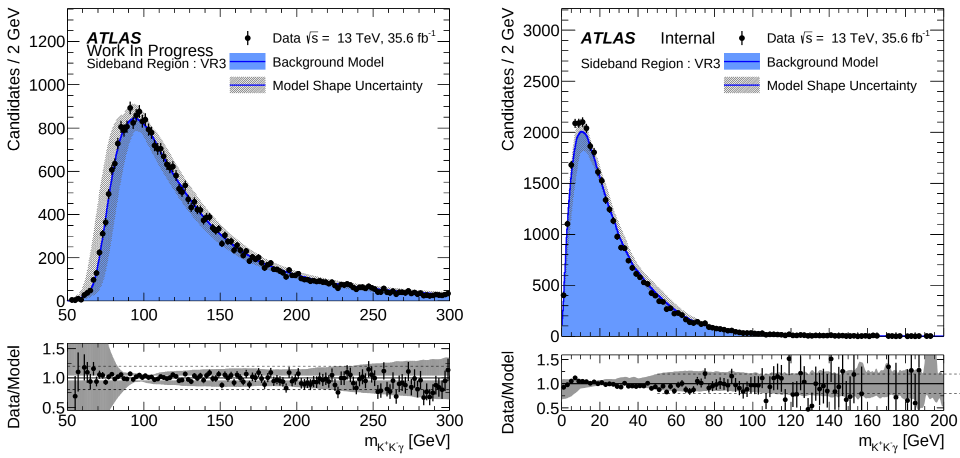

Figure 4.18: Sideband $m_{K^+K^-\gamma}$ and $p_T^{K^+K^-\gamma}$ distributions in data compared to the background model prediction. The systematic uncertainty band on the background represents the maximum deviation in the alternative background model from the nominal prediction. The distributions are shown for the `VR3` region.

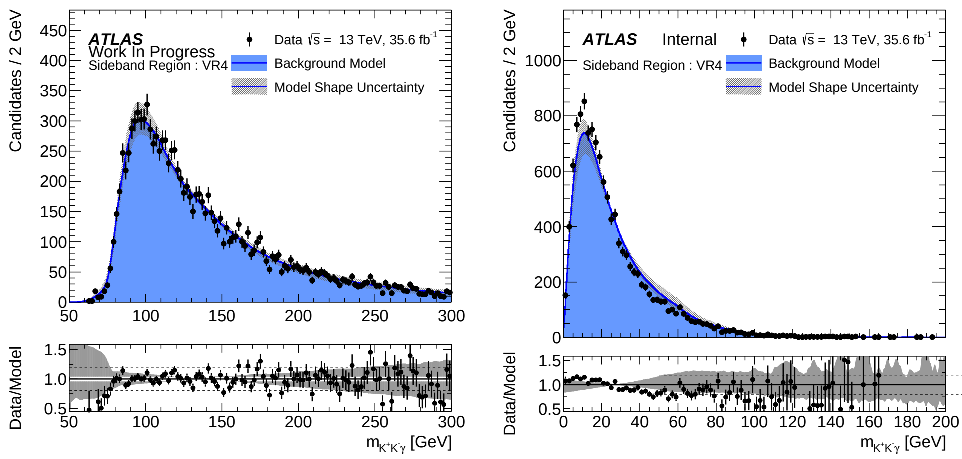

Figure 4.19: Sideband $m_{K^+K^-\gamma}$ and $p_T^{K^+K^-\gamma}$ distributions in data compared to the background model prediction. The systematic uncertainty band on the background represents the maximum deviation in the alternative background model from the nominal prediction. The distributions are shown for the `VR4` region.

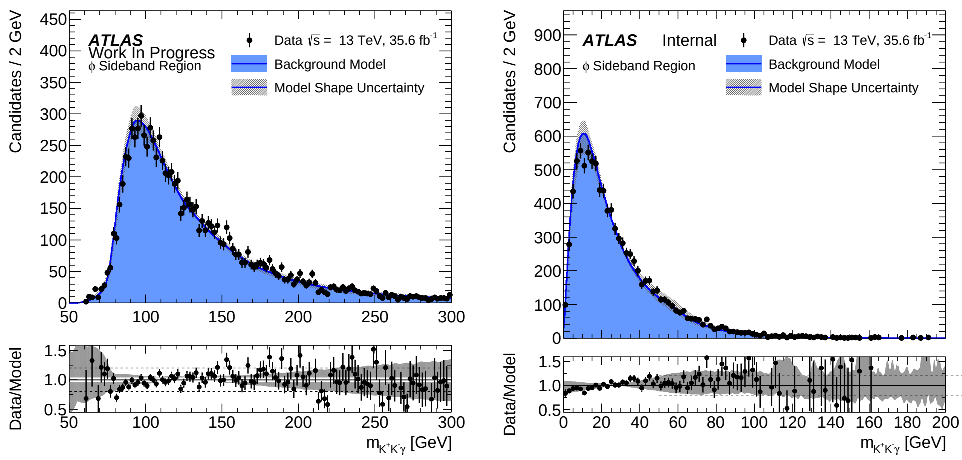

Figure 4.20: Sideband $m_{K^+K^-\gamma}$ and $p_T^{K^+K^-\gamma}$ distributions in data compared to the background model prediction. The systematic uncertainty band on the background represents the maximum deviation in the alternative background model from the nominal prediction. The distributions are shown for the `SR` region.

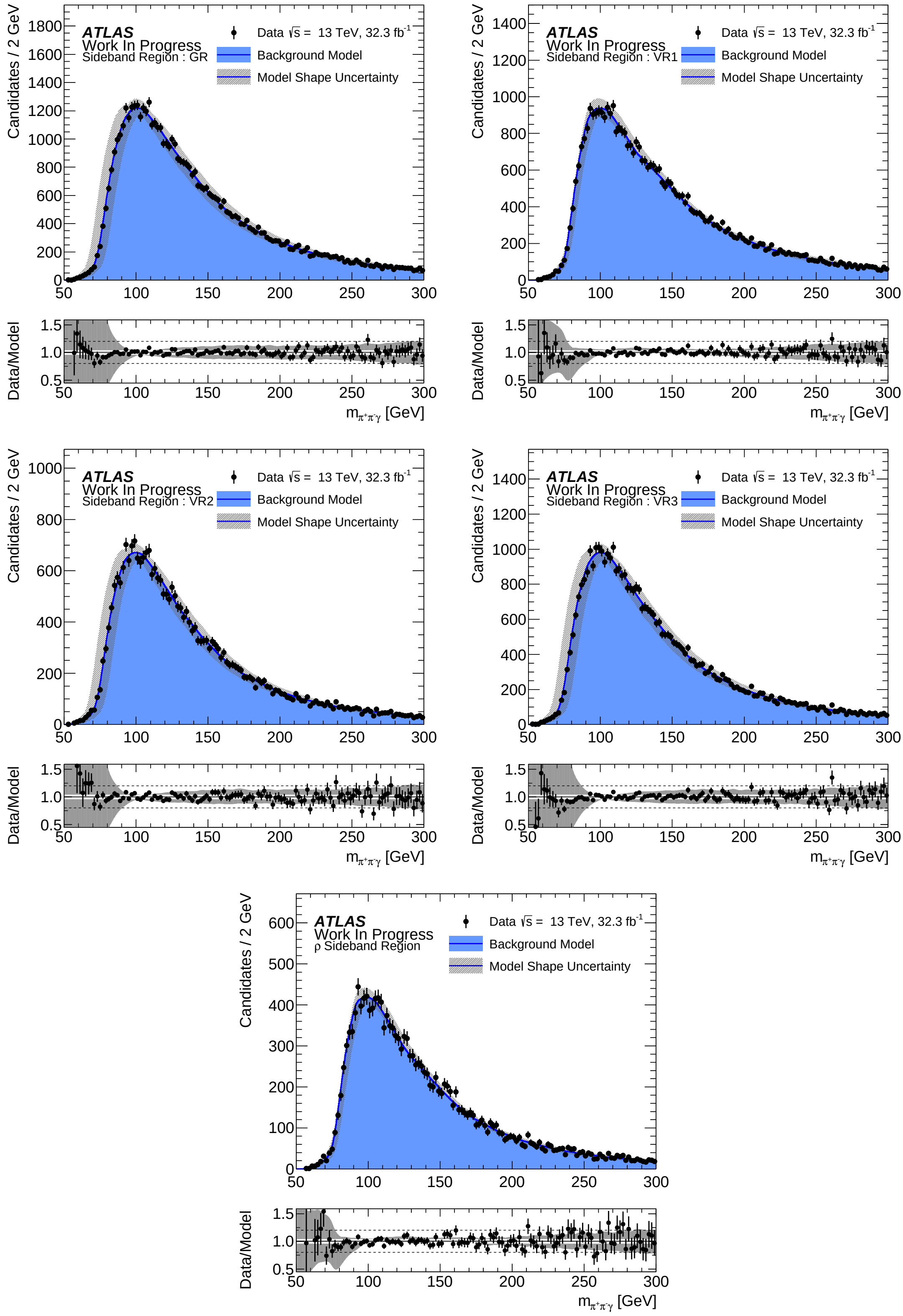

Figure 4.21: Three body mass of the $\rho^0\gamma$ system in the side band control region. The background modelling shows agreement with the data.

4.6.5 Resonant Backgrounds

One possible resonant background source relevant to the $Z \to \phi\gamma$ search is $Z \to \ell\ell\gamma$ decays, where inner detector tracks associated with the leptons are interpreted as $K^{\pm}$ candidates.

The $m_{\ell\ell}$ range relevant for a lepton pair from a $Z \to \ell\ell\gamma$ decay to be mis-identified (by having a ditrack mass falling within the ϕ selection window when assigned the kaon mass) as a $\phi \to K^+K^-$ candidate is around $0.2 < m_{\mu\mu} < 0.4$ GeV. The probability for a $Z \to \mu\mu$ decay to undergo an FSR such that $0.2 < m_{\mu\mu} < 0.4$ GeV is extremely low, since the $m_{\mu\mu}$ distribution in $Z \to \mu\mu\gamma$ is rapidly falling to zero for $m_{\mu\mu} \to 0$ [125].

The rate of such events was studied in detail during the ATLAS $H \to J/\psi\,\gamma$ search [31]. In this case, for an integrated luminosity of around 20fb^{-1} at $\sqrt{s} = 8$ TeV, the expected yield of $Z \to \mu^+\mu^-\gamma$ events passing the full selection (with a mass window of $|m_{\mu^+\mu^-} - m_{J/\psi}| < 0.25$ GeV) was 3 ± 1. This can used to estimate a conservative upper bound on the contribution from $Z \to \mu^+\mu^-\gamma$ decays in this case by simply scaling by the $\sigma \times \mathcal{L}$ used in each analysis and the width of the ditrack mass window. This estimate is further reduced by the significant phase space suppression of moving from $2.85 < m_{\ell\ell} < 3.35$ GeV to $0.2 < m_{\ell\ell} < 0.4$ GeV. This phase space suppression was estimated from $Z \to \mu^+\mu^-\gamma$ simulation to be around 0.03 by extrapolating the distribution below 1 GeV and evaluating the relative integral of the J/ψ ($2.85 < m_{\mu^+\mu^-} < 3.35$ GeV) and ϕ ($0.2 < m_{\mu^+\mu^-} < 0.4$ GeV) mass windows. This leads to an expected yield of $Z \to \mu^+\mu^-\gamma$ of around 0.20.

In the case of $Z \to e^+e^-\gamma$, further suppression is present due to the trigger requirement that the energy deposited in the EM calorimeter, in the region of the ditrack system, is small with respect to the momentum of the ditrack system. Based on these studies, this source of background is considered negligible and is not modelled explicitly, but is taken into account by the background model.

4.7 Systematic Uncertainties

4.7.1 Theoretical Systematic Uncertainties

The Higgs boson production cross sections and decay branching ratios, as well as their uncertainties, are taken from Refs. [14, 126, 127]. The QCD scale uncertainties on the cross-section for a 125 GeV H boson [14] amount to +7% and −8% for the ggF process, ±1% to ±4% for the VBF and associated WH/ZH production processes and +6% and −9% for the associated $t\bar{t}H$ production process. The uncertainty on the production cross section due to uncertainties on the parton distribution functions (PDF) and the strong coupling constant, α_s, is +7% and −6% for ggF processes, ±3.2% and ±2.2% for the VBF and associated WH/ZH production processes respectively and ±9% for the associated $t\bar{t}H$ production process.

For the Z signal the production cross sections as well as their uncertainties are taken from the measurement described in Section 3 and published in Ref. [1], with an uncertainty of 5.5%. The scale uncertainties are calculated by varying the factorisation and renormalisation scales independently up-and-down by a factor of two around their central values. The maximum changes in the resulting cross sections are taken as scale uncertainties and for the Z boson was found to be ±2.5 – 3.5% at NLO. The PDF uncertainties at NLO are found to be ±2%. The uncertainties from α_s are estimated using $MSTW2008$ fits which include PDF sets with α_s values corresponding to ±1 standard-deviation from its central value and for the Z boson are found to be ±1.9%.

4.7.2 $\phi\gamma$ Experimental Systematic Uncertainties

The effect of the experimental systematic uncertainties on the signal are discussed.

The normalisation uncertainty is evaluated by comparing the nominal event yield with the one after modifying the quantity of interest according to the related systematic uncertainty. The nominal yield (ΣA) is given by the integral of $m_{K^+K^-\gamma}$ distribution after all nominal corrections are applied. The modified yield (ΣB) is given by the same integral, but using the modified weights. The relative systematic uncertainty is then $|(\Sigma A - \Sigma B)/\Sigma A|$ and expressed in percent. Uncertainties on the track efficiencies are treated as fully uncorrelated.

The scale/resolutions uncertainties are obtained by comparing the $m_{K^+K^-\gamma}$ mass distribution, obtained with the nominal scale or resolution, with the one obtained with the modified energy scale or resolution by $\pm 1\sigma$ (Up/Down). The difference in the mean value of the $m_{K^+K^-\gamma}$ histogram between the nominal and modified energy scale is used as the energy scale systematic uncertainty on $m_{K^+K^-\gamma}$. Correspondingly, the difference in the width of the $m_{K^+K^-\gamma}$ histogram between the nominal and modified resolution is used as the resolution systematic uncertainty on $m_{K^+K^-\gamma}$.

Photon Reconstruction/Identification/Isolation The uncertainty on the signal yield due to a combination of the photon reconstruction and identification uncertainty, and the photon isolation uncertainty is estimated to be 2.4%. This value was calculated based on the studies described in Reference [57]. The break-down for the different categories is shown in Table 4.10.

Table 4.10: Break-down of the reconstruction and identification efficiency uncertainty for the photon in different categories.

Photon Eff sys	Category H signal		
	Inclusive	Barrel	End-cap
Converted-γ	2.36%	2.36%	2.35%
Unconverted-γ	2.43%	2.39%	2.54%

Track Reconstruction Track momenta are measured in the inner detector (ID). Their efficiency and resolution systematics are determined using the Moriond recommendations from the ID combined performance group [54]. These recommendations take the form of a series of tools which smear the track p_{T} or disqualify tracks based on the efficiency of the region.

15 variations on these tools are used to calculate the envelope of the systematic uncertainty. These can vary the smearing of the track momenta and impact parameters as well as affecting the probability of a track to be disqualified based on variation in the dead material model.

Of the 15 possible variations only those shown in Table 4.11 were found to have a significant impact. Due to the random nature of the tool removing tracks the effect on the nominal yield for each systematic variation was determined 10 times and the average difference was taken as the uncertainty.

Table 4.11: The uncertainty contributions from systematic variations of the track reconstruction.

Systematic Variation	Uncertainty (%)
`TRK_EFF_LOOSE_GLOBAL`	0.59
`TRK_EFF_LOOSE_IBL`	1.29
`TRK_EFF_LOOSE_PP0`	1.01
`TRK_FAKE_RATE`	0.52

An additional uncertainty is given for the track reconstruction in dense environments (TIDE) component of 3% based on previous studies [55], leaving a total uncertainty due to the tracking performance of 6%.

Track Isolation Uncertainty of Tracks The uncertainty on the signal yield to the track isolation uncertainty of the tracks is estimated to 1%, using the uncertainty estimation from the muons CP recommendations [58].

Photon Energy Scale and Resolution There are 30 independent sources for the photon energy scale uncertainty. The total photon energy scale uncertainty is evaluated by varying all these sources in a correlated manner. There are four independent sources for the photon energy resolution uncertainty. The total photon energy resolution uncertainty is evaluated by varying all the parameters in a correlated manner with a single nuisance parameter. From this we arrive at a normalisation uncertainty of 0.34% due to the photon energy scale and resolution uncertainty. The effect of the energy scale uncertainty to the mass is found to be approximately 0.2%.

4.7.3 $\rho^0\gamma$ Systematic Uncertainties

The scale/resolutions uncertainties are obtained by comparing the $m_{\pi\pi\gamma}$ mass distribution, obtained with the nominal scale or resolution, with the one obtained with the modified energy scale or resolution by $\pm 1\sigma$ (Up/Down). The difference in the mean value of the $m_{\pi\pi\gamma}$ histogram between the nominal and modified energy scale is used as the energy scale systematic uncertainty on $m_{\pi\pi\gamma}$. In the case of the photon scale uncertainty the effect was found to be 0.2%.

Photon Reconstruction/Identification/Isolation The uncertainty on the signal yield due to a combination of the photon reconstruction and identification uncertainty, and the photon isolation uncertainty is estimated to be 1.6%.

Track Reconstruction The determination of the track uncertainties was performed using the same procedure and recommendations as those mentioned above for the $\phi\gamma$ analysis. However in this case a different subset of the 15 variations were found to be dominant and are shown below in Table 4.12.

Table 4.12: The uncertainty contributions from systematic variations of the track reconstruction.

Systematic Variation	Uncertainty (%)
`TRK_EFF_LOOSE_GLOBAL`	0.56
`TRK_EFF_LOOSE_IBL`	0.80
`TRK_EFF_LOOSE_PP0`	0.65
`TRK_EFF_LOOSE_PHYSMODEL`	0.70

Again an additional uncertainty is given for the track reconstruction in dense environments (TIDE) component of 3%, leaving a total uncertainty due to the tracking performance of 6%.

4.8 Kinematic Distributions

4.8.1 Meson Mass Control Plots from the Signal Region

A test of the selection procedure is to investigate the di-track mass distributions. These should contain a resonance peak from the prompt meson component of the background as well as other combinatorial backgrounds where a pair of tracks, possibly belong to another resonance, happens to fall within the mass window.

The $m_{K^+K^-}$ distribution for the $\phi\gamma$ analysis is plotted in Figure 4.22(a). A simple fit is then performed using a Voigtian for the signal and generic background function (`RooDstD0BG`) to represent the combinatorial background.

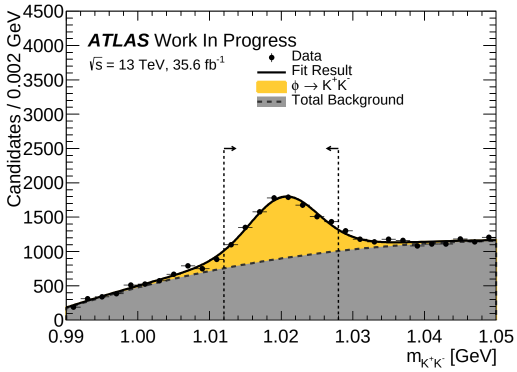

(a) $m_{K^+K^-}$ distribution for the $\phi\gamma$ analysis

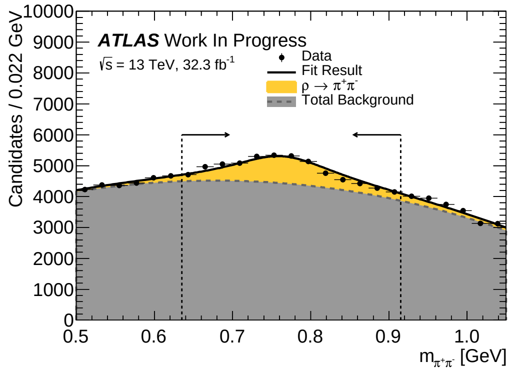

(b) $m_{\pi\pi}$ distribution for the $\rho^0\gamma$ analysis

Figure 4.22: Di-track invariant mass distribution for data at the SR level.

The $m_{\pi^\pm\pi^\mp}$ distribution for signal and data in the signal region is presented in Figure 4.22(b). The signal is modelled with a Breit-Wigner with the parameters fixed to the best fit to the simulated signal sample the signal line-shape is further re-weighted to account for the mass dependant width of the ρ^0 meson [128]. The continuum is modelled using a second order Chebychev polynomial with additional small contributions from other resonances within the signal acceptance (K^{*0} and f^0). Simple phase space templates are generated for these and included in the fit with an unconstrained normalisation. Here the purely combinatoric background is determined using an additional same-sign control region where the nominal signal selection is applied but instead of requiring oppositely charged tracks they are instead required to have the same sign. This contribution is small compare to the contribution from continuum pion with the ratio of same-sign to opposite-sign events being 0.066.

4.8.2 $\phi\gamma$ Control Plots

The model is validated in data by individually applying the isolation and kinematic requirements on top of the GR selection and checking the agreement with the model; these "Validation Regions" are defined as in Table 4.4. These are presented (also the GR and signal regions) in Figs 4.23 to 4.28, where the systematic uncertainty band on the background represents the maximum deviation in the alternative background model from the nominal prediction.

The $m_{K^+K^-\gamma}$ in two regions of $p_T^{K^+K^-\gamma}$ ($p_T^{K^+K^-\gamma} > 15$ GeV and $p_T^{K^+K^-\gamma} < 15$ GeV) is shown in 4.29. This cross-check was motivated by the different $p_T^{K^+K^-\gamma}$ distributions of the Higgs and Z boson signals to ensure both phase spaces were adequately modelled.

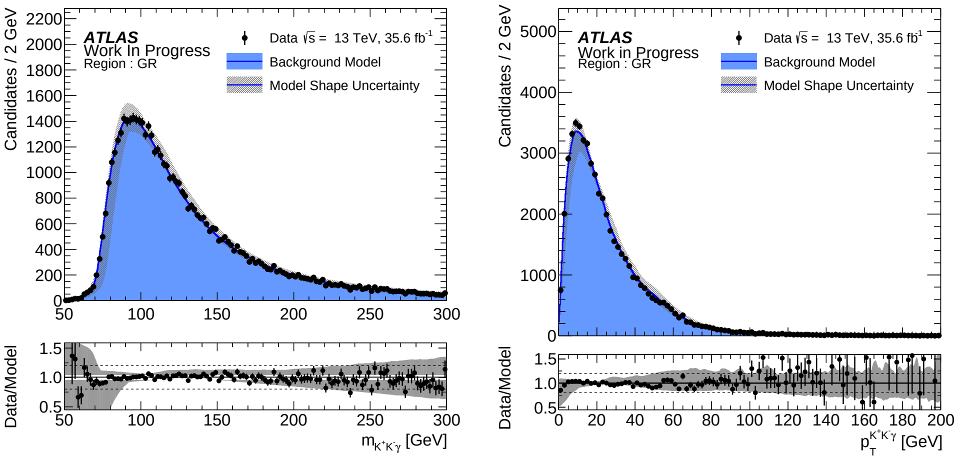

Figure 4.23: $m(K^+K^-\gamma)$ and $p_T^{K^+K^-\gamma}$ distributions in data compared to the background model prediction. The distributions are shown for the GR region.

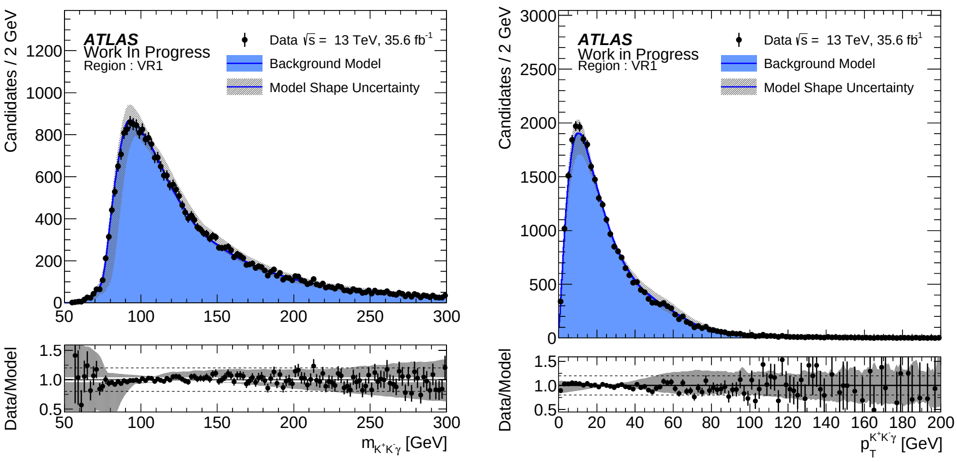

Figure 4.24: $m(K^+K^-\gamma)$ and $p_T^{K^+K^-\gamma}$ distributions in data compared to the background model prediction. The distributions are shown for the VR1 region.

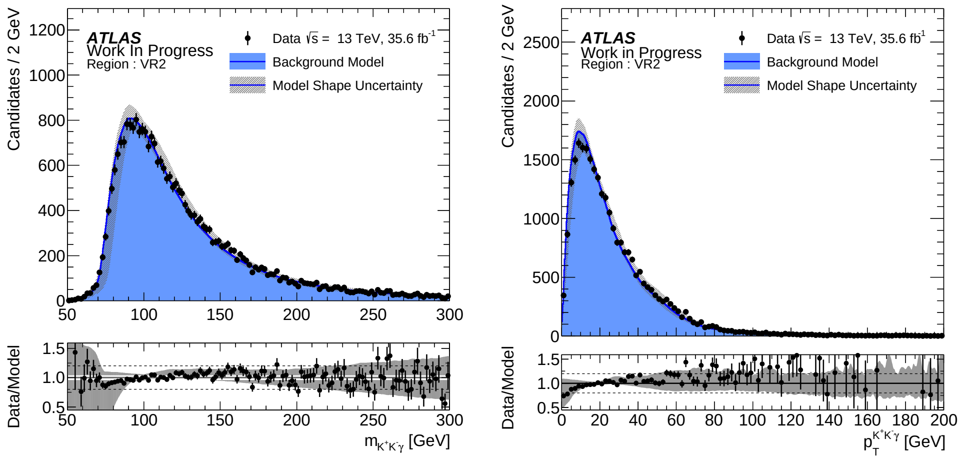

Figure 4.25: $m(K^+K^-\gamma)$ and $p_T^{K^+K^-\gamma}$ distributions in data compared to the background model prediction. The distributions are shown for the `VR2` region.

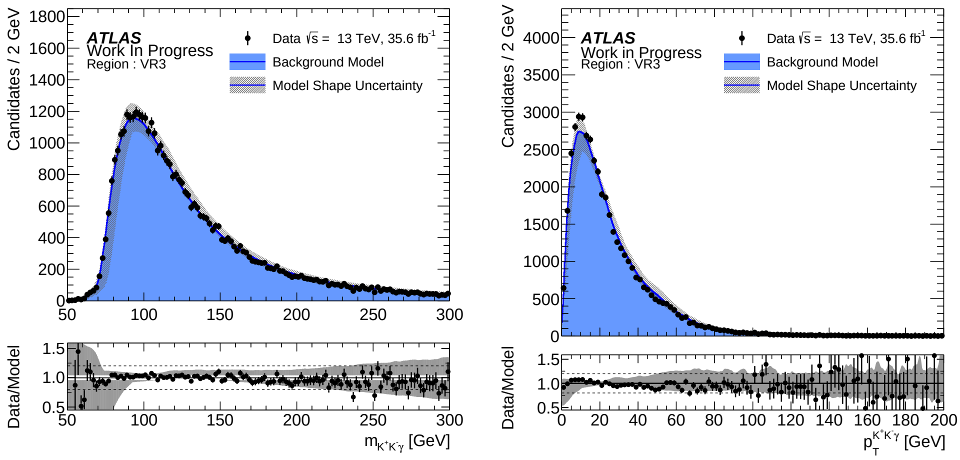

Figure 4.26: $m(K^+K^-\gamma)$ and $p_T^{K^+K^-\gamma}$ distributions in data compared to the background model prediction. The distributions are shown for the `VR3` region.

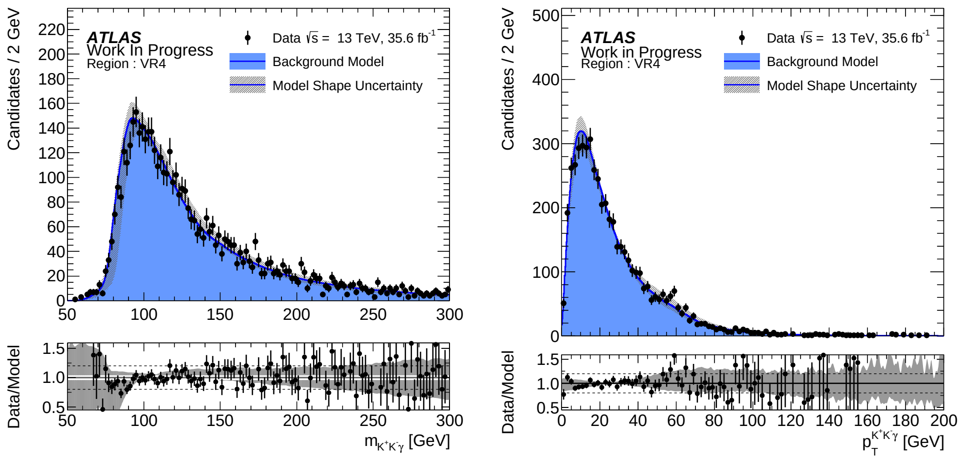

Figure 4.27: $m(K^+K^-\gamma)$ and $p_T^{K^+K^-\gamma}$ distributions in data compared to the background model prediction. The distributions are shown for the `VR4` region.

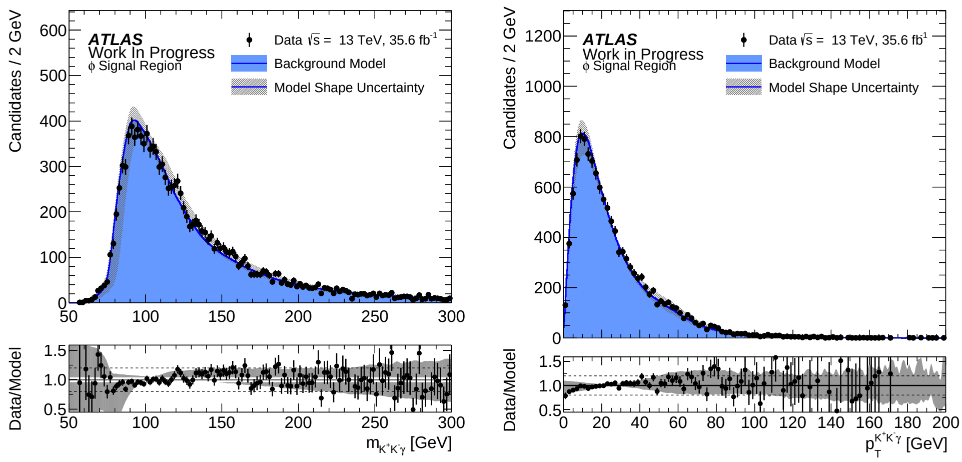

Figure 4.28: $m(K^+K^-\gamma)$ and $p_T^{K^+K^-\gamma}$ distributions in data compared to the background model prediction. The distributions are shown for the SR region.

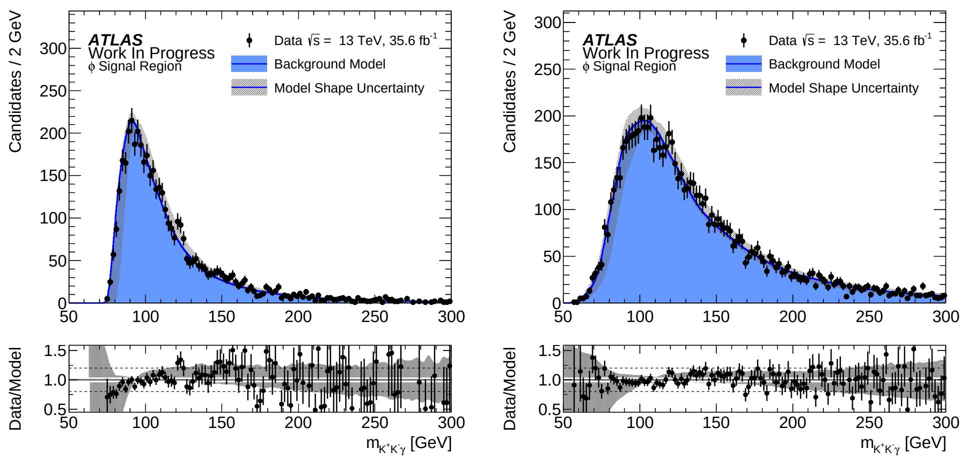

Figure 4.29: The distribution of $m(K^+K^-\gamma)$ in data compared to the background model prediction for $p_T^{K^+K^-\gamma} < 15$ GeV (left) and $p_T^{K^+K^-\gamma} > 15$ GeV (right). The distributions are shown for the SR region.

4.8.3 $\rho^0\gamma$ Control Plots

Figure 4.30 shows to corresponding smoothed templates of the background three-body mass in the control regions for the $\rho^0\gamma$ analysis. The $p_T^{\pi^+\pi^-}$ templates were not generated as they would not be used in the fit, however the distributions with the un-smoothed background model can be seen in Appendix D.

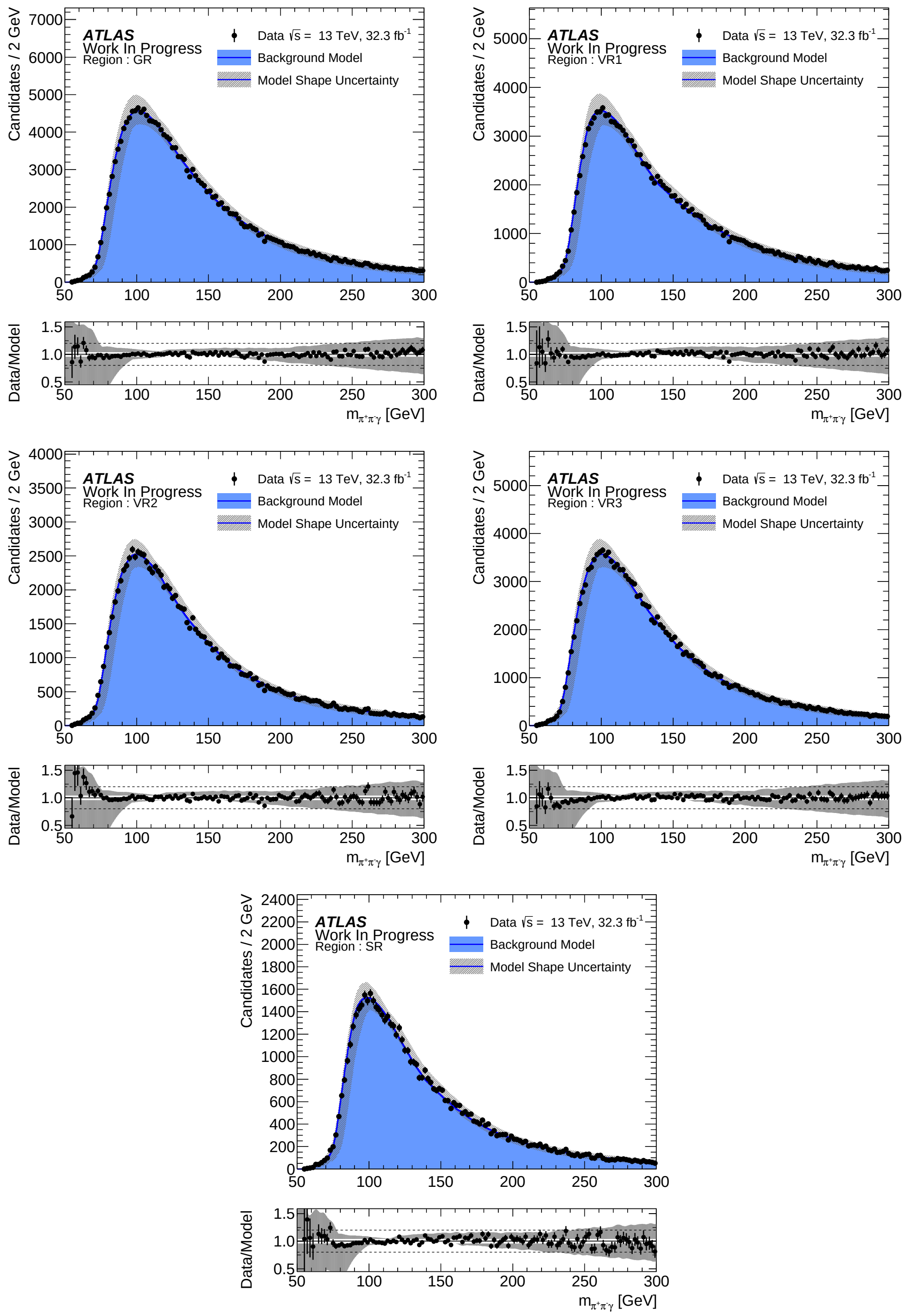

Figure 4.30: Plots of the three body mass of the $\rho^0\gamma$ system. The background modelling shows agreement with the data.

4.9 Statistical Model and Results

In this section the statistical analysis and fitting model are discussed, along with the expected sensitivity based on the background expectations derived from the blinded data-sample.

4.9.1 Fitting model

To extract the limit on the branching fractions of the $\mathcal{B}\,(H/Z \to \phi\,\gamma)$ and $\mathcal{B}\,(H/Z \to \rho^0\,\gamma)$ an unbinned maximum-likelihood fit is performed to the selected events using the three-body mass as the discriminant variable. The fits include probability density functions (PDF) for the signal ($H/Z \to \phi/\rho^0\,\gamma$) and the background process, the normalisation of which is free to float in the fit. Systematic uncertainties described in Section 4.7 are introduced in the fit as nuisance parameters and are profiled during the minimisation with Gaussian constraints. The shape of the PDF of the background observables are also varied within alternatives ones, according to the effect of the background modelling systematic described in Section 4.6. The shape systematic uncertainties are implemented using the interpolation technique described in Ref. [129].

The signal distribution is modelled with a double Gaussian for the Higgs signals and a double Voigtian for the Z signal following the discussion in Section 4.5.9. While one signal (H or Z) is being measured the other is free and is profiled in the fit.

The fit and limit setting is performed in the inclusive region as tests with the fit in separate categories yielded little to no benefit.

4.9.2 Statistical Interpretation

A likelihood function $\mathcal{L}$ that depends on the parameter of interest μ (the branching ratio) is constructed using the signal and background models defined above.

The statistical procedure used to interpret the data is described in Refs. [130, 131]. The confidence intervals (CL) are based on the profile likelihood ratio $\Lambda(\mu)$ that depends on the parameter of interest μ and on the nuisance parameters θ :

$$\Lambda(\mu) = \frac{L\Big(\mu, \hat{\hat{\theta}}(\mu)\Big)}{L(\hat{\mu}, \hat{\theta})} \tag{4.5}$$

The likelihood fit to the data is then performed for the parameters of interest; $\hat{\hat{\theta}}$ corresponds to the value of θ which maximises $\mathcal{L}$ for the specified μ, $\hat{\mu}$ denotes the unconditional maximum likelihood estimate of the parameters of interest, i.e. where the likelihood is maximised for both θ and μ. Due to technical reasons the actual computation performed is the minimisation on the negative of this function.

4.9.3 $\phi\gamma$ Sensitivity

The expected and observed 95% CL upper limits in the branching ratio are presented.

The pre-fit expected limits are presented in Table 4.13.

Table 4.13: Pre-fit expected branching fraction limit at 95% CL. The limits are estimated with no systematic uncertainties, with normalisation-only systematic uncertainties, and the complete normalisation and shape systematic uncertainties.

	Expected	$\pm1\sigma$	$\pm2\sigma$
	Higgs 10^{-3}		
No systematics	0.363	0.262/0.508	0.195/0.688
Norm	0.370	0.266/0.523	0.198/0.727
Shape+Norm	0.372	0.268/0.527	0.200/0.732
	Z 10^{-6}		
No systematics	1.153	0.831/1.609	0.619/2.172
Norm	1.165	0.839/1.637	0.625/2.242
Shape+Norm	1.298	0.936/1.804	0.697/2.454

4.9.4 $\rho^0\gamma$ Sensitivity

The expected sensitivity is summarised in Table 4.14.

Table 4.14: Pre-fit expected branching fraction limit at 95% CL. The limits are estimated with no systematics profiled in the fit as well as including the normalisation-only systematics and finally also including the shape morphing systematics.

	Expected	$\pm 1\sigma$	$\pm 2\sigma$
		Higgs 10^{-3}	
No systematics	0.825	0.594/1.149	0.443/1.548
Norm	0.834	0.601/1.168	0.447/1.595
Shape+Norm	0.911	0.656/1.369	0.489/1.781
		Z 10^{-5}	
No systematics	2.574	1.855/3.583	1.382/4.826
Norm	2.601	1.874/3.646	1.396/4.985
Shape+Norm	3.383	2.437/5.334	1.816/6.814

4.9.5 $\phi\gamma$ Fit Results and Limits

Following the unblinding approval this section summarises the obtained results. In Table 4.15 the results of the fully unblinded fit are presented for background only, and signal plus background fit. The final signal strength parameter for the Higgs signal is 0.1 ± 0.2 which is compatible with 0, the final signal strength for the Z boson signal was -0.7 ± 0.6 indicating a minor deficit of events.

Table 4.15: The resulting parameters from the background only (Background) and full signal and background (S+B) fit for the $\phi\gamma$ dataset

	Background		S+B	
Parameter	Value	Error	Value	Error
alpha_HZ_Lumi	0.00	1	0	1
alpha_H_PDF_Scale	0.00	1	0	1
alpha_H_QCD_Scale	0.00	1	0	1
alpha_Reco_ID_mu	0.00	1	0	1
alpha_Reco_ID_ph	0.00	1	0	1
alpha_Trigger	0.00	1	0	1
alpha_Z_xSec	0.00	1	0	1
alpha_backgroundShape_DITRACKPT_INC	0.5	0.2	0.5	0.3
alpha_backgroundShape_DPHI_INC	-1.1	0.9	-1	1
alpha_backgroundShape_TILT_INC	-0.09	0.07	-0.06	0.07
mu_Mix_KDE_INC	0.993	0.009	1.00	0.01
mu_H1S	-	-	0.1	0.2
mu_Z1S	-	-	-0.7	0.6

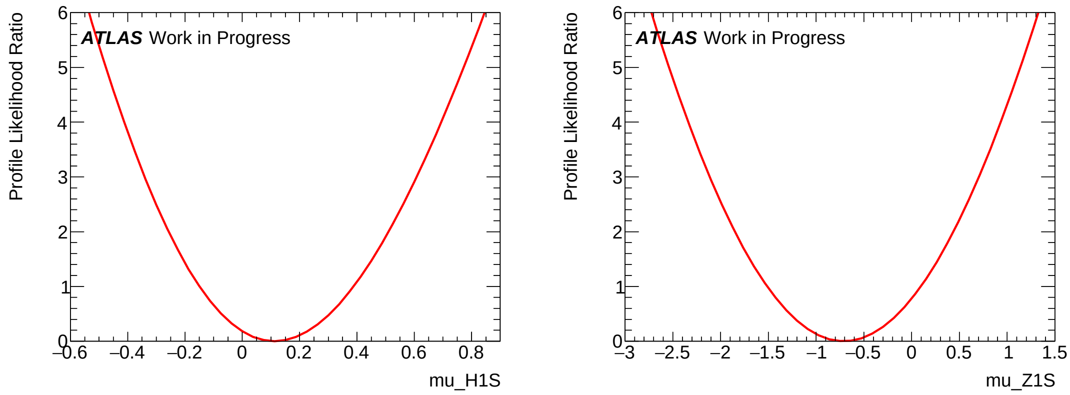

Figure 4.31: Profile likelihood ratio for both signal parameters for interest; `mu_H1S` for the Higgs boson signal and `mu_Z1S` for the Z boson signal.

The obtained 95% CL upper limits are shown in Table 4.16. Corresponding observed (expected) limits on cross-section times branching ratio for the Higgs boson are 25.3 fb (22.3 fb). Performing the limit setting procedure on the unblinded data then yields both the observed limit and the post-fit expectation based on the background fit to the data in the signal region. The resulting profile likelihood ratio for both signal parameters of interest can be seen in Figure 4.31.

Table 4.16: Post-fit branching fraction limit at 95% CL for the $\phi\gamma$ analysis.

	Observed	Expected	$\pm 1\sigma$	$\pm 2\sigma$
Higgs 10^{-3}	0.481	0.424	0.227/0.610	0.227/0.798
Z 10^{-6}	0.896	1.319	0.950/1.893	0.708/2.499

4.9.6 $\rho^0\gamma$ Fit Results and Limits

Below the Signal+Background and Background-only fit results are presented. In Table 4.17 the Background-only and signal plus background fits to the data are presented. The final signal strength parameter for the Higgs signal and Z boson signals are 0.0 ± 0.6 and -1 ± 5 respectively, both of which are is compatible with 0. The resulting profile likelihood ratio for both signal parameters of interest can be seen in Figure 4.32.

In Table 4.18 the post-fit expected and observed limits are shown. Corresponding limits on the observed (expected) cross-section times branching ratio for the Higgs boson are 45.5 fb (48.1 fb).

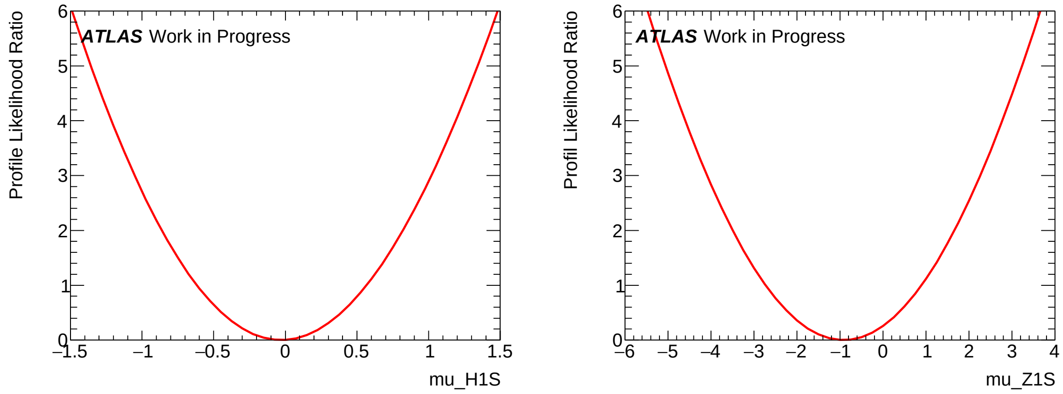

Figure 4.32: Profile likelihood ratio for both signal parameters for interest; `mu_H1S` for the Higgs boson signal and `mu_Z1S` for the Z boson signal.

Table 4.17: The resulting parameters from the background only (Background) and full signal and background (S+B) fit for the $\rho^0\gamma$ dataset

	Background		S+B	
Parameter	Value	Error	Value	Error
alpha_HZ_Lumi	0	1	0	1
alpha_H_PDF_Scale	0	1	0	1
alpha_H_QCD_Scale	0	1	0	1
alpha_Reco_ID_mu	0	1	0	1
alpha_Reco_ID_ph	0	1	0	1
alpha_Trigger	0	1	0	1
alpha_Z_xSec	0	1	0	1
alpha_backgroundShape_DITRACKPT_INC	0.6	0.1	1	1
alpha_backgroundShape_DPHI_INC	-2.4	0.5	-2	6
alpha_backgroundShape_TILT_INC	0.01	0.02	0.01	0.07
mu_Mix_KDE_INC	0.935	0.004	0.936	0.005
mu_H1S	-	-	0.0	0.6
mu_Z1S	-	-	-1	5

Table 4.18: Branching fraction limit at 95% CL for the $\rho^0\gamma$ analysis.

	Observed	Expected	$\pm 1\sigma$	$\pm 2\sigma$
Higgs 10^{-3}	0.875	0.843	0.608/1.253	0.453/1.667
Z 10^{-6}	25.14	32.44	23.38/45.52	17.41/57.53

4.10 Conclusion

This chapter presents the search with the ATLAS detector for the rare decays of the Higgs and Z bosons to a meson and a photon, specifically $\phi\gamma$ and $\rho^0\gamma$. Limits were set on the relevant branching ratios at 95% confidence levels and are given in Table 4.19.

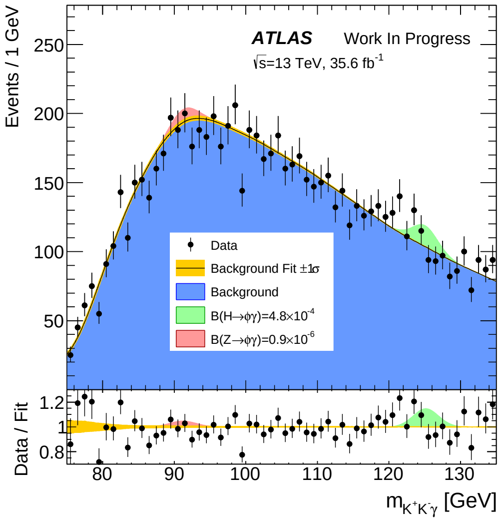

(a)

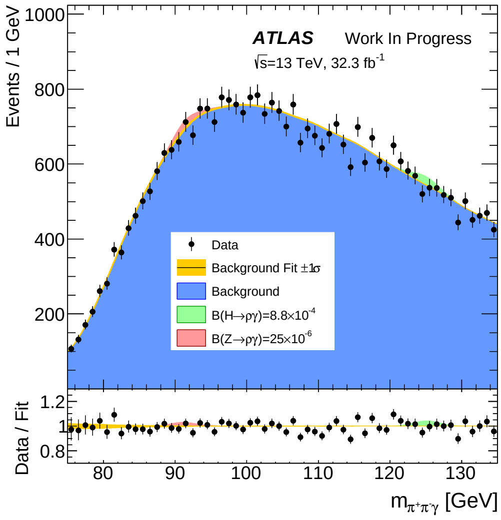

(b)

Figure 4.33: The $m_{K^+K^-\gamma}$ and $m_{\pi^+\pi^-\gamma}$ distributions of the selected $\phi\gamma$ and $\rho^0\gamma$ candidates, respectively, along with the results of the maximum-likelihood fit with a background-only model. The Higgs and Z boson contributions for the branching fraction values corresponding to the observed 95% CL upper limits are also shown. Below the figures the ratio of the data and the background only fit is shown.

Table 4.19: Expected and observed branching fraction upper limits at 95% CL for the $\phi\gamma$ and $\rho^0\gamma$ analyses. The $\pm 1\sigma$ intervals of the expected limits are also given.

Branching Fraction Limit (95% CL)	Expected	Observed
$\mathcal{B}\,(H \to \phi\gamma)\,[\,10^{-4}\,]$	$4.2^{+1.8}_{-1.2}$	4.8
$\mathcal{B}\,(Z \to \phi\gamma)\,[\,10^{-6}\,]$	$1.3^{+0.6}_{-0.4}$	0.9
$\mathcal{B}\,(H \to \rho^0\gamma)\,[\,10^{-4}\,]$	$8.4^{+4.1}_{-2.4}$	8.8
$\mathcal{B}\,(Z \to \rho^0\gamma)\,[\,10^{-6}\,]$	33^{+13}_{-9}	25

Chapter 5

Conclusion

In 2015 the LHC came out of its first long shutdown. During this period several improvements were made to the ATLAS detector to enable it to maintain and improve its operational performance.

The updated L1Calo trigger architecture means that the thresholds for single electron triggers which are essential for many analyses within the collaboration can remain low such that a wide range of physics can be explored at the electroweak scale.

Using the first data recorded after the long shutdown a measurement was made of the cross-sections of the electroweak W and Z bosons, which provided the first measurements of these quantities at the new centre-of-mass energy of $\sqrt{s} = 13$ TeV and a data-driven "sanity check" of the post-shutdown performance of the detector. The total inclusive W-boson production cross-sections times the leptonic branching ratios are $\sigma^{tot}_{W^+} = 11.83 \pm 0.02\ \text{(stat)}\ \pm 0.32\ \text{(syst)}\ \pm 0.25\ \text{(lumi)}$ nb and $\sigma^{tot}_{W^-} = 8.79 \pm 0.02\ \text{(stat)}\ \pm 0.24\ \text{(syst)}\ \pm 0.18\ \text{(lumi)}$ nb, while total inclusive Z-boson production cross-section times the charged leptonic branching ratio within the invariant mass window $66 < m_{\ell\ell} < 116$ GeV is $\sigma^{tot}_{Z} = 1.981 \pm 0.007\ \text{(stat)}\ \pm 0.038\ \text{(syst)}\ \pm 0.042\ \text{(lumi)}$ nb.

The Higgs boson and the exact nature of its interactions with fermions is an area of the standard model which is devoid of many existing constraints. The searches for the Higgs boson decaying to a meson and a photon exploit an interesting topology to trigger events at Level-1 using the optimised L1Calo triggers and then perform a more exacting selection in the HLT to produce a dedicated trigger with a manageable rate. These analyses then have the power to set direct limits on the previously unobserved couplings between the

Higgs boson and the light quarks. Branching ratio 95% confidence level limits were set at $\mathcal{B}(H \to \phi\gamma) < 4.8 \times 10^{-4}$ and $\mathcal{B}(H \to \rho^0\gamma) < 8.8 \times 10^{-4}$, which are compatible with the expectation given the SM prediction for the branching ratios.

The current plan for the LHC foresees a high luminosity upgrade culminating in total dataset of $3000\,\mathrm{fb}^{-1}$. Without any change in the centre-of-mass energies this factor of ≈ 100 increase in luminosity should lead to a factor of ≈ 10 improvement in the limits being set. Without further improvements in the analysis techniques this would leave the $\phi\gamma$ limits still an order of magnitude from the most recent standard model prediction of $\mathcal{B}(H \to \phi\gamma) = (2.31 \pm 0.11) \times 10^{-6}$, however the $\rho\gamma$ limit will naturally get very close to the prediction of $\mathcal{B}(H \to \rho\gamma) = (1.68 \pm 0.08) \times 10^{-5}$ [35].

Chapter 6

Bibliography

[1] ATLAS Collaboration, *Measurement of $W^{\pm}$ and Z-boson production cross sections in pp collisions at $\sqrt{s} = 13$ TeV with the ATLAS detector*, Phys. Lett. **B759** (2016) 601–621, arXiv: 1603.09222 [hep-ex].

[2] ATLAS Collaboration, *Search for Higgs and Z Boson Decays to $\phi\gamma$ with the ATLAS Detector*, Phys. Rev. Lett. **117**.11 (2016) 111802, arXiv: 1607.03400 [hep-ex].

[3] ATLAS Collaboration, *Search for exclusive Higgs and Z boson decays to $\phi\gamma$ and $\rho\gamma$ with the ATLAS Detector*, ATLAS-CONF-2017-057 (2017), URL: https://cds.cern.ch/record/2273873.

[4] ATLAS Collaboration, *Observation of a new particle in the search for the standard model Higgs boson with the ATLAS detector at the LHC*, Phys. Lett. B **716** (2012) 1–29, arXiv: 1207.7214 [hep-ex].

[5] CMS Collaboration, *Observation of a new boson at a mass of 125 GeV with the CMS experiment at the LHC*, Phys. Lett. B **716** (2012) 30–61, arXiv: 1207.7235 [hep-ex].

[6] Nobelprize.org, URL: https://www.nobelprize.org/nobel_prizes/physics/laureates/2013/ (visited on 05/09/2017).

[7] MissMJ et al., *Standard model of elementary particles: the 12 fundamental fermions and 4 fundamental bosons.* 27th June 2006, URL: https://commons.wikimedia.org/wiki/File:Standard_Model_of_Elementary_Particles.svg (visited on 05/09/2017).

[8] D. H. Perkins, *Introduction to high energy physics*, 1982, ISBN: 9780521621960.

[9] C. Gwenlan, *Combined HERA deep inelastic scattering data and NLO QCD fits*, Nuclear Physics B - Proceedings Supplements **191** (2009) 5 –15, Proceedings of the Ringberg Workshop, ISSN: 0920-5632, URL: http://www.sciencedirect.com/science/article/pii/S0920563209003612.

[10] F. Halzen et al., *Quarks and Leptons: An Introductory Course In Modern Particle Physics*, 1984, ISBN: 0471887412, 9780471887416.

[11] M. D. Schwartz, *Quantum Field Theory and the Standard Model*, Cambridge University Press, 2014, ISBN: 1107034736, 9781107034730, URL: http://www.cambridge.org/us/academic/subjects/physics/theoretical-physics-and-mathematical-physics/quantum-field-theory-and-standard-model.

[12] RupertMillard, *Mexican hat potential polar*, 11th Sept. 2011, URL: https://commons.wikimedia.org/wiki/File:Mexican_hat_potential_polar.svg (visited on 06/09/2017).

[13] LHC Higgs Cross Section Working Group, *Handbook of LHC Higgs Cross Sections: 4. Deciphering the Nature of the Higgs Sector* (2016), arXiv: 1610.07922 [hep-ph].

[14] LHC Higgs Cross Section Working Group et al., *Handbook of LHC Higgs Cross Sections: 3. Higgs Properties*, CERN-2013-004 (CERN, Geneva, 2013), arXiv: 1307.1347 [hep-ph].

[15] ATLAS Collaboration, *Combined measurements of Higgs boson production and decay in the $H \to ZZ^* \to 4\ell$ and $H \to \gamma\gamma$ channels using $\sqrt{s} =$ 13 TeV pp collision data collected with the ATLAS experiment*, ATLAS-CONF-2017-047 (2017), URL: http://cds.cern.ch/record/2273854.

[16] ATLAS Collaboration, *Measurement of the Higgs boson mass in the $H \to ZZ^* \to 4\ell$ and $H \to \gamma\gamma$ channels with $\sqrt{s}$=13TeV pp collisions using the ATLAS detector*, ATLAS-CONF-2017-046 (2017), URL: http://cds.cern.ch/record/2273853.

[17] CMS Collaboration, *The CMS Experiment at the CERN LHC*, JINST **3** (2008) S08004.

[18] A. M. Sirunyan et al., *Measurements of properties of the Higgs boson decaying into the four-lepton final state in pp collisions at sqrt(s) = 13 TeV* (2017), arXiv: 1706.09936 [hep-ex].

[19] ATLAS and CMS Collaborations, *Combined Measurement of the Higgs Boson Mass in pp Collisions at $\sqrt{s} = 7$ and 8 TeV with the ATLAS and CMS Experiments*, Phys. Rev. Lett. **114** (2015) 191803, arXiv: 1503.07589 [hep-ex].

[20] ATLAS Collaboration, *Evidence for the Higgs-boson Yukawa coupling to tau leptons with the ATLAS detector*, JHEP **04** (2015) 117, arXiv: 1501.04943 [hep-ex].

[21] ATLAS Collaboration, *Evidence for the $H \to b\bar{b}$ decay with the ATLAS detector* (2017), arXiv: 1708.03299 [hep-ex].

[22] G. D'Ambrosio et al., *Minimal flavor violation: An Effective field theory approach*, Nucl. Phys. **B645** (2002) 155–187, arXiv: hep-ph/0207036.

[23] C. D. Froggatt et al., *Hierarchy of Quark Masses, Cabibbo Angles and CP Violation*, Nucl. Phys. **B147** (1979) 277–298.

[24] G. F. Giudice et al., *Higgs-dependent Yukawa couplings*, Phys. Lett. B **665** (2008) 79–85, arXiv: 0804.1753 [hep-ph].

[25] L. Randall et al., *A Large mass hierarchy from a small extra dimension*, Phys. Rev. Lett. **83** (1999) 3370–3373, arXiv: hep-ph/9905221.

[26] M. J. Dugan et al., *Anatomy of a Composite Higgs Model*, Nucl. Phys. **B254** (1985) 299.

[27] ATLAS Collaboration, *Search for the dimuon decay of the Higgs boson in pp collisions at $\sqrt{s} =$ 13 TeV with the ATLAS detector*, Phys. Rev. Lett. **119**.5 (2017) 051802, arXiv: 1705.04582 [hep-ex].

[28] M. Doroshenko et al., *Vector quarkonium in decays of heavy Higgs particles*, Yad. Fiz. **46** (1987) 864–868.

[29] G. T. Bodwin et al., *Higgs boson decays to quarkonia and the $H\bar{c}c$ coupling*, Phys.Rev. **D88**.5 (2013) 053003, arXiv: 1306.5770 [hep-ph].

[30] G. T. Bodwin et al., *Relativistic corrections to Higgs-boson decays to quarkonia*, Phys. Rev. D **90** (2014) 113010, arXiv: 1407.6695 [hep-ph].

[31] ATLAS Collaboration, *Search for Higgs and Z Boson Decays to $J/\psi\,\gamma$ and $\Upsilon(nS)\,\gamma$ with the ATLAS Detector*, Phys. Rev. Lett. **114**.12 (2015) 121801, arXiv: 1501.03276 [hep-ex].

[32] CMS Collaboration, *Search for a Higgs boson decaying into $\gamma^*\gamma \rightarrow \ell\ell\gamma$ with low dilepton mass in pp collisions at $\sqrt{s}$ = 8 TeV*, Phys. Lett. **B753** (2016) 341–362, arXiv: 1507.03031 [hep-ex].

[33] R. Contino et al., *Physics at a 100 TeV pp collider: Higgs and EW symmetry breaking studies* (2016), arXiv: 1606.09408 [hep-ph].

[34] A. L. Kagan et al., *Exclusive Window onto Higgs Yukawa Couplings*, Phys. Rev. Lett. **114**.10 (2015) 101802, arXiv: 1406.1722 [hep-ph].

[35] M. König et al., *Exclusive Radiative Higgs Decays as Probes of Light-Quark Yukawa Couplings*, JHEP **08** (2015) 012.

[36] G. Perez et al., *Prospects for measuring the Higgs boson coupling to light quarks*, Phys. Rev. **D93**.1 (2016) 013001, arXiv: 1505.06689 [hep-ph].

[37] L. Evans et al., *LHC Machine*, JINST **3** (2008) S08001.

[38] M. Lamont, *Status of the LHC*, J. Phys. Conf. Ser. **455** (2013) 012001.

[39] E. Todesco et al., *Large Hadron Collider momentum calibration and accuracy*, Phys. Rev. Accel. Beams **20**.8 (2017) 081003.

[40] C. Pralavorio, *2016: an exceptional year for the LHC* (2016), URL: https://cds.cern.ch/record/2240055.

[41] ATLAS Collaboration, *The ATLAS Experiment at the CERN Large Hadron Collider*, Journal of Instrumentation **3**.08 (Aug. 2008) S08003–S08003, ISSN: 1748-0221, URL: http://stacks.iop.org/1748-0221/3/i=08/a=S08003.

[42] J Pequenao, *Computer generated image of the whole ATLAS detector*, 2008, URL: https://cds.cern.ch/record/1095924/ (visited on 21/04/2013).

[43] E. Abat et al., *The ATLAS TRT barrel detector*, JINST **3** (2008) P02014.

[44] X. Artru et al., *Practical Theory of the Multilayered Transition Radiation Detector*, Phys. Rev. **D12** (1975) 1289.

[45] D Adams et al., *The ATLAS Computing Model*, ATL-SOFT-2004-007. ATL-COM-SOFT-2004-009. CERN-ATL-COM-SOFT-2004-009. CERN-LHCC-2004-037-G-085 (2004), URL: https://cds.cern.ch/record/811058.

[46] I. Antcheva et al., *ROOT: A C++ framework for petabyte data storage, statistical analysis and visualization*, Comput. Phys. Commun. **180** (2009) 2499–2512, arXiv: 1508.07749.

[47] M. Clemencic et al., *Recent developments in the LHCb software framework Gaudi*, J. Phys. Conf. Ser. **219** (2010) 042006.

[48] LHCb Collaboration, *The LHCb Detector at the LHC*, JINST **3** (2008) S08005.

[49] S. Silverstein, *The digital algorithm processors for the ATLAS Level-1 Calorimeter Trigger*, **46**.0 (May 2009) 334–342, URL: http://ieeexplore.ieee.org/xpl/articleDetails.jsp?arnumber=5321731.

[50] E. Eisenhandler, *ATLAS Level-1 Calorimeter Trigger Algorithms*, CERN Document Server September 2004 (2004) 1–8, URL: http://inspirehep.net/record/1196395.

[51] R. Staley et al., *ATLAS Level-1 Calorimeter Trigger Firmware Upgrade of Cluster Processor Module Project Specification*, August (2014) 1–35, URL: http://epweb2.ph.bham.ac.uk/user/bracinik/CPMPhase0/.

[52] ATLAS Collaboration, *Level-1 EM isolation optimization for 2017 data taking*, 20th May 2017, URL: https://twiki.cern.ch/twiki/bin/view/AtlasPublic/EgammaTriggerPublicResults#Level_1_EM_isolation_optimizatio (visited on 24/09/2017).

[53] T. Cornelissen et al., *The new ATLAS track reconstruction (NEWT)*, J. Phys. Conf. Ser. **119** (2008) 032014.

[54] ATLAS Collaboration, *Early Inner Detector Tracking Performance in the 2015 data at $\sqrt{s}$ = 13 TeV*, ATL-PHYS-PUB-2015-051 (2015), URL: http://cds.cern.ch/record/2110140.

[55] ATLAS Collaboration, *Performance of the ATLAS Track Reconstruction Algorithms in Dense Environments in LHC run 2* (2017), arXiv: 1704.07983 [hep-ex].

[56] ATLAS Collaboration, *Electron efficiency measurements with the ATLAS detector using the 2015 LHC proton-proton collision data*, ATLAS-CONF-2016-024 (2016), URL: https://cds.cern.ch/record/2157687.

[57] ATLAS Collaboration, *Photon identification in 2015 ATLAS data*, ATL-PHYS-PUB-2016-014 (2016), URL: https://cds.cern.ch/record/2203125.

[58] ATLAS Collaboration, *Muon reconstruction performance of the ATLAS detector in proton–proton collision data at $\sqrt{s}$ =13 TeV*, Eur. Phys. J. **C76**.5 (2016) 292, arXiv: 1603.05598 [hep-ex].

[59] ATLAS Collaboration, *Performance of missing transverse momentum reconstruction for the ATLAS detector in the first proton-proton collisions at at $\sqrt{s}$= 13 TeV*, ATL-PHYS-PUB-2015-027 (2015), URL: https://cds.cern.ch/record/2037904.

[60] ATLAS Collaboration, *Proposal for truth particle observable definitions in physics measurements*, ATL-PHYS-PUB-2015-013 (2015), URL: https://cds.cern.ch/record/2022743.

[61] ATLAS Collaboration, *Improved luminosity determination in pp collisions at $\sqrt{s}$ = 7 TeV using the ATLAS detector at the LHC*, Eur. Phys. J. C **73** (2013) 2518, arXiv: 1302.4393 [hep-ex].

[62] O. Viazlo, *ATLAS LUCID detector upgrade for LHC Run 2*, PoS **EPS-HEP2015** (2015) 275.

[63] ATLAS Collaboration, *Validation of Monte Carlo event generators in the ATLAS Collaboration for LHC Run 2*, ATL-PHYS-PUB-2016-001 (2016), URL: https://cds.cern.ch/record/2119984.

[64] ATLAS Collaboration, *Monte Carlo Generators for the Production of a W or Z/γ^* Boson in Association with Jets at ATLAS in Run 2*, ATL-PHYS-PUB-2016-003 (2016), URL: https://cds.cern.ch/record/2120133.

[65] P. Nason, *A New method for combining NLO QCD with shower Monte Carlo algorithms*, JHEP **11** (2004) 040, arXiv: hep-ph/0409146 [hep-ph].

[66] S. Frixione et al., *Matching NLO QCD computations with Parton Shower simulations: the POWHEG method*, JHEP **11** (2007) 070, arXiv: 0709.2092 [hep-ph].

[67] S. Alioli et al., *A general framework for implementing NLO calculations in shower Monte Carlo programs: the POWHEG BOX*, JHEP **06** (2010) 043, arXiv: 1002.2581 [hep-ph].

[68] S. Alioli et al., *NLO vector-boson production matched with shower in POWHEG*, JHEP **0807** (2008) 060, arXiv: 0805.4802 [hep-ph].

[69] T. Sjostrand et al., *A Brief Introduction to PYTHIA 8.1*, Comput. Phys. Commun. **178** (2008) 852–867, arXiv: 0710.3820 [hep-ph].

[70] H.-L. Lai et al., *New parton distributions for collider physics*, Phys. Rev. **D82** (2010) 074024, arXiv: 1007.2241 [hep-ph].

[71] ATLAS Collaboration, *Measurement of the Z/γ^* boson transverse momentum distribution in pp collisions at $\sqrt{s} = 7$ TeV with the ATLAS detector*, JHEP **1409** (2014) 145, arXiv: 1406.3660 [hep-ex].

[72] D. J. Lange, *The EvtGen particle decay simulation package*, Nucl. Instrum. Meth. **A462** (2001) 152.

[73] N. Davidson et al., *PHOTOS Interface in C++: Technical and Physics Documentation* (2010), arXiv: 1011.0937 [hep-ph].

[74] C. Anastasiou et al., *High precision QCD at hadron colliders: Electroweak gauge boson rapidity distributions at NNLO*, Phys. Rev. **D69** (2004) 094008, arXiv: hep-ph/0312266 [hep-ph].

[75] A. D. Martin et al., *Parton distributions for the LHC*, Eur. Phys. J. **C63** (2009) 189–285, arXiv: 0901.0002 [hep-ph].

[76] S. Frixione et al., *A Positive-weight next-to-leading-order Monte Carlo for heavy flavour hadroproduction*, JHEP **0709** (2007) 126, arXiv: 0707.3088 [hep-ph].

[77] T. Sjostrand et al., *PYTHIA 6.4 Physics and Manual*, JHEP **05** (2006) 026, arXiv: hep-ph/0603175 [hep-ph].

[78] M. Czakon et al., *Top++: A Program for the Calculation of the Top-Pair Cross-Section at Hadron Colliders*, Comput. Phys. Commun. **185** (2014) 2930, arXiv: 1112.5675 [hep-ph].

[79] ATLAS Collaboration, *Comparison of Monte Carlo generator predictions to ATLAS measurements of top pair production at 7 TeV*, ATL-PHYS-PUB-2015-02, 2015, URL: https://cds.cern.ch/record/1981319.

[80] ATLAS Collaboration, *Summary of ATLAS Pythia 8 tunes*, ATLAS-PHYS-PUB-2012-003, 2012, URL: http://cdsweb.cern.ch/record/1474107.

[81] S. Agostinelli et al., *GEANT4: A Simulation toolkit*, Nucl. Instrum. Meth. **A506** (2003) 250–303.

[82] ATLAS Collaboration, *The ATLAS Simulation Infrastructure*, Eur. Phys. J. C **70** (2010) 823, arXiv: 1005.4568 [hep-ex].

[83] T. Gleisberg et al., *Event generation with SHERPA 1.1*, JHEP **02** (2009) 007, arXiv: 0811.4622 [hep-ph].

[84] ATLAS Collaboration, *Reconstruction of primary vertices at the ATLAS experiment in Run 1 proton-proton collisions at the LHC*, Eur. Phys. J. **C77**.5 (2017) 332, arXiv: 1611.10235 [physics.ins-det].

[85] ATLAS Collaboration, *Data-Quality Requirements and Event Cleaning for Jets and Missing Transverse Energy Reconstruction with the ATLAS Detector in Proton-Proton Collisions at a Center-of-Mass Energy of sqrts = 7 TeV*, ATLAS-CONF-2010-038 (2010), URL: `https://cds.cern.ch/record/1277678`.

[86] F. James et al., *Minuit: A System for Function Minimization and Analysis of the Parameter Errors and Correlations*, Comput. Phys. Commun. **10** (1975) 343–367.

[87] ATLAS Collaboration, *Precision measurement and interpretation of inclusive W^+, W^- and Z/γ^* production cross sections with the ATLAS detector*, Eur. Phys. J. **C77**.6 (2017) 367, arXiv: `1612.03016 [hep-ex]`.

[88] ATLAS Collaboration, *Jet Calibration and Systematic Uncertainties for Jets Reconstructed in the ATLAS Detector at $\sqrt{s} = 13$ TeV*, ATL-PHYS-PUB-2015-015 (2015), URL: `https://cds.cern.ch/record/2037613`.

[89] S. Catani et al., *An NNLO subtraction formalism in hadron collisions and its application to Higgs boson production at the LHC*, Phys. Rev. Lett. **98** (2007) 222002, arXiv: `hep-ph/0703012 [hep-ph]`.

[90] K. Melnikov et al., *Electroweak gauge boson production at hadron colliders through $\mathcal{O}(\alpha_s^2)$*, Phys. Rev. D **74** (2006) 114017, arXiv: `hep-ph/0609070 [hep-ph]`.

[91] R. Gavin et al., *FEWZ 2.0: A code for hadronic Z production at next-to-next-to-leading order*, Comput. Phys. Commun. **182** (2011) 2388, arXiv: `1011.3540 [hep-ph]`.

[92] R. Gavin et al., *W Physics at the LHC with FEWZ 2.1*, Comput. Phys. Commun. **184** (2013) 208, arXiv: `1201.5896 [hep-ph]`.

[93] Y. Li et al., *Combining QCD and electroweak corrections to dilepton production in FEWZ*, Phys. Rev. D **86** (2012) 094034, arXiv: `1208.5967 [hep-ph]`.

[94] J. Gao et al., *CT10 next-to-next-to-leading order global analysis of QCD*, Phys. Rev. **D89**.3 (2014) 033009, arXiv: `1302.6246 [hep-ph]`.

[95] ATLAS Collaboration, *Measurement of the inclusive $W^\pm$ and Z/gamma cross sections in the electron and muon decay channels in pp collisions at $\sqrt{s} = 7$ TeV with the ATLAS detector*, Phys. Rev. **D85** (2012) 072004, arXiv: `1109.5141 [hep-ex]`.

[96] G. Abbiendi et al., *Precise determination of the Z resonance parameters at LEP: 'Zedometry'*, Eur. Phys. J. **C19** (2001) 587–651, arXiv: `hep-ex/0012018 [hep-ex]`.

[97] P. Abreu et al., *Cross-sections and leptonic forward backward asymmetries from the Z0 running of LEP*, Eur. Phys. J. **C16** (2000) 371–405.

[98] M. Acciarri et al., *Measurements of cross-sections and forward backward asymmetries at the Z resonance and determination of electroweak parameters*, Eur. Phys. J. **C16** (2000) 1–40, arXiv: `hep-ex/0002046 [hep-ex]`.

[99] R. Barate et al., *Measurement of the Z resonance parameters at LEP*, Eur. Phys. J. **C14** (2000) 1–50.

[100] CMS Collaboration, *Measurement of inclusive W and Z boson production cross sections in pp collisions at $\sqrt{s} = 8$ TeV*, Phys. Rev. Lett. **112** (2014) 191802, arXiv: `1402.0923 [hep-ex]`.

[101] C. Patrignani et al., *Review of Particle Physics*, Chin. Phys. **C40**.10 (2016) 100001.

[102] A. Glazov, *Averaging of DIS cross section data*, AIP Conf. Proc. **792** (2005) 237–240, [,237(2005)].

[103] F. D. Aaron et al., *Measurement of the Inclusive ep Scattering Cross Section at Low Q^2 and x at HERA*, Eur. Phys. J. **C63** (2009) 625–678, arXiv: `0904.0929 [hep-ex]`.

[104] CMS Collaboration, *Measurement of the Inclusive W and Z Production Cross Sections in pp Collisions at $\sqrt{s} = 7$ TeV*, JHEP **10** (2011) 132, arXiv: `1107.4789 [hep-ex]`.

[105] J. Rojo et al., *The PDF4LHC report on PDFs and LHC data: Results from Run I and preparation for Run II* (2015), arXiv: `1507.00556 [hep-ph]`.

[106] D. Bardin et al., *SANC integrator in the progress: QCD and EW contributions*, JETP Lett. **96** (2012) 285–289, arXiv: `1207.4400 [hep-ph]`.

[107] A. Arbuzov et al., *QED Bremsstrahlung in decays of electroweak bosons* (2012), arXiv: `1212.6783 [hep-ph]`.

[108] W. F. L. Hollik, *Radiative Corrections in the Standard Model and their Role for Precision Tests of the Electroweak Theory*, Fortsch. Phys. **38** (1990) 165–260.

[109] K. A. Olive et al., *Review of Particle Physics*, Chin. Phys. **C38** (2014) 090001.

[110] S. Dittmaier et al., *Radiative corrections to the neutral-current Drell-Yan process in the Standard Model and its minimal supersymmetric extension*, JHEP **01** (2010) 060, arXiv: `0911.2329 [hep-ph]`.

[111] S. Dulat et al., *The CT14 Global Analysis of Quantum Chromodynamics* (2015), arXiv: `1506.07443 [hep-ph]`.

[112] R. D. Ball et al., *Parton distributions for the LHC Run II*, JHEP **04** (2015) 040, arXiv: `1410.8849 [hep-ph]`.

[113] L. A. Harland-Lang et al., *Parton distributions in the LHC era: MMHT 2014 PDFs*, Eur. Phys. J. **C75**.5 (2015) 204, arXiv: `1412.3989 [hep-ph]`.

[114] S. Alekhin et al., *The ABM parton distributions tuned to LHC data*, Phys. Rev. **D89**.5 (2014) 054028, arXiv: `1310.3059 [hep-ph]`.

[115] H. Abramowicz et al., *Combination of measurements of inclusive deep inelastic $e^{\pm}p$ scattering cross sections and QCD analysis of HERA data*, Eur. Phys. J. **C75**.12 (2015) 580, arXiv: `1506.06042 [hep-ex]`.

[116] ATLAS Collaboration, *Determination of the strange quark density of the proton from ATLAS measurements of the $W \to \ell\nu$ and $Z \to \ell\ell$ cross sections*, Phys. Rev. Lett. **109** (2012) 012001, arXiv: `1203.4051 [hep-ex]`.

[117] T.-C. Huang et al., *Rare exclusive decays of the Z-boson revisited*, Phys. Rev. **D92**.1 (2015) 014007, arXiv: `1411.5924 [hep-ph]`.

[118] Y. Grossman et al., *Exclusive Radiative Decays of W and Z Bosons in QCD Factorization*, JHEP **1504** (2015) 101.

[119] DELPHI Collaboration, *Measurement of the $e^+e^- \to \gamma\gamma(\gamma)$ cross-section at LEP energies*, Phys. Lett. **B327** (1994) 386–396.

[120] ATLAS Collaboration, *Luminosity determination in pp collisions at $\sqrt{s} = 8$ TeV using the ATLAS detector at the LHC*, Eur. Phys. J. **C76**.12 (2016) 653, arXiv: `1608.03953 [hep-ex]`.

[121] S. Alioli et al., *NLO Higgs boson production via gluon fusion matched with shower in POWHEG*, JHEP **04** (2009) 002, arXiv: `0812.0578 [hep-ph]`.

[122] P. Nason et al., *NLO Higgs boson production via vector-boson fusion matched with shower in POWHEG*, JHEP **02** (2010) 037, arXiv: 0911.5299 [hep-ph].

[123] T. Sjostrand et al., *PYTHIA 6.4 Physics and Manual*, JHEP **05** (2006) 026, arXiv: hep-ph/0603175.

[124] R. Kutschke, *An Angular Distribution Cookbook*, 18th Jan. 1996, URL: http://home.fnal.gov/~kutschke/Angdist/angdist.ps (visited on 19/09/2017).

[125] CMS Collaboration, *Study of Final-State Radiation in Decays of Z Bosons Produced in pp Collisions at 7 TeV*, Phys. Rev. **D91**.9 (2015) 092012, arXiv: 1502.07940 [hep-ex].

[126] LHC Higgs cross section working group et al., *Handbook of LHC Higgs cross sections: 1. Inclusive observables*, CERN-2011-002 (2011), arXiv: 1101.0593 [hep-ph].

[127] LHC Higgs cross section working group et al., *Handbook of LHC Higgs Cross Sections: 2. Differential distributions*, CERN-2012-002 (2012), arXiv: 1201.3084 [hep-ph].

[128] J. Beringer et al., *Review of Particle Physics (RPP)*, Phys. Rev. **D86** (2012) 010001.

[129] M. Baak et al., *Interpolation between multi-dimensional histograms using a new non-linear moment morphing method* (2014), arXiv: 1410.7388 [physics.data-an].

[130] ATLAS Collaboration, *Combined search for the Standard Model Higgs boson in pp collisions at $\sqrt{s}$=7 TeV with the ATLAS detector*, Phys. Rev. **D 86** (2012) 032003, arXiv: 1207.0319 [hep-ex].

[131] G Cowan et al., *Asymptotic formulae for likelihood-based tests of new physics*, Eur. Phys. J. **C 71** (2011) 1554, arXiv: 1007.1727 [physics.data-an].

Appendix A

Charge Separated W Boson Kinematic Distributions

This appendix features additional kinematic distributions for the W cross-section measurements described in detail in Chapter 3. The distributions are presented for both the $W \to e\nu$ and $W \to \mu\nu$ cases but additionally separated by the charge of the lepton.

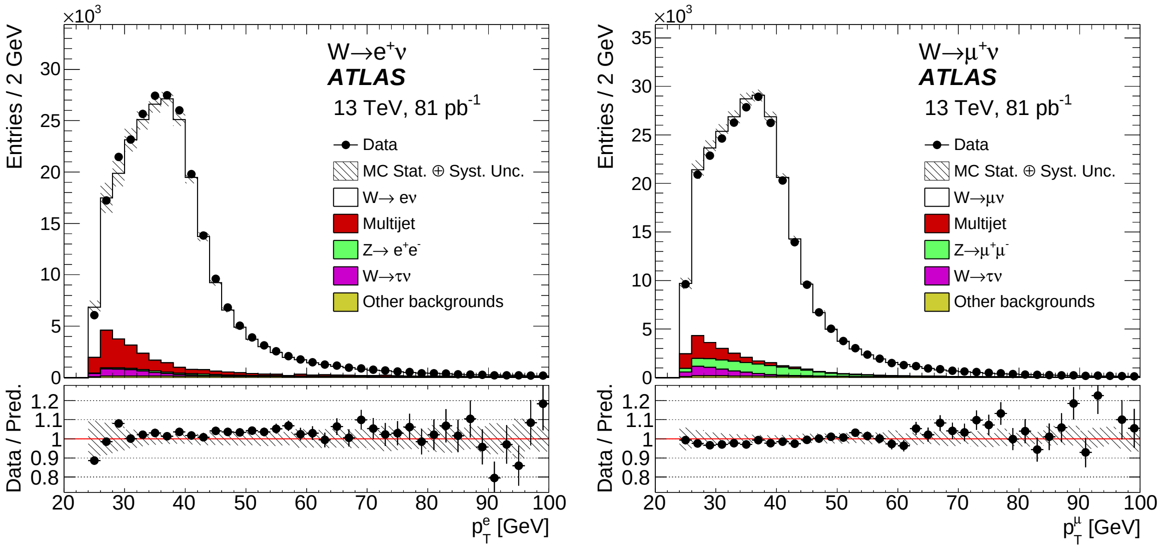

Figure A.1: Lepton transverse momentum distribution from the $W^+ \to e\nu$ selection (left) and the $W^+ \to \mu\nu$ selection (right).

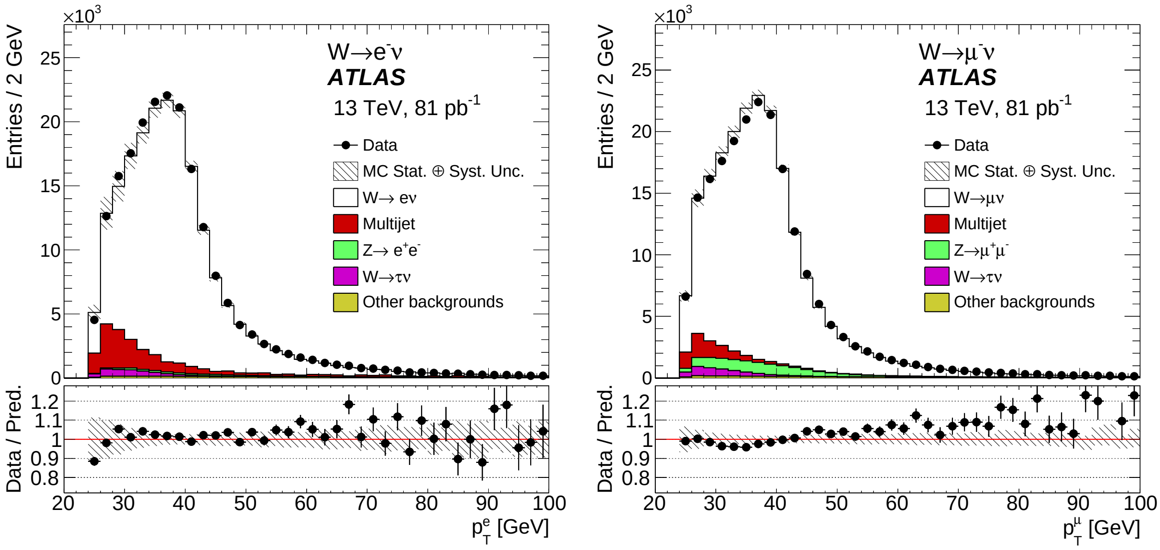

Figure A.2: Lepton transverse momentum distribution from the $W^- \to e\nu$ selection (left) and the $W^- \to \mu\nu$ selection (right).

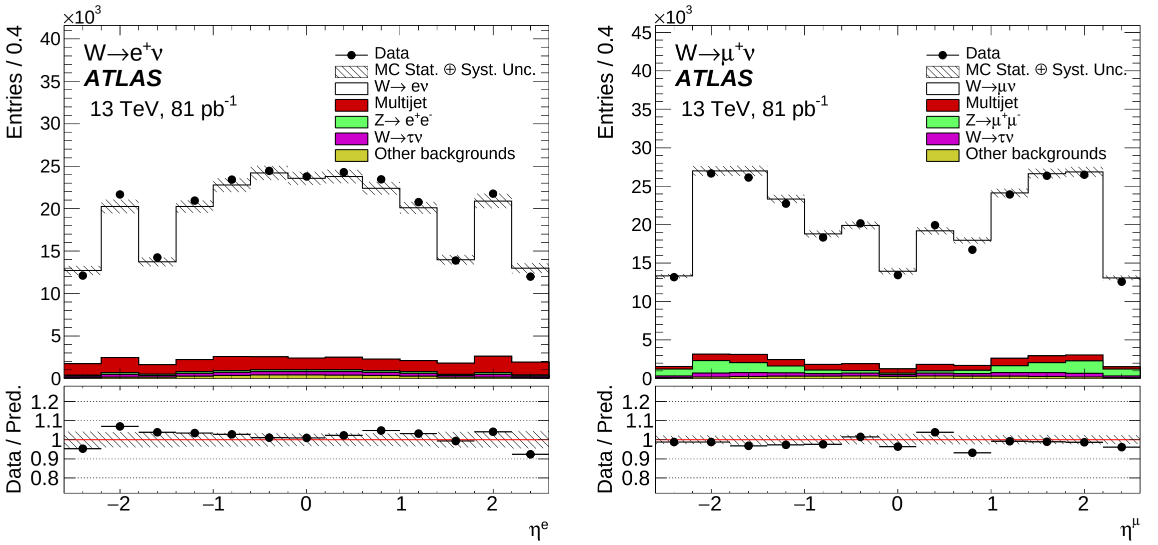

Figure A.3: Lepton pseudorapidity distribution from the $W^+ \to e\nu$ selection (left) and the $W^+ \to \mu\nu$ selection (right).

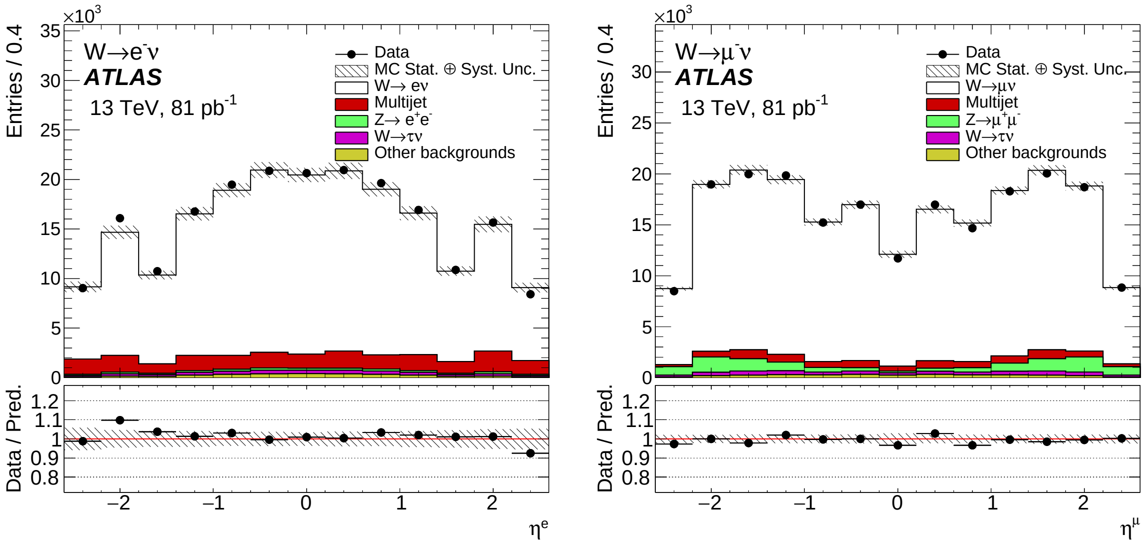

Figure A.4: Lepton pseudorapidity distribution from the $W^- \to e\nu$ selection (left) and the $W^- \to \mu\nu$ selection (right).

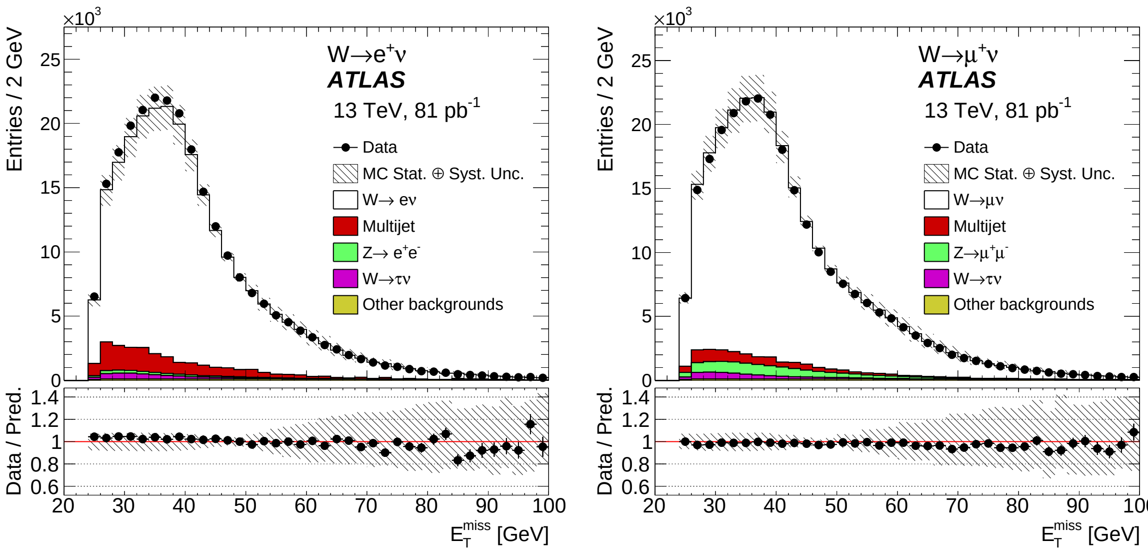

Figure A.5: Missing transverse energy distribution from the $W^+ \to e\nu$ selection (left) and the $W^+ \to \mu\nu$ selection (right).

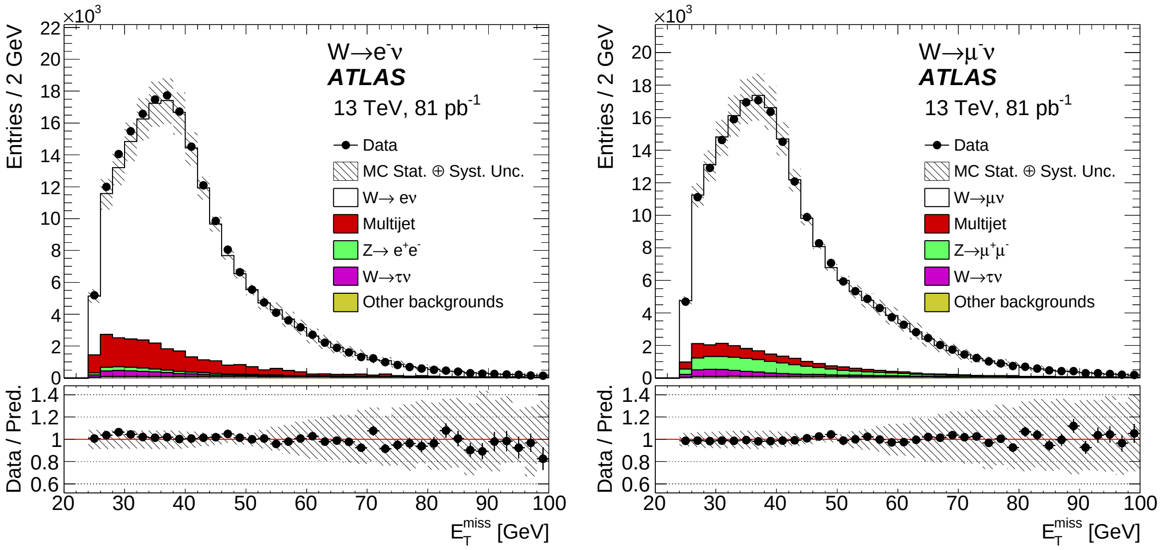

Figure A.6: Missing transverse energy distribution from the $W^- \to e\nu$ selection (left) and the $W^- \to \mu\nu$ selection (right).

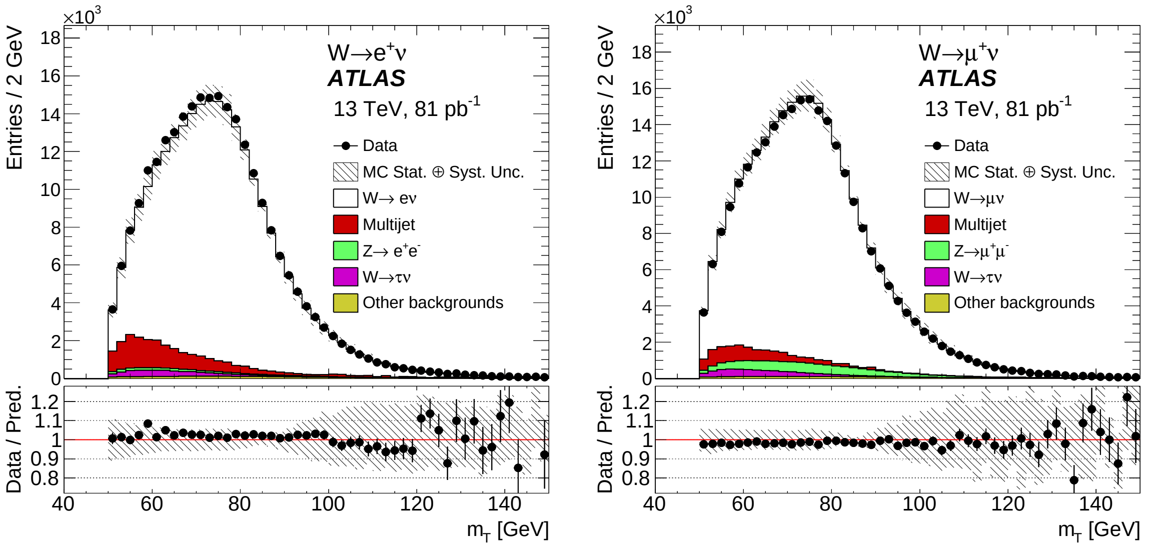

Figure A.7: Transverse mass distribution, calculated from the lepton and the $E_{\mathrm{T}}^{\mathrm{miss}}$ from the $W^+ \to e\nu$ selection (left) and the $W^+ \to \mu\nu$ selection (right).

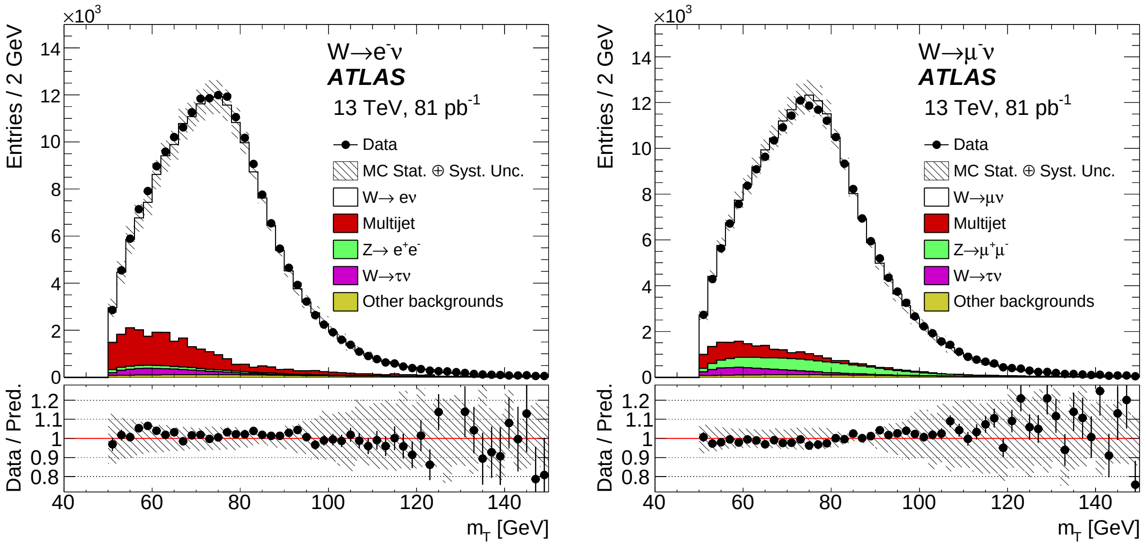

Figure A.8: Transverse mass distribution, calculated from the lepton and the $E_{\mathrm{T}}^{\mathrm{miss}}$ from the $W^- \to e\nu$ selection (left) and the $W^- \to \mu\nu$ selection (right).

Appendix B

Z Boson Kinematic Distributions

Following the desctiption in Section 3.5.2, these plots show the kinematic distributions for events falling in to the Z selection. They are presented seperately for the two considered lepton flavours.

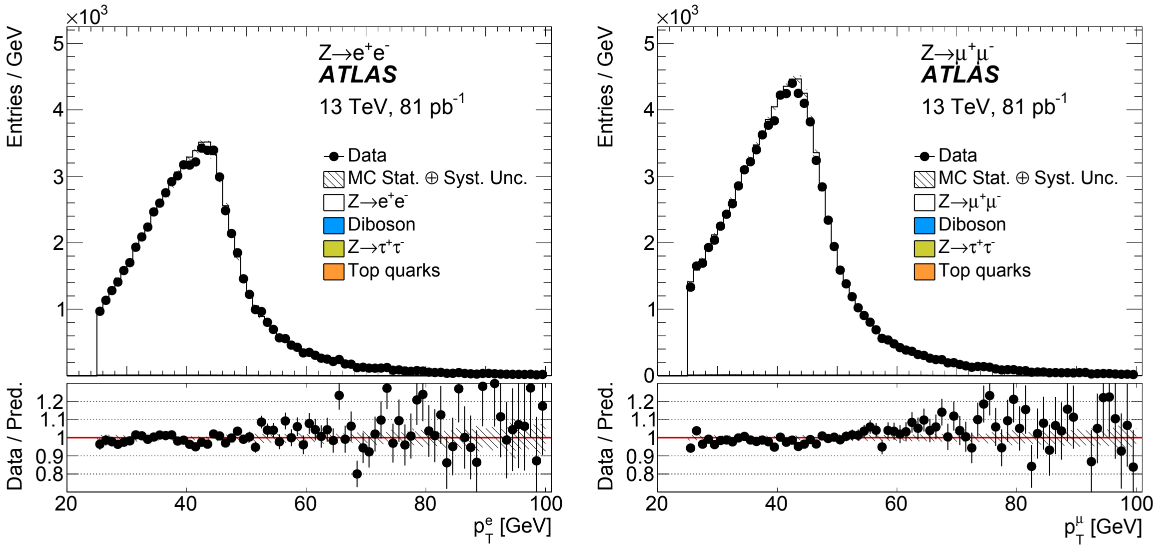

Figure B.1: Lepton transverse momentum distributions from the $Z \to e^+e^-$ selection (left) and the $Z \to \mu^+\mu^-$ selection (right).

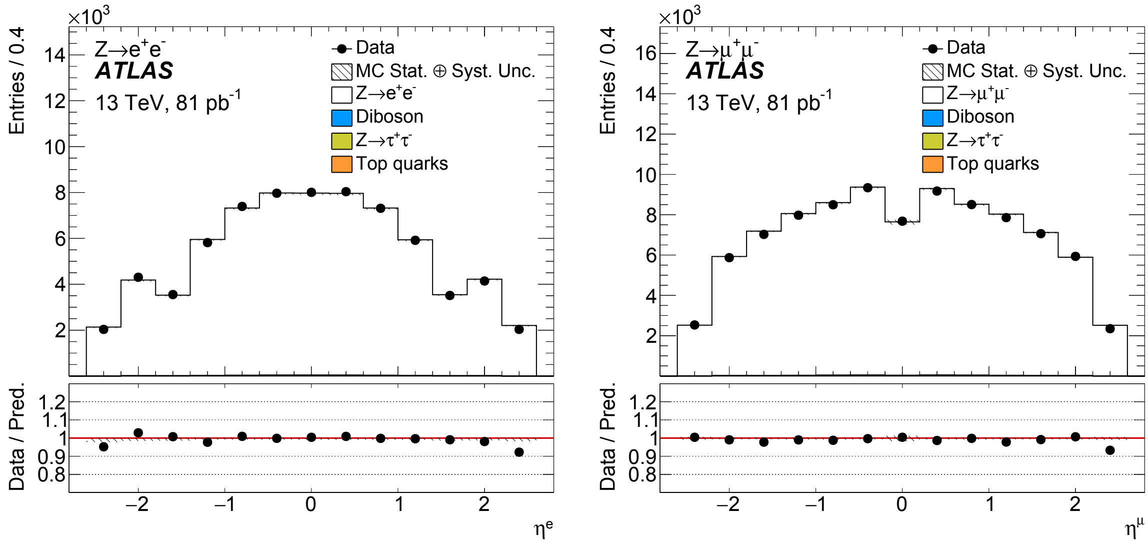

Figure B.2: Lepton pseudorapidity distribution from the $Z \to e^+e^-$ selection (left) and the $Z \to \mu^+\mu^-$ selection (right).

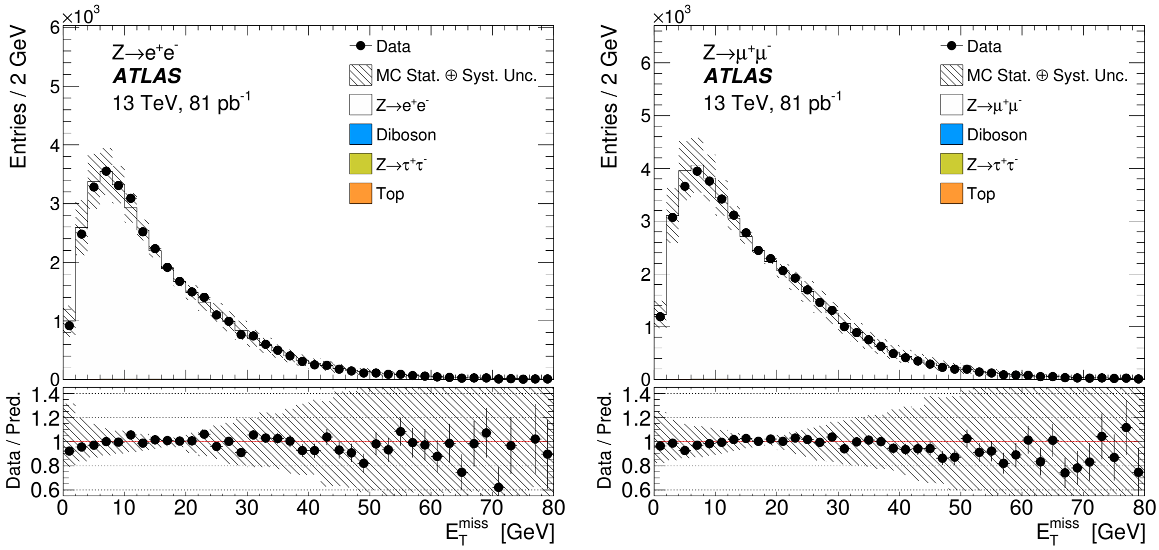

Figure B.3: Missing transverse energy distribution from the $Z \to e^+e^-$ selection (left) and the $Z \to \mu^+\mu^-$ selection (right).

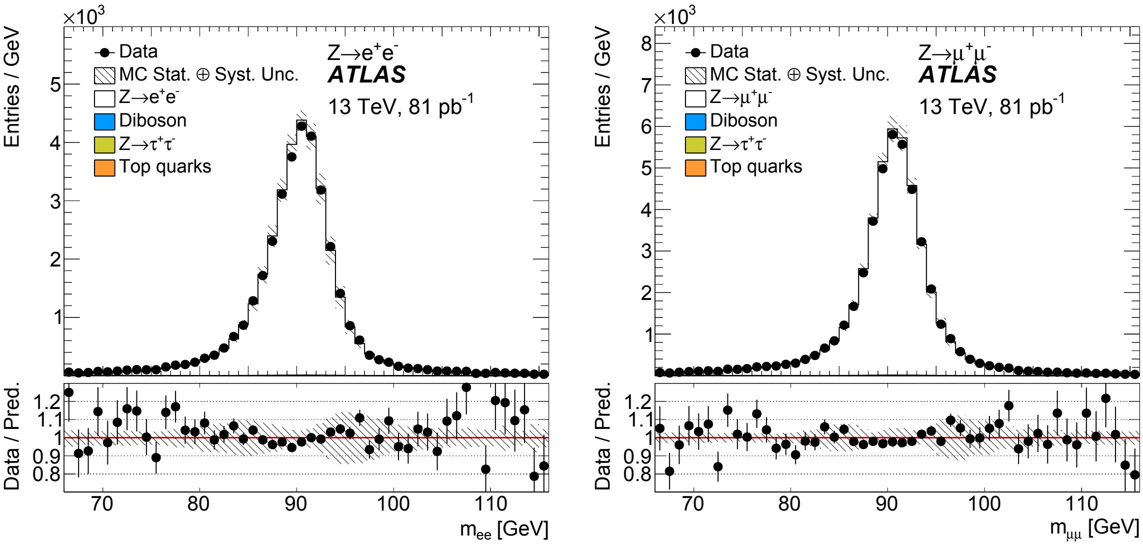

Figure B.4: Dilepton mass distribution after the $Z \to e^+e^-$ selection (left) and the $Z \to \mu^+\mu^-$ selection (right).

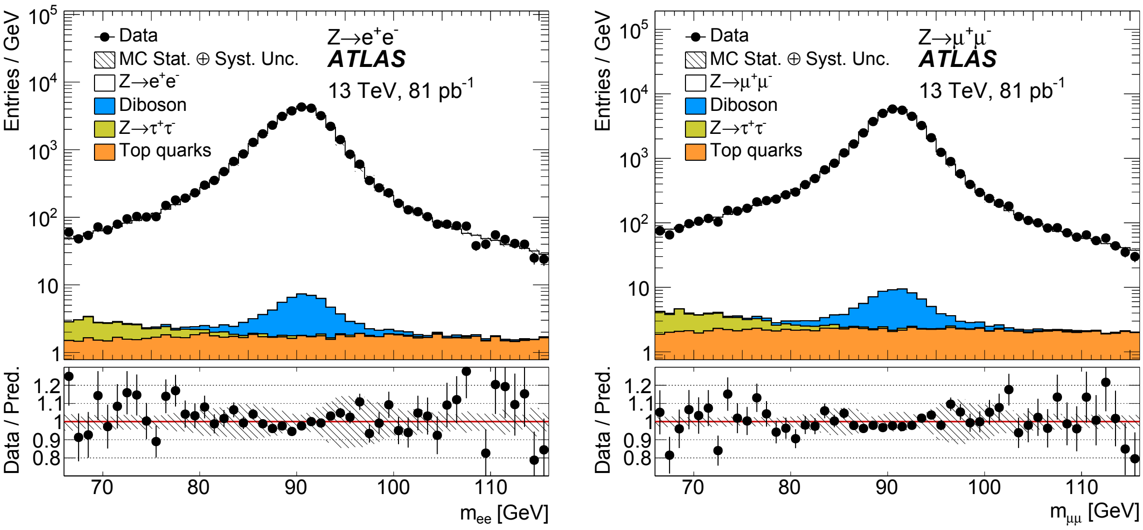

Figure B.5: Dilepton mass distribution after the $Z \to e^+e^-$ selection (left) and the $Z \to \mu^+\mu^-$ selection (right).

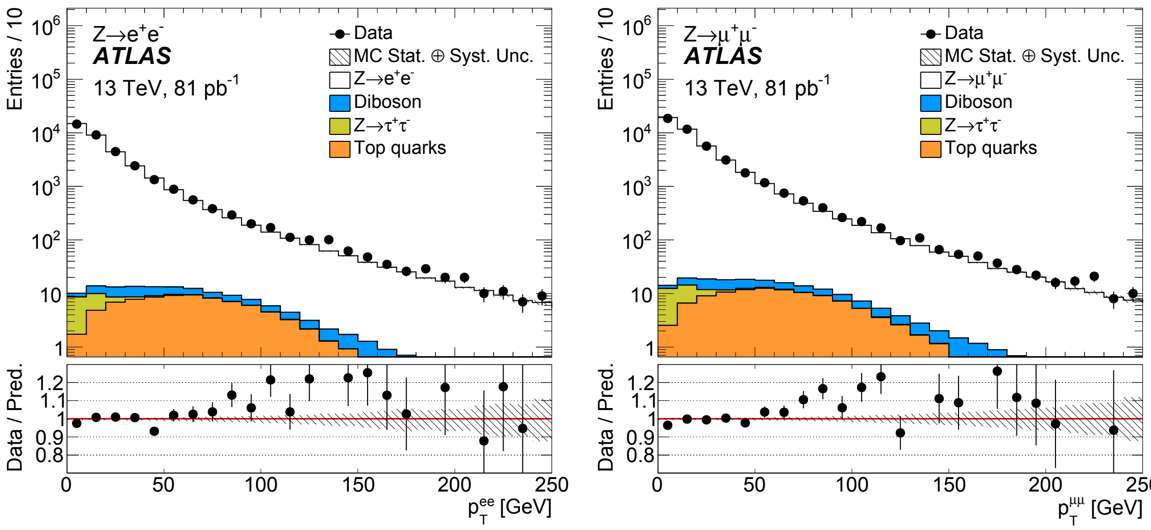

Figure B.6: Z boson transverse momentum distribution after the $Z \to e^+e^-$ selection (left) and the $Z \to \mu^+\mu^-$ selection (right).

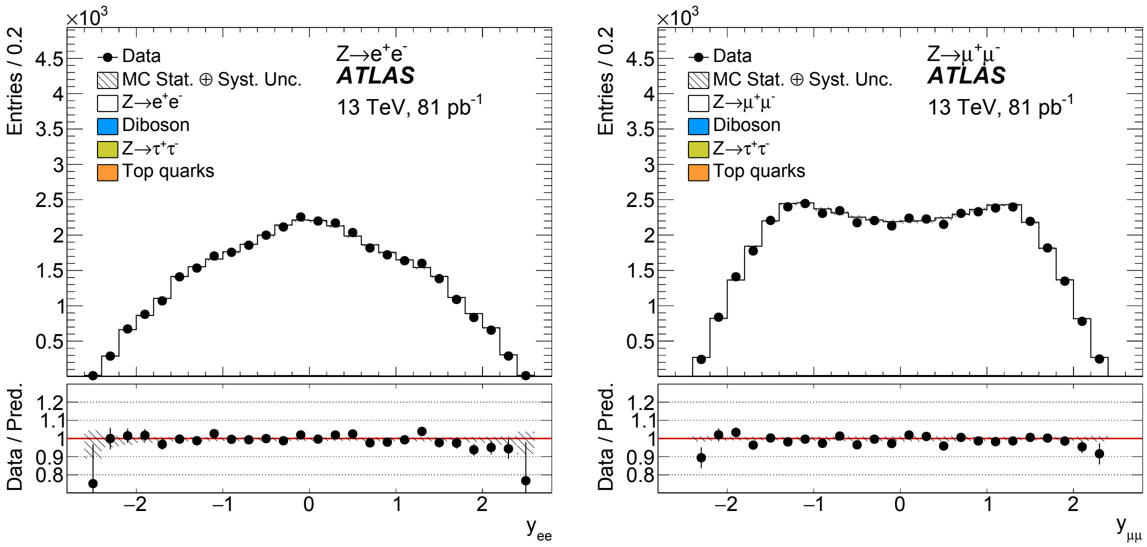

Figure B.7: Z boson rapidity distribution after the $Z \to e^+e^-$ selection (left) and the $Z \to \mu^+\mu^-$ selection (right).

Appendix C

$\phi\gamma$ Control Plots

During the development of the $\phi\gamma$ analysis it was necessary to generate several control plots in order to check the accuracy of the background model and to assess the impact of the selection criteria. The following appendix is split into sections based on the selection criteria for the events they contain (for details see Section 4.5). Each figure features a different kinematic variable or event property. The topmost large figure shows the inclusive distribution, whereas the smaller insets show the distributions where the events have been separated by the categories described in Section 4.5.8. The background component is represented by a binned histogram with the events normalised to the GR three-body mass distribution.

C.1 Control Plots in the GR

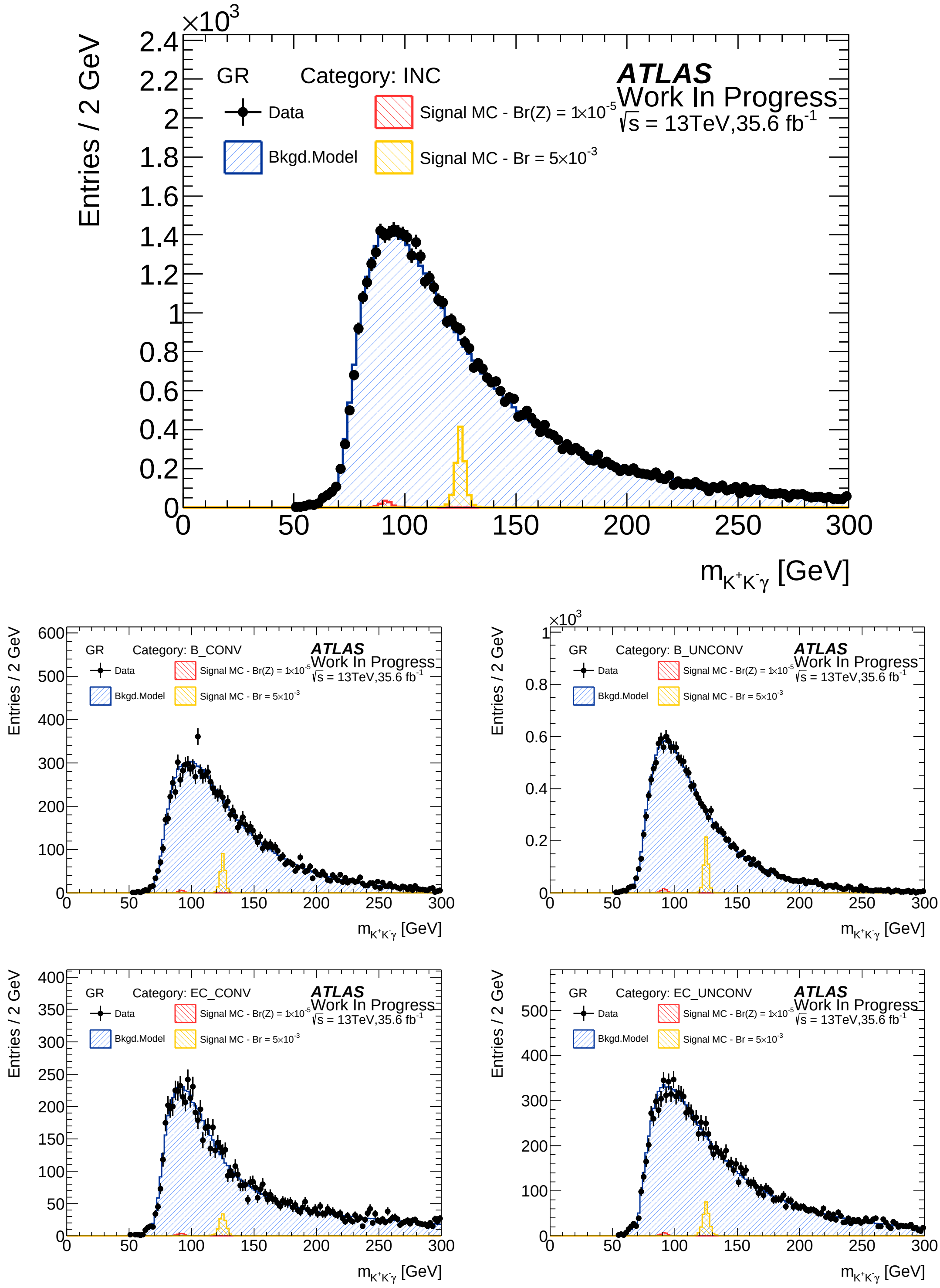

Figure C.1: $m_{K^+K^-\gamma}$ distribution for the four different categories and the inclusive.

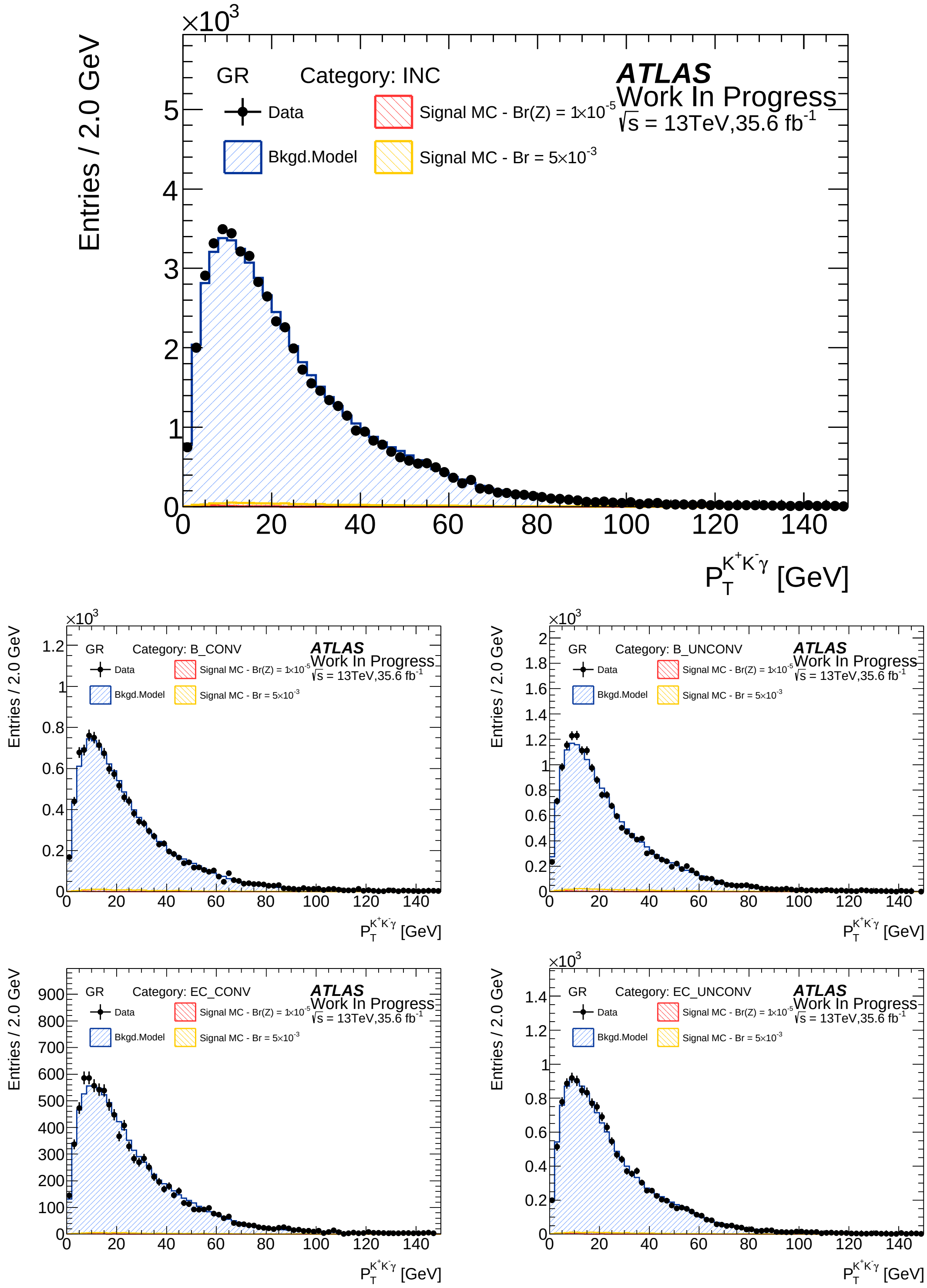

Figure C.2: $p_{\mathrm{T}}^{K^+K^-\gamma}$ distribution for the four different categories and the inclusive.

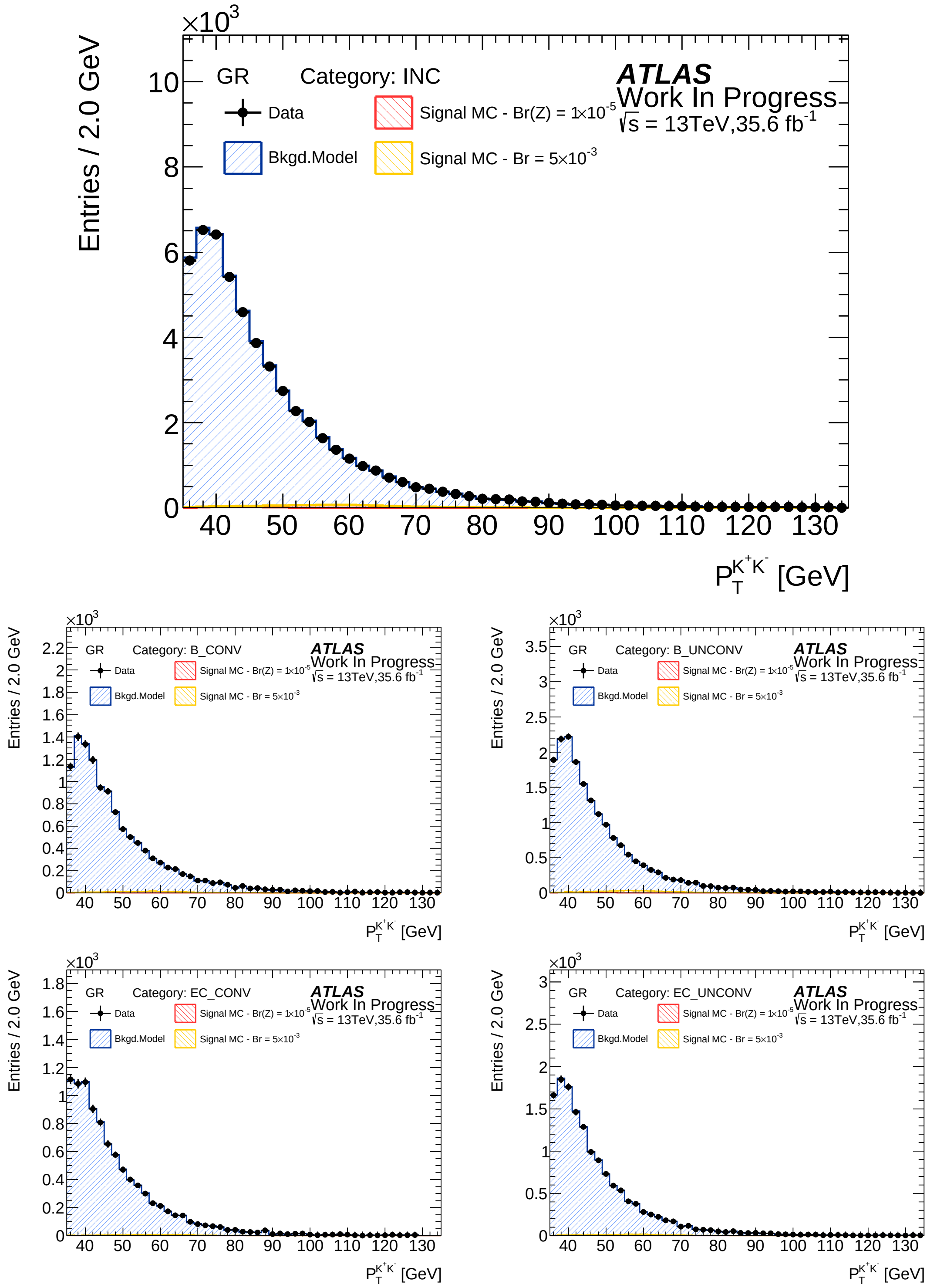

Figure C.3: $p_{\mathrm{T}}^{K^+K^-}$ distribution for the four different categories and the inclusive.

A small feature is observed in the p_{T}^{γ} control plot Fig C.4 around $\approx$ 60 GeV. This has been investigated further. The feature is most prominent in the converted photon categories and is further enhanced in the VR1 validation region, where the di-track p_{T} selection is added, as shown in Fig C.13. The feature is slightly enhanced by tightening the $\delta\phi$ requirement. Comparisons of the kinematic properties of these events with those of events in nearby p_{T} regions did not reveal any substantial differences. The current understanding is that this feature is due to a turn-on effect of back-to-back di-jet events entering the p_{T}^{γ} spectrum but which are subsequently suppressed in the signal region by the photon and di-track isolation requirements. The shift in turn-on between the di-track threshold of 45 GeV and the observed effect around 60 GeV is likely a result of the di-track and fake photon carrying different proportions of the p_{T} of the jets.

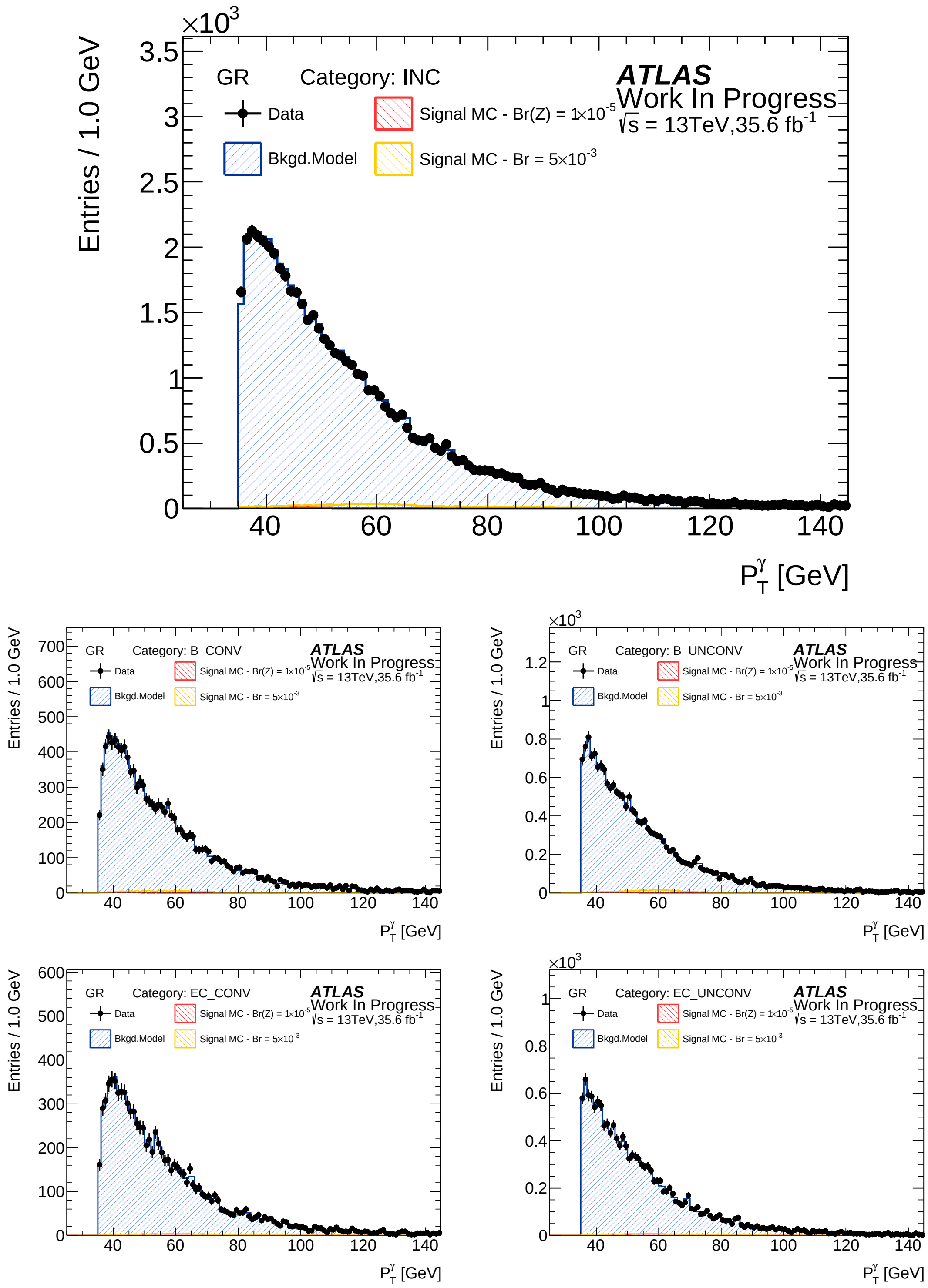

Figure C.4: p_{T}^{γ} distribution for the four different categories and the inclusive.

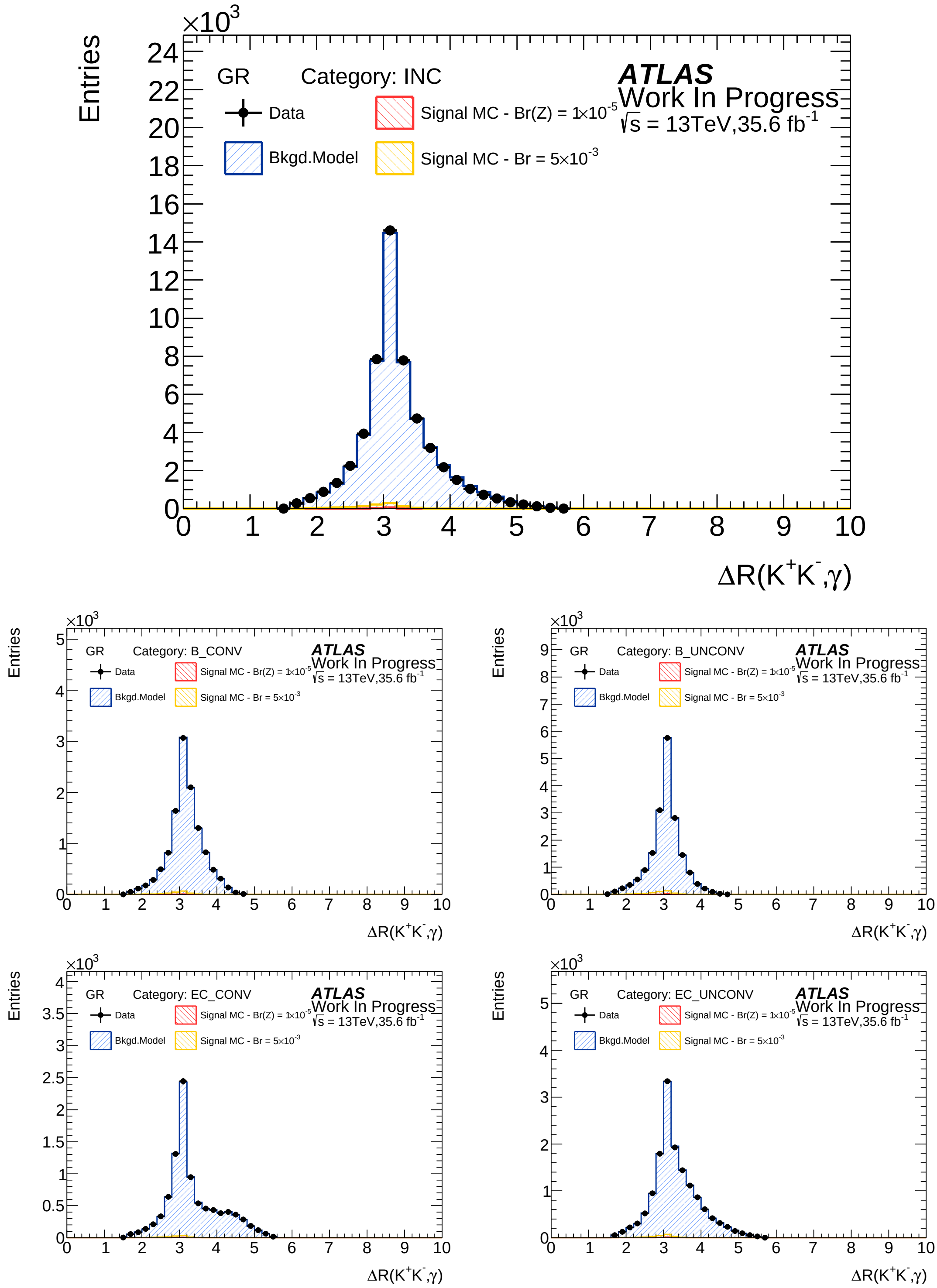

Figure C.5: $\Delta R^{K^+K^-,\gamma}$ distribution for the four different categories and the inclusive.

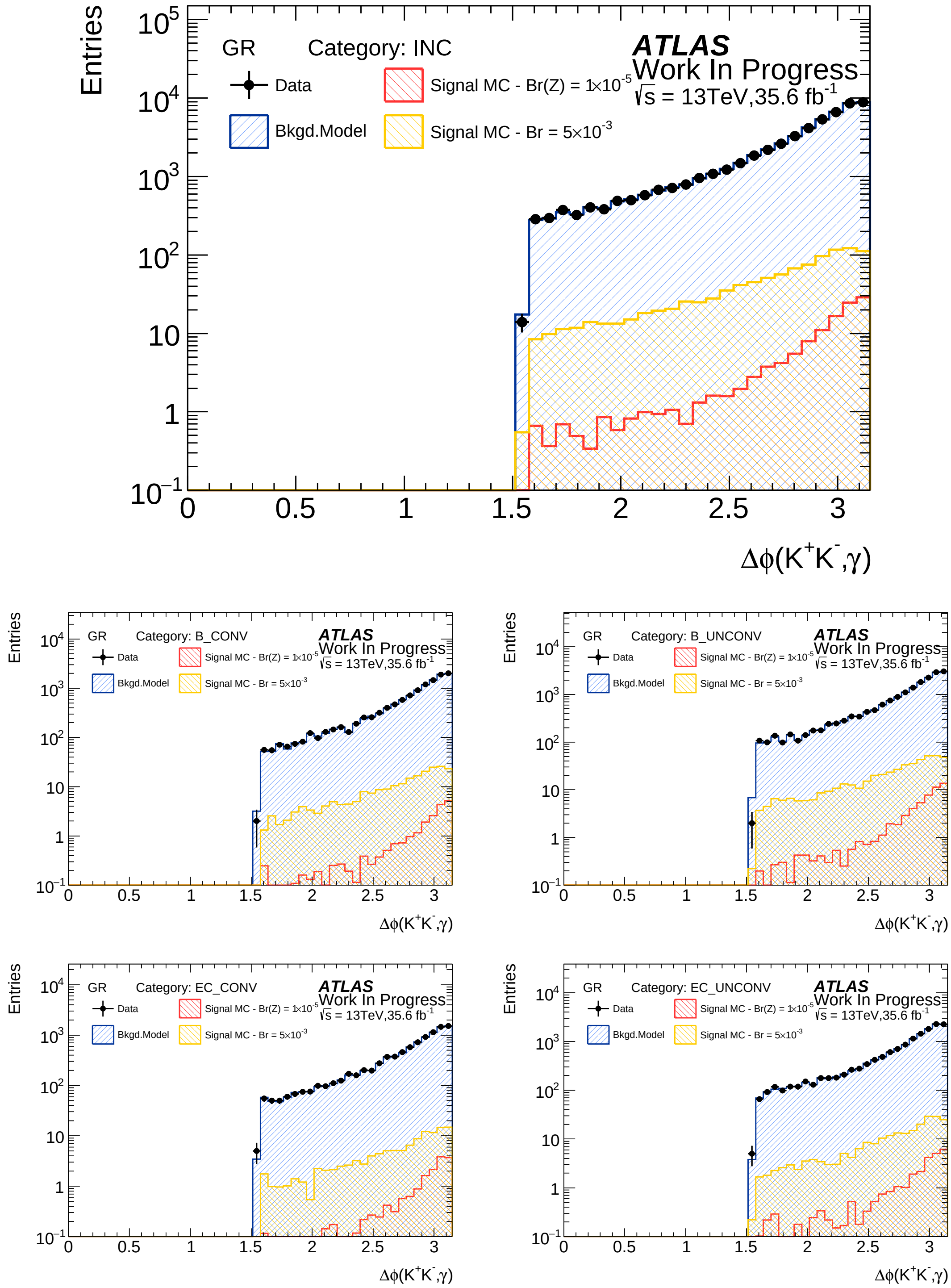

Figure C.6: $\Delta\phi^{K^+K^-,\gamma}$ distribution for the four different categories and the inclusive.

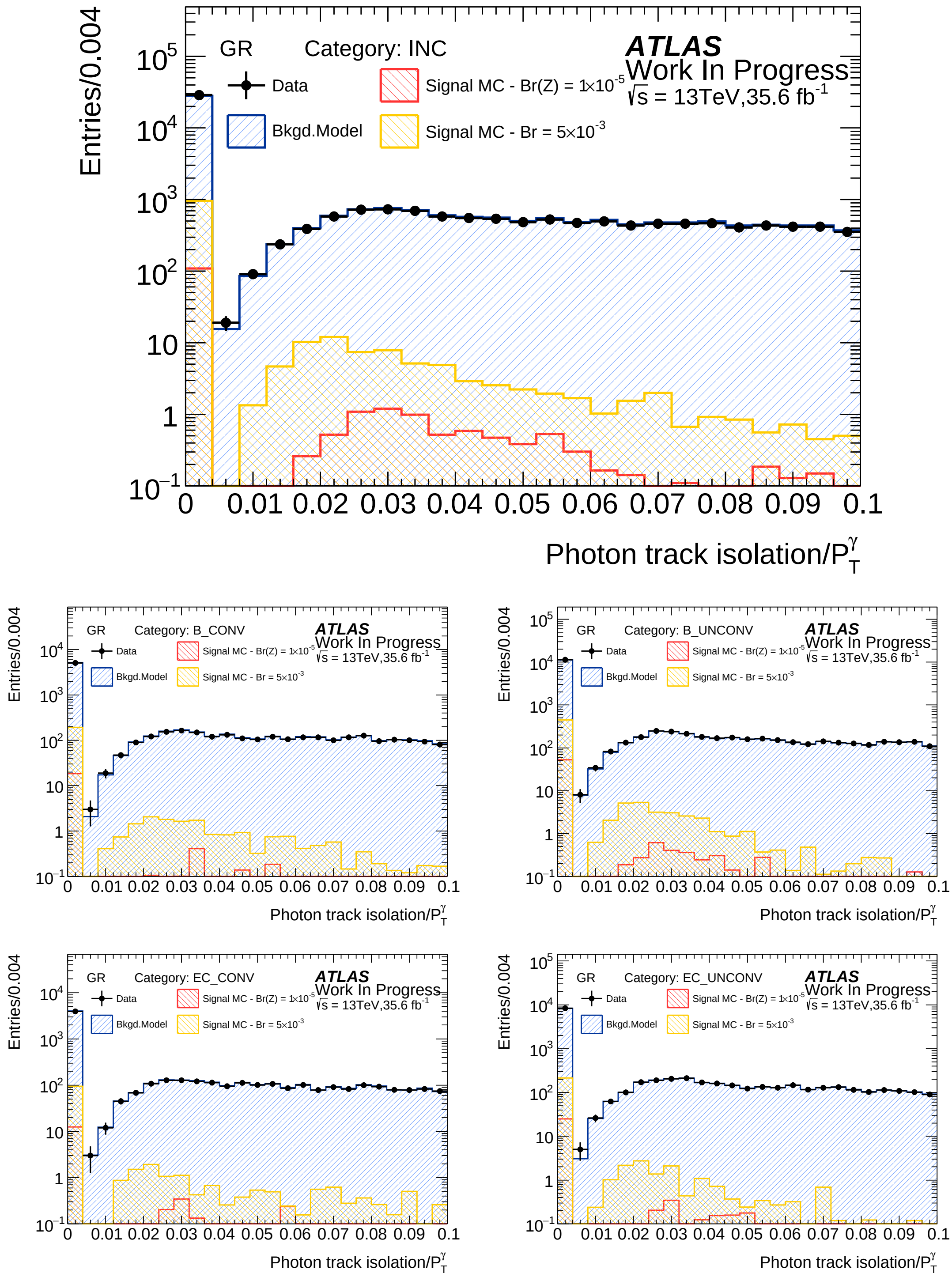

Figure C.7: Relative photon track isolation for the four different categories and the inclusive. The "FixedCutTight" selection cut is applied at < 0.05.

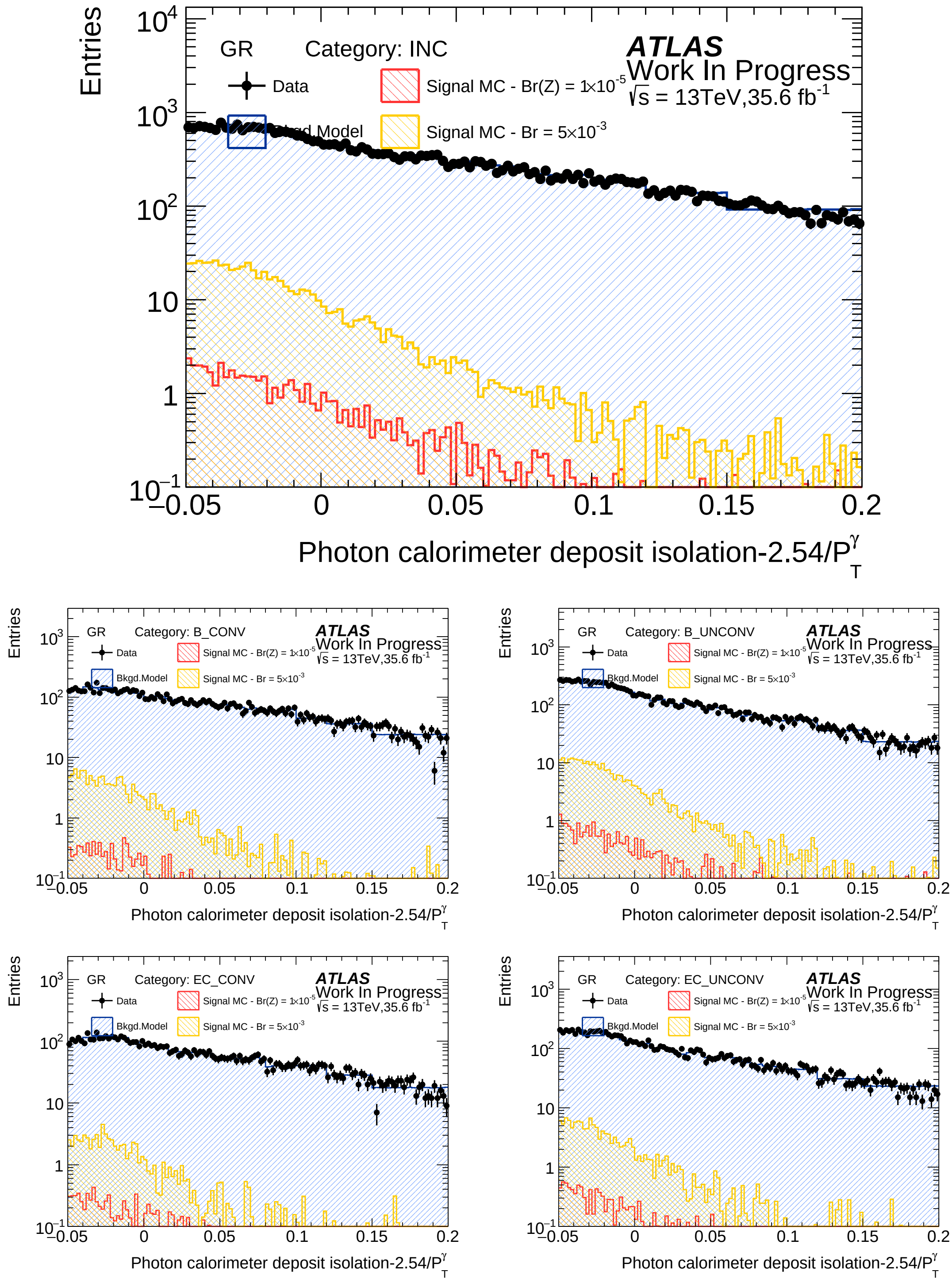

Figure C.8: Relative photon calo isolation (topoetcone40) for the four different categories and the inclusive. The “FixedCutTight” selection cut is applied at approxiamately 0.022 (the requirement is topoetcone40 $< 0.022 \times p_{\mathrm{T}}^{\gamma} + 2.45$ GeV.

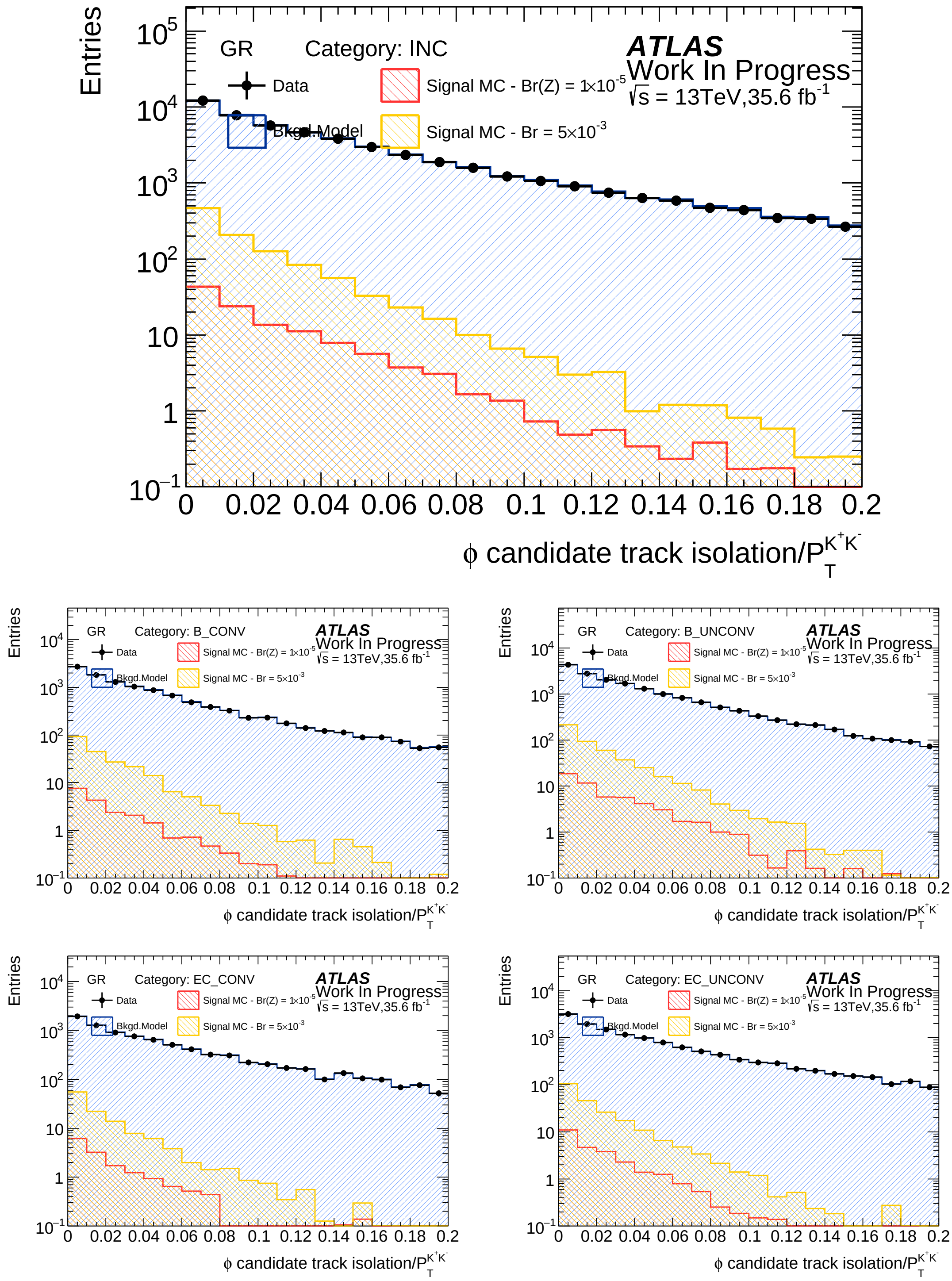

Figure C.9: Relative dikaon track isolation for the four different categories and the inclusive. The SR selection cut is applied at < 0.1.

C.2 Plots in the control region VR1: GR + SR $p_{\mathrm{T}}^{K^+K^-}$ requirement

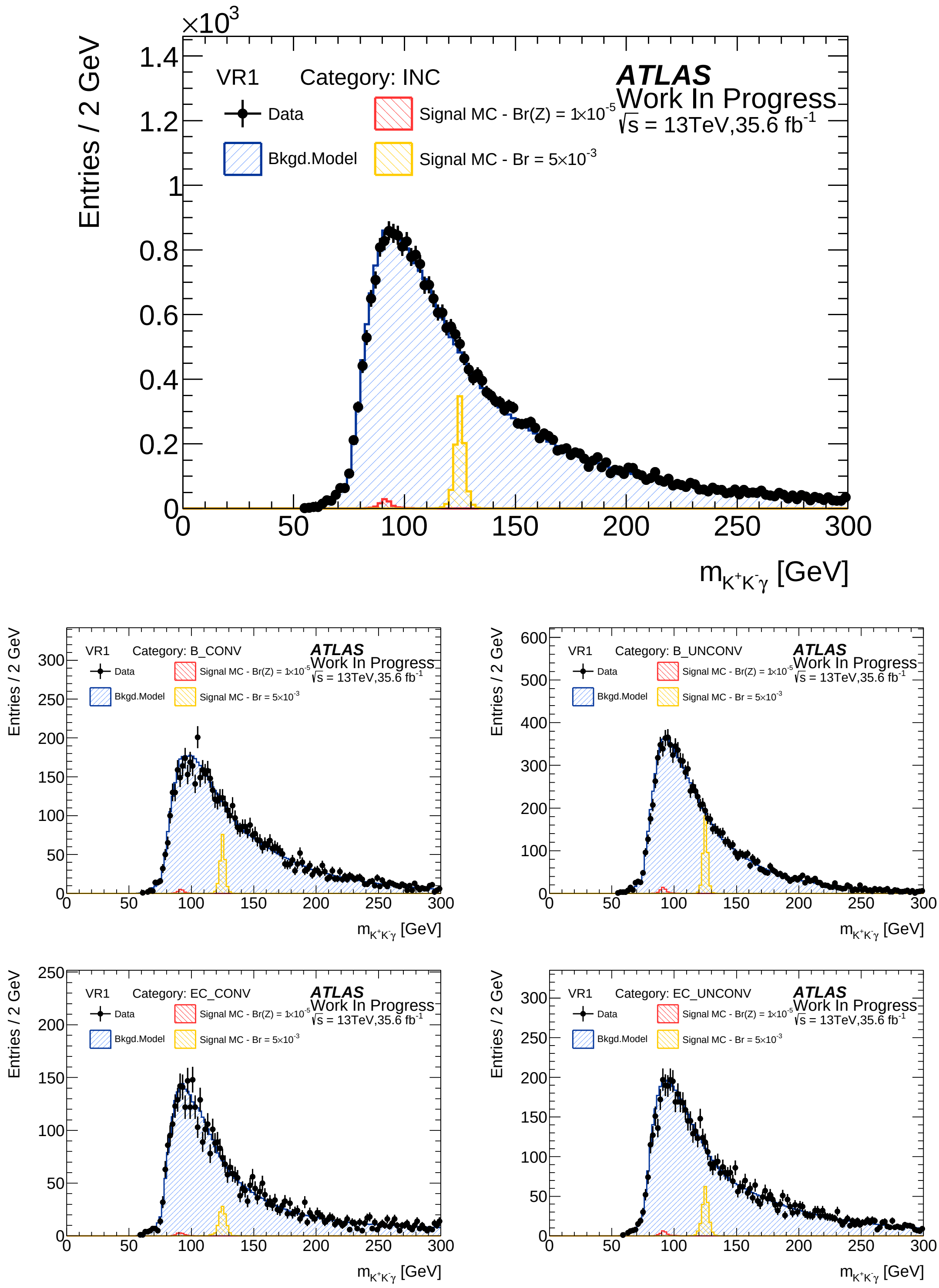

Figure C.10: Blinded $m_{K^+K^-\gamma}$ distribution for the four different categories and the inclusive.

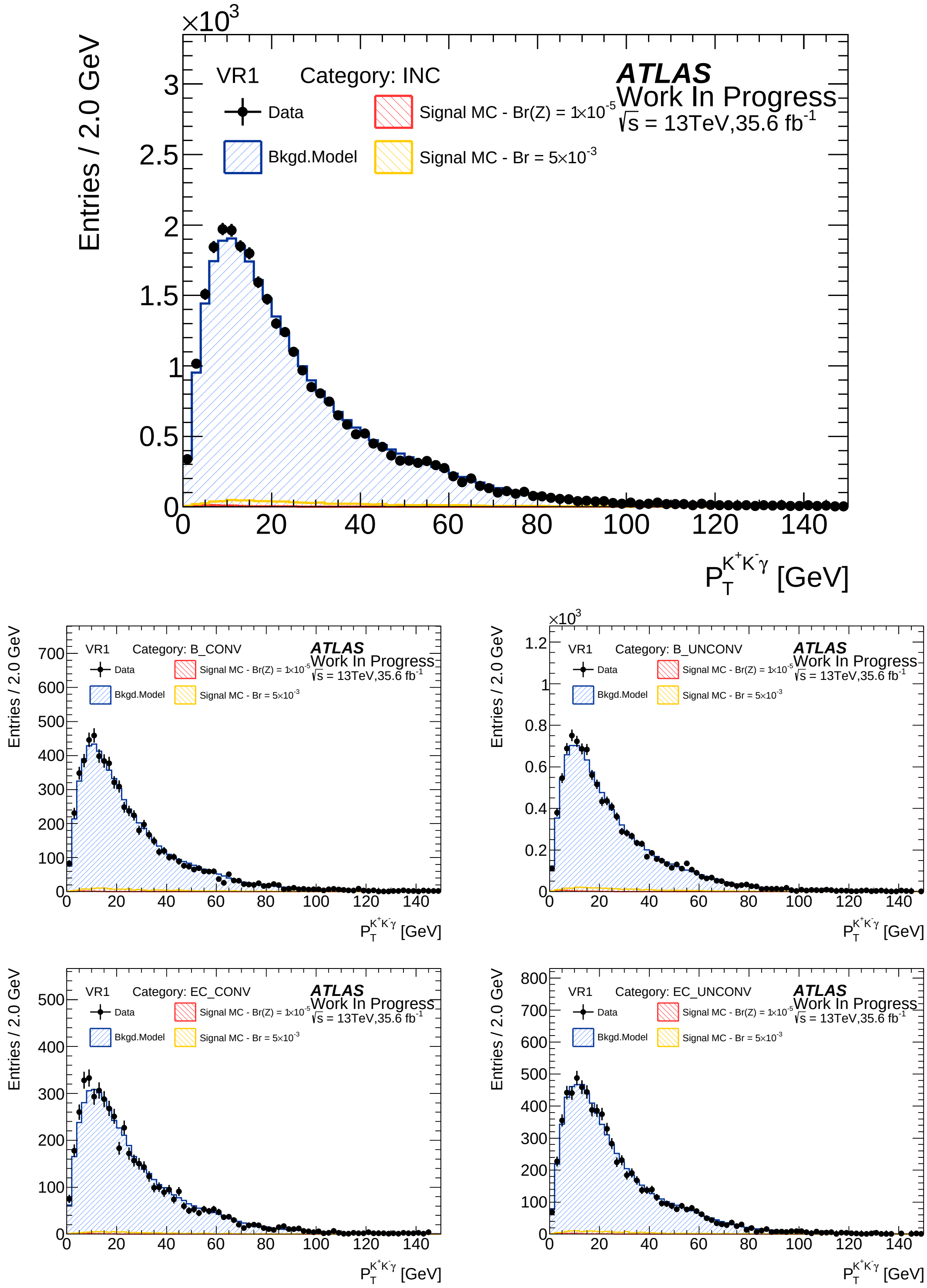

Figure C.11: $p_{\mathrm{T}}^{K^{+}K^{-}\gamma}$ distribution for the four different categories and the inclusive.

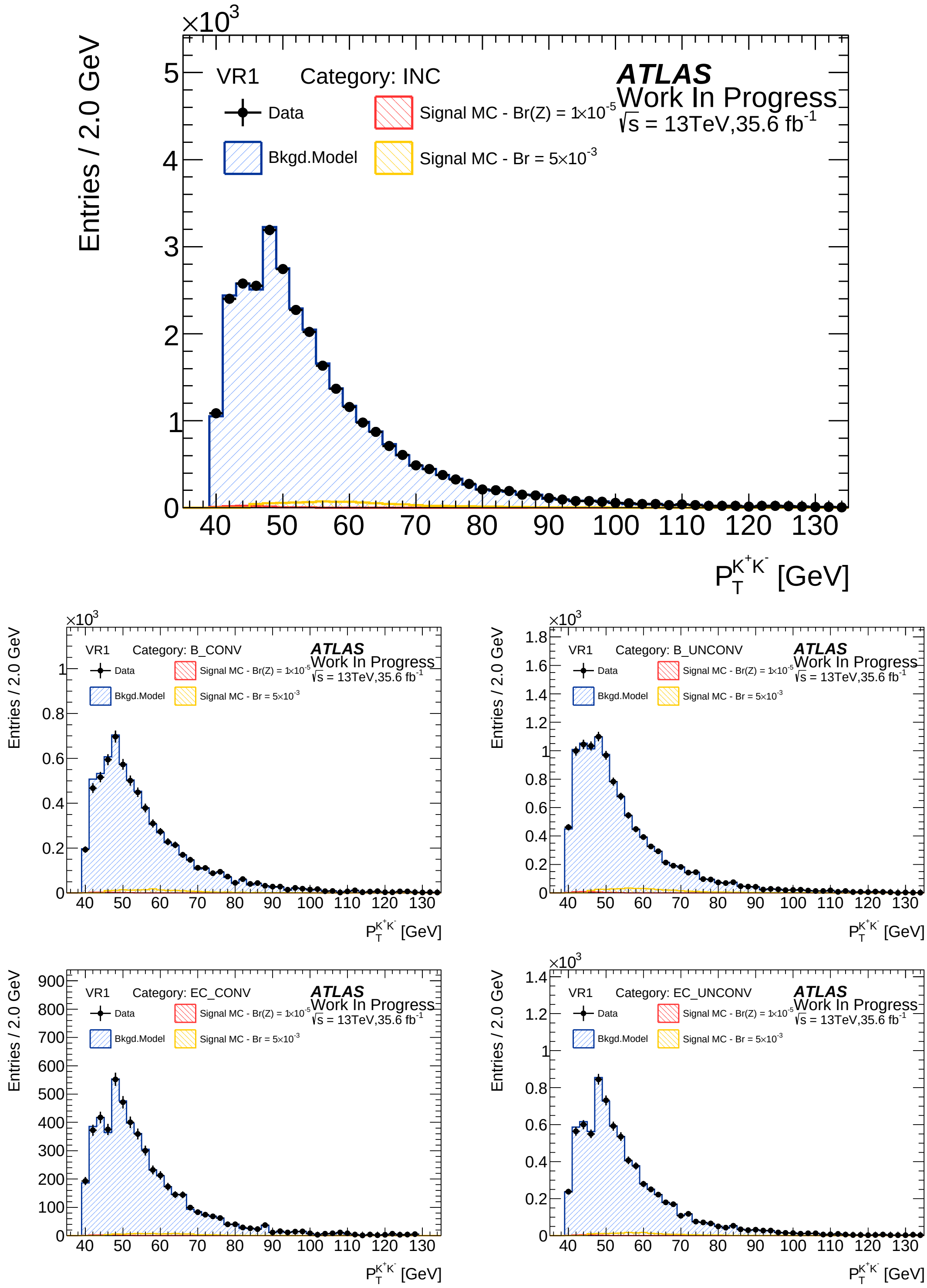

Figure C.12: $p_{\mathrm{T}}^{K^+K^-}$ distribution for the four different categories and the inclusive.

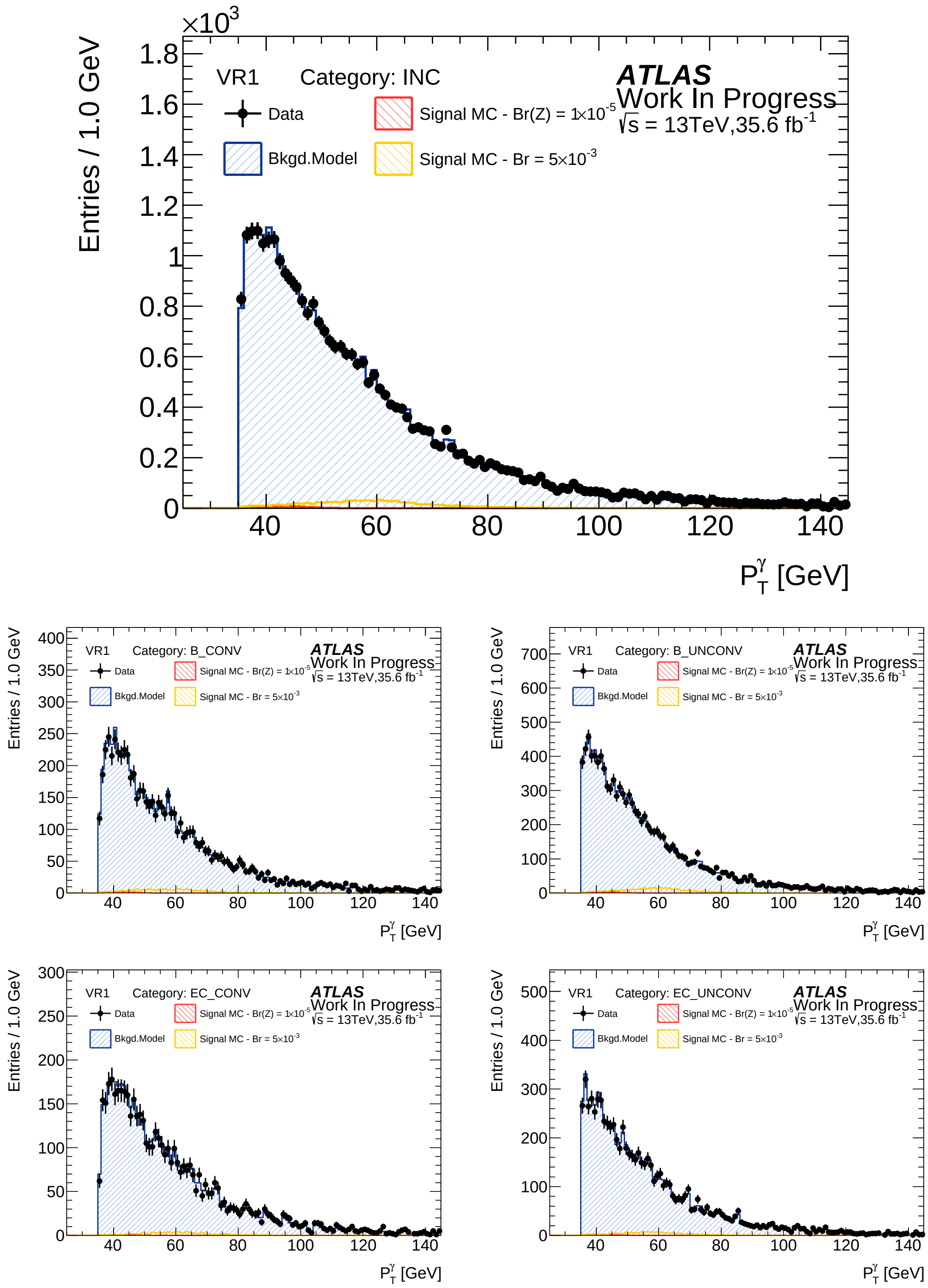

Figure C.13: p_{T}^{γ} distribution for the four different categories and the inclusive.

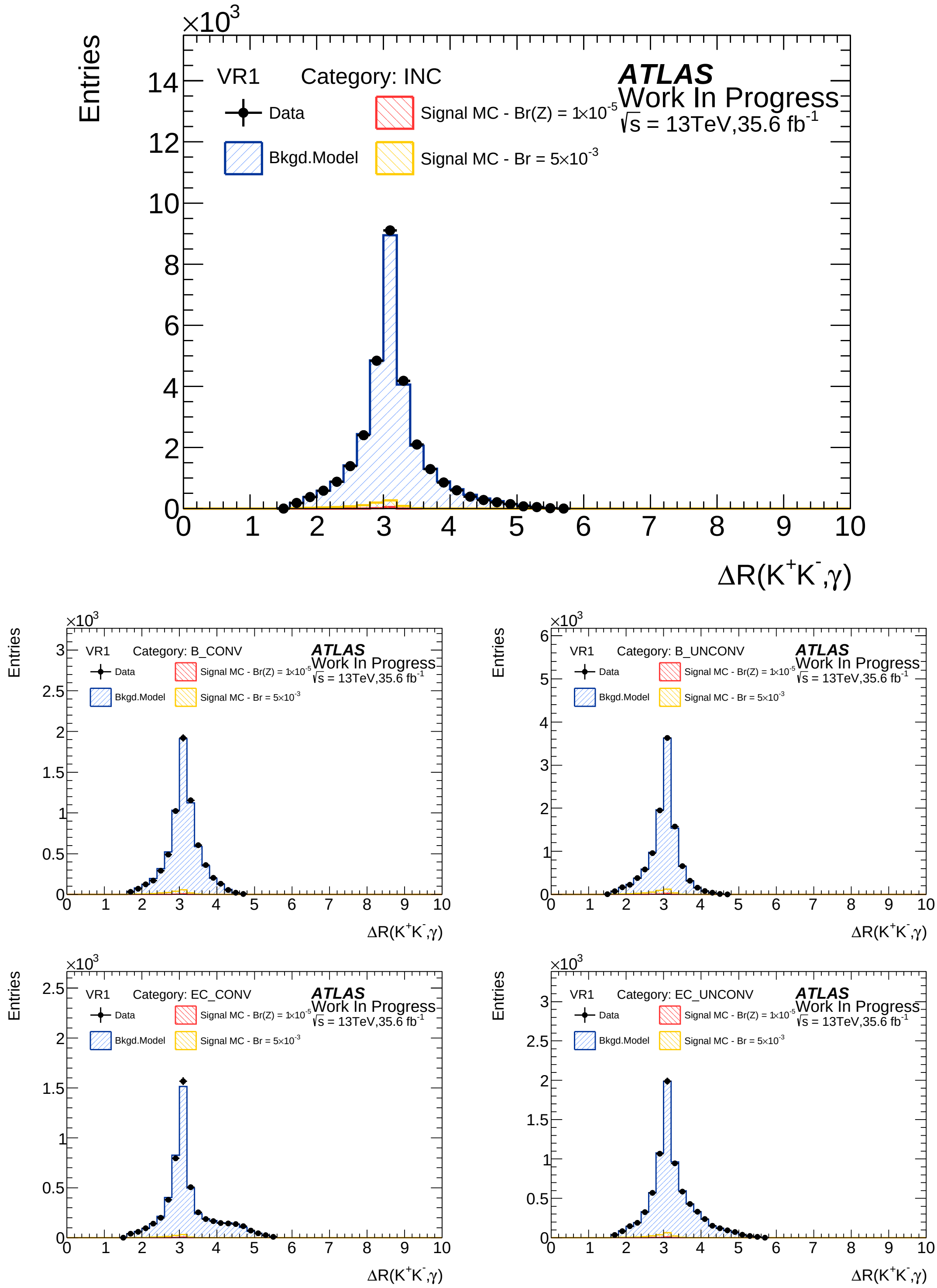

Figure C.14: $\Delta R^{K^+K^-,\gamma}$ distribution for the four different categories and the inclusive.

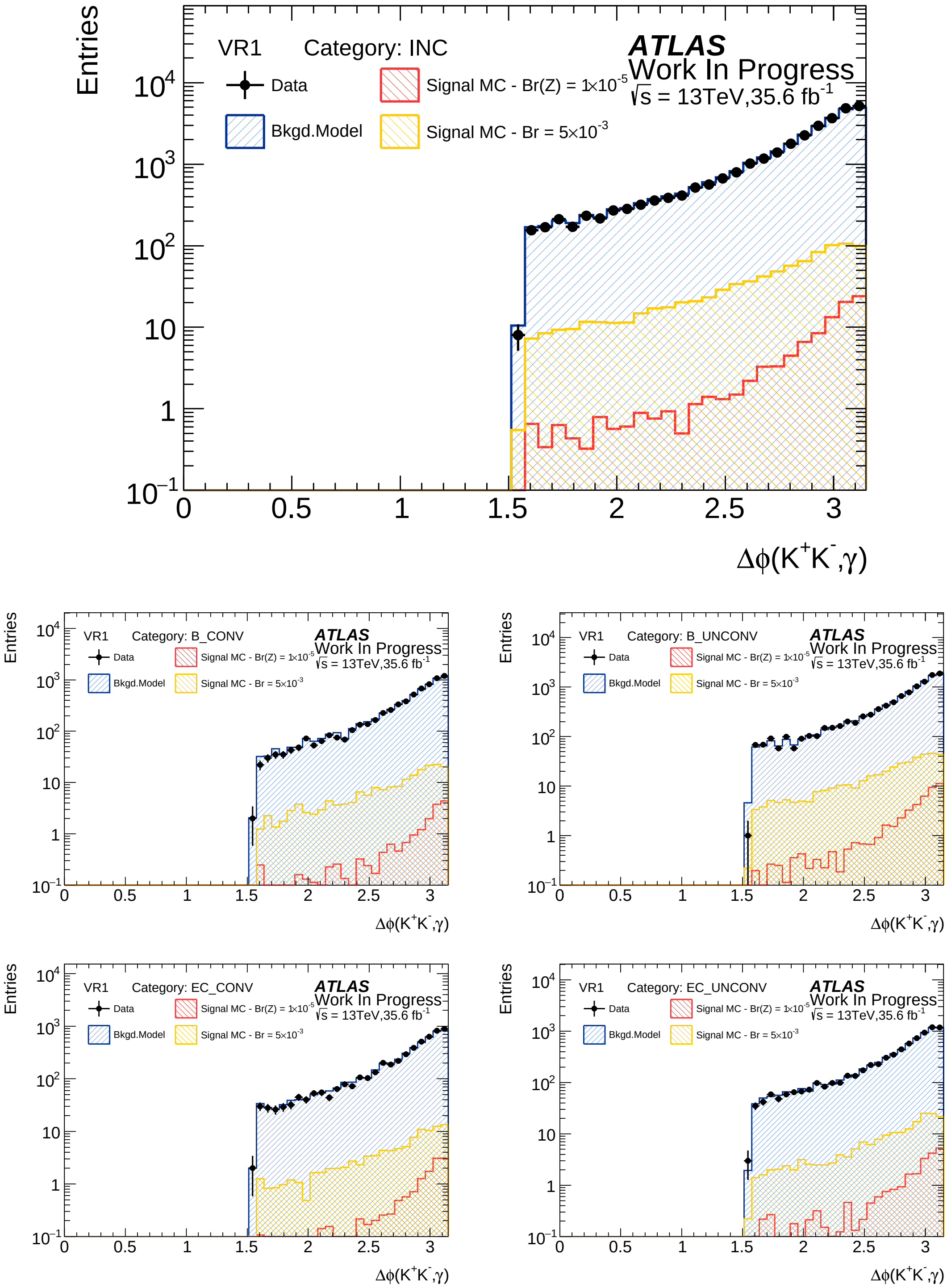

Figure C.15: $\Delta\phi^{K^+K^-,\gamma}$ distribution for the four different categories and the inclusive.

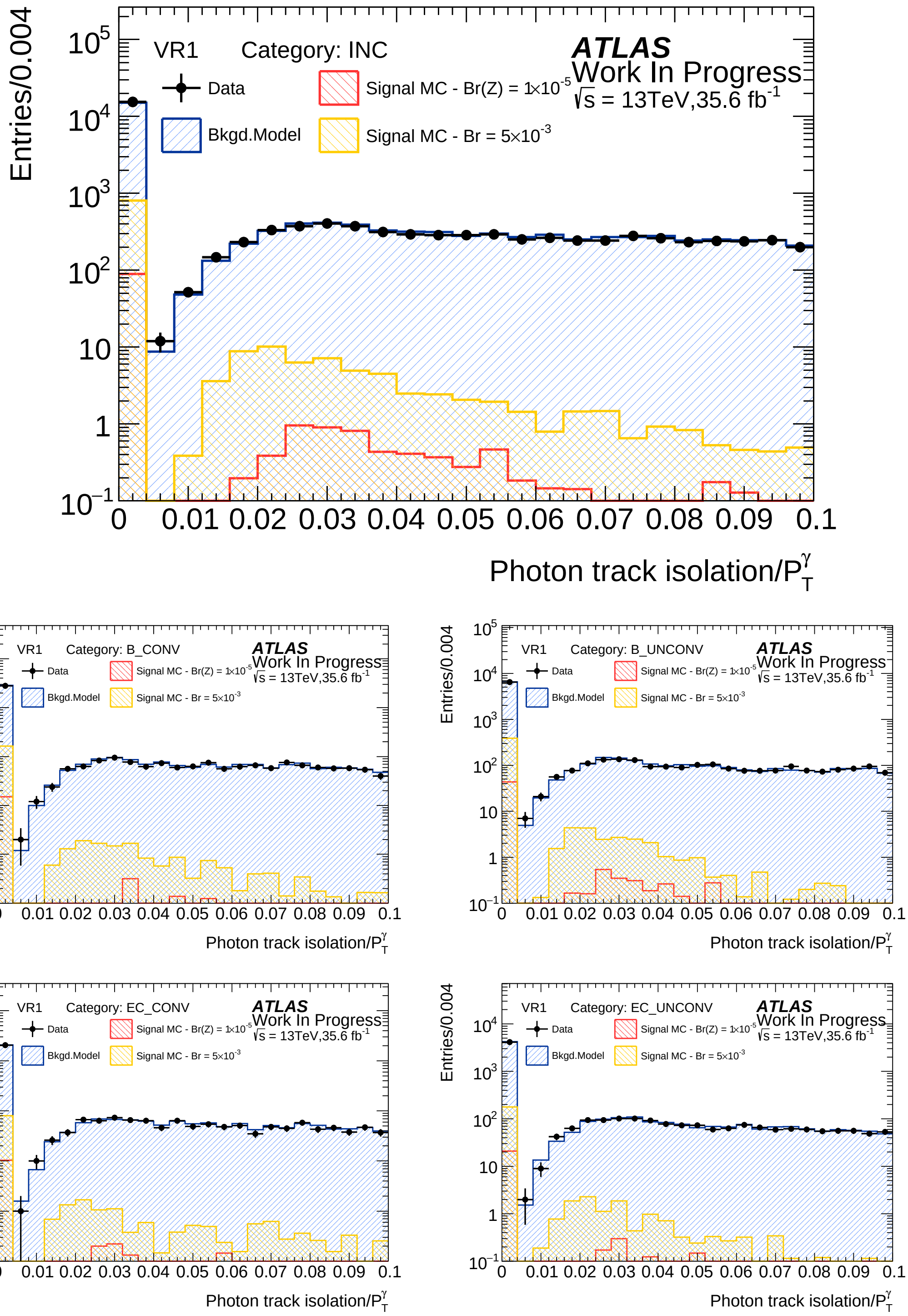

Figure C.16: Relative photon track isolation for the four different categories and the inclusive.

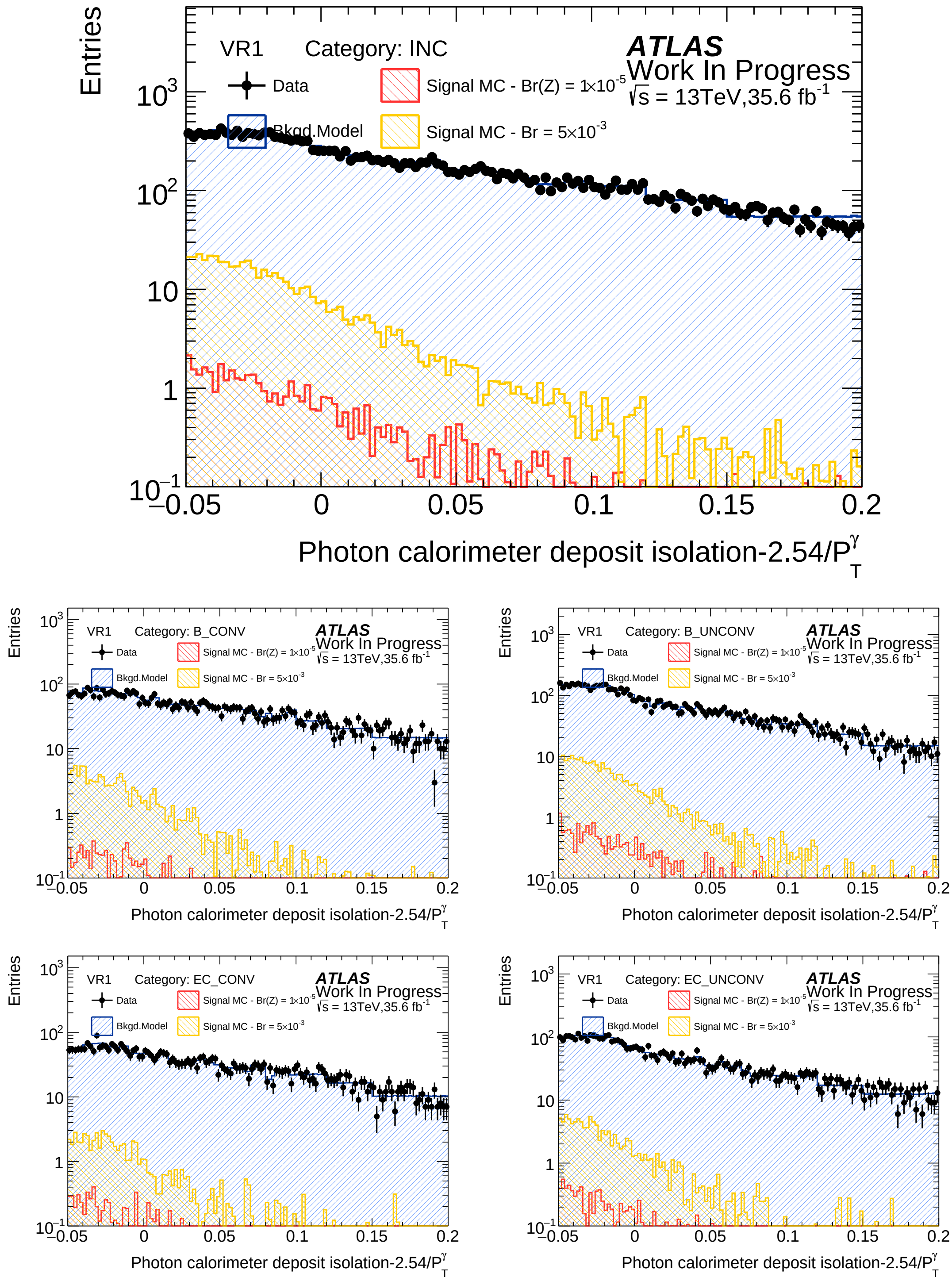

Figure C.17: Relative photon calo isolation (FixedCutTight) for the four different categories and the inclusive.

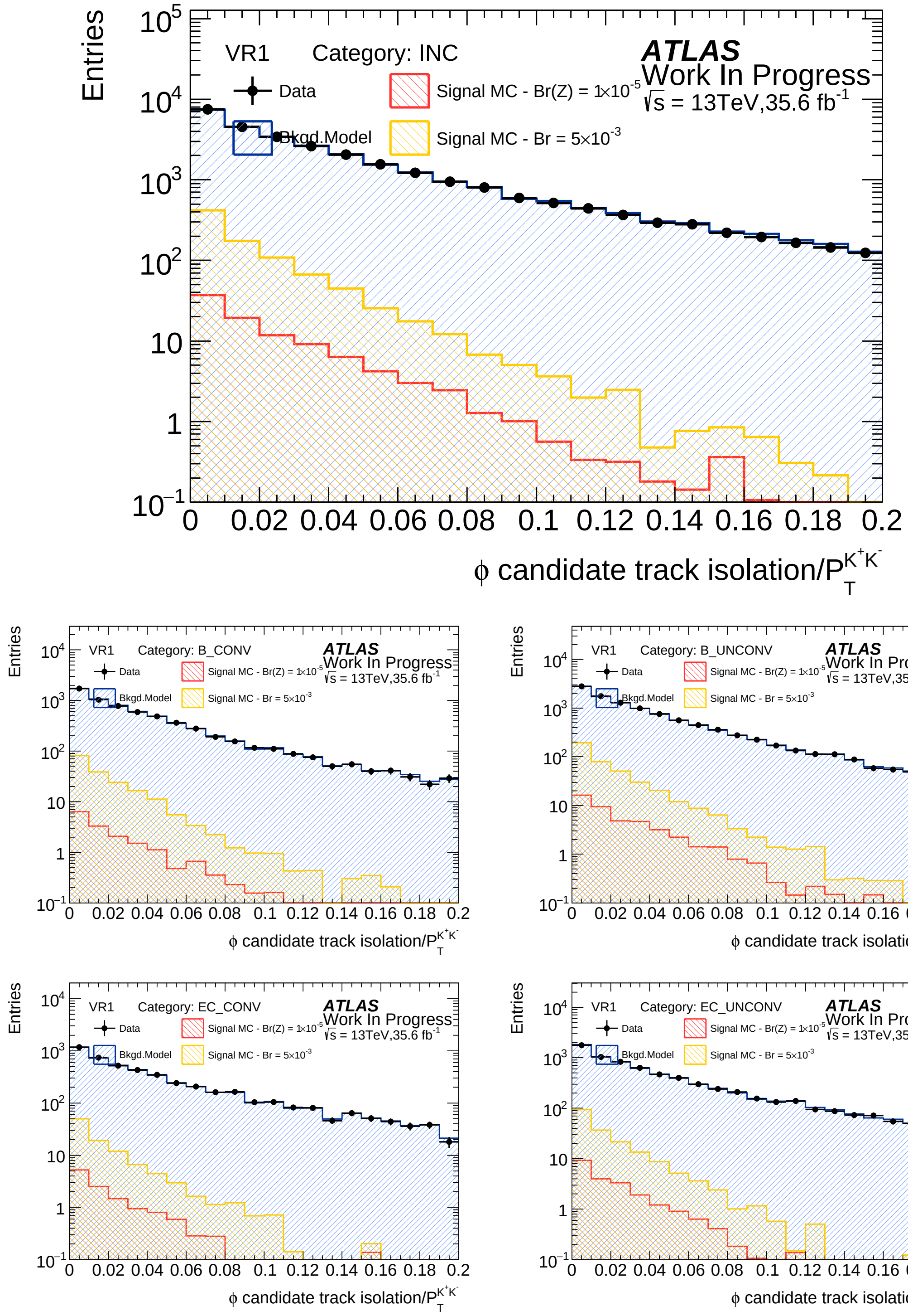

Figure C.18: Relative dikaon track isolation for the four different categories and the inclusive.

C.3 Plots in the control region VR2: GR + SR photon isolationrequirement

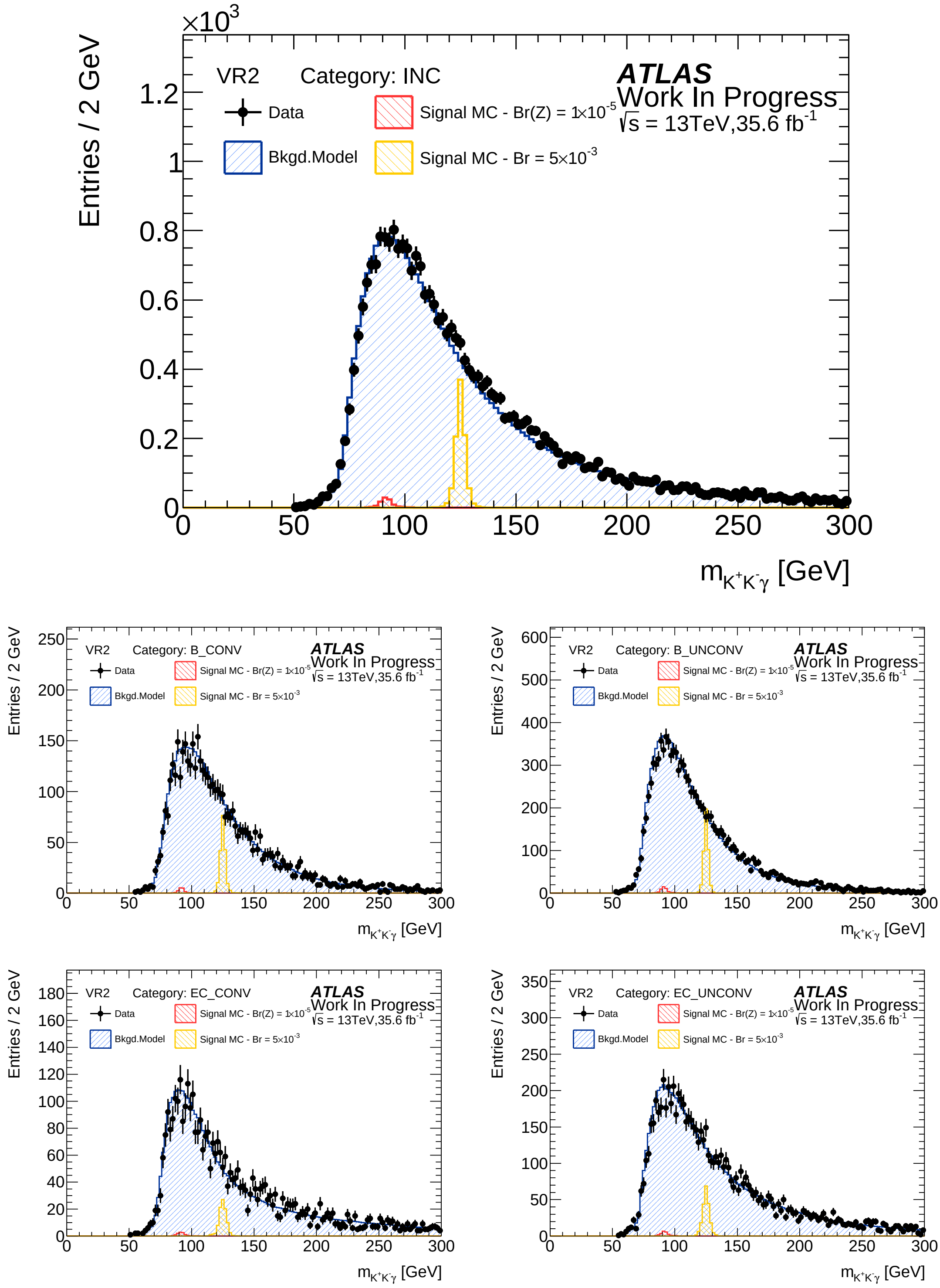

Figure C.19: Blinded $m_{K^+K^-\gamma}$ distribution for the four different categories and the inclusive.

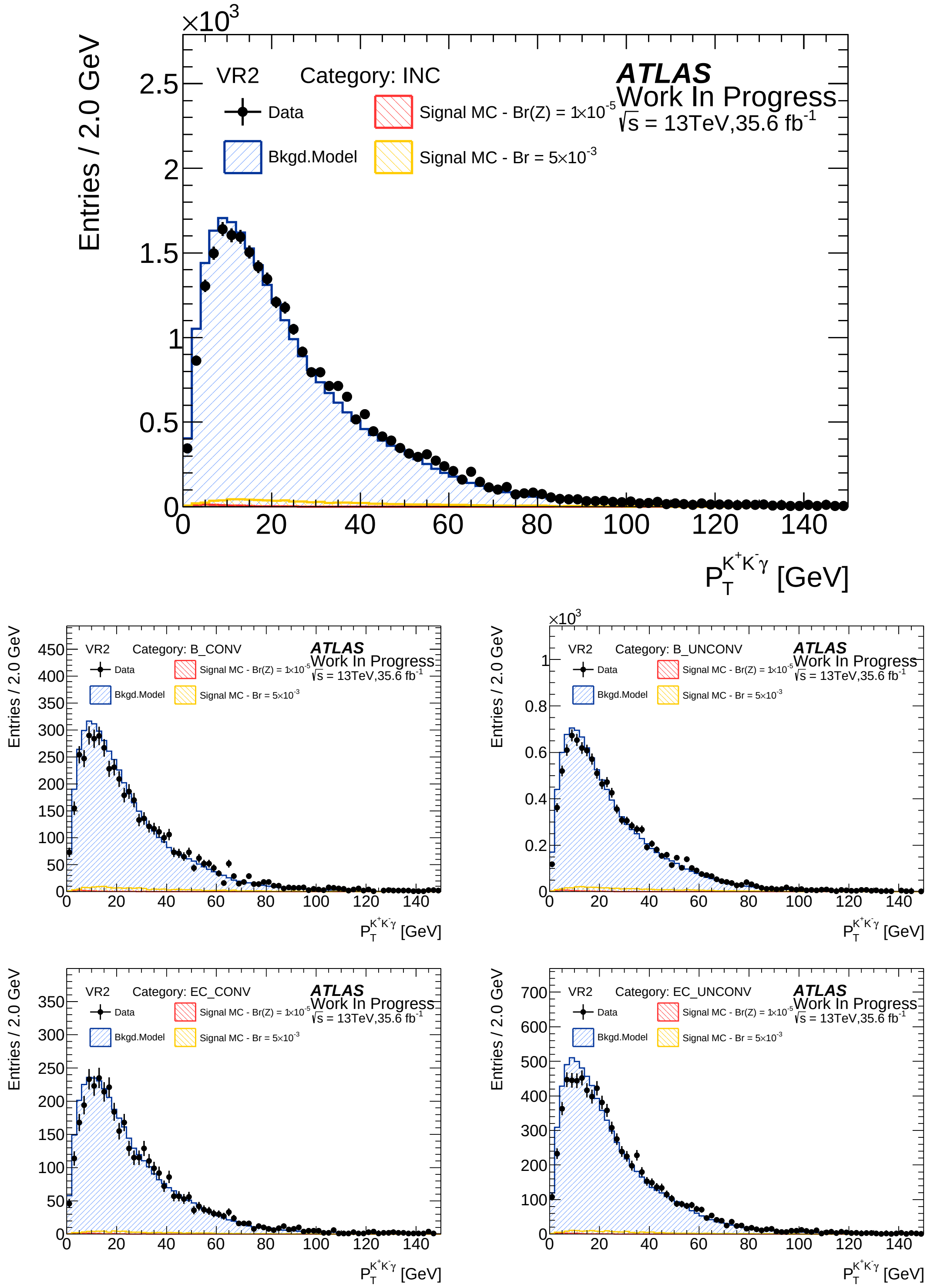

Figure C.20: $p_{\mathrm{T}}^{K^+K^-\gamma}$ distribution for the four different categories and the inclusive.

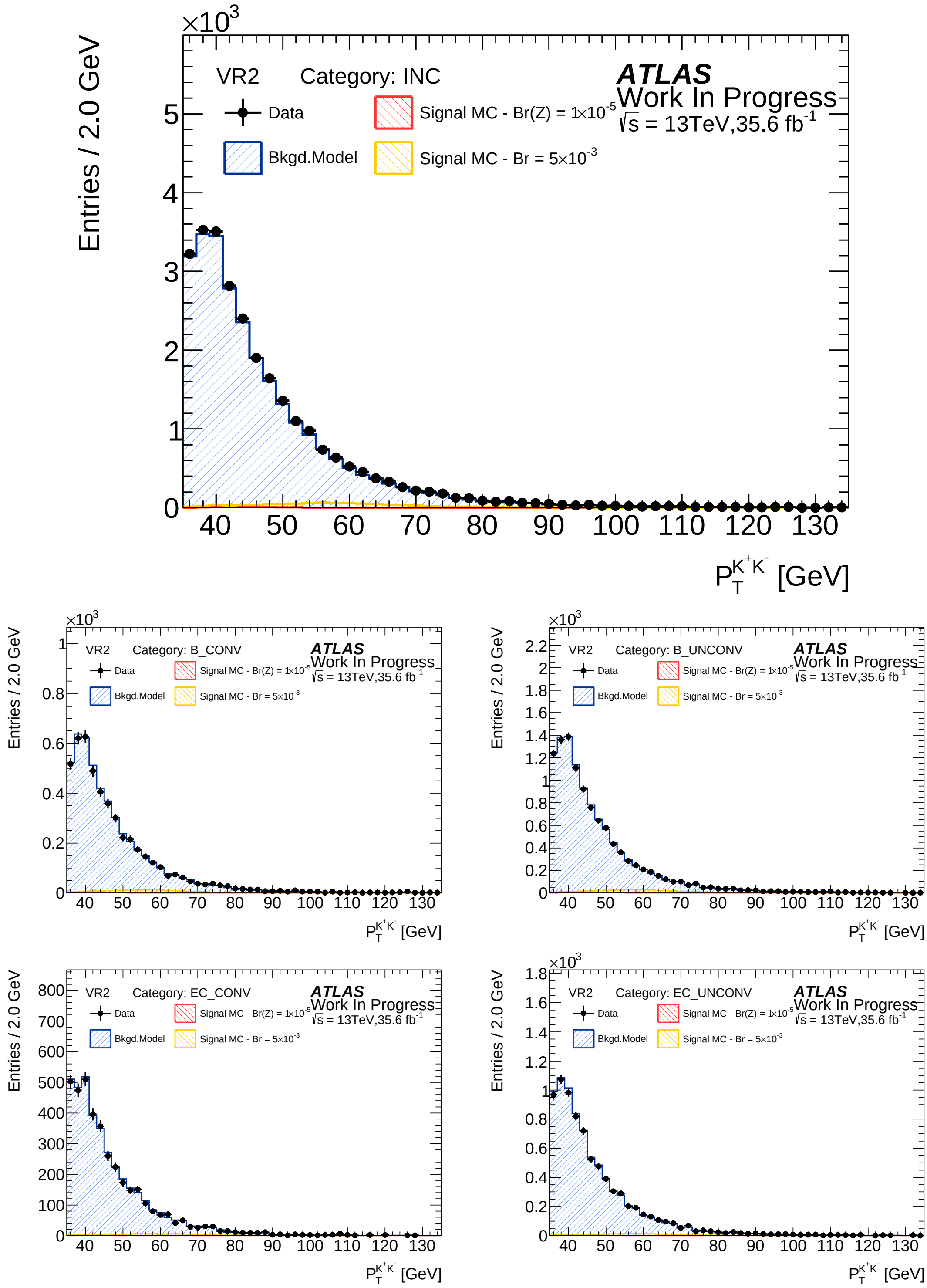

Figure C.21: $p_{\mathrm{T}}^{K^+K^-}$ distribution for the four different categories and the inclusive.

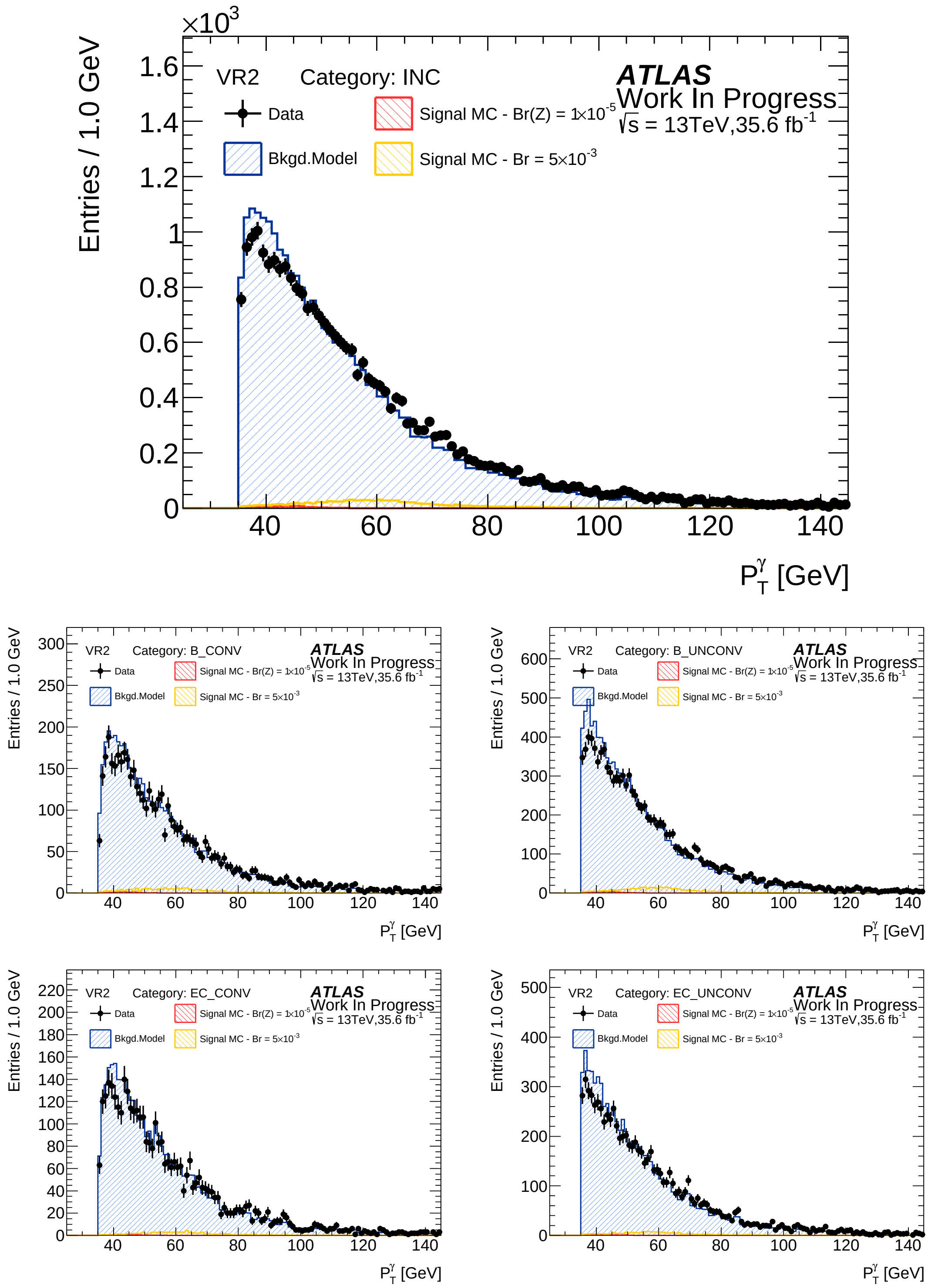

Figure C.22: p_{T}^{γ} distribution for the four different categories and the inclusive.

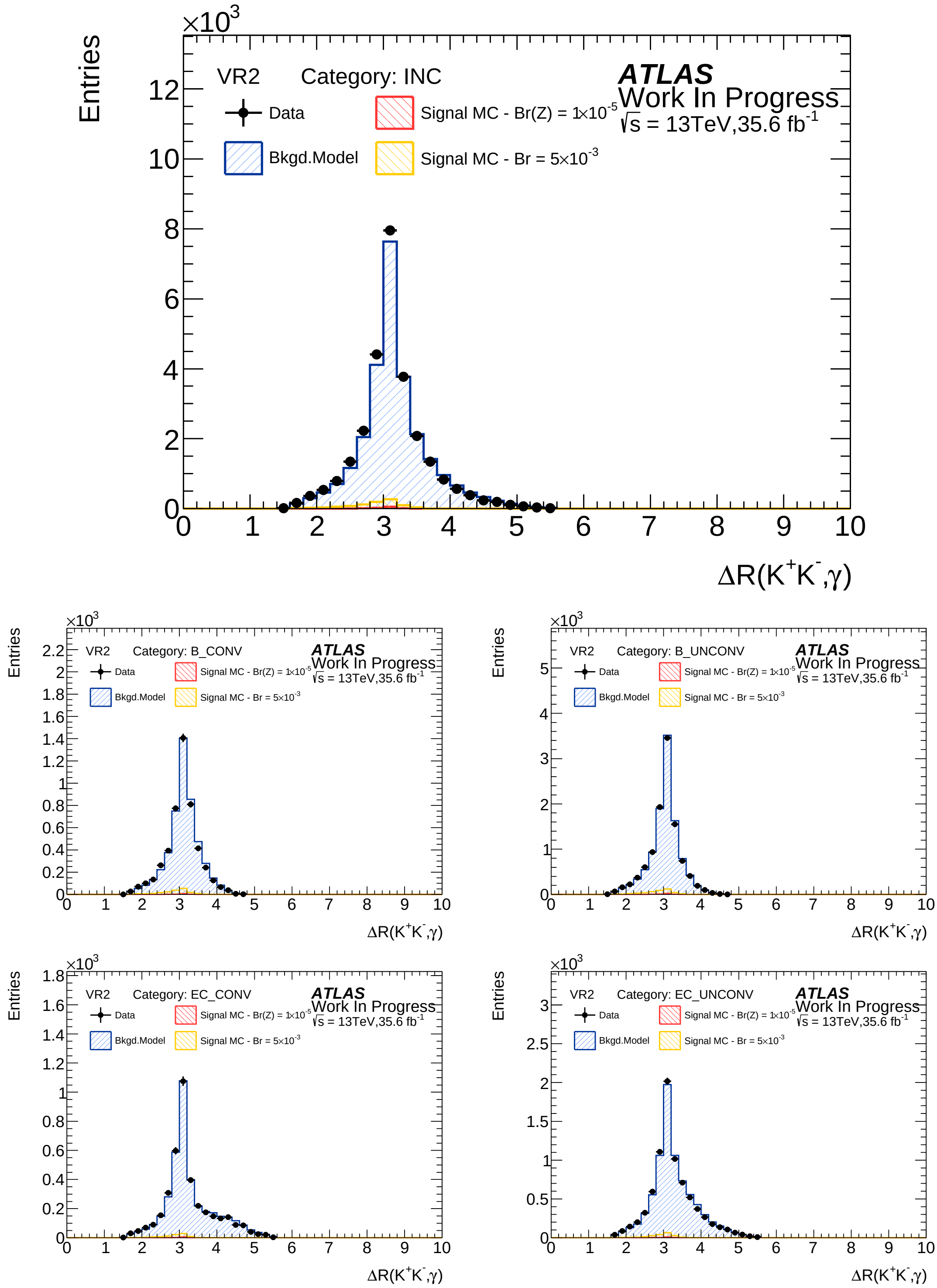

Figure C.23: $\Delta R^{K^+K^-,\gamma}$ distribution for the four different categories and the inclusive.

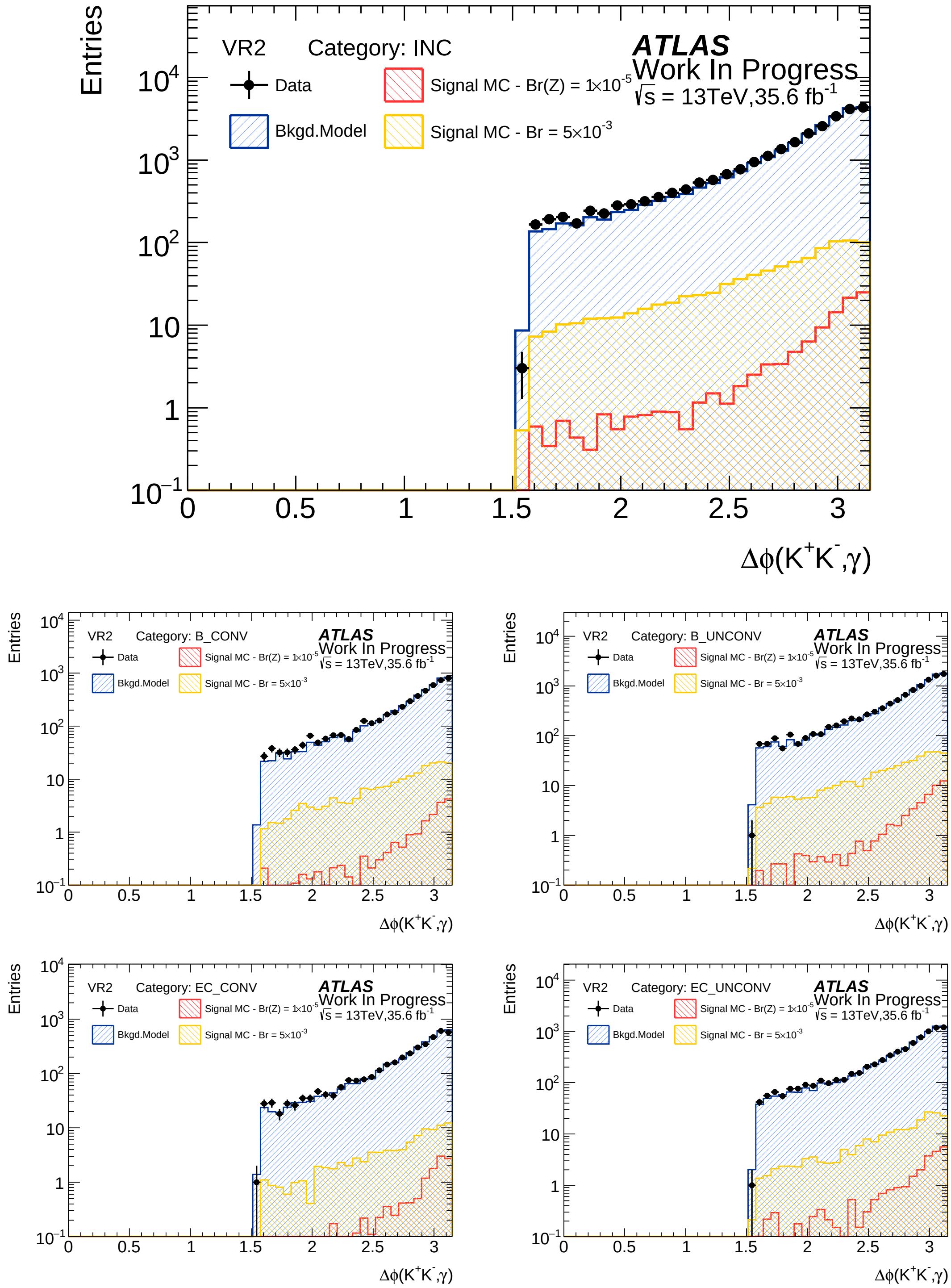

Figure C.24: $\Delta\phi^{K^+K^-,\gamma}$ distribution for the four different categories and the inclusive.

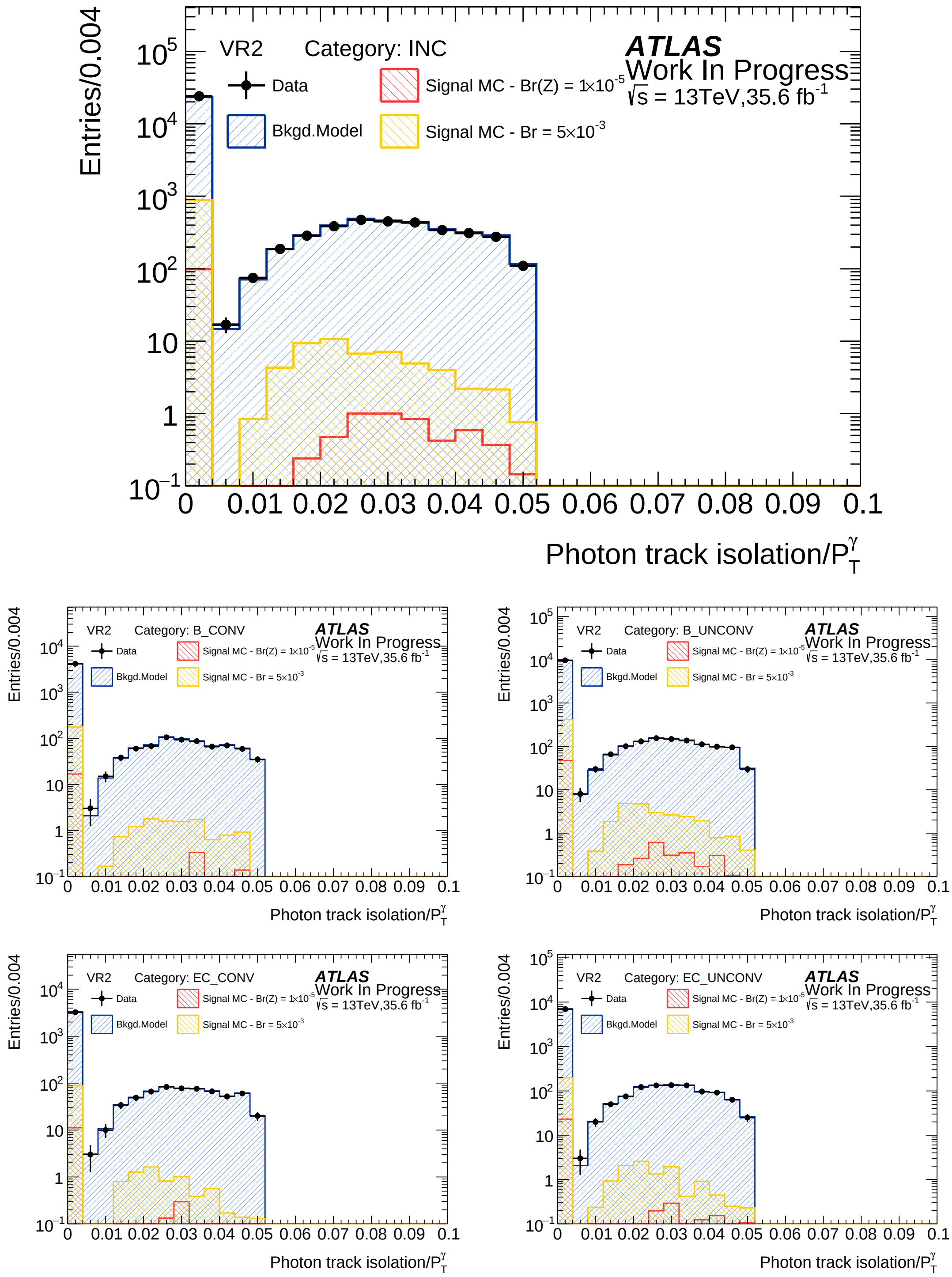

Figure C.25: Relative photon track isolation for the four different categories and the inclusive.

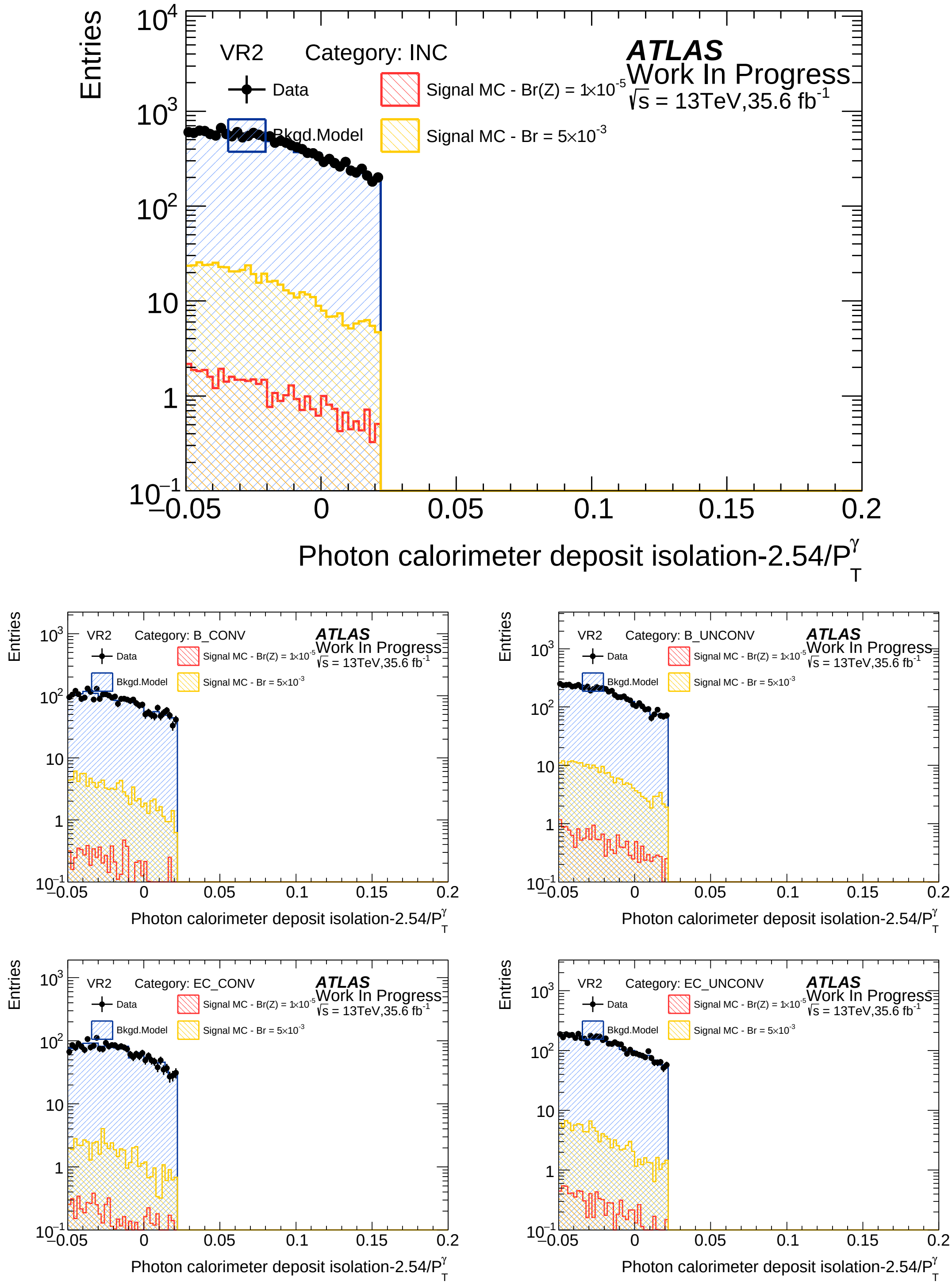

Figure C.26: Relative photon calo isolation (FixedCutTight) for the four different categories and the inclusive.

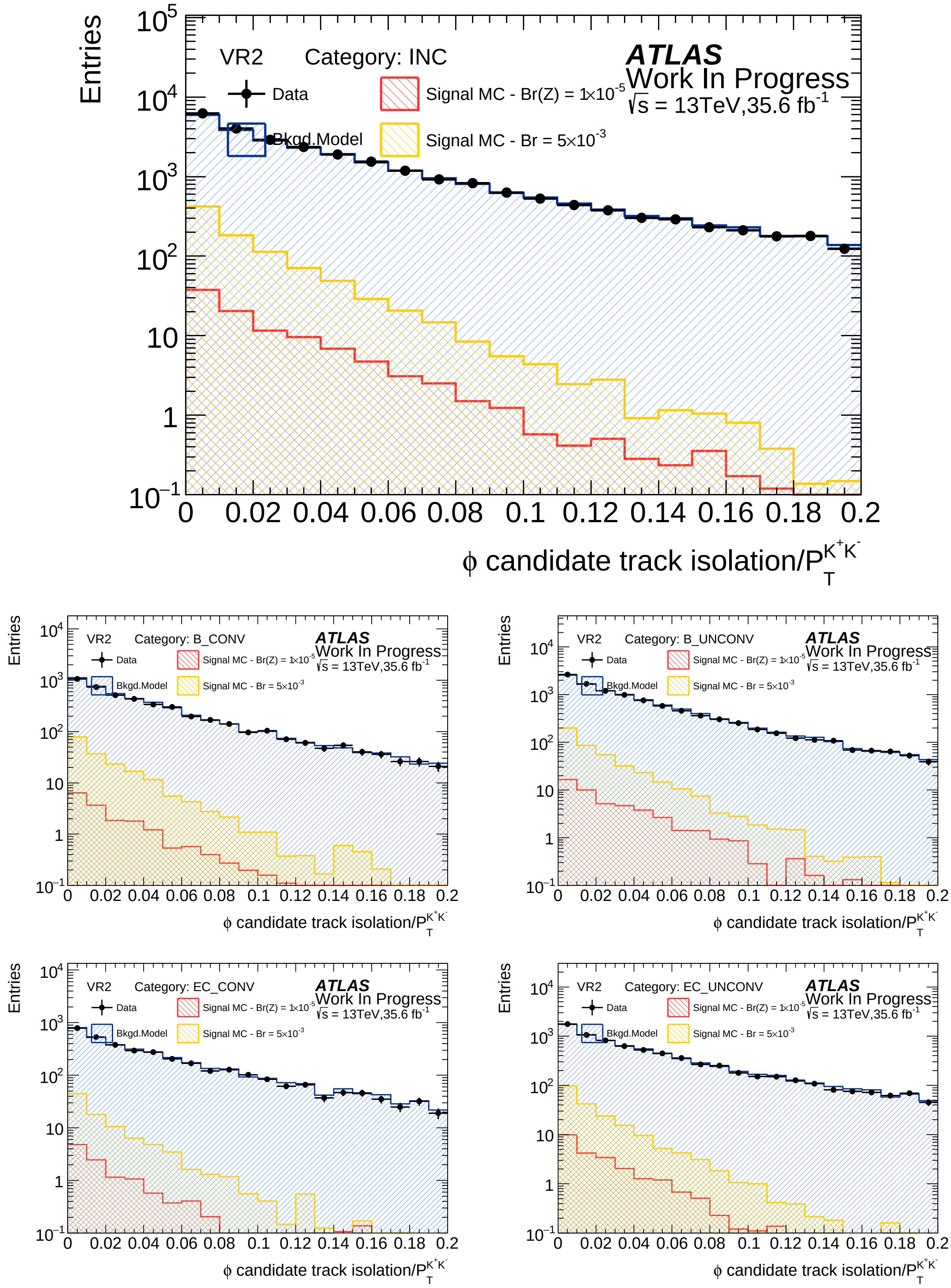

Figure C.27: Relative dikaon track isolation for the four different categories and the inclusive.

C.4 Plots in the control region VR3: GR + SR di-track isolation requirement

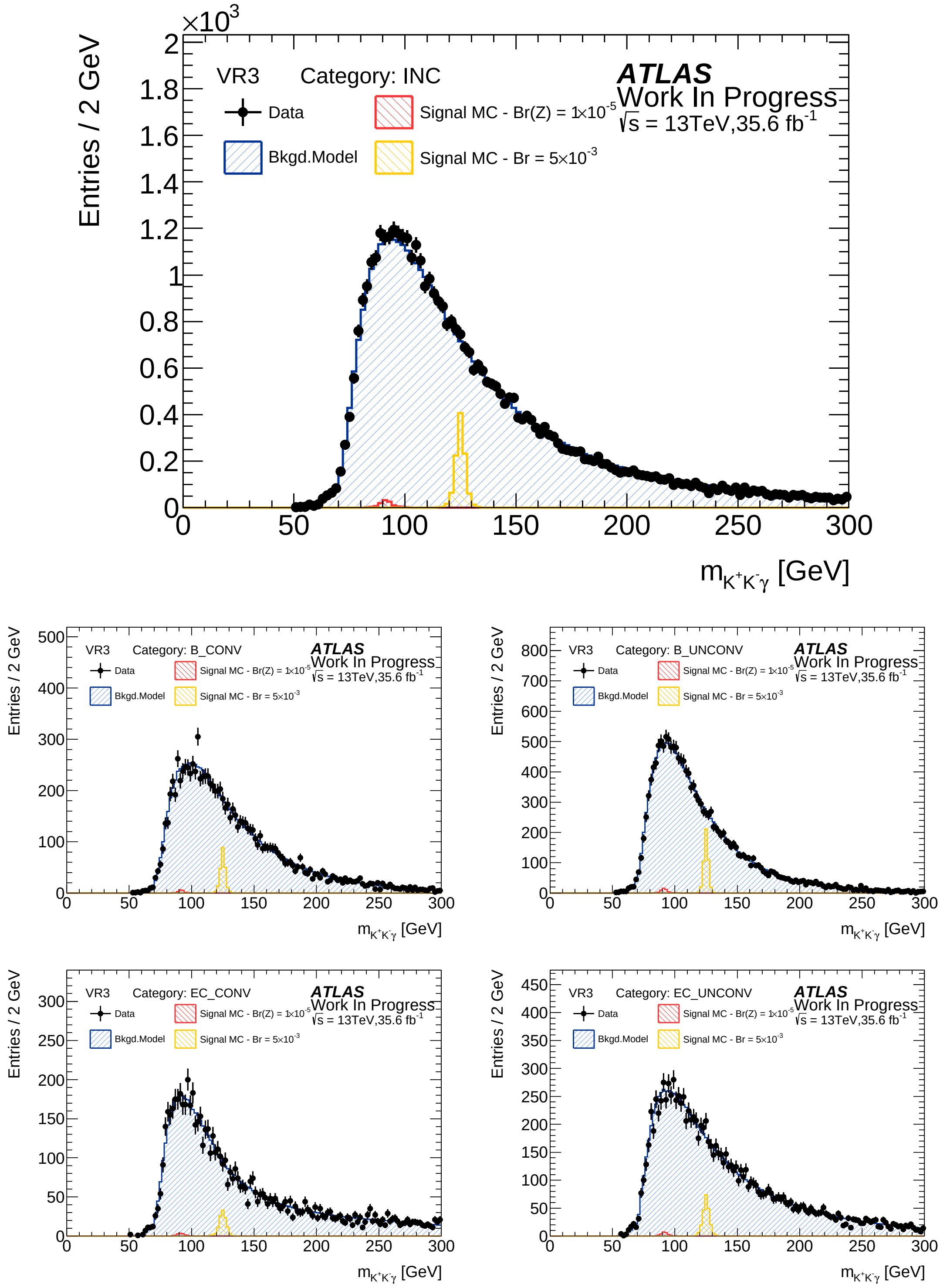

Figure C.28: Blinded $m_{K^+K^-\gamma}$ distribution for the four different categories and the inclusive.

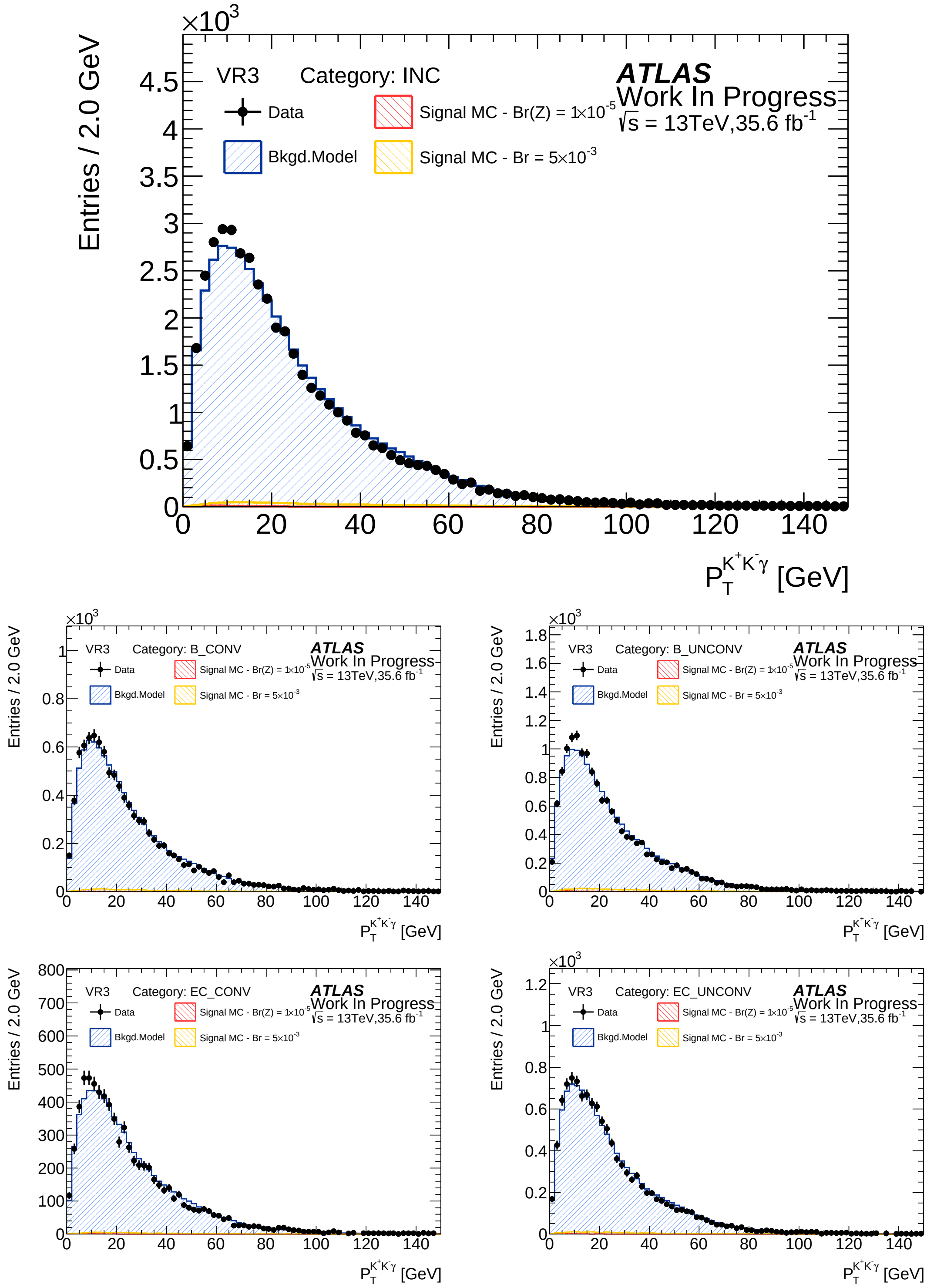

Figure C.29: $p_{\mathrm{T}}^{K^+K^-\gamma}$ distribution for the four different categories and the inclusive.

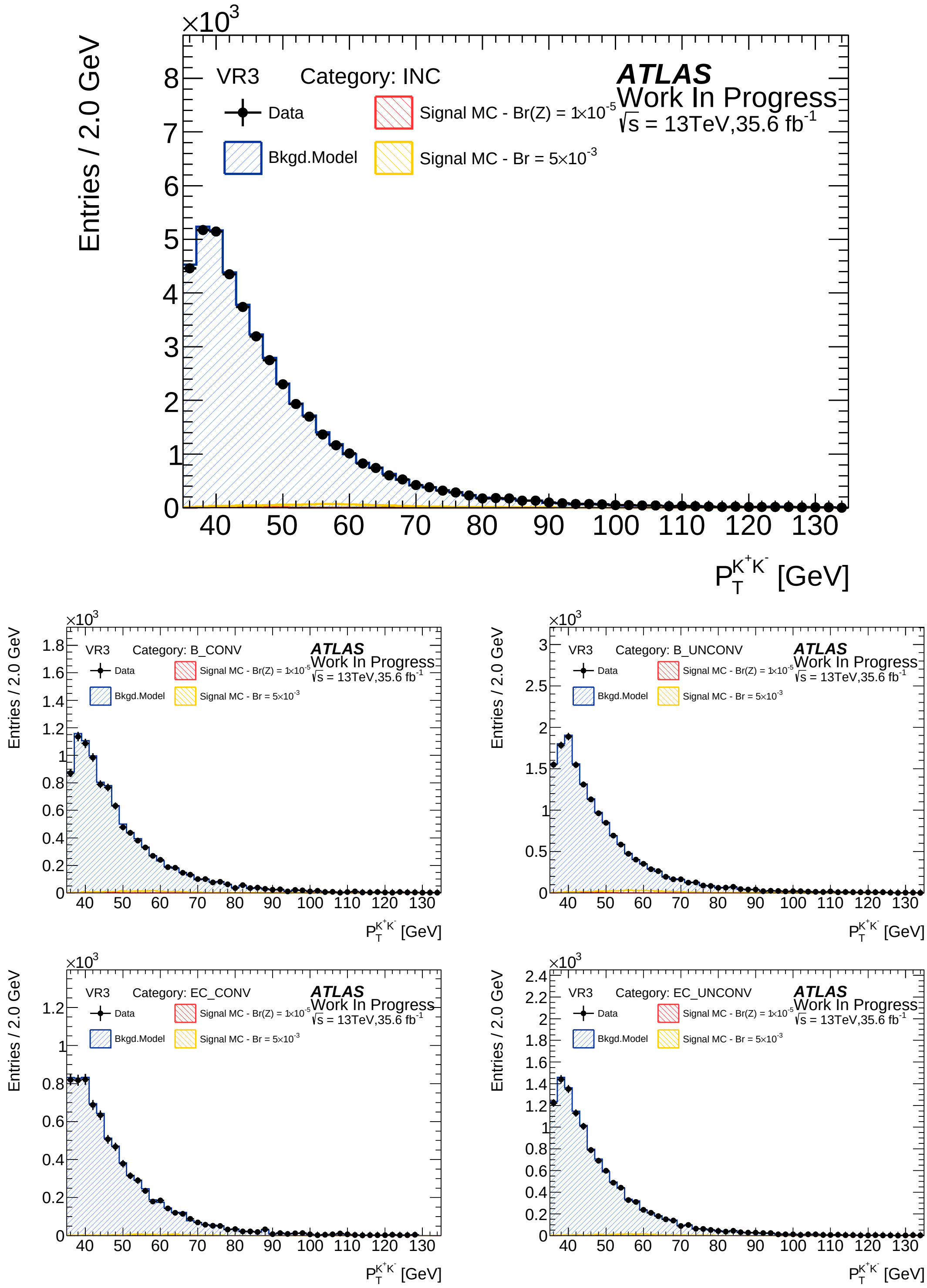

Figure C.30: $p_{\mathrm{T}}^{K^+K^-}$ distribution for the four different categories and the inclusive.

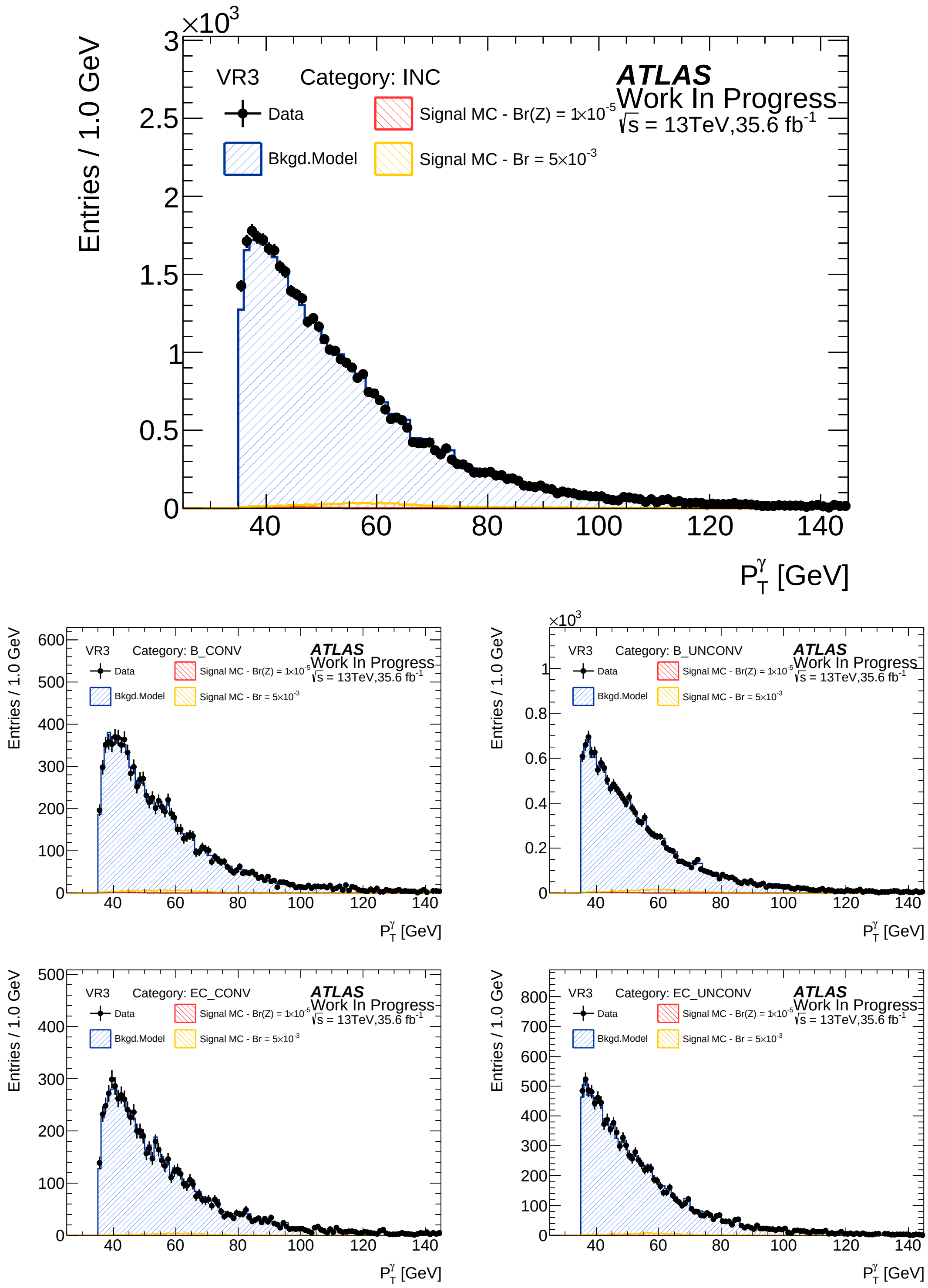

Figure C.31: p_T^{γ} distribution for the four different categories and the inclusive.

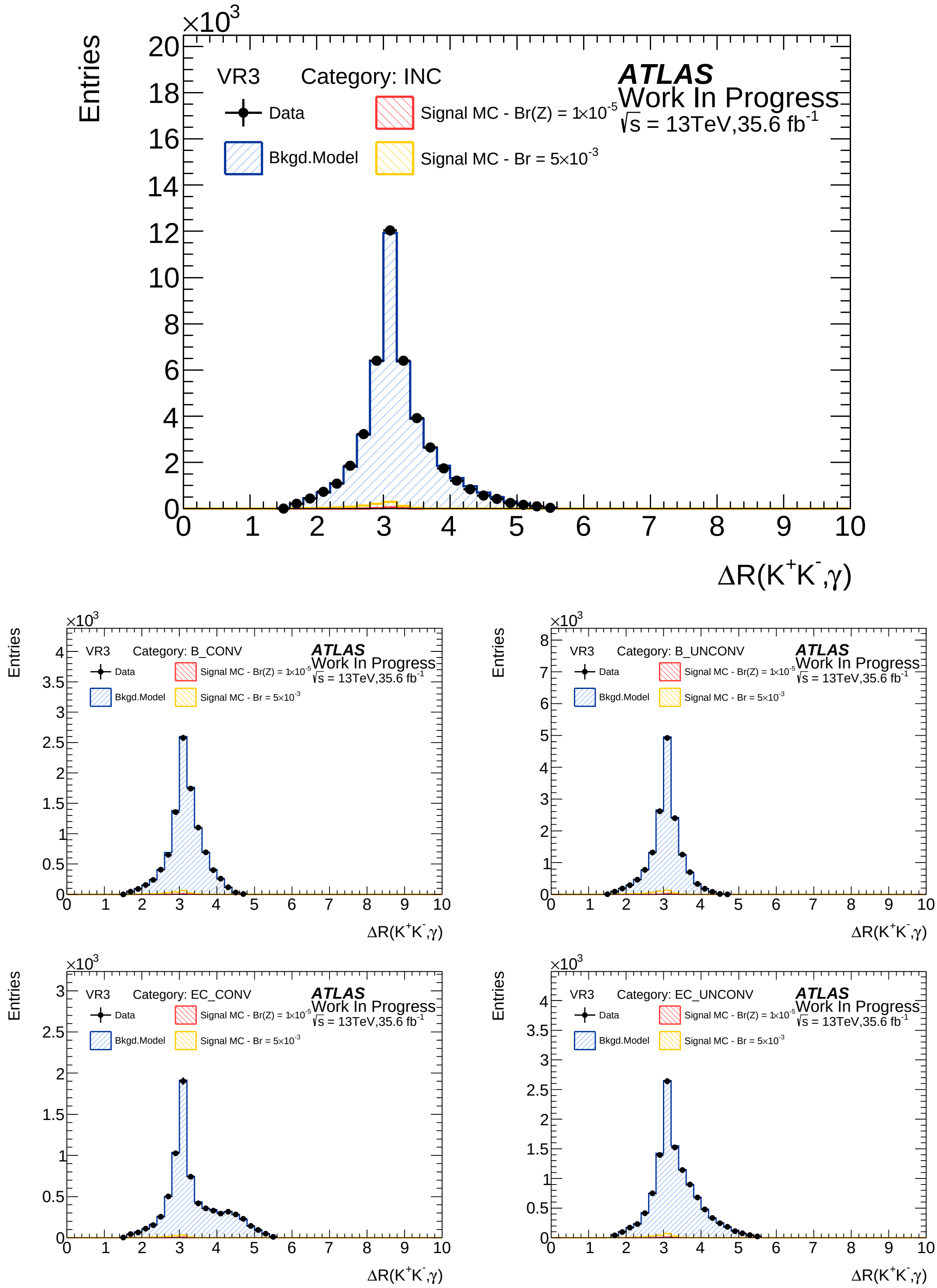

Figure C.32: $\Delta R^{K^+K^-,\gamma}$ distribution for the four different categories and the inclusive.

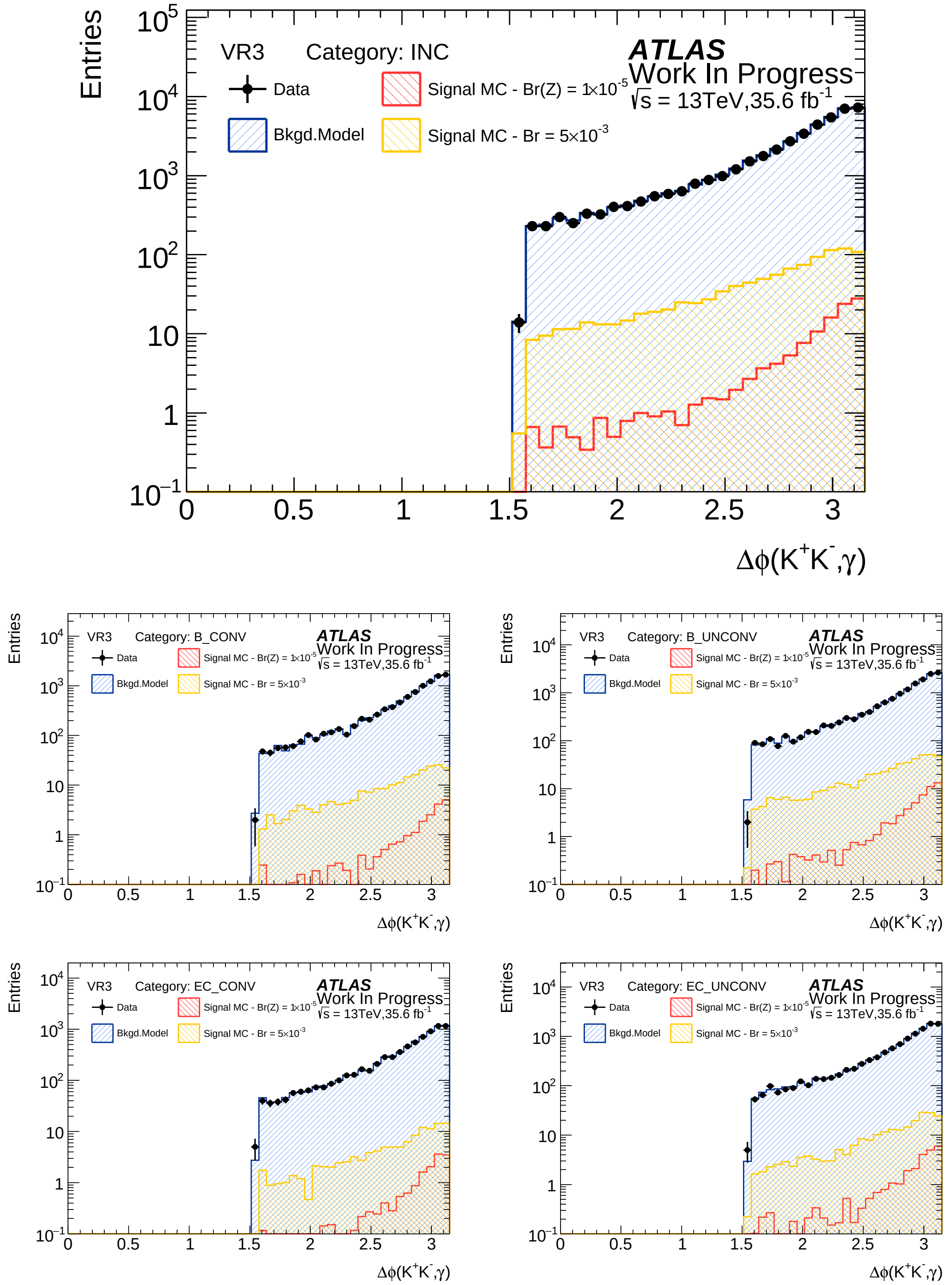

Figure C.33: $\Delta\phi^{K^+K^-,\gamma}$ distribution for the four different categories and the inclusive.

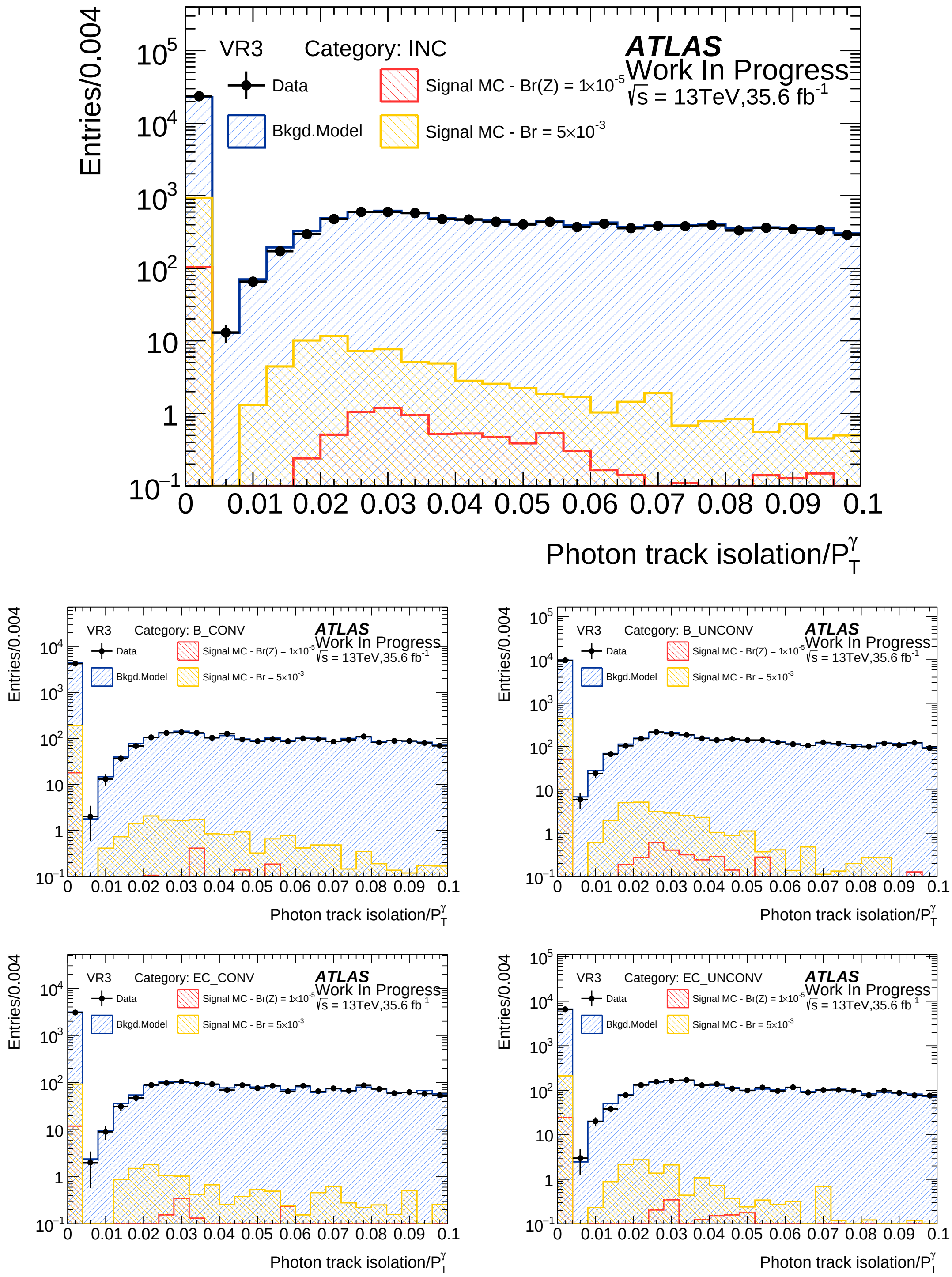

Figure C.34: Relative photon track isolation for the four different categories and the inclusive.

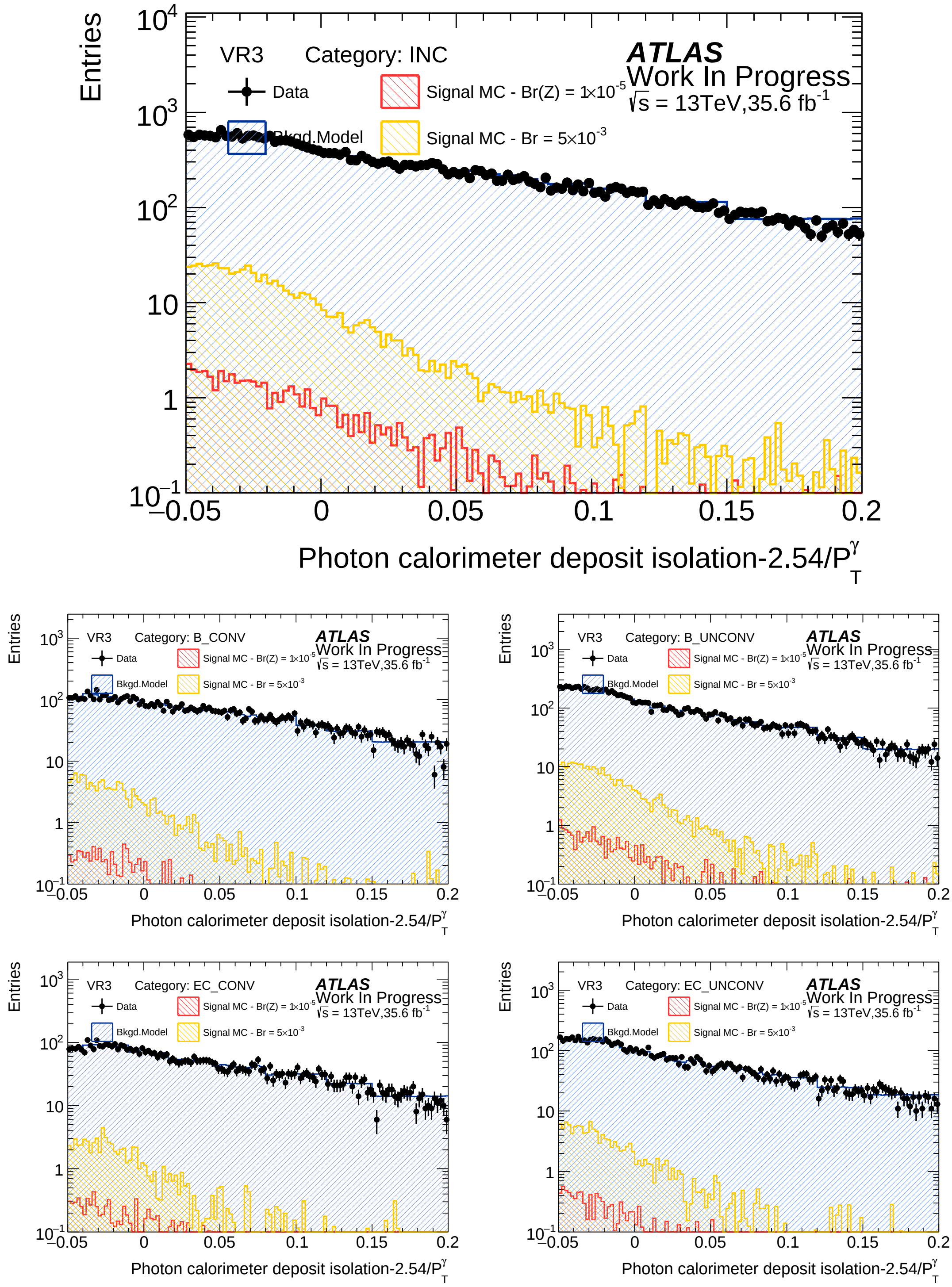

Figure C.35: Relative photon calo isolation (FixedCutTight) for the four different categories and the inclusive.

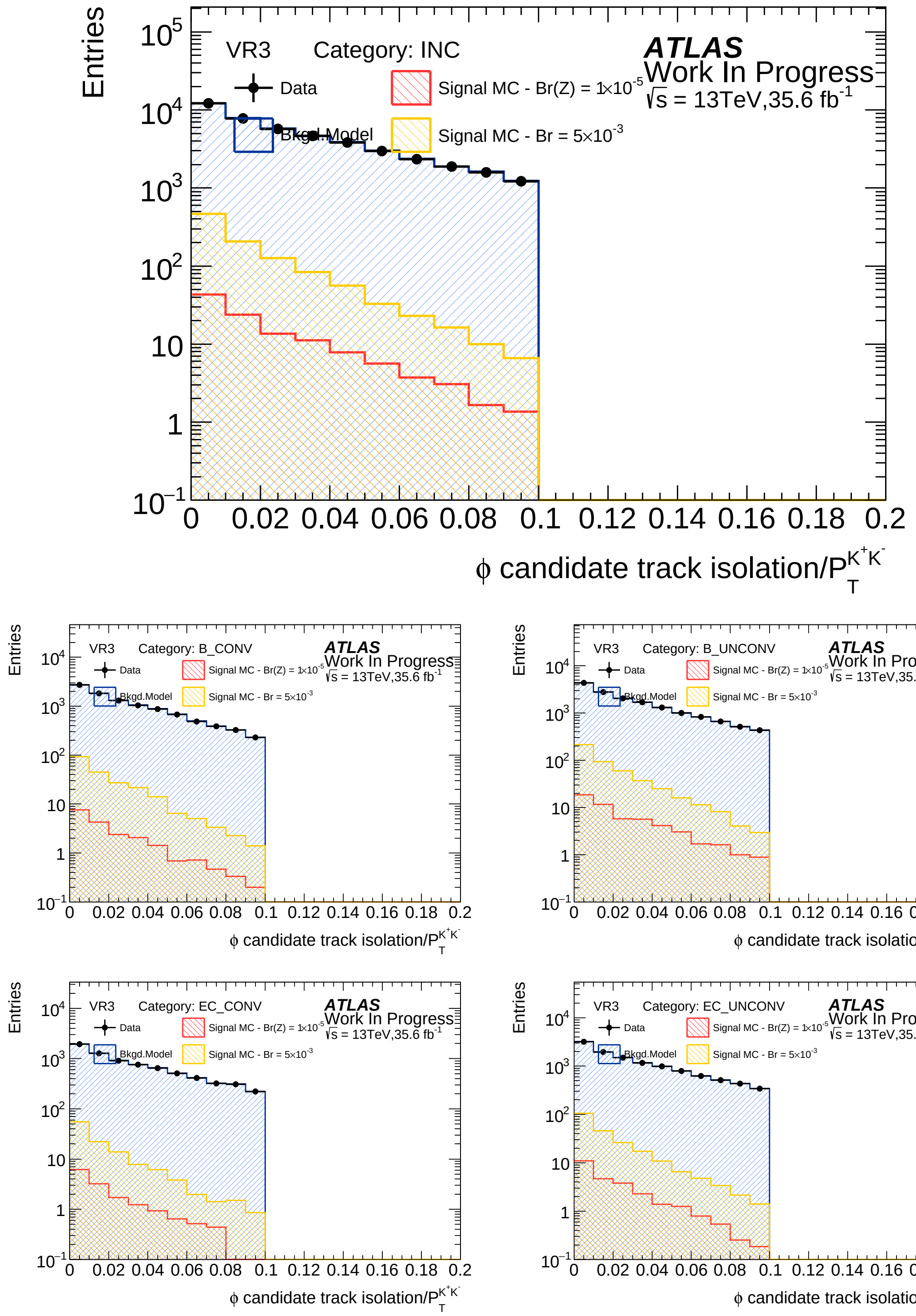

Figure C.36: Relative dikaon track isolation for the four different categories and the inclusive.

Appendix D

$\rho\gamma$ Control Plots

During the development of the $\rho\gamma$ analysis it was necessary to generate several control plots in order to check the accuracy of the background model and to assess the impact of the selection criteria. The following appendix is split into sections based on the selection criteria for the events they contain (for details see Section 4.5). The background component is represented by a binned histogram with the events normalised to the GR three-body mass distribution.

D.1 Control Plots from the GR

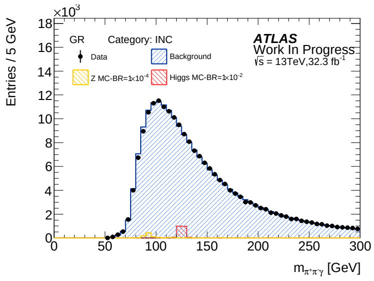

(a) $m_{\pi^{\pm}\pi^{\mp}\gamma}$ distribution.

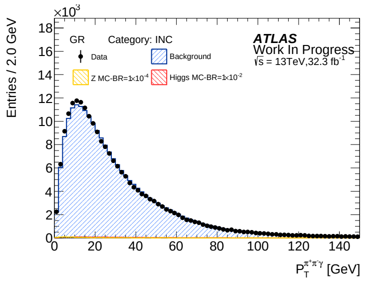

(b) $p_{\mathrm{T}}^{\pi^{\pm}\pi^{\mp}\gamma}$ distribution.

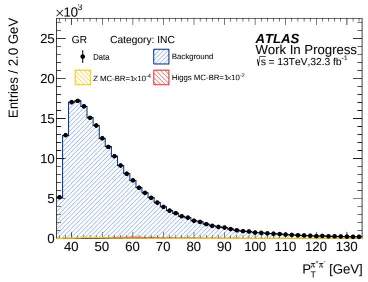

(c) $p_{\mathrm{T}}^{\pi^{\pm}\pi^{\mp}}$ distribution.

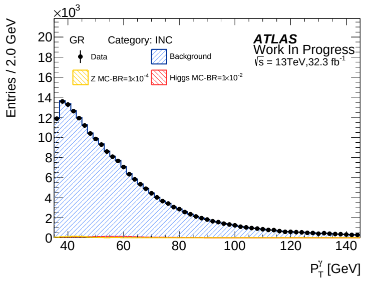

(d) p_{T}^{γ} distribution.

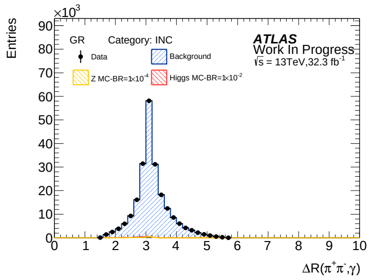

(e) $\Delta R^{\pi^{\pm}\pi^{\mp},\gamma}$ distribution.

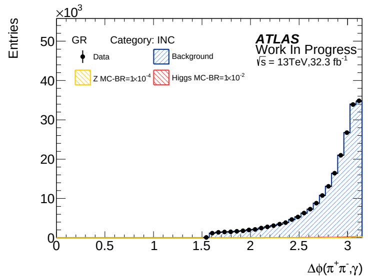

(f) $\Delta\phi^{\pi^{\pm}\pi^{\mp},\gamma}$ distribution.

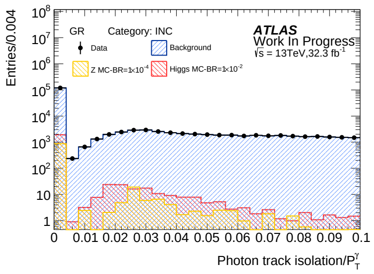

(g) Relative photon track isolation.

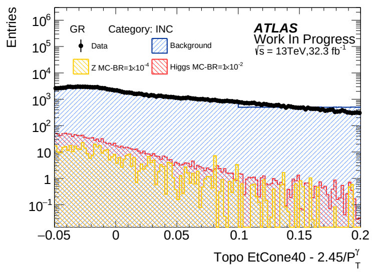

(h) Relative photon calo isolation.

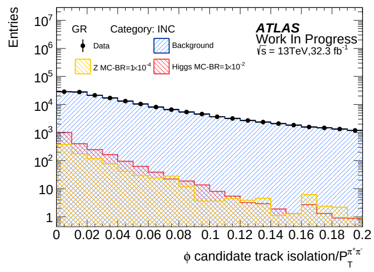

(i) Relative dipion track isolation.

Figure D.1: Various control plots showing data and the background modeling as well as the simulated signal samples. For the Photon isolation the "FixedCutTight" selection cut is applied at approximately 0.022 (the requirement is topoetcone40 $< 0.022 \times p_{\mathrm{T}}^{\gamma} + 2.45$ GeV and ptcone20 $< 0.05 \times p_{\mathrm{T}}^{\gamma}$). For the relative dipion isolation the SR selection cut is applied at < 0.1.

D.2 ρ Mass Control Plots from the Generation Region

The $m_{\pi^\pm\pi^\mp}$ distribution for signal and data in the generation regionis presented in Fig. D.2

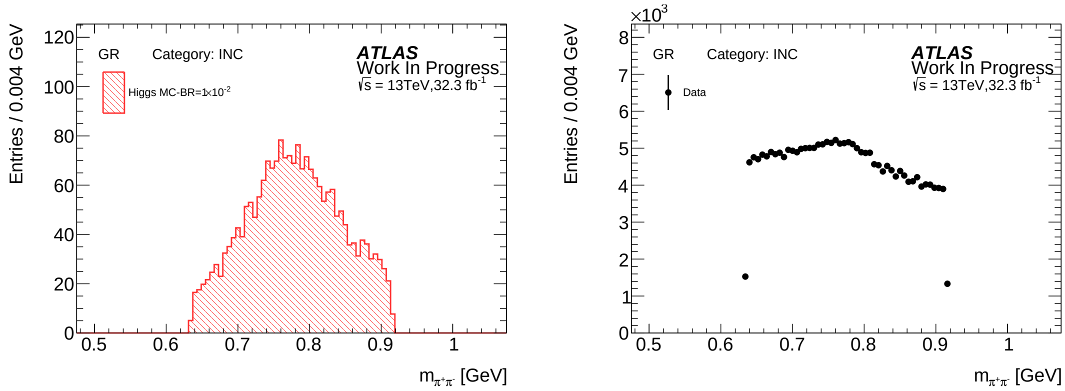

(a) (b)

Figure D.2: (a) Signal and (b) $m_{\pi^\pm\pi^\mp}$ distribution in the Generation Region.

D.3 Control Plots from VR1

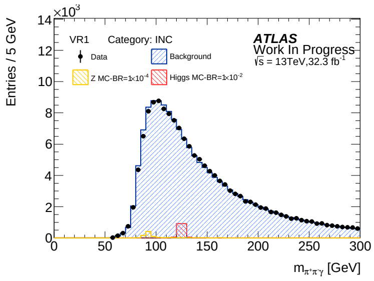

(a) Blinded $m_{\pi^\pm\pi^\mp\gamma}$ distribution.

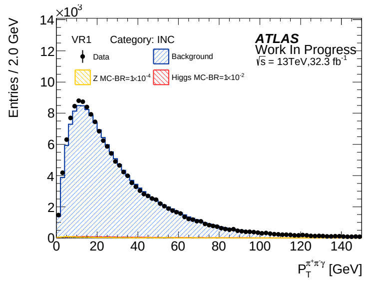

(b) $p_{\mathrm{T}}^{\pi^\pm\pi^\mp\gamma}$ distribution.

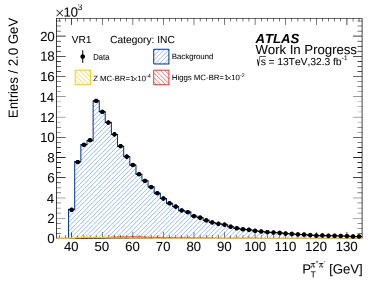

(c) $p_{\mathrm{T}}^{\pi^\pm\pi^\mp}$ distribution.

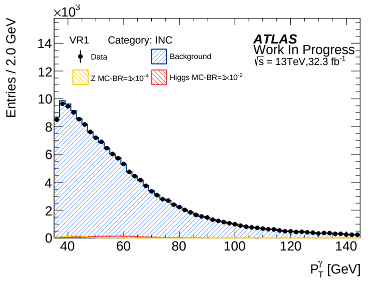

(d) p_{T}^{γ} distribution.

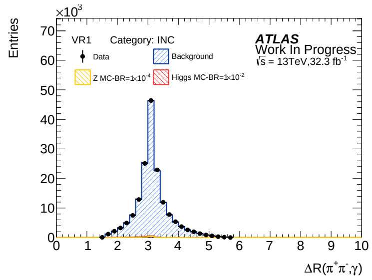

(e) $\Delta R^{\pi^\pm\pi^\mp,\gamma}$ distribution.

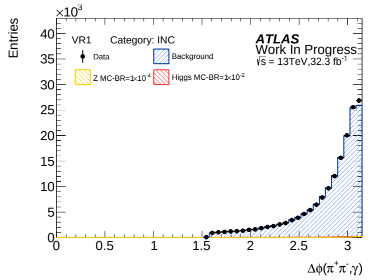

(f) $\Delta\phi^{\pi^\pm\pi^\mp,\gamma}$ distribution.

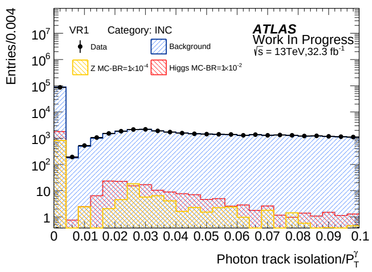

(g) Relative photon track isolation.

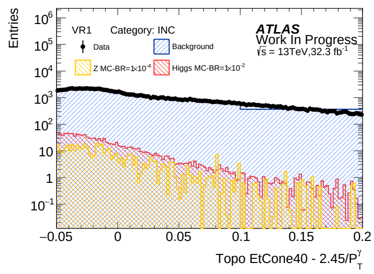

(h) Relative photon calo isolation.

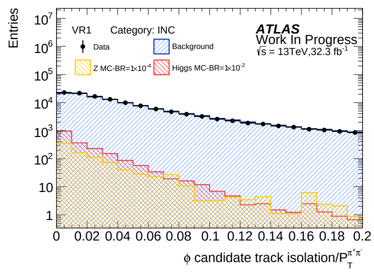

(i) Relative dipion track isolation.

Figure D.3: Various control plots showing data and the background modeling as well as the simulated signal samples. For the Photon isolation the “FixedCutTight” selection cut is applied at approximately 0.022 (the requirement is topoetcone40 $< 0.022 \times p_{\mathrm{T}}^{\gamma} + 2.45$ GeV and ptcone20 $< 0.05 \times p_{\mathrm{T}}^{\gamma}$). For the relative dipion isolation the SR selection cut is applied at < 0.1.

D.4 Control Plots from VR2

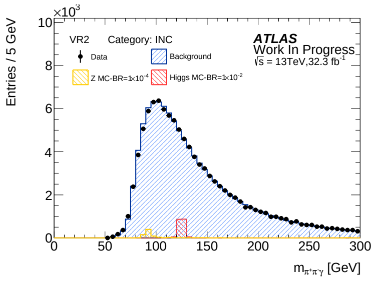

(a) Blinded $m_{\pi^\pm\pi^\mp\gamma}$ distribution.

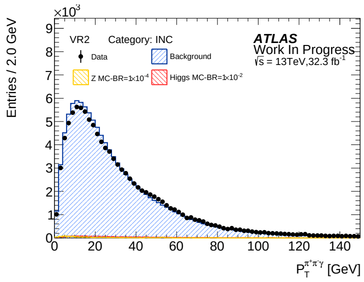

(b) $p_{\mathrm{T}}^{\pi^\pm\pi^\mp\gamma}$ distribution.

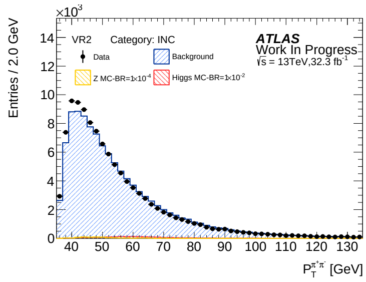

(c) $p_{\mathrm{T}}^{\pi^\pm\pi^\mp}$ distribution.

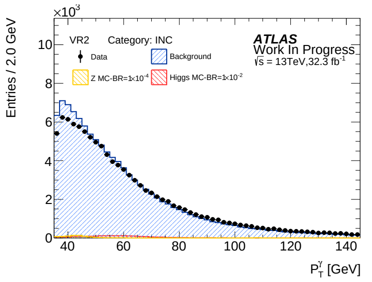

(d) p_{T}^{γ} distribution.

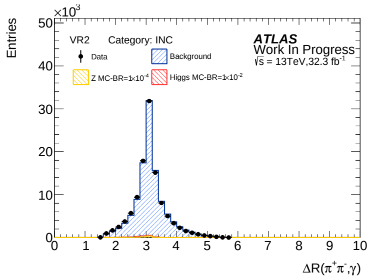

(e) $\Delta R^{\pi^\pm\pi^\mp,\gamma}$ distribution.

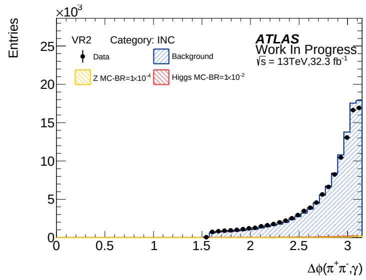

(f) $\Delta\phi^{\pi^\pm\pi^\mp,\gamma}$ distribution.

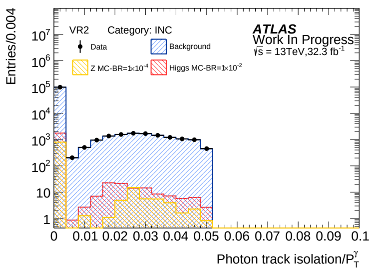

(g) Relative photon track isolation.

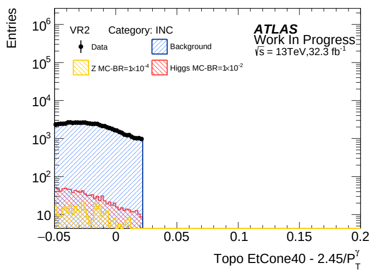

(h) Relative photon calo isolation.

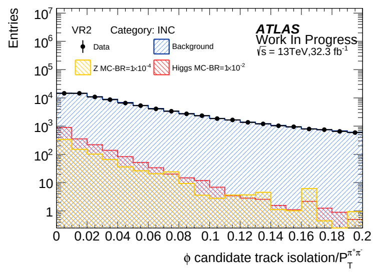

(i) Relative dipion track isolation.

Figure D.4: Various control plots showing data and the background modeling as well as the simulated signal samples. For the Photon isolation the “FixedCutTight” selection cut is applied at approximately 0.022 (the requirement is topoetcone40 $< 0.022 \times p_{\mathrm{T}}^{\gamma} + 2.45$ GeV and ptcone20 $< 0.05 \times p_{\mathrm{T}}^{\gamma}$). For the relative dipion isolation the SR selection cut is applied at < 0.1.

D.5 Control Plots from VR3

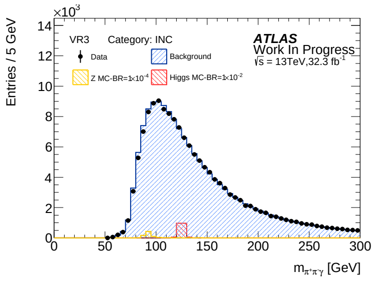

(a) Blinded $m_{\pi^\pm\pi^\mp\gamma}$ distribution.

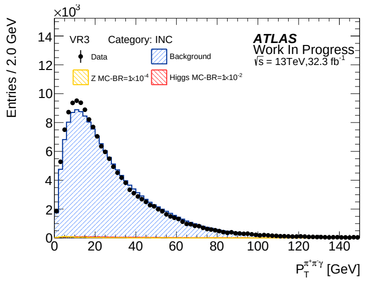

(b) $p_{\mathrm{T}}^{\pi^\pm\pi^\mp\gamma}$ distribution.

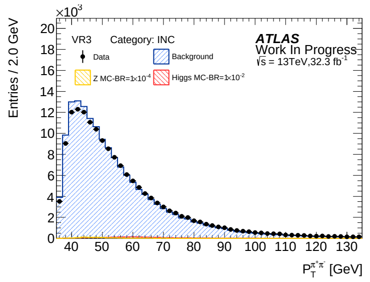

(c) $p_{\mathrm{T}}^{\pi^\pm\pi^\mp}$ distribution.

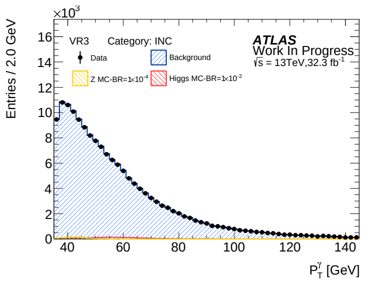

(d) p_{T}^{γ} distribution.

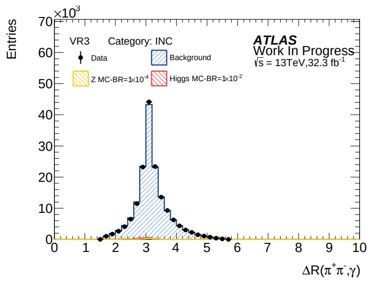

(e) $\Delta R^{\pi^\pm\pi^\mp,\gamma}$ distribution.

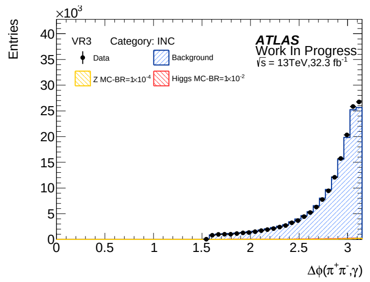

(f) $\Delta\phi^{\pi^\pm\pi^\mp,\gamma}$ distribution.

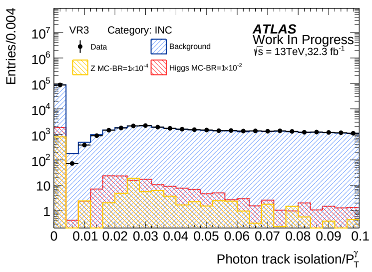

(g) Relative photon track isolation.

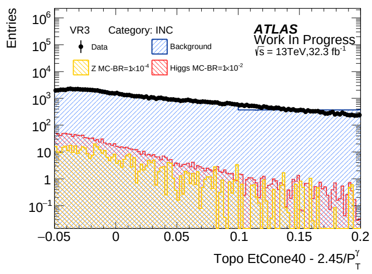

(h) Relative photon calo isolation.

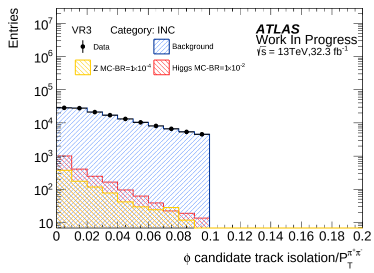

(i) Relative dipion track isolation.

Figure D.5: Various control plots showing data and the background modeling as well as the simulated signal samples. For the Photon isolation the “FixedCutTight” selection cut is applied at approximately 0.022 (the requirement is topoetcone40 $< 0.022 \times p_{\mathrm{T}}^{\gamma} + 2.45$ GeV and ptcone20 $< 0.05 \times p_{\mathrm{T}}^{\gamma}$). For the relative dipion isolation the SR selection cut is applied at < 0.1.

D.6 Control Plots from SR

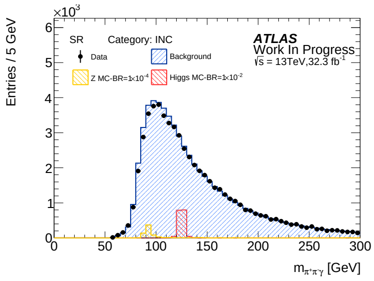

(a) Blinded $m_{\pi^{\pm}\pi^{\mp}\gamma}$ distribution.

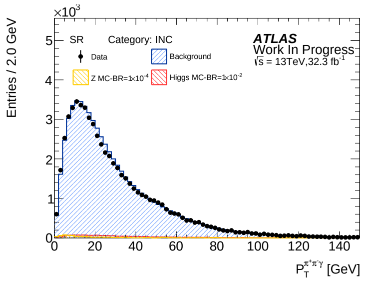

(b) $p_{\mathrm{T}}^{\pi^{\pm}\pi^{\mp}\gamma}$ distribution.

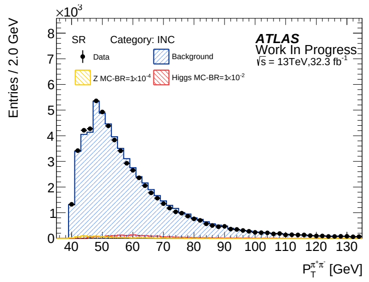

(c) $p_{\mathrm{T}}^{\pi^{\pm}\pi^{\mp}}$ distribution.

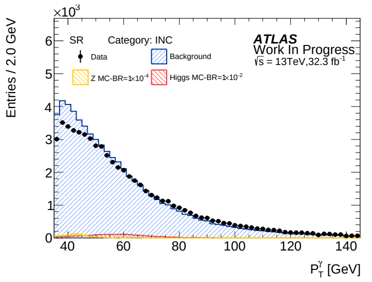

(d) p_{T}^{γ} distribution.

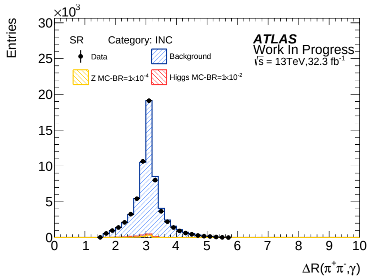

(e) $\Delta R^{\pi^{\pm}\pi^{\mp},\gamma}$ distribution.

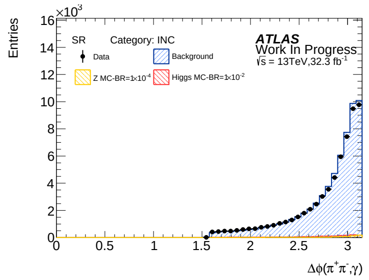

(f) $\Delta\phi^{\pi^{\pm}\pi^{\mp},\gamma}$ distribution.

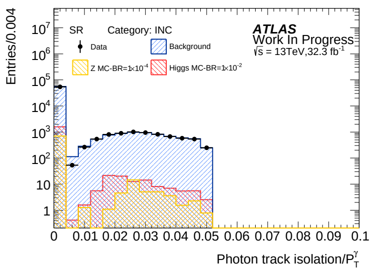

(g) Relative photon track isolation.

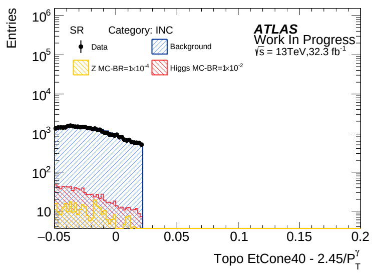

(h) Relative photon calo isolation.

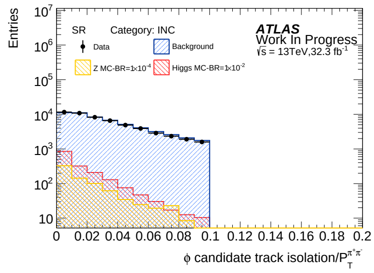

(i) Relative dipion track isolation.

Figure D.6: Various control plots showing data and the background modeling as well as the simulated signal samples. For the Photon isolation the “FixedCutTight” selection cut is applied at approximately 0.022 (the requirement is topoetcone40 $< 0.022 \times p_{\mathrm{T}}^{\gamma} + 2.45$ GeV and ptcone20 $< 0.05 \times p_{\mathrm{T}}^{\gamma}$). For the relative dipion isolation the SR selection cut is applied at < 0.1.

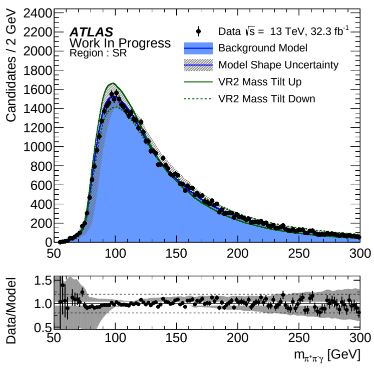

(a) Three body mass “TILT”.

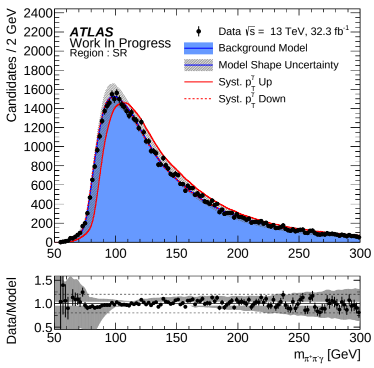

(b) p_{T}^{γ}shift.

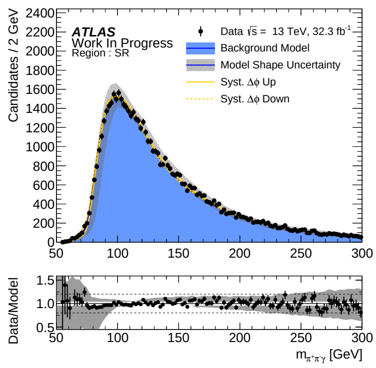

(c) $\Delta\phi(\rho\,\gamma)$ shift.

Figure D.7: Plots of the three body mass of the $\rho\gamma$ system in the signal region, the separate systematic “morphs” are shown independently.